



Forschungszentrum Karlsruhe
in der Helmholtz-Gemeinschaft

Wissenschaftliche Berichte
FZKA 7340

**Contributions to the
30th International Cosmic Ray Conference,
Merida, Mexico, 2007
by Forschungszentrum Karlsruhe
Institut für Kernphysik,
Institut für Prozessdatenverarbeitung
und Elektronik
and Universität Karlsruhe
Institut für Experimentelle Kernphysik**

J. Blümer, R. Engel, A. Haungs (Editors)
Institut für Kernphysik

August 2007

Forschungszentrum Karlsruhe

in der Helmholtz-Gemeinschaft

Wissenschaftliche Berichte

FZKA 7340

Contributions to the
30th International Cosmic Ray Conference,
Merida, Mexico, 2007

by

Forschungszentrum Karlsruhe

Institut für Kernphysik,

Institut für Prozessdatenverarbeitung und Elektronik

and

Universität Karlsruhe

Institut für Experimentelle Kernphysik

Johannes Blümer, Ralph Engel, Andreas Haungs (Editors)

Institut für Kernphysik

Forschungszentrum Karlsruhe GmbH, Karlsruhe

2007

Für diesen Bericht behalten wir uns alle Rechte vor

Forschungszentrum Karlsruhe GmbH
Postfach 3640, 76021 Karlsruhe

Mitglied der Hermann von Helmholtz-Gemeinschaft
Deutscher Forschungszentren (HGF)

ISSN 0947-8620

urn:nbn:de:0005-073408

ABSTRACT

The bi-annual International Cosmic Ray Conferences have become the most central meetings for discussing new results and recent progress in the field of cosmic ray research. The contributions to these conferences cover a wide range of subjects extending from the physics of the sun and heliosphere, over gamma-ray observations to direct and indirect cosmic ray measurements and their interpretation. Many new results are announced for the first time at these meetings.

The present volume is a compilation of the contributions of Institutes of Forschungszentrum Karlsruhe and University Karlsruhe to the 30th International Cosmic Ray Conference (ICRC), held in Merida, Mexico from July 3 to 11, 2007. The collection of contributions provides an up-to-date review of the current activities and research projects related to cosmic rays that are pursued in Karlsruhe. The articles also demonstrate the enormous progress that has been made during the last years, in particular in the field of ultra-high energy cosmic rays. Most of these contributions are the result of close and fruitful collaboration of many different groups worldwide, first of all within international collaborations such as the Pierre Auger, LOPES and KASCADE-Grande Collaborations, but also within smaller groups.

The articles compiled in this report are sorted according to the main research foci of the Karlsruhe groups. These include the physics of the knee in the cosmic ray spectrum, the transition between galactic and extra-galactic cosmic rays, and extragalactic cosmic rays of the highest energies.

Cosmic rays in the energy range from just below the knee in the cosmic ray spectrum ($10^{14.5}$ eV) to the energy of the conjectured transition between galactic and extra-galactic cosmic rays are studied with the **KASCADE-Grande** detector at the site of Forschungszentrum Karlsruhe. KASCADE-Grande is a multi-detector air shower array, which combines the electron and muon detectors of the KASCADE (KARlsruhe Shower Core and Array Detector) array with a 0.5 km^2 array of scintillators. Based on a data set from about 3 years of operation, first shower size spectra have been derived and limits on the anisotropy of the cosmic ray flux were presented at the conference.

An alternative method of air shower detection is the measurement of radio signals produced by the particles showers in the atmosphere. The physics potential of this detection technique is investigated with the **LOPES** (LOFAR PrototypE Station) array of dipole antennas at the site of the KASCADE-Grande installation. Measuring the electric field strength in the frequency range from 40 to 80 MHz, a very good correlation between the shower energy reconstructed with KASCADE-Grande and the radio signal was found. Important contributions presented at the conference include the investigation of the influence of thunderstorms on the measured field strength and the measurement of showers with large zenith angles as well as significant progress in the modelling of the emission processes of the radio signals during the shower development.

The study of cosmic rays at the highest energies and the transition between galactic and extra-galactic cosmic rays is the aim of the **Pierre Auger Project**. The Pierre Auger Observatory is the largest cosmic ray detector with one installation in the northern and southern

hemisphere to ensure full sky coverage. The southern detector is currently under construction in the Province of Mendoza, Argentina. After completion it will consist of 24 fluorescence telescopes and a surface detector array of 1600 water Cherenkov tanks, covering an area of 3000 km². A site near Lamar in Colorado, USA has been selected for the northern observatory and preparatory R&D work has begun. The data taken with the southern observatory during construction correspond to about 75% of one year of operation with the completed observatory. Even with this limited data set, the Auger results represented the highlights of the conference. The Auger data provide unambiguous proof of a suppression of the ultra-high energy cosmic ray flux. They also show that the fraction of photons in the highest energy cosmic rays is very small, ruling out many exotic physics scenarios. Furthermore, a significant discrepancy between the characteristics of simulated and measured air showers at ultra-high energy has been found.

Due to the indirect character of cosmic ray measurements with air showers, all analyses discussed above depend on the detailed simulation of cosmic ray interactions and extensive air showers. Recent progress in this field is summarized in the contributions related to the **CORSIKA** (Cosmic Ray Simulations for KASCADE and Auger) simulation package, the measurement of the characteristics of hadronic interactions, and air shower simulation studies.

Other contributions to the conference in Merida include the measurement of the fluorescence light yield with the **AIRLIGHT** experiment in Karlsruhe, the direct measurement of cosmic rays at lower energy with the balloon borne instrument **TRACER** (Transition Radiation Array for Cosmic Energetic Radiation) and possible theoretical interpretations, and the search for signals from dark matter annihilation.

Beiträge zur 30th International Cosmic Ray Conference (ICRC), Merida, Mexico, 2007
des Forschungszentrums Karlsruhe, Institut für Kernphysik und Institut für Prozess-
datenverarbeitung und Elektronik, sowie der Universität Karlsruhe, Institut für experi-
mentelle Kernphysik

Zusammenfassung

Die zweijährlich stattfindende internationale Konferenz zur kosmischen Strahlung (ICRC) ist die in diesem Forschungsbereich weltweit wichtigste Tagung um Resultate und neueste Entwicklungen vorzustellen und zu diskutieren. Beiträge zu diesen Konferenzen umfassen einen weiten wissenschaftlichen Bereich mit experimentellen Ergebnissen aus der Sonnen- und Heliosphären-Physik, über die Quellenbeobachtung mit hochenergetischen Gammas bis zu direkter und indirekter Messung kosmischer Teilchen, sowie die Interpretation all dieser Beobachtungen. Viele neue Resultate werden bei dieser Konferenzreihe erstmalig der Öffentlichkeit vorgestellt.

Die in diesem Band zusammengestellten Beiträge sind von den herausgebenden Instituten des Forschungszentrums und der Universität Karlsruhe in enger und fruchtbarer Zusammenarbeit mit weiteren nationalen und internationalen Universitäten und Instituten entstanden und auf der diesjährigen ICRC vorgestellt worden. Die Zusammenarbeit betrifft insbesondere Studien und Datenanalysen innerhalb der großen internationalen Kollaborationen wie der Pierre-Auger-, der KASCADE-Grande-, und der LOPES-Kollaborationen, aber auch Arbeiten innerhalb kleinerer Gruppen. Die Sammlung stellt damit einen Überblick über alle die kosmische Strahlung betreffenden, aktuellen Karlsruher Aktivitäten und Projekte dar. Die Beiträge belegen auch den enormen Fortschritt im in diesem Forschungsgebiet der letzten Jahre, insbesondere bei der Messung und Analyse der hochenergetischen kosmischen Strahlung.

Die Beiträge in diesem Band sind geordnet gemäß den Forschungsschwerpunkten der Karlsruher Gruppen. Dies betrifft die kosmische Strahlung im Energiebereich des so genannten Knies, dem Bereich des Übergangs von galaktischer zu extragalaktischer kosmischer Strahlung und der Messung extragalaktischer Teilchen höchster Energien.

Luftschauermessungen von kosmischen Teilchen mit einer Energie gerade unterhalb des Knies im Spektrum ($10^{14.5}$ eV) bis in etwa zu einem Energiebereich, bei dem der Übergang von galaktischem zu extragalaktischem Teilchenursprung vermutet wird, werden mit dem **KASCADE-Grande** Experiment gemessen, das sich auf dem Gelände des Forschungszentrums Karlsruhe befindet. Cascade-Grande ist ein Multi-Detektor Aufbau, das die Detektoren des ursprünglichen KASCADE Experimentes mit einem neuen Detektorfeld verbindet, das aus 37 Stationen besteht, verteilt auf einer Fläche von 0.5 km^2 . Basierend auf einen Datensatz von nunmehr drei Betriebsjahren, konnten auf der Konferenz erste Ergebnisse bezüglich Spektren der gemessenen Schauergößen, sowie Grenzen für Anisotropien in der Verteilung der Ankunftsrichtungen der kosmischen Teilchen vorgestellt werden.

Als eine alternative Messmethode hochenergetischer Teilchen wird die Messung der Radioemission während der Luftschauerentwicklung in der Atmosphäre betrachtet. Das physikalische Potential dieser neuen Messtechnik wird mit Hilfe der **LOPES** (LOFAR Prototype Station) Dipolantennen untersucht. LOPES ist aufgebaut innerhalb des KASCADE-Grande Experimentes und misst in Koinzidenz mit den Teilchendetektoren. Mit LOPES wird die elektrische Feldstärke im Frequenzbereich von 40-80 MHz gemessen, und es konnte eine sehr starke Korrelation mit der primären Energie der Schauer auslösenden Teilchen gefunden werden. Weitere wichtige Ergebnisse dieser Untersuchungen, wie der Einfluss von Gewitterstürmen auf die Feldstärke oder das Verhalten der Radioemission für sehr waagrechte Schauer konnten ebenfalls präsentiert werden. Zudem konnte über einen signifikanten Fortschritt in der Simulation der Emissionsprozesse des Radiosignals berichtet werden.

Das Studium der höchstenergetischsten kosmischen Teilchen und des Übergangs von galaktischer zu extragalaktischer kosmischer Strahlung ist das Ziel des Pierre Auger Projektes. Das **Pierre Auger Observatorium** ist das weltweit größte seiner Art mit je einer Installation auf der Nord- und der Südhalbkugel der Erde. Der südliche Experimentteil in der Provinz Mendoza in Argentinien steht kurz vor der Fertigstellung. Nach dem vollständigen Aufbau wird es aus 24 Fluoreszenz-Teleskopen und einem Feld von 1600 Wasser-Tscherenkow Detektoren bestehen, das eine Fläche von 3000 km² abdeckt. Die Kleinstadt Lamar in Colorado, USA wurde als Areal für das Nord-Observatorium ausgesucht, und erste vorbereitende Entwicklungsarbeiten vor Ort wurden begonnen und auf der Konferenz präsentiert. Die im südlichen Observatorium bereits genommenen Daten entsprechen ungefähr 75% der Messzeit eines Jahres des vollständig aufgebauten Experimentes. Bereits mit diesem begrenzten Datensatz waren die ersten Auger Ergebnisse das wissenschaftliche Highlight auf der diesjährigen Konferenz. Die Analysen der Daten beweisen eindeutig eine Unterdrückung im Fluss der höchstenergetischsten kosmischen Strahlung. Auch konnte gezeigt werden, dass der Anteil primärer Gammastrahlung in diesem Energiebereich sehr klein ist, und dass damit bereits viele exotische Theorien zur Entstehung der kosmischen Strahlung ausgeschlossen sind. Des Weiteren wurde eine signifikante Diskrepanz in der Charakteristik von simulierten zu gemessenen Luftschauern bei den allerhöchsten Energien gefunden und auf der Konferenz diskutiert.

Da alle Messungen dieser kosmischen Teilchen nur indirekt über den Nachweis von Luftschauer durchgeführt werden können, basieren alle Analyse Ergebnisse auf detaillierten Simulationen der Luftschauerentwicklung und hier insbesondere der hadronischen Wechselwirkungen. Fortschritte auf diesem Gebiet wurden präsentiert in Beiträgen im Zusammenhang mit der Weiterentwicklung und Verbesserung des **CORSIKA** (Cosmic Ray Simulations for KASCADE and Auger) Simulation-Programmes, der besseren Beschreibung hadronischer Wechselwirkungen auch durch Beteiligung an Beschleunigerexperimenten, und allgemeinen Studien zur Luftschauerentwicklung.

Weitere Beiträge aus Karlsruhe zur Konferenz in Merida hatten zum Thema die Messung der Fluoreszenz-Lichtausbeute mit dem **AIRLIGHT**-Experiment in Karlsruhe, die direkte Messung kosmischer Teilchen niedrigerer Energien und deren Interpretation mit dem Ballon-Experiment **TRACER** (Transition Radiation Array for Cosmic Energetic Radiation) und die Suche nach Signalen der Annihilation von Teilchen der dunklen Materie.

CONTENTS

KASCADE-Grande

| | |
|--|----|
| The KASCADE-Grande Experiment A. Haungs et al., KASCADE-Grande Collaboration | 1 |
| Shower size spectrum reconstructed with KASCADE-Grande F. Di Pierro et al., KASCADE-Grande Collaboration | 5 |
| Electron shower size spectra reconstructed with KASCADE-Grande data F. Cossavella et al., KASCADE-Grande Collaboration | 9 |
| Muon spectra reconstructed from inclined air showers measured by KASCADEGrande J.C. Arteaga et al., KASCADE-Grande Collaboration | 13 |
| Features of the S(500) distribution for large air showers detected with the KASCADE-Grande array G. Toma et al., KASCADE-Grande Collaboration | 17 |
| Search for anisotropy and point sources of cosmic rays with the KASCADE-Grande experiment S. Over, M. Stümpert et al., KASCADE-Grande Collaboration | 21 |
| The muon component of air showers measured by the KASCADE-Grande Experiment V. De Souza, J. van Buren et al., KASCADE-Grande Collaboration | 25 |
| Separation of the electromagnetic and the muon component in EAS by their arrival times M. Brüggemann et al., KASCADE-Grande Collaboration | 29 |
| Muon Production Height in the Air-Shower Experiment KASCADE-Grande P. Doll et al., KASCADE-Grande Collaboration | 33 |
| Tests of hadronic interaction models with muon pseudorapidities measured with KASCADE-Grande J. Zabierowski et al., KASCADE-Grande Collaboration | 37 |
| Reconstruction of primary mass group energy spectra with KASCADE H. Ulrich et al., KASCADE-Grande Collaboration | 41 |
| Measurement of attenuation lengths of hadrons in air showers with KASCADE D. Hildebrand et al., KASCADE-Grande Collaboration | 45 |

LOPES and radio signal simulation studies

| | |
|--|----|
| Investigations of the lateral extension of radio emission in air showers by LOPES30 measurements S. Nehls et al., LOPES Collaboration | 49 |
| Operation of LOPES-30 for Polarization Measurements of the Radio Emission of Cosmic Ray Air Showers P.G. Isar et al., LOPES Collaboration | 53 |
| Update on radio detection of inclined air showers with LOPES-10 A. Saftoiu et al., LOPES Collaboration | 57 |
| Radio emission of air showers in electric fields S. Buitink et al., LOPES Collaboration | 61 |
| Trigger Strategy for Radio Detection of Atmospheric Air Showers with LOPES ^{STAR} T. Asch, O. Krömer et al., LOPES Collaboration | 65 |
| REAS2: CORSIKA-based Monte Carlo simulations of geosynchrotron radio emission T. Huege, R. Ulrich, R. Engel | 69 |
| Energy and composition sensitivity of geosynchrotron radio emission from EAS T. Huege, R. Ulrich, R. Engel | 73 |
| Calculation of radio emission from high-energy air showers N.N. Kalmykov, A.A. Konstantinov, R. Engel | 77 |
| Radio Detection of Neutrinos from Behind a Mountain O. Brusova, L. Anchordoqui, T. Huege, K. Martens | 81 |
| The LOFAR air shower front evolution library S. Lafebre, T. Huege, H. Falcke, J. Kuijpers | 85 |

Pierre-Auger-Project

| | |
|--|-----|
| Measurement of the UHECR energy spectrum using data from the Surface Detector of the Pierre Auger Observatory M. Roth for the Pierre Auger Collaboration | 89 |
| Study of the Cosmic Ray Composition above 0.4 EeV using the Longitudinal Profiles of Showers observed at the Pierre Auger Observatory M. Unger for the Pierre Auger Collaboration | 93 |
| Test of hadronic interaction models with data from the Pierre Auger Observatory R. Engel for the Pierre Auger Collaboration | 97 |
| HEAT – Enhancement Telescopes for the Pierre Auger Southern Observatory H.O. Klages for the Pierre Auger Collaboration | 101 |
| Longitudinal Shower Profile Reconstruction from Fluorescence and Cherenkov Light M. Unger, R. Engel, F. Schüssler and R. Ulrich | 105 |

| | |
|--|------------|
| Comparison of preshower characteristics at Auger South and North P. Homola, M. Risse, R. Engel, D. Gora, J. Pekala, B. Wilczynska, H. Wilczynski | 109 |
| Variation of the shower lateral spread with air temperature at the ground B. Wilczynska, R. Engel, P. Homola, B. Keilhauer, H. Klages, J. Pekala, H. Wilczynski | 113 |
| Simulation study of shower profiles from ultra-high energy cosmic rays V. Scherini, F. Schüssler, R. Engel, K.-H. Kampert, M. Risse, M. Unger | 117 |
| Contribution of atmospheric scattering of light to shower signal in a fluorescence detector J. Pekala, D. Gora, P. Homola, M. Risse, B. Wilczynska, H. Wilczynski | 121 |
| New statistical parameters for mass composition studies with energy above 10^{17} eV F. Catalani, J.A. Chinellato, V. De Souza, J. Takahashi | 125 |
| A MC simulation of neutrino showers and their detection with the Pierre Auger Observatory D. Gora, M. Roth, A. Tamborero | 129 |
| Investigation of backgrounds for horizontal neutrino showers at ultra-high energy O. Tascau, R. Engel, K.-H. Kampert, M. Risse | 133 |
| Pierre-Auger-Project: Abstracts of further contributions | 137 |
| | |
| Air shower simulation and hadronic interactions | |
| Latest Results from the Air Shower Simulation Programs CORSIKA and CONEX T. Pierog, R. Engel, D. Heck, S. Ostapchenko, K. Werner | 149 |
| The Hadronic Interaction Model EPOS and Air Shower Simulations: New Results on Muon Production T. Pierog, K. Werner | 153 |
| Pion production in proton- and pion-carbon collisions at 12 GeV/c measured with HARP C. Meurer, J. Blümer, R. Engel, A. Haungs, A. Roth and the HARP Collaboration | 157 |
| On the relation between the proton-air cross section and fluctuations of the shower longitudinal profile R. Ulrich, J. Blümer, R. Engel, F. Schüssler, M. Unger | 161 |
| Simulation studies of the charge ratio of the muon density distribution in EAS as measured by the WILLI detector triggered by a mini-array B. Mitrica, O. Sima, I.M. Brancus, H. Rebel, A. Haungs, A. Saftoiu | 165 |
| The muon charge ratio in cosmic ray air showers H. Rebel, O. Sima, A. Haungs, J. Oehlschläger | 169 |

Further articles

- Measurement of the Air Fluorescence Yield with the AirLight Experiment 173
T. Waldenmaier, J. Blümer, D. Gonzalez, H.O. Klages
- Laser Calibration of the Air Fluorescence Yield Experiment AirLight 177
D. Gonzalez, J. Blümer, H.O. Klages, T. Waldenmaier
- The TRACER Project: Instrument Concept, Balloon Flights, and Analysis Procedures 181
D. Müller, M. Ave, P.J. Boyle, F. Gahbauer, C. Höppner, J. Hörandel, M. Ichimura,
A. Romero-Wolf
- Cosmic Ray Energy Spectra of Primary Nuclei from Oxygen to Iron: Results from 185
the TRACER 2003 LDB Flight
P.J. Boyle, M. Ave, C. Höppner, J. Hörandel, M. Ichimura, D. Müller, A. Romero-Wolf
- Propagation of High-Energy Cosmic Rays through the Galaxy: Discussion and 189
Interpretation of TRACER Results
M. Ave, P. Boyle, C. Höppner, J. Hörandel, M. Ichimura, D. Müller,
- On the origin of the knees in the cosmic-ray energy spectrum 193
J. Hörandel, N.N. Kalmykov, A.a. Silaev, A.V. Timokhin
- Confinement of Cosmic Rays in Dark Matter clumps 197
W. De Boer, V. Zhukov

Collaboration lists 201



The KASCADE-Grande Experiment

A. HAUNGS^a, W.D. APEL^a, J.C. ARTEAGA^a, F. BADEA^a, K. BEKK^a, M. BERTAINA^b, J. BLÜMER^{a,c}, H. BOZDOĞ^a, I.M. BRANCUS^d, M. BRÜGGEMANN^e, P. BUCHHOLZ^e, A. CHIAVASSA^b, F. COSSAVELLA^c, K. DAUMILLER^a, V. DE SOUZA^c, F. DI PIERRO^b, P. DOLL^a, R. ENGEL^a, J. ENGLER^a, M. FINGER^c, D. FUHRMANN^f, P.L. GHIA^g, H.J. GILS^a, R. GLASSTETTER^f, C. GRUPEN^e, D. HECK^a, J.R. HÖRANDEL^c, T. HUEGE^a, P.G. ISAR^a, K.-H. KAMPERT^f, D. KICKELBICK^e, H.O. KLAGES^a, Y. KOLOTAEV^e, P. LUCZAK^h, H.J. MATHES^a, H.J. MAYER^a, C. MEURER^a, J. MILKE^a, B. MITRICA^d, A. MORALES^a, C. MORELLO^g, G. NAVARRA^b, S. NEHLS^a, J. OEHLISCHLÄGER^a, S. OSTAPCHENKO^a, S. OVER^e, M. PETCU^d, T. PIEROG^a, S. PLEWNIA^a, H. REBEL^a, M. ROTH^a, H. SCHIELER^a, O. SIMAⁱ, M. STÜMPERT^c, G. TOMA^d, G.C. TRINCHERO^g, H. ULRICH^a, J. VAN BUREN^a, W. WALKOWIAK^e, A. WEINDL^a, J. WOCHOLEA^a, J. ZABIEROWSKI^h.

^a *Institut für Kernphysik, Forschungszentrum Karlsruhe, Germany*

^b *Dipartimento di Fisica Generale dell'Università Torino, Italy*

^c *Institut für Experimentelle Kernphysik, Universität Karlsruhe, Germany*

^d *National Institute of Physics and Nuclear Engineering, Bucharest, Romania*

^e *Fachbereich Physik, Universität Siegen, Germany*

^f *Fachbereich Physik, Universität Wuppertal, Germany*

^g *Istituto di Fisica dello Spazio Interplanetario, INAF Torino, Italy*

^h *Soltan Institute for Nuclear Studies, Lodz, Poland*

ⁱ *Department of Physics, University of Bucharest, Romania*

andreas.haungs@ik.fzk.de

Abstract: KASCADE-Grande is an extensive air shower experiment at Forschungszentrum Karlsruhe, Germany. Main parts of the experiment are the Grande array spread over an area of $700 \times 700\text{m}^2$, the original KASCADE array covering $200 \times 200\text{m}^2$ with unshielded and shielded detectors, and additional muon tracking devices. This multi-detector system allows to investigate the energy spectrum, composition, and anisotropies of cosmic rays in the energy range up to 1 EeV. An overview on the performance of the apparatus, shower reconstruction methods, and first results will be given.

Introduction

The major goal of KASCADE-Grande (covering a primary energy range of $10^{14} - 10^{18}$ eV) is the observation of the 'iron-knee' in the cosmic-ray spectrum at around 100 PeV, which is expected following KASCADE observations where the positions of the knees of individual mass groups suggest a rigidity dependence [1, 2]. The capability of KASCADE-Grande will allow to reconstruct the energy spectra of various mass groups similar to KASCADE, which will give the possibility to distinguish between astrophysical models for the transition region from cosmic rays of galactic to extra-

galactic origin; i.e. between models of the type claimed by Berezhinsky [3] (prediction of pure extragalactic proton composition already at energies around 10^{18} eV) and models which have an extension of the galactic component up to the ankle and therefore a mixed composition in the energy range of KASCADE-Grande (e.g. [4, 5]). Additionally, the validity of hadronic interaction models used in CORSIKA Monte Carlo simulations of ultra-high energy air showers will be tested with KASCADE-Grande. Investigations of the radio emission in air showers are continued at the site of KASCADE-Grande with promising results paving the way for this new detection technique [6].

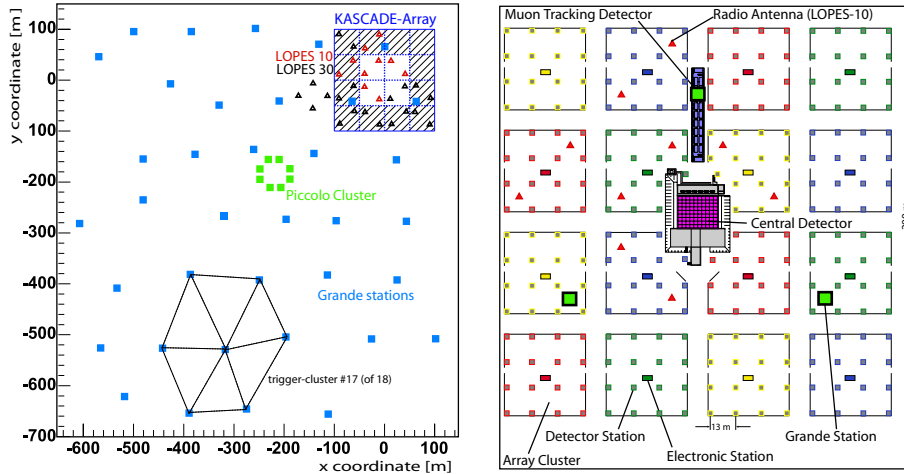


Figure 1: Layout of the KASCADE-Grande experiment: The KASCADE array, the distribution of the 37 stations of the Grande array, and the small Piccolo cluster for fast trigger purposes are shown. The location of the 30 LOPES radio antennas is also displayed. The right part zooms into the KASCADE array where the muon tracking and the central detector are located. The outer 12 clusters of the KASCADE array consists of μ - and e/γ -detectors, the inner 4 clusters of e/γ -detectors, only.

The Set-Up

The existing multi-detector experiment KASCADE [7] (located at 49.1°n , 8.4°e , 110 m a.s.l.), which takes data since 1996, was extended to KASCADE-Grande in 2003 by installing a large array of 37 stations consisting of 10 m^2 scintillation detectors each, with an average spacing of 137 m (Figure 1). The stations comprise 16 photomultipliers each providing a high dynamic range from 1/3 to 30000 charged particles per station for the reconstruction of particle densities and timing measurements. The signals are amplified and shaped inside the Grande stations, and after transmission to a central DAQ station digitized in peak sensitive ADCs. KASCADE-Grande provides an area of 0.5 km^2 and operates jointly with the existing KASCADE detectors. Grande is electronically subdivided in 18 trigger clusters (see Fig. 1) and read out and jointly analyzed with KASCADE for showers fulfilling at least one of these 7-fold coincidences. The joint measurements are ensured by an additional cluster (Piccolo) close to the center of KASCADE-Grande for trigger purposes. Piccolo consists of $8 \times 10\text{ m}^2$ stations equipped with plastic scintillators. While the Grande detectors are sensitive to charged particles, the KASCADE detec-

Table 1: Compilation of the KASCADE-Grande main detector components.

| Detector Particles | sensitive area [m^2] |
|---|------------------------------------|
| Grande charged | 370 |
| Piccolo charged | 80 |
| KASCADE array e/γ electrons | 490 |
| KASCADE array μ muons ($E_\mu^{\text{thresh}} = 230\text{ MeV}$) | 622 |
| MTD muons ($E_\mu^{\text{thresh}} = 800\text{ MeV}$) | 3×128 |
| MWPCs/LSTs muons ($E_\mu^{\text{thresh}} = 2.4\text{ GeV}$) | 3×129 |
| LOPES 30 antennas radio emission | $> 5 \cdot 10^5$ |

tors measure the electromagnetic component and the muonic components separately. The 252 KASCADE stations covering an area of $200 \times 200\text{ m}^2$ consist of unshielded liquid scintillators on top of shielded plastic scintillators. The latter enables to reconstruct the lateral distributions of muons on an event-by-event basis. Further muon detector systems at a muon tracking detector (MTD) and at the

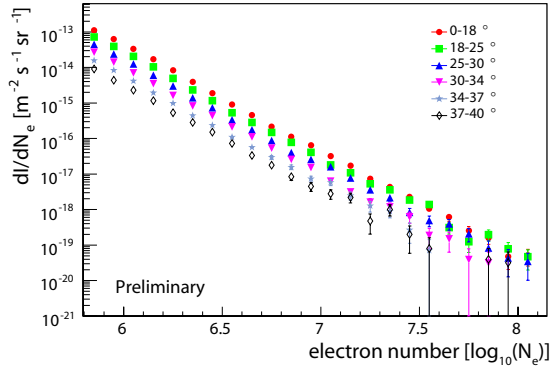


Figure 2: KASCADE-Grande shower size (total number of electrons) spectra for different zenith angular ranges.

Central Detector of KASCADE allow to investigate the muon component of EAS at three different threshold energies.

Capabilities

Basic shower observables like the core position, angle-of-incidence, or total number of charged particles are provided by the Grande stations. A core position resolution of ≈ 15 m and a direction resolution of $\approx 0.5^\circ$ is reached. The estimation of energy and mass of the primary particles is based on a combined investigation of the charged particle [8, 9], electron and muon components measured by the detector arrays of Grande and KASCADE [10, 11]. In particular the possibility to reconstruct the total muon number for Grande measured showers is the salient feature of KASCADE-Grande compared to other experiments in this energy range. A common fit to the energy deposits with the relative muon to electron ratio as additional free parameter enables a resolution of electron and muon numbers in the order of 15% and 20%, respectively, for primary energies of 100 PeV. Additional sensitivity for composition estimates and interaction model tests is provided by muon density measurements and muon tracking at different muon energy thresholds [12]. The MTD measures the incidence angles of muons in EAS. These angles provide sensitivity to the longitudinal development of the showers [13, 14]. Below the hadron calorimeter of the central detector there

are three layers of position sensitive muon detectors, measuring high-energy muons also in case of Grande triggered showers. The complementary information of the showers measured by the central and the muon tracking detectors is predominantly being used for a better understanding of the features of an air-shower and for tests and improvements of the hadronic interaction models underlying the analyses.

First Analyses

In the following some examples are given for first analyses based on the present available data set of KASCADE-Grande.

Figure 2 presents the differential shower size spectra for various zenith angular ranges, where the shower size here describes the number of electrons, only, corrected for the muon content in the shower [15]. Full efficiency is reached for a shower size of approximately one million corresponding to a primary energy of $\approx 3 \cdot 10^{16}$ eV.

For each event also the total muon number is reconstructed and the muon size spectra can be determined. It was found [16], that this works for showers with inclination angles up to 70° with sufficient accuracy. In particular, inclined showers allow a cross-check of the predictions of hadronic interaction models concerning the muon content in EAS. Figure 3 compares for three zenith angular ranges the measured muon size spectra with the simulated ones (full simulations including detector response and reconstruction), where the simulations are normalized to the number of vertical showers. The increasing deviation with increasing zenith angle hints to a too less muon number predicted by the Monte Carlo simulations (QGSJET II) or an insufficient description of the muon energy spectrum in the simulations.

In addition to the total muon number KASCADE-Grande allows to reconstruct the muon density at a certain distance to the shower core, which gives a sensitivity to changes in the elemental composition [17].

Analyzing the arrival directions of the detected showers a preliminary result on limits of the large scale anisotropy in terms of the Rayleigh ampli-

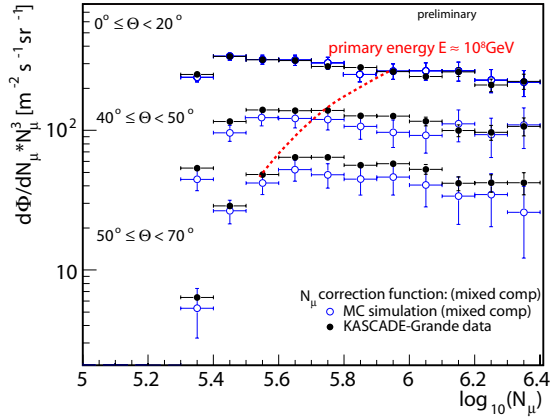


Figure 3: Muon Shower size spectra for different zenith angular ranges. The data are compared with QGSJETII simulations (including detector response and reconstruction), which are normalized to the vertical shower sample.

tude [18] could be obtained (Fig. 4) applying two different methods.

Conclusions

At the KASCADE experiment, the two-dimensional distribution shower size - number of muons played the fundamental role in reconstruction of energy spectra of single mass groups. By the first analyses shown here we illustrate the capability of KASCADE-Grande to perform an unfolding procedure like in KASCADE. KASCADE-Grande is fully efficient at energies above $3 \cdot 10^{16}$ eV, thus providing a large overlap with the KASCADE energy range. Due to the fact that also for KASCADE-Grande a wealth of information on individual showers is available, tests of the hadronic interaction models and anisotropy studies will be possible in addition to the reconstruction of energy spectrum and composition.

References

- [1] T. Antoni et al. KASCADE Coll., *Astrop. Phys.* 24, 1 (2005).
- [2] H. Ulrich et al. KASCADE-Grande Coll., 30th ICRC, these proceedings.

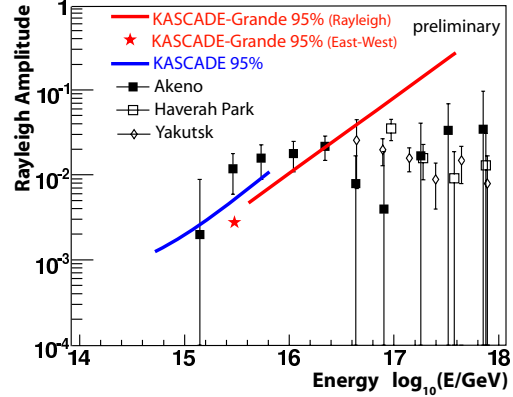


Figure 4: Rayleigh amplitude of the harmonic analyses of KASCADE-Grande data compared with results of other experiments.

- [3] R. Aloisio et al., *Astrop. Phys.* 27, 76 (2007).
- [4] D. Allard et al., submitted *Astron. Astrophys.*, e-Print: astro-ph/0703633 (2007).
- [5] M. Hillas, *J. Phys. Conf. Ser.* 47, 168 (2006).
- [6] A. Horneffer et al. LOPES Coll., 30th ICRC, these proceedings; S. Nehls et al. LOPES Coll., 30th ICRC, these proceedings.
- [7] T. Antoni et al KASCADE Coll., *Nucl. Instr. and Meth. A* 513, 490 (2003).
- [8] F. Di Piero et al. KASCADE-Grande Collab., 30th ICRC, these proceedings.
- [9] G. Toma et al. KASCADE-Grande Collab., 30th ICRC, these proceedings.
- [10] R. Glasstetter et al. KASCADE-Grande Coll., *Proc of 29th ICRC*, Pune 6, 295 (2005).
- [11] J. van Buren et al. KASCADE-Grande Coll., *Proc of 29th ICRC*, Pune 6, 301 (2005).
- [12] A. Haungs et al. KASCADE-Grande Coll., *Proc. ISVHECRI, Weihei*, *Nucl. Phys. B (Proc. Suppl.)*, in press (2007).
- [13] P. Doll et al. KASCADE-Grande Collab., 30th ICRC, these proceedings.
- [14] J. Zabierowski et al. KASCADE-Grande Collab., 30th ICRC, these proceedings.
- [15] F. Cossavella et al. KASCADE-Grande Collab., 30th ICRC, these proceedings.
- [16] J.C. Arteaga et al. KASCADE-Grande Coll., 30th ICRC, these proceedings.
- [17] V. de Souza, J. van Buren et al. KASCADE-Grande Coll., 30th ICRC, these proceedings.
- [18] S. Over, M. Stümpert et al. KASCADE-Grande Coll., 30th ICRC, these proceedings.



Shower size spectrum reconstructed with KASCADE-Grande

F. DI PIERRO^b, W.D. APEL^a, J.C. ARTEAGA^a, F. BADEA^a, K. BEKK^a, M. BERTAINA^b, J. BLÜMER^{a,c}, H. BOZDOG^a, I.M. BRANCUS^d, M. BRÜGGEMANN^e, P. BUCHHOLZ^e, A. CHIAVASSA^b, F. COSSAVELLA^c, K. DAUMILLER^a, V. DE SOUZA^c, P. DOLL^a, R. ENGEL^a, J. ENGLER^a, M. FINGER^c, D. FUHRMANN^f, P.L. GHIA^g, H.J. GILS^a, R. GLASSTETTER^f, C. GRUPEN^e, A. HAUNGS^a, D. HECK^a, J.R. HÖRANDEL^c, T. HUEGE^a, P.G. ISAR^a, K.-H. KAMPERT^f, D. KICKELBICK^e, H.O. KLAGES^a, Y. KOLOTAEV^e, P. LUCZAK^h, H.J. MATHES^a, H.J. MAYER^a, C. MEURER^a, J. MILKE^a, B. MITRICA^d, A. MORALES^a, C. MORELLO^g, G. NAVARRA^b, S. NEHLS^a, J. OEHLSCHLÄGER^a, S. OSTAPCHENKO^a, S. OVER^e, M. PETCU^d, T. PIEROG^a, S. PLEWNIA^a, H. REBEL^a, M. ROTH^a, H. SCHIELER^a, O. SIMAⁱ, M. STÜMPERT^c, G. TOMA^d, G.C. TRINCHERO^g, H. ULRICH^a, J. VAN BUREN^a, W. WALKOWIAK^e, A. WEINDL^a, J. WOCHOLE^a, J. ZABIEROWSKI^h.

^a *Institut für Kernphysik, Forschungszentrum Karlsruhe, Germany*

^b *Dipartimento di Fisica Generale dell'Università Torino, Italy*

^c *Institut für Experimentelle Kernphysik, Universität Karlsruhe, Germany*

^d *National Institute of Physics and Nuclear Engineering, Bucharest, Romania*

^e *Fachbereich Physik, Universität Siegen, Germany*

^f *Fachbereich Physik, Universität Wuppertal, Germany*

^g *Istituto di Fisica dello Spazio Interplanetario, INAF Torino, Italy*

^h *Soltan Institute for Nuclear Studies, Lodz, Poland*

ⁱ *Department of Physics, University of Bucharest, Romania*

dipierr@to.infn.it

Abstract: The Grande array as main part of the KASCADE-Grande experiment consists of $37 \times 10 \text{ m}^2$ scintillation detectors spread over an area of $700 \times 700 \text{ m}^2$. Grande enables triggers and reconstruction of primary cosmic rays in the energy range of $\sim 3 \cdot 10^{15} \text{ eV}$ to 10^{18} eV . The detectors and the shower size (i.e.: total number of charged particles) reconstruction accuracies are discussed. The KASCADE-Grande set-up allows, for a subsample of the registered showers, detailed comparisons of the data with measurements of the original KASCADE array on an event-by-event basis. The lateral distributions of charged particles and the resulting preliminary shower size spectrum for vertical showers are presented.

Introduction

The KASCADE-Grande experiment [1, 2] located at Forschungszentrum Karlsruhe, extends the energy range covered by KASCADE [3] up to 10^{18} eV by means of the Grande array which increases the acceptance area up to 0.5 km^2 . Grande, obtained reassembling the EAS-TOP detectors [4], measures the lateral distribution of charged particles up to 700 m from the core and the KASCADE muon detectors allow to reconstruct the muon lateral distribution up to the same distances [5].

The Grande Array

The Grande array consists of 37 stations with an average spacing of 137 m over a $700 \times 700 \text{ m}^2$ area. Every detector station consists of 10 m^2 of plastic scintillator (NE102A) organized in 16 units ($80 \times 80 \times 4 \text{ cm}^3$). Each unit is equipped with a high gain (HG) photomultiplier (Philips XP3462B, $\approx 1.6 \text{ pC/m.i.p.}$) and the 4 central units are additionally equipped with a low gain (LG) photomultiplier ($\approx 0.08 \text{ pC/m.i.p.}$). The signals from the PMTs are added up through passive mixers, one for the HG and one for the LG PMTs. The out-

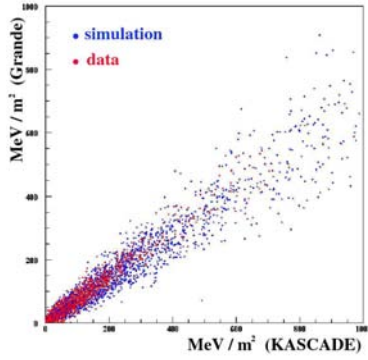


Figure 1: Energy deposits in Grande and KASCADE detectors for data and simulations.

put signals are preamplified and shaped by Shaping Amplifier ($8 \mu s$ rising time) into 3 analog signals, digitized by 3 Peak-ADCs (CAEN V785), covering the dynamic ranges 0.3 - 8, 2 - 80, 20 - 800 $particles/m^2$ respectively. The overlapping ranges between the scales are used for cross-calibration. Each detector is continuously monitored and calibrated by means of single muon spectra. The systematic uncertainty on the measured particle density by each detector is less than 15% and the statistical uncertainties are dominated by the poissonian fluctuations. The individual detector calibration is checked by comparing the 37 integral particle spectra and the spread (RMS) of the particle densities measured at fixed fluxes is 15%. For 3 Grande stations, co-located with the KASCADE array, the energy deposits in the Grande and in the 4 surrounding KASCADE detectors are compared on an event-by-event basis. The measured energy deposits are compared to full shower and detectors simulations (fig. 1) and the result is that the difference between the mean energy deposits in the Grande detectors for data and simulations is less than 10% [6]. The array is divided in 18 trigger clusters of 7 modules each (6 modules in an hexagon and a central one). A whole cluster at the same time fired (7/7 modules) provides a trigger with a rate of 0.5 Hz and becomes fully efficient for all primaries at $\approx 3 \times 10^{16} eV$ [7]. In the following analysis additional cuts have been applied: all 37 stations working, all 18 clusters active (290 days of data taking), more than 19 stations fired, *shower age* (s) in the range 0.4-1.4 and *shower size* greater than $10^{6.3}$.

Reconstruction accuracies

Beside the evaluation of the accuracies on the reconstructed EAS parameters by means of shower and detector simulations [7], it is possible to infer the Grande reconstruction accuracies by means of the comparison with the KASCADE reconstruction. The subsample is obtained accordingly to the following additional selection criteria: maximum in the central station of the hexagon overlapping with KASCADE, core position within a circle of 90 m radius from KASCADE center, zenith angle less than 42° . Using KASCADE reconstruction as reference the Grande accuracies result to be:

- core position (fig. 2): 6.4 m;
- shower size (fig. 3): systematic -5%, single event fluctuation 13%;
- arrival direction (fig. 4): 0.6° .

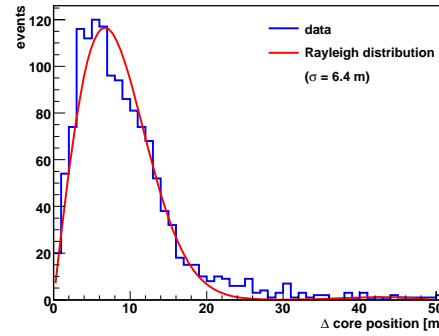


Figure 2: Core position accuracy: difference in reconstructed core position by KASCADE and Grande.

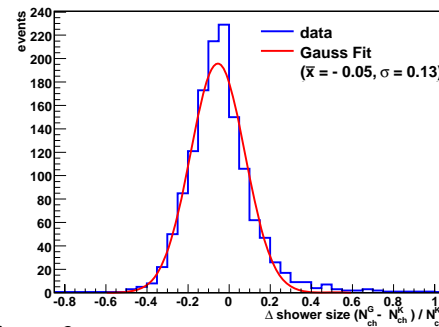


Figure 3: Shower size accuracy: difference in reconstructed shower size by KASCADE and Grande.

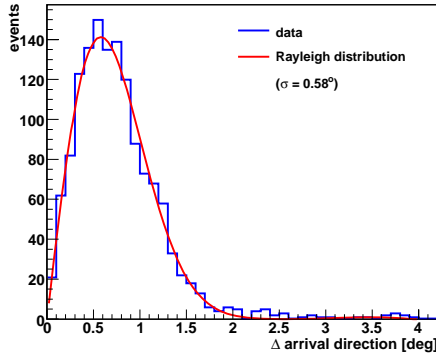


Figure 4: Arrival direction accuracy: difference between the arrival direction reconstructed by KASCADE and by Grande.

Comparing these results to the KASCADE accuracies [3] we can conclude that despite the 2 arrays are rather different (the KASCADE array is composed of 252 detectors over an area of $200 \times 200 \text{ m}^2$ with a spacing of 13 m) the Grande shower reconstruction has a good accuracy with respect to KASCADE and adequate for its aims.

Mean lateral distributions

In fig. 5 the experimental mean lateral distributions for vertical showers ($0^\circ - 18^\circ$) and for different shower sizes in the range $6.3 < \text{Log}_{10} N_{ch} < 8.1$ are shown. The line represents a fit with a slightly modified NKG function, optimized by means of shower simulations [8]:

$$\rho_{ch} = N_{ch} \cdot C(s) \cdot \left(\frac{r}{r_0}\right)^{s-\alpha} \left(1 + \frac{r}{r_0}\right)^{s-\beta} \quad (1)$$

with the normalization factor:

$C(s) = \Gamma(\beta-s) / (2\pi r_0^2 \Gamma(s-\alpha+2) \Gamma(\alpha+\beta-2s-2))$, the shower size N_{ch} , age parameter s and $\alpha=1.5$, $\beta=3.6$ and $r_0=40$ m. The lateral distributions measured by the Grande array extend up to more than 700 m and the used lateral distribution function well represents data over the whole range. An effect due to the saturation of the detectors starts to be evident only very close to the core ($r < 75$ m) and for the highest energies. The "shower age (s)" has been studied as a function of the shower size (N_{ch}) for different angular bins of equal acceptance. Fig. 6 shows that the s (age) value, as ex-

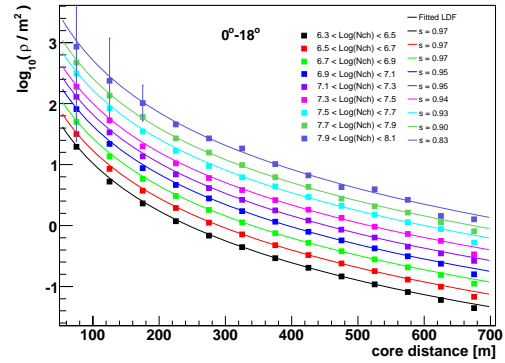


Figure 5: Experimental mean lateral distributions fitted with the LDF (eq. 1).

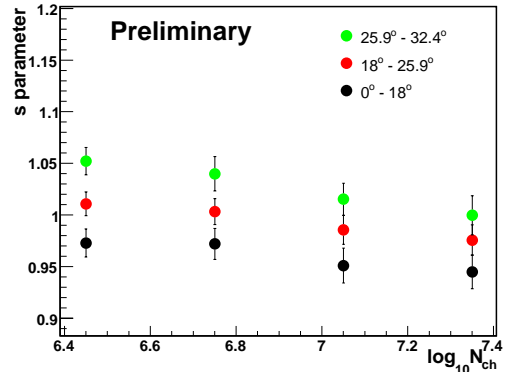


Figure 6: Age parameter values (s) as a function of shower size (N_{ch}), for different zenith angles.

pected, increases with increasing zenith angle and decreases with increasing shower size.

The experimental lateral distributions are compared to simulated ones, obtained for proton and iron primaries in the energy range $10^{16} - 10^{18}$ eV with QGSjet-II interaction model (fig. 7). The measured particle densities by each detector are normalized to the total number of particles. The obtained lateral distributions are multiplied by the mean N_{ch} of the bin in order to distinguish the different graphs (for the same reason only 4 N_{ch} bins are plotted). Data, as expected, lie between iron and proton simulations and show the same shape. This result shows that the lateral distribution can be indeed an efficient composition estimator.

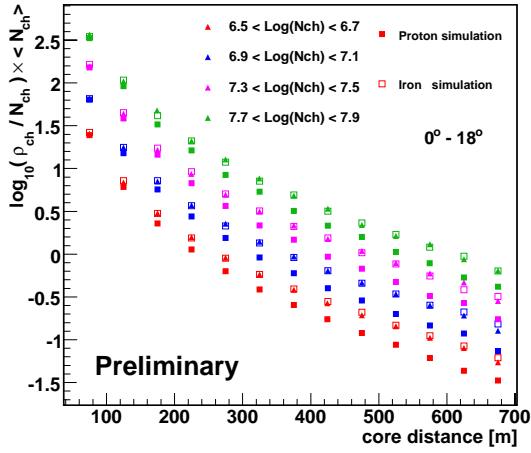


Figure 7: Comparison between experimental (dots) and simulated (open squares = iron, full squares = proton) mean lateral distributions.

Shower size spectrum

A preliminary shower size spectrum, for vertical events ($0^\circ - 18^\circ$), selecting an internal area of 0.3 km^2 and 290 days of effective data taking is shown in fig. 8. Reconstruction accuracies are not deconvoluted. Fluxes are multiplied by N_{ch}^3 . The spectrum extends from $\log_{10}(N_{ch}) = 6.3$ corresponding to efficiency ≈ 1 up to $\log_{10}(N_{ch}) = 8$ where still few events are collected. The limited statistics considered in this analysis does not allow conclusions for sizes larger than $\log_{10}(N_{ch}) = 7$. Statistics can be increased using less restrictive selection criteria and mainly by means of the analysis of different zenith angles.

Conclusions

The KASCADE-Grande reconstruction accuracies have been discussed. The charged particle lateral distribution is measured up to 700 m from the core and is well reproduced by simulations. A preliminary shower size spectrum is shown in a range corresponding to energies $3 \cdot 10^{16} - 10^{18} \text{ eV}$.

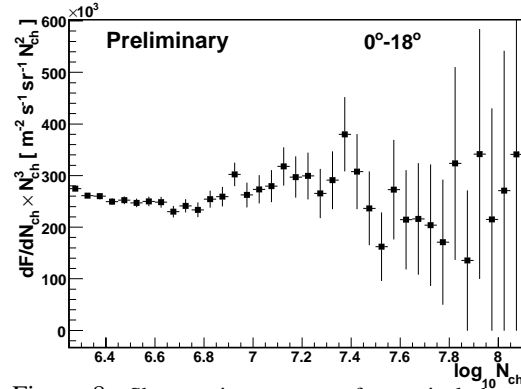


Figure 8: Shower size spectrum for vertical showers ($0^\circ - 18^\circ$), not deconvoluted for reconstruction accuracies. Fluxes are multiplied by N_{ch}^3 .

References

- [1] G. Navarra et al. KASCADE-Grande Coll., Nucl. Instr. and Meth. A 518, (2004).
- [2] A. Haungs et al. KASCADE-Grande Coll., Proc of 30th ICRC, Merida (2007), these proceedings.
- [3] T. Antoni et al. KASCADE Coll., Nucl. Instr. and Meth. A 513, (2003).
- [4] M. Aglietta et al. EAS-TOP Coll., Nucl. Instr. and Meth. A 336, (1993).
- [5] J. van Buren et al. KASCADE-Grande Coll., Proc of 29th ICRC, Pune 6, 301 (2005).
- [6] A. Chiavassa et al. KASCADE-Grande Coll., Proc of the 29th ICRC, Pune 6, 313 (2005).
- [7] F. Cossavella et al. KASCADE-Grande Coll., Proc of 30th ICRC, Merida (2007), these proceedings.
- [8] R. Glasstetter et al. KASCADE-Grande Coll., Proc of 29th ICRC, Pune 6, 295 (2005).



Electron shower size spectra reconstructed with KASCADE-Grande data

F. COSSAVELLA^c, W.D. APEL^a, J.C. ARTEAGA^a, F. BADEA^a, K. BEKK^a, M. BERTAINA^b, J. BLÜMER^{a,c}, H. BOZDOG^a, I.M. BRANCUS^d, M. BRÜGGEMANN^e, P. BUCHHOLZ^e, A. CHIAVASSA^b, K. DAUMILLER^a, V. DE SOUZA^c, F. DI PIERRO^b, P. DOLL^a, R. ENGEL^a, J. ENGLER^a, M. FINGER^c, D. FUHRMANN^f, P.L. GHIA^g, H.J. GILS^a, R. GLASSTETTER^f, C. GRUPEN^e, A. HAUNGS^a, D. HECK^a, J.R. HÖRANDEL^c, T. HUEGE^a, P.G. ISAR^a, K.-H. KAMPERT^f, D. KICKELBICK^e, H.O. KLAGES^a, Y. KOLOTAEV^e, P. LUCZAK^h, H.J. MATHES^a, H.J. MAYER^a, C. MEURER^a, J. MILKE^a, B. MITRICA^d, A. MORALES^a, C. MORELLO^g, G. NAVARRA^b, S. NEHLS^a, J. OEHLISCHLÄGER^a, S. OSTAPCHENKO^a, S. OVER^e, M. PETCU^d, T. PIEROG^a, S. PLEWNIA^a, H. REBEL^a, M. ROTH^a, H. SCHIELER^a, O. SIMAⁱ, M. STÜMPERT^c, G. TOMA^d, G.C. TRINCHERO^g, H. ULRICH^a, J. VAN BUREN^a, W. WALKOWIAK^e, A. WEINDL^a, J. WOCHLE^a, J. ZABIEROWSKI^h.

^a *Institut für Kernphysik, Forschungszentrum Karlsruhe, Germany*

^b *Dipartimento di Fisica Generale dell'Università Torino, Italy*

^c *Institut für Experimentelle Kernphysik, Universität Karlsruhe, Germany*

^d *National Institute of Physics and Nuclear Engineering, Bucharest, Romania*

^e *Fachbereich Physik, Universität Siegen, Germany*

^f *Fachbereich Physik, Universität Wuppertal, Germany*

^g *Istituto di Fisica dello Spazio Interplanetario, INAF Torino, Italy*

^h *Soltan Institute for Nuclear Studies, Lodz, Poland*

ⁱ *Department of Physics, University of Bucharest, Romania*

fabiana.cossavella@ik.fzk.de

Abstract: KASCADE-Grande, located at Forschungszentrum Karlsruhe, is a multi-detector experiment for the measurement of extensive air showers induced by primary cosmic rays in the energy range of $10^{14} - 10^{18}$ eV. With its 0.5 km^2 large field detector, in combination with the muon detectors of the KASCADE array, it allows the reconstruction of both the total electron and muon numbers, which are important observables for estimating the mass and the energy of the primary particles. In this work we will present the status of the electron size spectrum as well as the 2-dimensional ($N_e - N_\mu$) shower size spectrum after 626 days of effective data taking.

Introduction

The field array of the original KASCADE [1] experiment consists of 252 detector stations placed on a grid of $200 \times 200 \text{ m}^2$. Due to the low flux of cosmic rays in the order of $10^{-10} \text{ m}^{-2} \text{ s}^{-1} \text{ sr}^{-1}$ for energies above 10^{17} eV, the collective area of KASCADE is not sufficient for investigations in this energy range. Thus, the Grande array [2], with its 37 detector stations organised in 18 hexagonal trigger cells of 7 stations each, is the natural extension of KASCADE over an area of approximately 0.5 km^2 , suitable for detection of primary

particles up to energies of 10^{18} eV. Each station consists of 16 scintillation detectors ($80 \times 80 \times 4 \text{ cm}^3$), arranged in a 4×4 grid, with a total surface of 10 m^2 sensitive to the charged particles of the shower. With the present set-up Grande measures densities up to 800 charged particles/ m^2 , while the muon component of the shower is estimated from the 622 m^2 muon detectors of the KASCADE array, with an energy threshold for muons of 230 MeV. Full efficiency for the coincident KASCADE-Grande array is reached with a 7 out of 7 stations coincidence (0.5 Hz) at $\log(N_e) \approx 6.3$ (corresponding roughly to a primary energy of

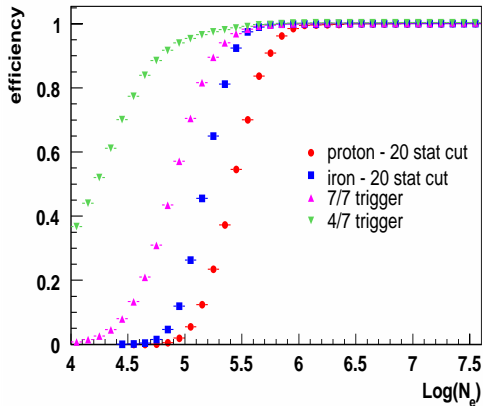


Figure 1: Reconstruction efficiency for showers between 10^{14} and 10^{18} eV, with zenith angles smaller than 40° . Requiring a 7/7 trigger at Grande with muon number successfully reconstructed by KASCADE, a full efficiency is reached at $N_e = 2 \times 10^6$. Applied data quality cuts require at least 20 active Grande detector stations, for which case the efficiency is plotted for proton and iron.

few times 10^{16} eV) as shown in Fig. 1, where primary iron reach for a bit smaller electron number full efficiency. This is due to the fact that we trigger to charged particles, where also muons contribute, in particular for small showers.

KASCADE-Grande main goals are the investigation of the position of the expected iron knee and the nature of the second knee.

Shower reconstruction

Analysis of Grande array data provides information on core position, arrival direction and the total number of charged particles (N_{ch}) in the shower [3]; the information on muon densities comes instead from the KASCADE array.

The lateral distribution of electrons has been studied through detailed CORSIKA [4] simulations and is described best in case of KASCADE-Grande by a modified NKG-function [5]:

$$\rho_e = N_e \cdot C(s) \cdot \left(\frac{r}{r_0}\right)^{s-\alpha} \cdot \left(1 + \frac{r}{r_0}\right)^{s-\beta}$$

where the normalisation factor $C(s)$ depends on the shower age s . From simulations, values of $\alpha = 1.5$, $\beta = 3.6$ and $r_0 = 40$ m were found as optimum for the radial distances relevant for Grande. For the lateral distribution of muons, a modified Lagutin function [6]:

$$\rho_\mu = N_\mu \frac{0.28}{r_0^2} \left(\frac{r}{r_0}\right)^{p1} \cdot \left(1 + \frac{r}{r_0}\right)^{p2} \cdot \left[1 + \left(\frac{r}{10 \cdot r_0}\right)^2\right]^{p3}$$

is used, with $r_0 = 320$ m and $p1$, $p2$, $p3$ respectively -0.69 , -2.39 and -1 , also found by simulation.

The analysis procedure develops in several steps. First, the total muon number and total number of charged particles are separately obtained fitting the respective lateral distributions. In a second step the contribution of muons to the densities of charged particles measured by Grande is taken into account: a likelihood fit compares for each detector the measured number of particles with the expected number given by the sum of electrons and muons estimated from the corresponding lateral distribution functions. The combined fit of the muonic and electromagnetic components is delivering in the final step the shower size N_e , the age parameter s , the muon size N_μ , the position of the shower core and the arrival direction of the shower. To test the reconstruction procedure and estimate the uncertainty, showers generated by CORSIKA, with the QGSJetII interaction model, have been used as input for a detailed GEANT [7] simulation of the apparatus. Approx. 260,000 proton and iron showers in the energy range of $10^{14} - 10^{18}$ eV, with zenith angles between 0° and 40° , have been analysed with the same procedure used for real data. In order to reduce effects of misreconstructed shower cores at the edges of the Grande array, a fiducial area of $\approx 190,000$ m² centered in the middle of Grande has been chosen. The results for spatial resolution are shown as a function of the shower size in Fig. 2: above the threshold of 6.3×10^6 electrons the core resolution is better than 12 m and shows no significant dependence on the primary particle. The points mark the mean deviation from the true value in percent, while the error bars describe the spread of the distribution. Fig. 2, left part, displays the accuracy of the reconstructed electron number: the statistical uncertainty, expressed by the er-

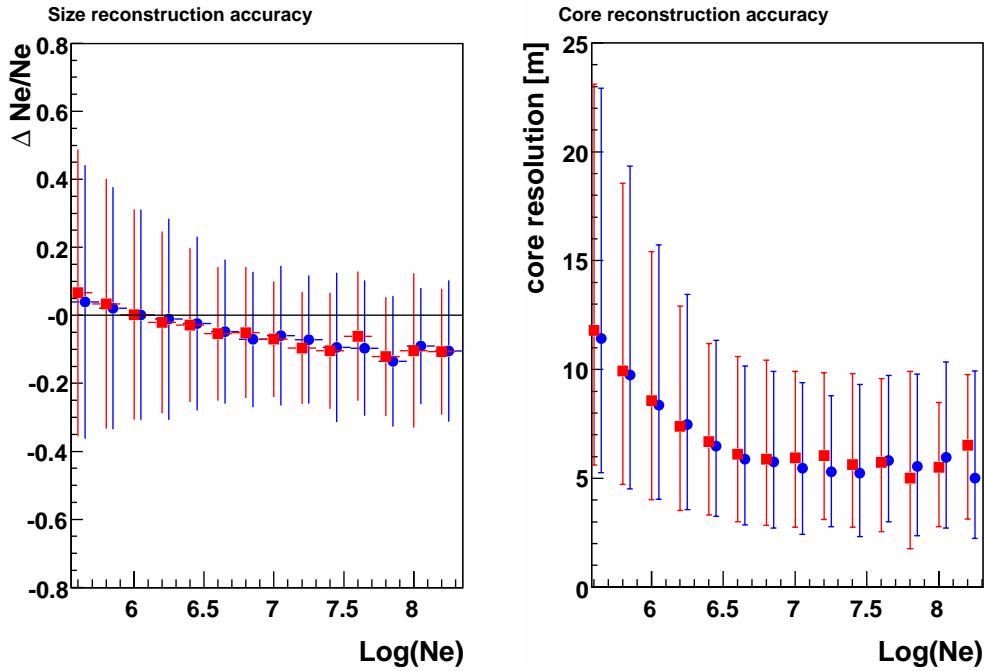


Figure 2: Left: reconstruction accuracy of the reconstructed electron number as function of the true electron number. The errors bars indicate the spread of the distribution (statistical error). Right: reconstruction accuracy of the core position. Showers between 10^{14} and 10^{18} eV with zenith angles smaller than 40° have been considered, corresponding to proton (circles) or iron (square symbol) primaries.

ror bars, is around 25% at threshold and decreases slightly with increasing shower size as expected, while the bias decreases from 0 to -15%. For details about the muon reconstruction see [8].

Comparison of measured events reconstructed independently by both Grande and KASCADE confirms the values we obtained [3].

Size spectra

We present in this work a preliminary version of the shower size spectrum measured by KASCADE-Grande. Fig. 3 shows the spectra for six different zenith angular ranges, each corresponding to a change of the slant depth of 50 g cm^{-2} , multiplied by N_e^3 in order to better appreciate possible features. The errors represent pure statistical uncertainty due to the number of events in each bin, there is no estimation of a sys-

tematic uncertainty yet, and no correction for the biases introduced by the reconstruction procedure is applied. Clearly, we are still missing statistics at the highest energies, i.e. at $N_e > 3 \cdot 10^7$, especially for inclined events, but the capability of the experiment can be determined.

The features appearing in the spectra at $\text{log}(N_e) \geq 7.3$ are currently under investigation, in order to exclude possible effects of misreconstructed total muon number on the estimation of the shower size. The spectra are based on a data set of 1.9×10^6 well reconstructed events inside the fiducial area. The effective time of combined data taking with both KASCADE array and Grande is equivalent to 626 days. With the capability of reconstructing both, muon and electron numbers, it is possible to investigate the two-dimensional size spectrum like in KASCADE. In Fig. 4 the two-dimensional spectrum for zenith angles between 18° and 25° is shown. The dashed lines show an estimation of

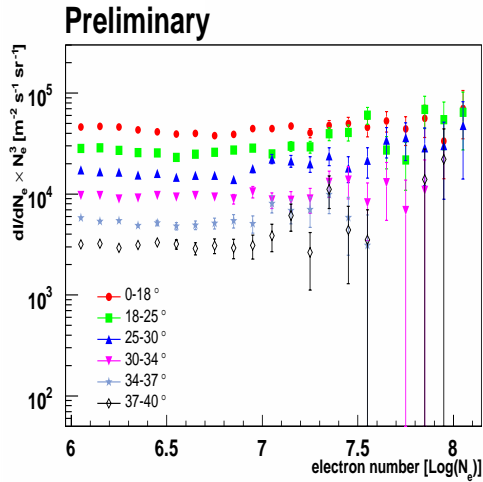


Figure 3: Differential shower size spectra for five different zenith angle ranges.

the primary energy based on simulations with the interaction model QGSjet01 [5].

Conclusions

In this paper, it has been shown that it is possible with the current setup of the KASCADE-Grande experiment to measure cosmic ray showers up to 10^{18} eV, although up to now only few events have been detected at these energies. Size spectra for different zenith angular ranges have been presented as well as an example of electron vs muon numbers distribution. At the moment the statistics are too small to make further concise statement of spectrum and mass composition for energies above 10^{17} eV, moreover the reconstruction procedure needs still some minimal refinements. In future the two-dimensional spectrum will be the starting point for the application of an unfolding analysis that will lead to the determination of spectra for different mass groups (as done for KASCADE [9]).

References

- [1] T.Antoni et al. KASCADE Coll., Nucl. Instr. Meth., A 513, 490 (2003)

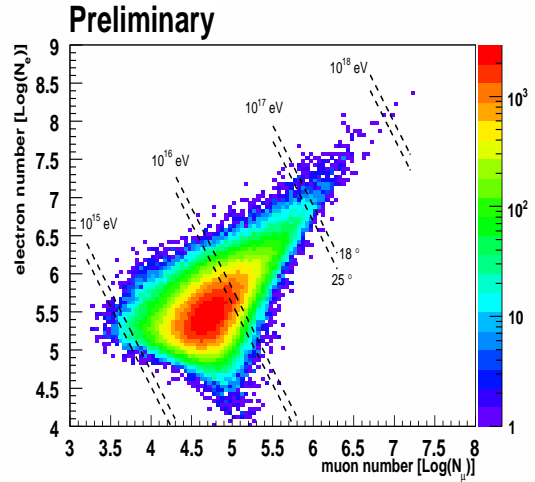


Figure 4: Reconstructed electron and muon number distribution of air showers measured by KASCADE-Grande in the zenith range $18^\circ - 25^\circ$. The dashed lines indicate average lines of constant energy derived from CORSIKA simulations

- [2] A. Haungs et al. KASCADE-Grande Collab., Proc of 28th ICRC, Tsukuba (2003) 2, 985.
 [3] F.Di Pierro et al. KASCADE-Grande Collab., Proc. of 30th ICRC, Merida (2007).
 [4] D.Heck et al., Report FZKA 6019, Forschungszentrum Karlsruhe (1998).
 [5] R.Glasstetter et al. KASCADE-Grande Coll., Proc. of the 29th ICRC 6 (2005), p. 293-296.
 [6] J.van Buren et al. KASCADE-Grande Coll., Proc. of the 29th ICRC 6 (2005), p. 301-304.
 [7] GEANT - Detector Desc. and Sim. Tool, CERN Program Library Long Writeup, W5013, CERN (1993).
 [8] J.C. Arteaga et al. KASCADE-Grande Collab., Proc. of 30th ICRC, Merida (2007).
 [9] T.Antoni et al. KASCADE Coll., Astrop. Phys. 24 (2005), p. 1-25.



Muon spectra reconstructed from inclined air showers measured by KASCADE-Grande

J.C. ARTEAGA^a, W.D. APEL^a, F. BADEA^a, K. BEKK^a, M. BERTAINA^b, J. BLÜMER^{a,c}, H. BOZDOĞ^a, I.M. BRANCUS^d, M. BRÜGGEMANN^e, P. BUCHHOLZ^e, A. CHIAVASSA^b, F. COSSAVELLA^c, K. DAUMILLER^a, V. DE SOUZA^c, F. DI PIERRO^b, P. DOLL^a, R. ENGEL^a, J. ENGLER^a, M. FINGER^c, D. FUHRMANN^f, P.L. GHIA^g, H.J. GILS^a, R. GLASSTETTER^f, C. GRUPEN^e, A. HAUNGS^a, D. HECK^a, J.R. HÖRANDEL^c, T. HUEGE^a, P.G. ISAR^a, K.-H. KAMPERT^f, D. KICKELBICK^e, H.O. KLAGES^a, Y. KOLOTAEV^e, P. LUCZAK^h, H.J. MATHES^a, H.J. MAYER^a, C. MEURER^a, J. MILKE^a, B. MITRICA^d, A. MORALES^a, C. MORELLO^g, G. NAVARRA^b, S. NEHLS^a, J. OEHLISCHLÄGER^a, S. OSTAPCHENKO^a, S. OVER^e, M. PETCU^d, T. PIEROG^a, S. PLEWNIA^a, H. REBEL^a, M. ROTH^a, H. SCHIELER^a, O. SIMAⁱ, M. STÜMPERT^c, G. TOMA^d, G.C. TRINCHERO^g, H. ULRICH^a, J. VAN BUREN^a, W. WALKOWIAK^e, A. WEINDL^a, J. WOCHLE^a, J. ZABIEROWSKI^h.

^a *Institut für Kernphysik, Forschungszentrum Karlsruhe, Germany*

^b *Dipartimento di Fisica Generale dell'Università Torino, Italy*

^c *Institut für Experimentelle Kernphysik, Universität Karlsruhe, Germany*

^d *National Institute of Physics and Nuclear Engineering, Bucharest, Romania*

^e *Fachbereich Physik, Universität Siegen, Germany*

^f *Fachbereich Physik, Universität Wuppertal, Germany*

^g *Istituto di Fisica dello Spazio Interplanetario, INAF Torino, Italy*

^h *Soltan Institute for Nuclear Studies, Lodz, Poland*

ⁱ *Department of Physics, University of Bucharest, Romania*

arteaga@ik.fzk.de

Abstract: Inclined air showers (i.e. showers with zenith angle above 40 degrees) are registered by the KASCADE-Grande experiment, which is designed to address fundamental questions about the origin, composition and acceleration mechanisms of primary cosmic rays between 10^{14} and 10^{18} eV. Despite the aggravate reconstruction due to the thin scintillation detectors used in KASCADE-Grande these inclined events are valuable since they offer a good opportunity to both, study the penetrating component of the air showers and cross-checks of hadronic interaction models. Working in this direction, a first analysis of the KASCADE-Grande data from inclined events has been performed. In particular, the muon spectra have been reconstructed for different zenith angle intervals and features of the resulting spectra have been studied and confronted with expectations from Monte Carlo simulations.

Introduction

The main objective of the KASCADE-Grande experiment is the search for a knee in the heavy component of the cosmic ray spectrum. The presence or not of this feature will shed light on the origin of the cosmic rays in the energy region of $10^{14} - 10^{18}$ eV. The experiment studies this region of the cosmic ray spectrum indirectly, by observing the extensive air showers produced by cosmic rays in the atmosphere. For this purpose, KASCADE-Grande

makes use of an 0.5 km^2 array of $37 \times 10 \text{ m}^2$ plastic scintillator detectors, which measures the arrival time and the density of charged particles in the shower front [1]. The advantage of the experiment is that it can directly measure the penetrating component of the air shower by using the array of $192 \times 3.2 \text{ m}^2$ shielded scintillator detectors of the original KASCADE observatory [2].

KASCADE-Grande is sensitive to air showers up to 70° degrees of zenith angle, but only showers

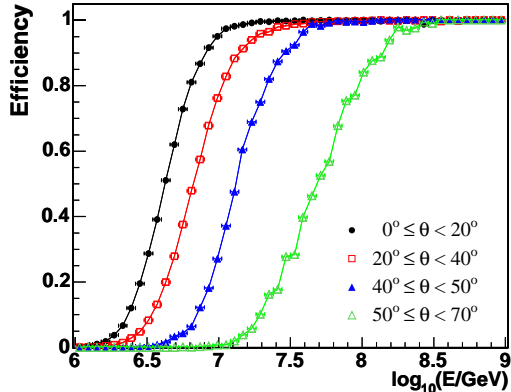


Figure 1: KASCADE-Grande triggering and reconstruction efficiency as a function of primary energy for different zenith angle intervals.

below 40° have been used up to now in the general analyses. Before using the data on inclined showers (i.e., on events above $\theta = 40^\circ$) a very good understanding of the precision of the employed reconstruction techniques in this zenith angle range is required. This task has recently begun, led by the different opportunities that the study of inclined showers offers, e.g.: 1) to increase the statistics of the experiment, 2) to understand in more detail the penetrating component of the shower, which is dominant in these kind of events, and 3) to cross-check hadronic interaction models, taking advantage of the close relation existing between the hadronic processes and the production of muons in the shower. In the following, the results of a first analysis of the penetrating component of inclined showers measured with the KASCADE-Grande experiment will be discussed.

Efficiency and systematics

To study the systematics and performance of the KASCADE-Grande detector at different zenith angles, both the air shower and the secondary particle interaction with the detector were carefully simulated. The air showers were generated with CORSIKA [3], employing the high-energy hadronic interaction model QGSJET II [4] for the range $\theta = 0^\circ - 70^\circ$, the energy interval $E = 10^{15} - 10^{18}$ eV and different primaries with equal abundances: H,

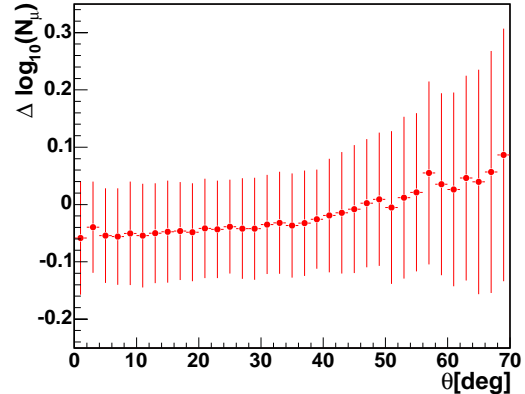


Figure 2: Zenith angle dependence of the systematic error for the reconstructed muon number.

He, C, Si and Fe. A power law cosmic ray flux with spectral index $\gamma = -2$ was used to generate the air showers. The cosmic ray events were isotropically distributed and their core homogeneously scattered over the entire Grande array. The same reconstruction procedure used for the experimental data was applied to the simulations.

The total muon number, N_μ , in the air shower is estimated from a log-likelihood fit to the measured muon densities at the KASCADE muon detectors [5]. On the other hand, the arrival direction of the shower is obtained from a χ^2 fit to the arrival times of the shower front to the KASCADE-Grande stations [6]. In this fit, sampling effects, fluctuations and the curvature of the shower front are properly modeled based on Monte Carlo simulations following [6], but with the difference that for inclined showers also muons are taken into account when parametrizing the shower front dependence on the zenith angle.

Several quality cuts were applied to the simulated data. A fiducial area of 0.4 km^2 with octagonal shape, centered at KASCADE-Grande, was chosen for the analysis to avoid showers with misreconstructed cores. Additionally, only events that triggered more than 19 Grande stations and passed successfully the charged particle reconstruction were considered. Cuts on the electron number N_e and the electron age parameter, s , were also introduced. For events with $\theta < 50^\circ$, the cut $N_e > 10^5$ was imposed. The same cut can not be applied to showers with higher zenith angles, in other case

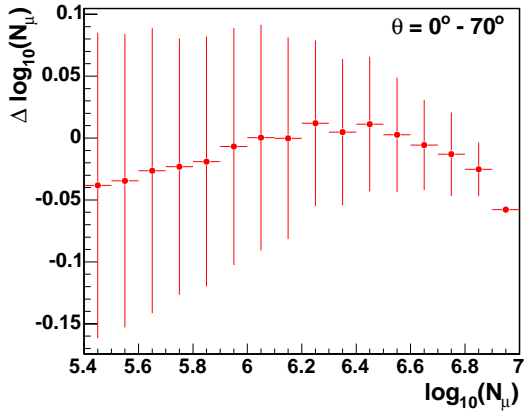


Figure 3: Systematic error in the estimation of the muon number shown as a function of the reconstructed N_μ .

the Grande detector loses efficiency. Instead, the cut $N_e > 10^4$ was employed. A final condition $N_\mu > 10^{5.4}$ was applied overall. With these cuts, it is found that the energy threshold at which the KASCADE-Grande detector achieves its full efficiency increases from $E = 10^{7.3}$ GeV for vertical showers up to $10^{8.5}$ GeV for very inclined ones (see Fig. 1).

Regarding the KASCADE-Grande pointing resolution, the analysis of the simulated data showed that it is better than 0.6° inside the whole zenith angle interval $\theta = 0^\circ - 70^\circ$. For the systematic error in the reconstruction of the muon number, the result was $\Delta \log_{10}(N_\mu) \leq 0.1$ (with reference to Figs. 2 and 3), which was estimated as the difference between the true $\log_{10}(N_\mu)$ and the reconstructed one. The uncertainty in the shower core position, on the other hand, was found to be less than 40 m. The achieved accuracy in the reconstruction of N_μ and θ for inclined showers is good enough to perform a more detailed analysis of these events.

Muon size spectra

For the present work, 81593 events were subject to analysis. These events were selected from a vast set of experimental data collected by KASCADE-Grande, from which it resulted an effective time of observation of about 498 days. The selection was

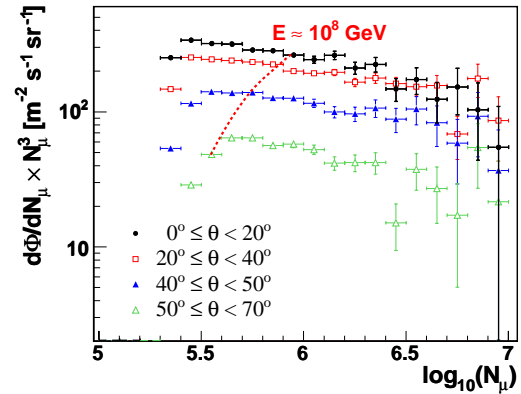


Figure 4: Reconstructed muon number spectra from KASCADE-Grande data on vertical and inclined showers. The intersections between the dotted line and the spectra give the respective muon numbers at which the expected primary energy is $E \approx 10^{17}$ eV.

done by imposing the quality cuts described in the preceding section and discarding those experimental runs where one or more of the muon detector clusters of KASCADE were not active. Around 22% from the set of quality events were classified as inclined showers.

Before reconstructing the muon spectra, the muon number of each event was corrected for its systematic uncertainties through a correction function obtained from simulations. This function takes into account the dependence of the N_μ systematic uncertainty on the zenith angle (see Fig. 2), core position and $\log_{10}(N_\mu)$ (with reference to Fig. 3).

The resulting muon number spectra from the KASCADE-Grande data analysis for different zenith angle intervals are shown in Fig. 4 multiplied by N_μ^3 . Clearly the threshold behavior for the different zenith angle ranges are seen. At this stage, the lack of statistics prevents us to perform a detailed analysis on the shape of the muon number spectra for $N_\mu \geq 10^{6.4}$.

Comparison with simulations

In Figure 5, the observed muon number spectra are confronted with expectations from simulations. In both cases, the same reconstruction techniques

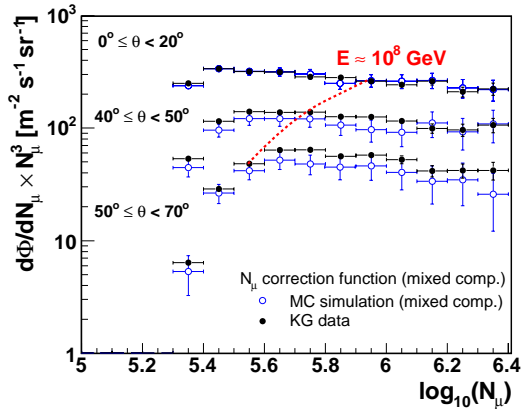


Figure 5: Comparison between the reconstructed muon spectrum from experimental data and simulations at different zenith angle ranges.

were applied. The simulated data set here employed was similar to the one described in section 2, but multiplied with an appropriate weight function, according to the energy of the event, in order to reproduce an energy power law spectrum with $\gamma = -3$. To compare the measured and simulated N_μ spectra, the latter ones had to be multiplied by a common normalization factor, which was chosen in such a way that for the range $\theta < 20^\circ$, the muon spectra obtained from the experimental and simulated data have the same magnitude. The analysis is restricted to the interval $\log_{10}(N_\mu) = 5.4 - 6.4$ in order to avoid statistical fluctuations, in particular, due to a low number of inclined events at high energies.

Small differences in magnitude between the measured and expected N_μ spectra for inclined showers are revealed in Fig. 5. The difference is also present for the range $\theta = 20^\circ - 40^\circ$ (not shown in Fig. 5 for clarity reasons), and grows from 12% at this zenith angle interval up to 20% for $\theta = 50^\circ - 70^\circ$. When iron nuclei or protons are used as primaries in the simulations, the above systematic trend is also observed, only the magnitude of the differences changes slightly. A lower muon number in the predictions from Monte Carlo simulations (CORSIKA/QGSJET II) for inclined showers than in the measurements or a reconstruction bias could be responsible for the observed differences. To find the reasons behind these discrepancies more analyses are needed.

Conclusions

It was shown that the KASCADE-Grande detector is sensitive to very high energy inclined air showers ($40^\circ \leq \theta < 70^\circ$), which can be well reconstructed. Besides that the angular resolution of the detector and the achieved accuracy reconstruction of N_μ are sufficient to allow detailed analyses with inclined air showers in KASCADE-Grande. From a first analysis of measured inclined showers the muon number spectra, corrected by the corresponding N_μ systematic uncertainties, were reconstructed. These fluxes were compared with expectations from simulations based on CORSIKA/QGSJET II. After normalizing the simulated N_μ spectra with a common factor, which allowed us to match the measured and simulated fluxes for $\theta < 20^\circ$, a systematic difference between the experimental and the simulated spectra was found, which increases with the zenith angle. The origin of this discrepancy has to be investigated.

Acknowledgments

One of us, J.C. Arteaga, would like to thank to the DAAD (grant A/05/12380) and the Institut für Kernphysik at FZK for all its support.

References

- [1] A. Haungs *et al.*, KASCADE-Grande Coll., Proc. of 28th ICRC Tsukuba 2, 985 (2003).
- [2] T. Antoni *et al.*, Nucl. Instrum. Meth. **A513**, 490 (2003).
- [3] D. Heck *et al.*, Forschungszentrum Karlsruhe, Report FZKA 6019 (1998).
- [4] S.S. Ostapchenko, Phys. Rev. **D74**, 014026 (2006).
- [5] J. van Buren *et al.*, KASCADE-Grande Coll., Proc. of 29th ICRC Pune 6, 301 (2005).
- [6] R. Glasstetter *et al.*, KASCADE-Grande Coll., Proc. of 29th ICRC Pune 6, 293 (2005).
- [7] W.D. Apel *et al.*, KASCADE-Grande Coll., Astropart. Phys. **24**, 467 (2006).



Features of the S(500) distribution for large air showers detected with the KASCADE-Grande array

G. TOMA^d, W.D. APEL^a, J.C. ARTEAGA^a, F. BADEA^a, K. BEKK^a, M. BERTAINA^b, J. BLÜMER^{a,c}, H. BOZDOG^a, I.M. BRANCUS^d, M. BRÜGGEMANN^e, P. BUCHHOLZ^c, A. CHIAVASSA^b, F. COSSAVELLA^c, K. DAUMILLER^a, V. DE SOUZA^c, F. DI PIERRO^b, P. DOLL^a, R. ENGEL^a, J. ENGLER^a, M. FINGER^c, D. FUHRMANN^f, P.L. GHIA^g, H.J. GILS^a, R. GLASSTETTER^f, C. GRUPEN^c, A. HAUNGS^a, D. HECK^a, J.R. HÖRANDEL^c, T. HUEGE^a, P.G. ISAR^a, K.-H. KAMPERT^f, D. KICKELBICK^e, H.O. KLAGES^a, Y. KOLOTAEV^e, P. LUCZAK^h, H.J. MATHES^a, H.J. MAYER^a, C. MEURER^a, J. MILKE^a, B. MITRICA^d, A. MORALES^a, C. MORELLO^g, G. NAVARRA^b, S. NEHLS^a, J. OEHLSCHLÄGER^a, S. OSTAPCHENKO^a, S. OVER^e, M. PETCU^d, T. PIEROG^a, S. PLEWNIA^a, H. REBEL^a, M. ROTH^a, H. SCHIELER^a, O. SIMAⁱ, M. STÜMPERT^c, G.C. TRINCHERO^g, H. ULRICH^a, J. VAN BUREN^a, W. WALKOWIAK^e, A. WEINDL^a, J. WOCHOLE^a, J. ZABIEROWSKI^h.

^a *Institut für Kernphysik, Forschungszentrum Karlsruhe, Germany*

^b *Dipartimento di Fisica Generale dell'Università Torino, Italy*

^c *Institut für Experimentelle Kernphysik, Universität Karlsruhe, Germany*

^d *National Institute of Physics and Nuclear Engineering, Bucharest, Romania*

^e *Fachbereich Physik, Universität Siegen, Germany*

^f *Fachbereich Physik, Universität Wuppertal, Germany*

^g *Istituto di Fisica dello Spazio Interplanetario, INAF Torino, Italy*

^h *Soltan Institute for Nuclear Studies, Lodz, Poland*

ⁱ *Department of Physics, University of Bucharest, Romania*

toma@ik.fzk.de

Abstract: For the experimental conditions of the KASCADE-Grande experiment, the density of charged particles of large air showers (EAS) at the distance of about 500 m from the shower core S(500) has been shown by detailed simulation studies to be an approximate energy estimator, being nearly independent of the mass of the primary particle. This report presents some first experimentally observed features of the S(500) observable of EAS registered with the KASCADE-Grande array installed at the Forschungszentrum Karlsruhe, Germany. The measured energy deposits of particles in the 37 scintillation detector stations have been used to reconstruct the lateral charged particle distributions which are described by a Linsley LDF. With adjusting the charged particle density distribution and applying various cuts, the S(500) distribution of the data has been evaluated. Among other features, the S(500) dependence from the EAS angle of incidence has been studied.

Introduction

It has been first shown by Hillas et al. [1] that the lateral charged particle density at a particular distance from the EAS core, dependent on the specific layout of the considered array, proves to be nearly independent of primary mass and maps only the primary energy. An estimate of the primary energy on this basis has been applied for various arrays [2]. KASCADE-Grande [3] consists as main

component of an array of 37 detector stations of 10 m² scintillation counters, that covers a total area of ~0.5 km². Dedicated simulation studies [4] have shown for the particular case of the layout of the KASCADE-Grande array that the charged particle density at the distance of around 500 m from shower centre appears most appropriate for the energy estimate.

Reconstruction of S(500)

In context of the present studies, a software tool has been developed [5] and was used for analyzing the lateral particle density distributions event by event. The energy deposits of particles in detectors are converted into particle numbers [6] using appropriate lateral energy correction functions, dependent of the angle of incidence. Furthermore, the reconstructed particle numbers are converted into particle densities in the detectors. The next step of the analysis approximates the shape of the lateral particle density distribution by a Linsley LDF [7]. The Linsley LDF depends on three parameters, defining the total size and the lateral shape, which are determined by fitting the data. The results are used to deduce the value of the lateral particle density at 500 m from shower core, a quantity we refer as S(500). In order to explore the influence of the considered radial range of the data, the Linsley LDF has been adjusted in different radial ranges of the registered charged particle lateral distribution (0-1000 m, 40-700 m, 200-400 m, 300-700 m). The fit in different radial ranges shows that the LDF is pushed to the limits of a good reproduction of the data when trying to describe larger radial ranges, covering the very steep decrease close to shower core and the very shallow slope at large distances. This indicates that the Linsley LDF, though found quite appropriate in the simulation studies [3], is not perfect. As expected, the quality of the fit improves when fitting the lateral distribution in restricted radial ranges (inside which the slope of the distribution does not change strongly). For the observable S(500) investigated here, the best quality of the fits is achieved for the use of the 300 - 700 m radial range. The relation of S(500) to the primary energy, resulting from simulations is shown in Fig.1 (simulations use the QGSJET II model as high energy interaction model embedded in CORSIKA; in this case, S(500) is evaluated for each shower with the same reconstruction procedure as for the experimental data). We apply this energy estimator to the measured data in the primary energy range of about 10^{16} - 10^{18} eV. Fig. 2 shows a preliminary plot of the electron shower size (N_e) dependence with the S(500) for the given shower sample. The electron shower size is obtained using the standard reconstruction technique

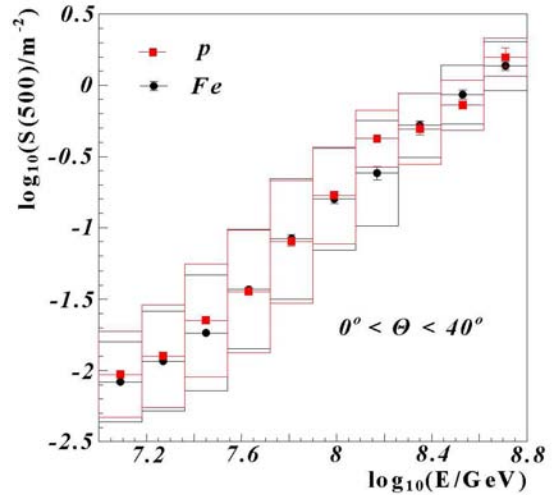


Figure 1: The relation of the mean values of S(500) to the primary energy E resulting from simulation studies for proton (squares) and Fe (dots) induced EAS: $\log S(500)$ vs. $\log E$. In addition to the error of the mean (in many cases smaller than the dot size) the dispersion (standard deviation) is indicated by the error boxes.

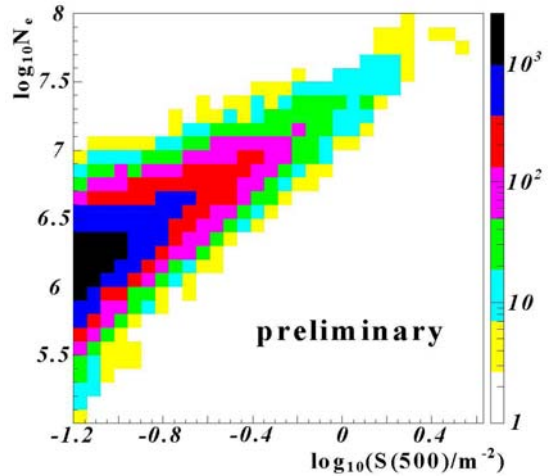


Figure 2: The dependence between electron shower size (N_e) and the S(500) for the given shower sample - a minimum of 20 triggered stations, showers inclined up to 45° degrees and shower cores reconstructed inside the array.

[8], while the S(500) is obtained with the described technique. The origin of the visible fluctuations is

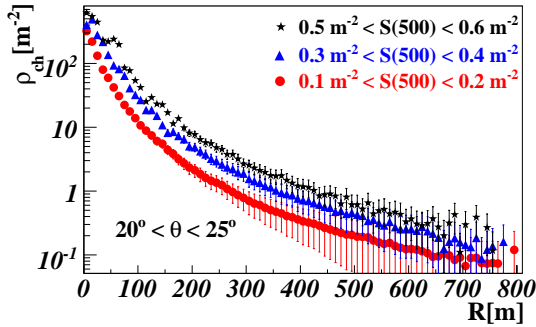


Figure 3: The measured charged particle lateral distributions for different S(500) ranges.

subject of further investigations. Fig. 3 shows for some S(500) ranges the measured charged particle distributions.

Dependence of S(500) on the angle of EAS incidence

A sample of the events detected by KASCADE-Grande has been studied in order to reconstruct the lateral distributions of charged particles and to determine S(500) distributions for EAS with different angles of incidence. In order to ensure a good quality of the shower sample, some restrictions have been applied with following requirements: (i) showers for which a minimum of 20 detector stations have been triggered, (ii) showers for which the reconstructed shower core falls inside the array and (iii) for which the Linsley LDF provided a good quality fit (as reported by MINUIT). Furthermore, only the showers for which the reconstructed zenith angle does not exceed 45° are considered. For values of $S(500) > 0.6 \text{ m}^{-2}$, the trigger threshold for all angular ranges is exceeded. Fig. 4 shows the distributions for all the showers and also specified for showers from different angles of EAS incidence in the full efficiency range of the KASCADE-Grande array. It is obvious from Fig.4 that in the range of the full detection efficiency, the S(500) distribution exhibits a power law behavior. This important feature maps the primary energy spectrum. In addition, the influence of attenuation in the Earth's atmosphere (reducing the value of S(500) for same number of events with in-

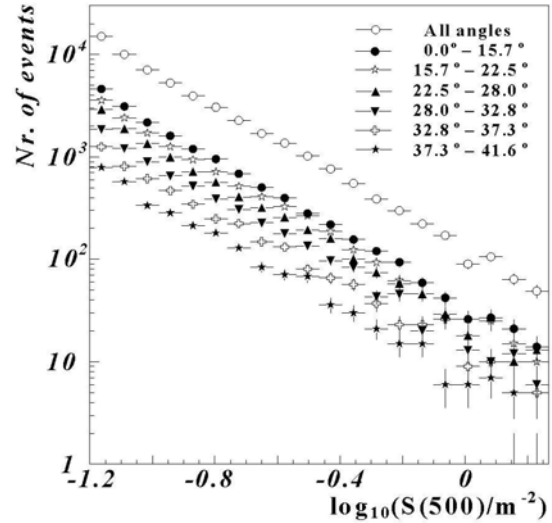


Figure 4: Differential spectra of the reconstructed S(500) observable for different EAS zenith angles opening equal solid angles and for the total shower sample (LDF adjustment performed in the radial range of 300 m-700 m).

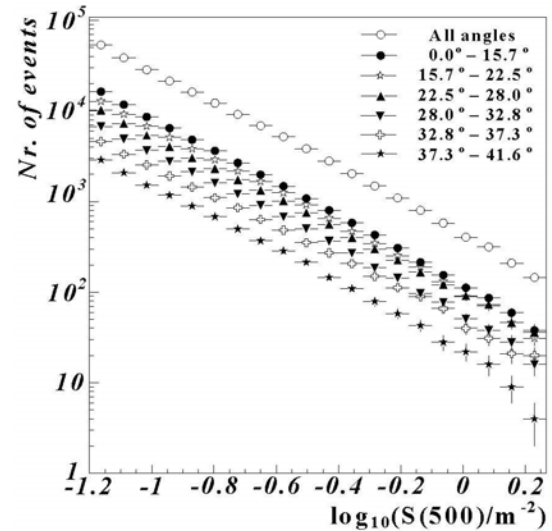


Figure 5: Integral spectra of the reconstructed S(500) observable for different zenith angles of EAS incidence as compared to that of the total shower sample.

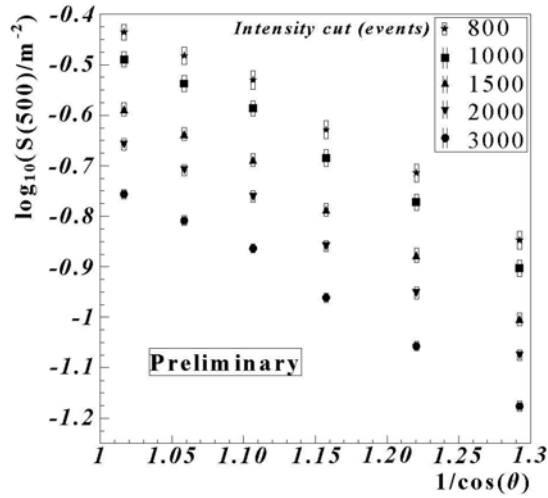


Figure 6: The $S(500)$ dependence of the angle of incidence for various pre-chosen intensities (number of events). For a given angle of incidence, the $\log_{10}S(500)$ value on the vertical axis is the corresponding $\log_{10}S(500)$ in the integral spectrum for which we have an intensity equal to the one used for the constant intensity cut.

creasing angle of EAS incidence), the spectra follow approximately the same slope for all angular intervals. This is a consequence of the isotropic incidence of the primary cosmic radiation. In Fig. 5 the integral $S(500)$ spectrum is shown as derived from the data. Fig. 6 shows the $S(500)$ dependence on the angle of EAS incidence for different pre-chosen constant intensities in the integral spectrum. The spectra have been approximated with power-laws. After choosing different values for the intensity, the corresponding $S(500)$ value has been calculated using the inverse function of the power-law. Since the $1/\cos(\theta)$ value shows the atmospheric depth, the constant intensity cut provides a method for observing the $S(500)$ attenuation with the atmospheric depth.

Conclusions

The value of particle density at 500 m from shower core was indicated by simulation studies to be a suitable energy estimator for EAS in the range of 10^{16} - 10^{18} eV. With this aspect, the experimental lateral density distribution of charged particles has

been investigated for EAS events detected with the KASCADE-Grande array. The reconstructed experimental lateral density distributions have been approximated with a Linsley LDF and the values of particle density at 500 m distance from shower core $S(500)$ are derived. The distribution of $S(500)$, assumed to reflect the primary energy spectrum, and the dependence of $S(500)$ on the angle of EAS incidence have been shown.

Acknowledgements

The corresponding author of this paper would like to thank Deutscher Akademischer Austausch Dienst (DAAD) for a research scholarship (Desk322 A/06/09016).

References

- [1] A.M. Hillas et. al., Proc.12th ICRC, Hobart 3 (1971) 1001
- [2] D.M. Edge et. al., J. Phys. A: Math. Nucl. Gen.6 (1973) 1612; M. Nagano et. al., J. Phys. G:Nucl. Part. Phys.10(1984) 1295; Y. Dai et.al., J.Phys.G: Nucl. Part. Phys. 14(1998) 793; M. Roth et al.- Auger collaboration Proc. 28th ICRC, Tsukuba, Japan, vol. 2 (2003) 333
- [3] A. Haungs et al., KASCADE-Grande collaboration, Proc. 28th ICRC, Tsukuba, Japan, vol.2 (2003)985
- [4] H. Rebel and O. Sima et al. KASCADE-Grande collaboration, Proc. 29th ICRC, Pune, India, vol.6 (2005)297
I.M. Brancus et al. KASCADE-Grande collaboration, Proc. 29th ICRC, Pune, India, vol.6 (2005)361
- [5] O. Sima et. al., Report FZKA 6985, Forschungszentrum Karlsruhe 2004
- [6] G. Toma et al., Proc.26th ECRS 2006, Lisbon, Portugal ; CERN program library, GEANT user's guide, (1997)
- [7] J. Linsley et. al., Journ. Phys. Soc. Japan 17 (1962) A-III
- [8] F. Cossavella et. al. KASCADE-Grande collaboration, 30th ICRC Proc., Merida, Mexico 2007, these proceedings



Search for anisotropy and point sources of cosmic rays with the KASCADE-Grande experiment

S. OVER^e, M. STÜMPERT^c, W.D. APEL^a, J.C. ARTEAGA^a, F. BADEA^a, K. BEKK^a, M. BERTAINA^b, J. BLÜMER^{a,c}, D. BORLA TRIDON^b, H. BOZDOĞA^a, I.M. BRANCUS^d, M. BRÜGGEMANN^e, P. BUCHHOLZ^e, A. CHIAVASSA^b, F. COSSAVELLA^c, K. DAUMILLER^a, V. DE SOUZA^c, F. DI PIERRO^b, P. DOLL^a, R. ENGEL^a, J. ENGLER^a, M. FINGER^c, D. FUHRMANN^f, P.L. GHIA^g, H.J. GILS^a, R. GLASSTETTER^f, C. GRUPEN^e, A. HAUNGS^a, D. HECK^a, J.R. HÖRANDEL^c, T. HUEGE^a, P.G. ISAR^a, K.-H. KAMPERT^f, D. KICKELBICK^e, H.O. KLAGES^a, Y. KOLOTAEV^e, P. LUCZAK^h, H.J. MATHES^a, H.J. MAYER^a, C. MEURER^a, J. MILKE^a, B. MITRICA^d, A. MORALES^a, C. MORELLO^g, G. NAVARRA^b, S. NEHLS^a, J. OEHLSCHLÄGER^a, S. OSTAPCHENKO^a, M. PETCU^d, T. PIEROG^a, S. PLEWNIA^a, H. REBEL^a, M. ROTH^a, H. SCHIELER^a, O. SIMAⁱ, G. TOMA^d, G.C. TRINCHERO^g, H. ULRICH^a, J. VAN BUREN^a, W. WALKOWIAK^e, A. WEINDL^a, J. WOCHOLE^a, J. ZABIEROWSKI^h.

^a *Institut für Kernphysik, Forschungszentrum Karlsruhe, Germany*

^b *Dipartimento di Fisica Generale dell'Università Torino, Italy*

^c *Institut für Experimentelle Kernphysik, Universität Karlsruhe, Germany*

^d *National Institute of Physics and Nuclear Engineering, Bucharest, Romania*

^e *Fachbereich Physik, Universität Siegen, Germany*

^f *Fachbereich Physik, Universität Wuppertal, Germany*

^g *Istituto di Fisica dello Spazio Interplanetario, INAF Torino, Italy*

^h *Soltan Institute for Nuclear Studies, Lodz, Poland*

ⁱ *Department of Physics, University of Bucharest, Romania*

over@hep.physik.uni-siegen.de

Abstract: The KASCADE-Grande experiment, located on site of the Forschungszentrum Karlsruhe in Germany, is a multi-detector setup for measuring extensive air showers of primary energies up to 1 EeV. The main component for measuring showers of the highest energies is the newly added Grande array, which consists of 37 scintillation detector stations, spanning an area of nearly 0.5 km². Based on the reconstruction of the arrival directions of individual showers, searches for both large scale anisotropies and point sources are performed. The present state of the ongoing analysis will be presented.

Introduction

Charged cosmic rays are deflected by galactic magnetic fields, causing an almost isotropic distribution of their arrival directions. Low energy charged cosmic rays from distant sources cannot be traced back to their origin, whereas at large energies this effect decreases substantially, so even particles from more remote sources can keep their directional information. Small scale anisotropies, thus clustering of arrival directions, could lead to the identification of point sources. Also neutrons, which are not affected by magnetic fields but have

limited range due to decay, can reach further at higher energies. Therefore the search for point sources should be focussed on the highest available primary energies. On the other hand, the quantification of the large scale anisotropy can yield valuable results for the discussion of models of cosmic ray propagation in our galaxy.

The KASCADE-Grande experiment

The KASCADE-Grande experiment[1] is located on site of the Forschungszentrum Karlsruhe, Ger-

many (49.1° north, 8.4° east, 110m above sea level). It has primarily been designed for the observation of cosmic rays in the energy range around 100 PeV, where a drop of the flux of the heavy elements (the ‘iron knee’) is suggested by the findings of the KASCADE experiment[2]. Since then, the original KASCADE setup has been extended by the Grande array to form the KASCADE-Grande experiment. While KASCADE is already a multi-detector setup, including an array of 252 scintillator detectors placed in a regular squareshaped grid with an edge length of 200 m, the added Grande array consists of 37 scintillator detector stations, spanning a much bigger area of nearly 0.5 km^2 . Thus the Grande array aims to raise the experiment’s energy range to up to 10^{18} eV . The full setup of KASCADE-Grande performs continuous and stable data taking since January 2004. Following the multi-detector approach, a common trigger signal induces joint data taking of all components. In the analysis presented here, only data from the Grande array were used. The shower directions, which are of particular interest for the anisotropy search, are reconstructed by evaluating the arrival times of the first particles hitting each detector, as well as the energy deposits. The accuracy of the shower axis reconstruction typically amounts to values around 0.8° . Depending on shower size and inclination angle, it is worse for more inclined showers, reaching about 1.5° for a zenith distance of 42° . See figure 1. Showers even more inclined are cut from the data set, not only due to the less accurate reconstruction, but also because of low statistics in this zenith angle range.

Large scale anisotropy

The large scale anisotropy is investigated by means of a harmonic analysis of the right ascension distribution of the air shower arrival directions. The Rayleigh formalism produces an amplitude value A , as well as a phase Φ , which corresponds to the right ascension of the direction of the excess. The procedure is sensitive to changes of the event rate during data taking, caused by meteorological effects. To reduce these influences, a small fraction of events is discarded or counted double respectively, depending on measured air temperature and

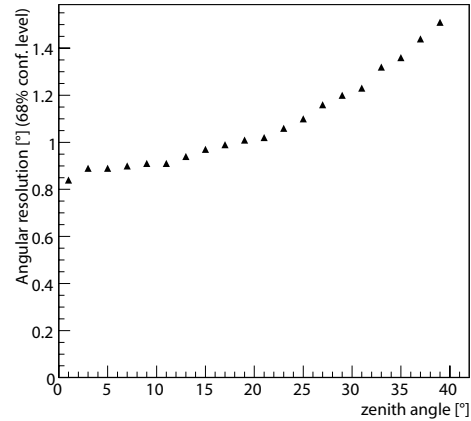


Figure 1: Angular resolution of the Grande array versus inclination angle, derived from Monte Carlo studies.

barometric pressure at the time of data taking. The resulting effective event rate is considerably less fluctuating. Much more hazardous are interruptions of data taking, which is why usually only periods of full sidereal days are taken into account for this kind of analysis. In the case of the present data set, this approach would lead to a reduction of the available statistics of 45%. Therefore, a modification of the Rayleigh formalism[3] has been developed, which takes right ascension dependent exposure times into account, allowing analysis of the full data set and thus increasing the available statistics almost by a factor of two.

Figure 3 shows the obtained upper limits at 95% confidence level for the Rayleigh amplitude versus estimated primary energy, in comparison to results of other experiments. An independent analysis of the KASCADE-Grande data with the east-west method[4] delivers an additional limit for $3 \cdot 10^{15} \text{ eV}$.

Autocorrelation analysis

An autocorrelation analysis can give evidence for clustering of air shower events and thus for the presence of point sources, while it cannot deliver any information on the number or location of such sources. For a given data set, the angular distance for each combination of two events is calculated. The distribution of these is compared with one cre-

ated from an artificial data set, which represents the hypothesis of an isotropic distribution and was created from the original data set using the shuffling technique[5]. Figure 4 shows the autocorrelation as proposed in [6]: $w_{LS} = (DD - 2DR + RR)/RR$, where DD , DR and RR denote the angular distance distributions of data-data, data-random (i.e. from the isotropic set) and random-random combinations of events. Since the number of angular distances to be computed increases quadratically with the number of events considered, this analysis was limited to the 1000 events of highest estimated primary energy.

Point sources would lead to an excess of small angular distances. As shown in figure 4, no such excess can be seen. No data points contradict with the assumption of an isotropic distribution, for which a two sigma confidence interval is indicated by the shaded area.

Search for point sources

The search for point sources is accomplished by comparing the measured arrival direction distribution in equatorial coordinates with an isotropic background distribution, obtained from the original data, using again the shuffling technique. The background distribution is made to contain 50 times as many events as the original data set. For each bin of the sky map, the significance of the excess of real data compared to the background is calculated according to Li and Ma[7]. The resulting significance map, with a bin width of 1° is shown in figure 5. Figure 2 shows the distribution of significances from the sky map. The expected shape of this distribution is a gaussian function with a mean value of 0 and a spread of 1. The histogram obtained from the data is in good compliance with this. Point sources present in the data set would lead to a distortion of this distribution.

Conclusions

We present results of the KASCADE-Grande experiment on anisotropy of cosmic rays on both the small scale (i.e. point sources) and the large scale (i.e. dipole like). The Rayleigh analysis of the measured right ascension distribution sets signifi-

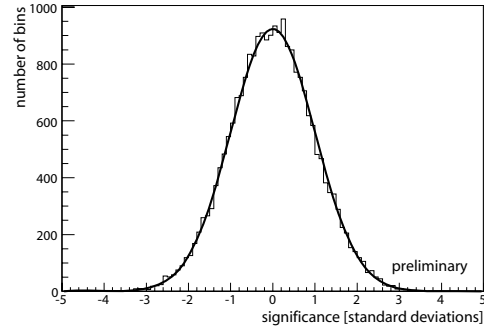


Figure 2: Distribution of the significance values of the 23216 bins containing events of the sky map. The plotted function depicts the expected behaviour: a gaussian function centered at 0 with a sigma of 1.

cant upper limits over the whole energy range. It is shown that with the full KASCADE-Grande statistics improved anisotropy measurements will be obtained over a crucial energy region.

Data taken by KASCADE-Grande reveal no evidence for point sources of cosmic rays. Neither the angular correlation analysis, nor the direct search for significant excesses of certain arrival directions can contradict the assumption of isotropy. For advanced analyses, the data set will be restricted to either the highest energy events, or to muon-poor air showers, enriching the data set with possible candidates of photon induced air showers.

References

- [1] A. Haungs et al. KASCADE-Grande Coll., in Proc. of the 30th ICRC, Merida (2005), these proceedings.
- [2] T. Antoni et al. KASCADE Coll., *Astrop. Phys.* 24, 1 (2005).
- [3] S. Mollerach and E. Roulet, *JCAP* 08 (2005).
- [4] D. Borla Tridon, Master Thesis, University of Turin/Italy (2007)
- [5] G.L. Cassiday et al., *Nucl. Phys. B (Proc. Suppl.)* 14 (1990).
- [6] S.D. Landy and A.S. Szalay, *ApJ* 412 (1993).
- [7] T.-P. Li and Y.-Q. Ma, *ApJ* 272 (1983).

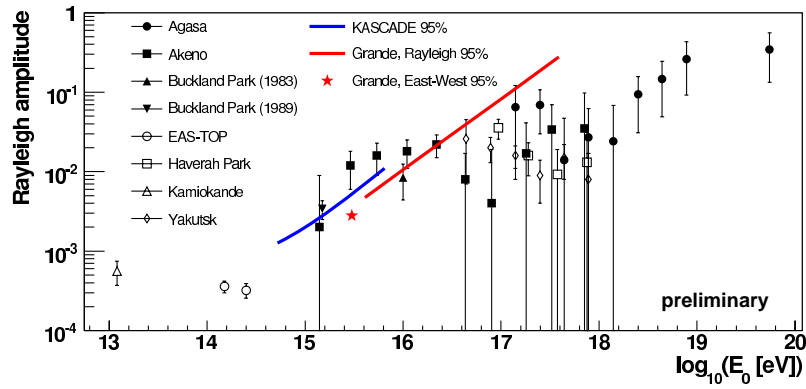


Figure 3: Upper limits for the Rayleigh amplitude, as obtained by a harmonic analyses of the distribution of the right ascension of arrival directions, compared to the results of other experiments.

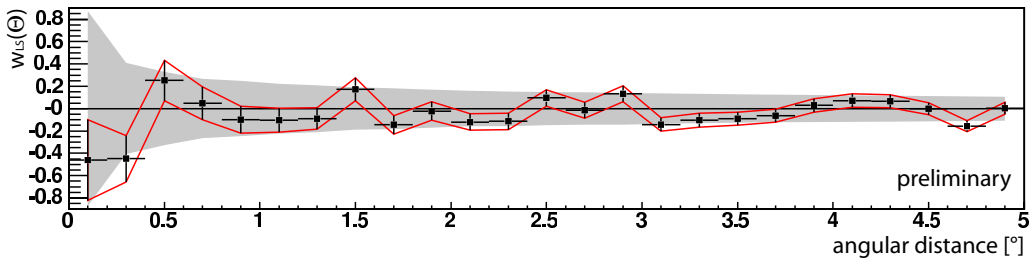


Figure 4: Autocorrelation of the arrival directions of the 1000 showers of highest estimated primary energy. The shaded area is the 2σ confidence region for isotropic distributions.

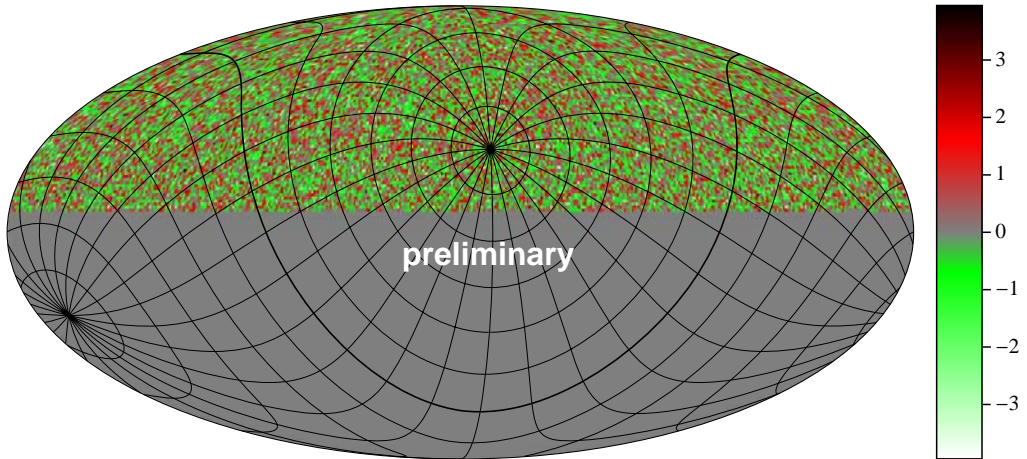


Figure 5: Significance map in equatorial coordinates. The exclusion of events more inclined than 42° results in the clear cut-off at declination 7° . The grid indicates galactic coordinates, with the thick curve representing the galactic plane.



The muon component of air showers measured by the KASCADE-Grande Experiment

V. DE SOUZA^c, J. VAN BUREN^a, W.D. APEL^a, J.C. ARTEAGA^a, F. BADEA^a, K. BEKK^a, M. BERTAINA^b, J. BLÜMER^{a,c}, H. BOZDOĞ^a, I.M. BRANCUS^d, M. BRÜGGEMANN^e, P. BUCHHOLZ^e, A. CHIAVASSA^b, F. COSSAVELLA^c, K. DAUMILLER^a, F. DI PIERRO^b, P. DOLL^a, R. ENGEL^a, J. ENGLER^a, M. FINGER^c, D. FUHRMANN^f, P.L. GHIA^g, H.J. GILS^a, R. GLASSTETTER^f, C. GRUPEN^e, A. HAUNGS^a, D. HECK^a, J.R. HÖRANDEL^c, T. HUEGE^a, P.G. ISAR^a, K.-H. KAMPERT^f, D. KICKELBICK^e, H.O. KLAGES^a, Y. KOLOTAEV^e, P. LUCZAK^h, H.J. MATHES^a, H.J. MAYER^a, C. MEURER^a, J. MILKE^a, B. MITRICA^d, A. MORALES^a, C. MORELLO^g, G. NAVARRA^b, S. NEHLS^a, J. OEHLISCHLÄGER^a, S. OSTAPCHENKO^a, S. OVER^e, M. PETCU^d, T. PIEROG^a, S. PLEWNIA^a, H. REBEL^a, M. ROTH^a, H. SCHIELER^a, O. SIMAⁱ, M. STÜMPERT^c, G. TOMA^d, G.C. TRINCHERO^g, H. ULRICH^a, W. WALKOWIAK^e, A. WEINDL^a, J. WOCHOLE^a, J. ZABIEROWSKI^h.

^a *Institut für Kernphysik, Forschungszentrum Karlsruhe, Germany*

^b *Dipartimento di Fisica Generale dell'Università Torino, Italy*

^c *Institut für Experimentelle Kernphysik, Universität Karlsruhe, Germany*

^d *National Institute of Physics and Nuclear Engineering, Bucharest, Romania*

^e *Fachbereich Physik, Universität Siegen, Germany*

^f *Fachbereich Physik, Universität Wuppertal, Germany*

^g *Istituto di Fisica dello Spazio Interplanetario, INAF Torino, Italy*

^h *Soltan Institute for Nuclear Studies, Lodz, Poland*

ⁱ *Department of Physics, University of Bucharest, Romania*

desouza@ik.fzk.de

Abstract: KASCADE-Grande is a multi detector setup for the investigation of extensive air showers in the $10^{16} - 10^{18}$ eV energy range. With the Grande array it is possible to reconstruct the shower core position, the arrival direction and the total number of charged particles in the shower. The Grande array measures in coincidence with the original KASCADE muon array consisting of 622 m² shielded scintillators. The data of the combined measurements are used to extract information from the muonic and electromagnetic parts of the shower independently. In this paper, the muon density in a ring from 380 to 400 m distance from the shower axis is studied and compared to predictions of hadronic interaction models. We report first results of these muon measurements at KASCADE-Grande which indicates the primary composition evolution.

Introduction

The KASCADE-Grande experiment [1] has been set up to measure primary cosmic rays in the energy range from 10^{16} to 10^{18} eV. Its main goal is to study the expected knee of the iron component. These observations would confirm the hypothesis that explains the proton knee of the primary cosmic rays spectrum at a few PeV and determine the as-

trophysical mechanism which operates in this energy range.

The experiment is located at the Forschungszentrum Karlsruhe, Germany, where, beside the existing KASCADE [2] array, two new detector setups (Grande and Piccolo) have been installed. The experiment is able to sample different components of extensive air showers (electromagnetic, muonic and hadronic) with high accuracy and covering a surface of 0.5 km². For an overview of the ac-

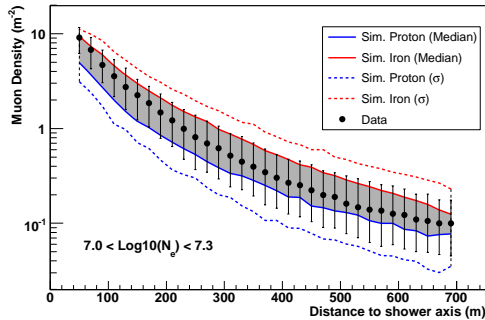


Figure 1: Density of muons as a function of the distance from the shower axis. Only showers with zenith angle below 40° were used. Error bars represent one sigma of the data distribution. See text for details.

tual setup of the KASCADE-Grande Experiment see ref. [8].

In this article we present studies of the muon component of the shower. The energy deposited by muons can be measured by the KASCADE stations separately from the electromagnetic component with a threshold of $E_\mu > 230$ MeV for vertical muons. Muons are the messengers of the hadronic interactions of the particles in the shower and therefore are a powerful tool to determine the primary particle mass and to study the hadronic interaction models.

Figure 1 shows the density of muons as a function of the distance from the shower axis for events with total number of electron (N_e) in the range $7.0 < \text{Log}10(N_e) < 7.3$. The density of muons is calculated for each shower as the sum of the signal measured by all stations in rings of 20 m divided by the effective detection area of the stations. Similar plots were obtained for other N_e ranges.

In the same plot, two limits for iron and proton simulations are also shown. The shaded area was determined by taking the median of the iron (full red line) and proton (full blue line) simulation. The dashed lines represents the simulation limits when the 16th quantile of the proton (dashed blue line) distribution and the 84th quantile of the iron (dashed red line) distribution were taken. It represents the one sigma (σ) limit of the simulation.

For all the studies in this paper we have used the CORSIKA [3] simulation program with

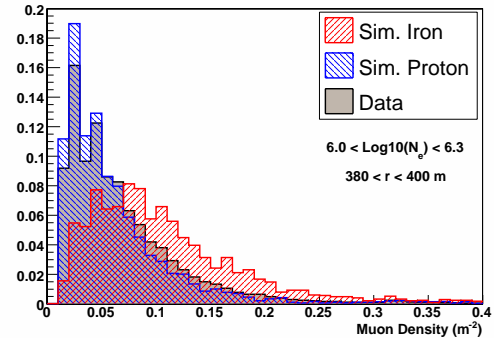


Figure 2: Density of muons in a ring from 380 to 400 m distance from the shower axis. See text for details.

FLUKA [4] and QGSJetII [5] hadronic interaction models. CORSIKA showers are simulated through the detectors and reconstructed in the same way as the measured data, such that a direct comparison between data and simulation is possible.

In the following, the density of muons in the ring from 380 to 400 m distance from the shower axis is going to be studied in more details. This distance range has been chosen in order to minimize the fluctuation of the signal and the reconstruction inaccuracy and to maximize the number of showers for which we have data.

The evaluation of the density of muons in the ring from 380 to 400 m is going to be determined as a function of the total number of electrons in the shower and a comparison to simulations is going to be shown.

Reconstruction Accuracy

The main parameters used in this study are the density of muons and the total number of electrons in the shower for which the reconstruction accuracy is going to be discussed below. For the reconstruction accuracy of the shower geometry see ref. [7].

The density of muons is directly measured by the KASCADE scintillators. These detectors are shielded by 10 cm of lead and 4 cm of iron, corresponding to 20 radiation lengths and a threshold of 230 MeV for vertical muons. The error in the measurement of the energy deposit was experimentally determined to be smaller than 10% [2].

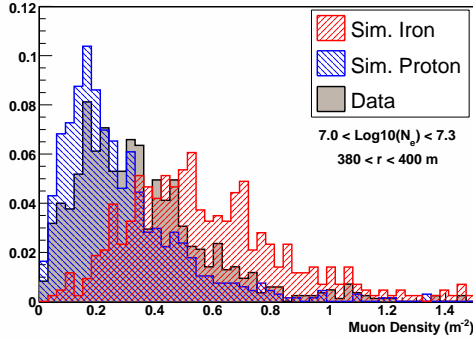


Figure 3: Density of muons in a ring from 380 to 400 m distance from the shower axis. See text for details.

The total number of electrons in the shower is reconstructed in a combined way using KASCADE and KASCADE-Grande stations. A lateral distribution function (LDF) of the Lagutin type can be fitted to the density of muons measured by the KASCADE detector [6]. After that, using the fitted function, the number of muons at any distance from the shower axis can be estimated. The KASCADE-Grande stations measure the number of charged particles. The number of electrons at each KASCADE-Grande stations is determined by subtracting from the measured number of charged particles the number of muons estimated with the LDF fitted to the KASCADE stations.

At this stage, the number of electrons at each KASCADE-Grande station is known. Latest, a modified NKG function is fitted to this data and the total number of electrons is determined in the fit. The accuracy of the reconstruction of N_e can be seen in ref. [9].

Quality cuts have been applied to the events in this analysis procedure. We have required the zenith angle to be smaller than 40 degrees and the event should have more than 19 KASCADE-Grande stations with signal. The same quality cuts were applied to the simulated events used for reconstruction studies and to the data presented in the following section. After the quality cuts, the total number of electrons can be estimated with a systematic shift smaller than 10% and a statistical uncertainty smaller than 20% along the entire range considered in this paper [9].

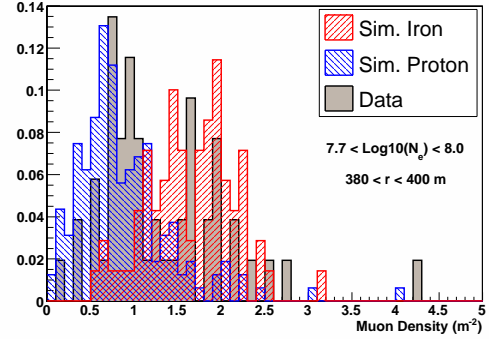


Figure 4: Density of muons in a ring from 380 to 400 m distance from the shower axis. See text for details.

Data Analysis

All showers measured by KASCADE-Grande which survived the quality cuts explained above have their muon density measured as a function of the distance from the shower axis. The distributions of the measured densities in a ring from 380 to 400 meters distance from the axis are shown in figure 3,4 and 5 in comparison with simulation.

We show the distributions for three cuts in total electron number: $6.0 < \text{Log}_{10}(N_e) < 6.3$, $7.0 < \text{Log}_{10}(N_e) < 7.3$ and $7.7 < \text{Log}_{10}(N_e) < 8.0$ in figures 2, 3 and 4, respectively.

Figure 2 shows that the data could be better described by a proton dominant abundance at this N_e selection. However, figures 3 and 4, with higher N_e selections, show that the data could only be described if a mixed composition is considered. From the three figures it is clear that an enhancement of the heavy component occurs with increasing N_e .

Figure 5 shows the evolution of the median muon density as a function of N_e . Two limits for the simulation are shown. The shaded area shows the limits determined by the median values of the proton (full blue line) and iron simulations (full red line). These limits can be used to visualize the evolution of the primary composition.

The dashed lines delimit the one sigma range of the proton and iron simulations. For that, it was taken the lower one sigma limit (16th quantile) of the proton (dashed blue line) distribution and the

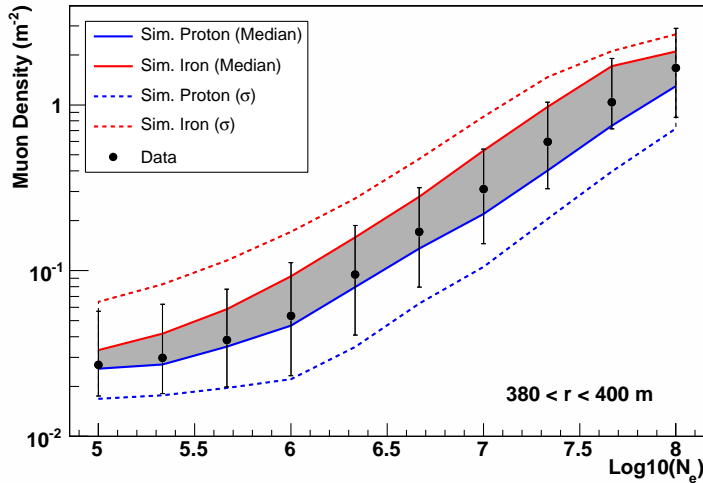


Figure 5: Muons density from 380 to 400 m distance from the shower axis as a function of total electron number. Error bars represent one sigma of the data distribution. See text for details.

upper one sigma limit (84th quantile) for the iron (dashed red line) distribution. These limits can be used to understand the fluctuations of the data when compared to the simulation. Note that a combined proton and iron composition shows about the same fluctuation of the data.

The change in slope seen in figure 6 for $\text{Log}_{10}(N_e) < 6.0$ corresponds to the threshold of the experiment and the fact that both data and simulation shows the same behavior illustrates the good level of understanding of our detectors. For the highest N_e values the simulations run out of sufficient statistics.

Conclusions

The Grande array is in continuous and stable data taking since January 2004. In this article, we have briefly described the procedure used to measure the density of muons with the KASCADE array and studied its correlation with the total number of electrons in the shower.

The density of muons in the shower is measured directly by the KASCADE detectors. We have used this data to study the hadronic interaction model (QGSJetII) and the primary composition. The median and the fluctuation of the density of muons in a ring from 380 to 400 m distance from the shower

axis lies within the limits of proton and iron simulations calculated by CORSIKA-QGSJetII in the range $6.0 < \text{Log}_{10}(N_e) < 8.0$. We have also shown that this parameter can be used for composition studies. A preliminary evolution from more light to a more heavy composition with increasing N_e was observed.

References

- [1] A. Haungs et al. KASCADE-Grande Collab., Proc. of 28th ICRC, Tsukuba (2003) 2, 985.
- [2] T. Antoni et al. KASCADE Coll., Nucl. Instr. and Meth. A 513, 490 (2003).
- [3] D. Heck et al., Report FZKA 6019 (1998)
- [4] G. Battistonia et al., ISVHECRI (2006) hep-ph/0612075v1
- [5] S.S. Ostapchenko, Phys. Rev. D 74 (2006) 014026
- [6] J. van Buren et al. KASCADE-Grande Coll., Proc. 29th ICRC, Pune (2005)
- [7] J.C.Arteaga et al. KASCADE-Grande Coll., Proc. 30th ICRC, Merida (2007).
- [8] A. Haungs et al. KASCADE-Grande Coll., Proc. 30th ICRC, Merida (2007).
- [9] F. Cossavela et al. KASCADE-Grande Coll., Proc. 30th ICRC, Merida (2007).



Separation of the electromagnetic and the muon component in EAS by their arrival times

M. BRÜGGEMANN^e, W.D. APEL^a, J.C. ARTEAGA^a, F. BADEA^a, K. BEKK^a, M. BERTAINA^b, J. BLÜMER^{a,c}, H. BOZDOG^a, I.M. BRANCUS^d, P. BUCHHOLZ^e, A. CHIAVASSA^b, F. COSSAVELLA^c, K. DAUMILLER^a, V. DE SOUZA^c, F. DI PIERRO^b, P. DOLL^a, R. ENGEL^a, J. ENGLER^a, M. FINGER^c, D. FUHRMANN^f, P.L. GHIA^g, H.J. GILS^a, R. GLASSTETTER^f, C. GRUPEN^e, A. HAUNGS^a, D. HECK^a, J.R. HÖRANDEL^c, T. HUEGE^a, P.G. ISAR^a, K.-H. KAMPERT^f, D. KICKELBICK^e, H.O. KLAGES^a, Y. KOLOTAEV^e, P. LUCZAK^h, H.J. MATHES^a, H.J. MAYER^a, C. MEURER^a, J. MILKE^a, B. MITRICA^d, A. MORALES^a, C. MORELLO^g, G. NAVARRA^b, S. NEHLS^a, J. OEHLISCHLÄGER^a, S. OSTAPCHENKO^a, S. OVER^e, M. PETCU^d, T. PIEROG^a, S. PLEWNIA^a, H. REBEL^a, M. ROTH^a, H. SCHIELER^a, O. SIMAⁱ, M. STÜMPERT^c, G. TOMA^d, G.C. TRINCHERO^g, H. ULRICH^a, J. VAN BUREN^a, W. WALKOWIAK^e, A. WEINDL^a, J. WOCHLE^a, J. ZABIEROWSKI^h.

^a *Institut für Kernphysik, Forschungszentrum Karlsruhe, Germany*

^b *Dipartimento di Fisica Generale dell'Università Torino, Italy*

^c *Institut für Experimentelle Kernphysik, Universität Karlsruhe, Germany*

^d *National Institute of Physics and Nuclear Engineering, Bucharest, Romania*

^e *Fachbereich Physik, Universität Siegen, Germany*

^f *Fachbereich Physik, Universität Wuppertal, Germany*

^g *Istituto di Fisica dello Spazio Interplanetario, INAF Torino, Italy*

^h *Soltan Institute for Nuclear Studies, Lodz, Poland*

ⁱ *Department of Physics, University of Bucharest, Romania*

brueggemann@hep.physik.uni-siegen.de

Abstract: KASCADE-Grande is a ground based multi-detector experiment measuring extensive air showers in order to study the primary cosmic ray energy spectrum in the energy range from 10^{14} eV to 10^{18} eV. A Flash-ADC based data acquisition system in KASCADE-Grande allows to study the temporal structure of extensive air showers. Muons in extensive air showers are thought to arrive on average earlier than the particles of the electromagnetic shower component. The separation of electrons and muons according to their arrival times poses an alternative to the measurement of the shower muon content with muon detectors. Approximately one year of KASCADE-Grande data have been analyzed to study the arrival times of the electromagnetic and the muonic shower components.

Introduction

The differences in the shower development of the electromagnetic and the muonic shower components suggest an arrival time difference between electrons and muons at the observation level. According to the model of the shower development, muons are on average produced higher in the atmosphere and move under the production angle with respect to the shower axis rectilinearly towards the observation point. The electromagnetic particles

are on average produced deeper in the atmosphere and close to the shower axis. They reach the observation point by multiple scattering creating longer path lengths and thus longer times of flight. Furthermore, electromagnetic particles which are produced at the early phase of the shower development are absorbed in the atmosphere before they reach the observation level. Therefore, the bulk of electromagnetic particles, which are detected at sea level, are produced deeper in the atmosphere or at a later stage of the shower development. At

this point, the energy available for the production of secondaries has already decreased. Hence, the average kinetic energy of the electromagnetic particles is smaller than the kinetic energy of the muons. The resulting effect of the different development of the electromagnetic and the muonic shower components is that muons arrive earlier at the observation level than particles of the electromagnetic shower component. The difference in the arrival time increases with the radial distance from the shower core.

Analysis

In order to study particle arrival times with KASCADE-Grande, data from a Flash-ADC based data acquisition system have been analyzed. The FADC system comprises 16 FADC modules of 8 bit resolution and a sampling frequency of 1 GHz. The 16 FADC modules are installed in eight detector stations of the KASCADE detector array. The two modules per station are connected to the electromagnetic and the muonic detectors in order to measure the electromagnetic and the muonic shower components separately. The FADC modules digitize the full shape of the photomultiplier signal. In this way the arrival times of shower particles at the detectors are being stored since the detector signal corresponds to a convolution of the particle arrival time distribution with the single particle detector response. This means that an extraction of the particle arrival time distribution is possible by applying an unfolding algorithm if the single particle detector response is known.

The single particle detector response has been determined by averaging single particle events from usual air shower data. A single particle detector response has been determined for the e/γ - and the μ -detector separately. The single particle detector response is used to construct the response matrix for the Gold unfolding algorithm. Figure 1 shows an example of an FADC pulse shape and the result of the unfolding.

The data used to study the arrival times of shower particles were recorded during approximately one year between January 2005 and February 2006. The minimum requirement for a data taking run to be analyzed was that at least the KASCADE

array, the Grande array and the Flash-ADC system participated in the data taking. From these runs only showers were selected which had their shower core reconstructed within a fiducial area of $600\text{ m} \times 600\text{ m}$ around the center of the Grande array, and which triggered at least 20 Grande detector stations. To assure a high quality of the reconstructed shower observables only showers which had a zenith angle smaller than 30° were used for the analysis. In total, approximately 290,000 extensive air showers measured by KASCADE-Grande entered the analysis. The used events belongs to primary energies of approximately $10^{16}\text{ eV} - 10^{18}\text{ eV}$. The signals in these selected air showers were only used for the analysis if no saturation occurred and the KASCADE array time measurement of the corresponding detector stations was available.

The signals which passed these quality requirements were unfolded as described above. The resulting arrival time distributions were filled into overall particle arrival time distributions. In order to study the temporal structure of the shower component in dependence on the distance from the shower center, the overall arrival time distributions were created for 13 intervals of the distance from the shower core. As an example, the arrival time distributions of electrons and muons are shown in figure 1. As the detectors for the electromagnetic shower component are located above the detectors for the muonic shower component, the arrival time distributions of electrons contain also the arrival times generated by muons passing the electromagnetic detector. This contribution had to be subtracted on a statistical basis by subtracting the muon arrival time distribution from the electron arrival time distribution after scaling down the muon arrival time distribution by the ratio of the electron detector area and muon detector area. As an example, the resulting particle arrival time distributions of electrons and muons are shown on the right hand side of figure 1 for the distance interval $R = (250 - 300)\text{ m}$.

Results

The arrival time distributions are used to generate the time profile of the electromagnetic and the

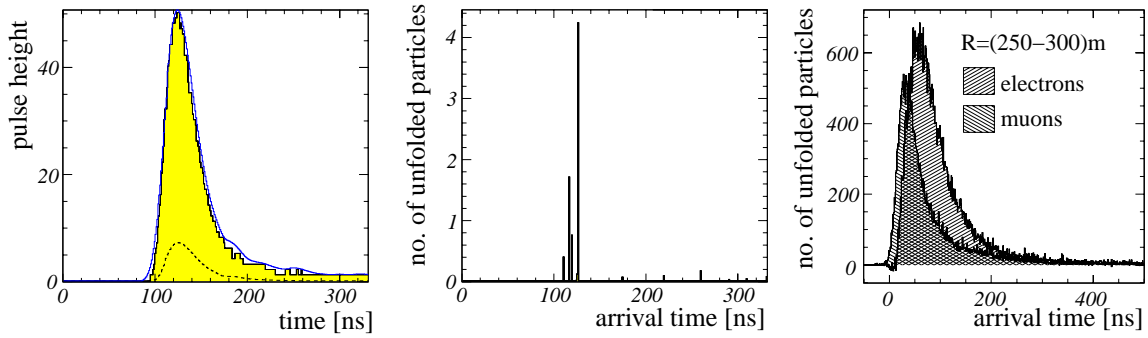


Figure 1: *Left:* The histogram depicts an example of an unfolded FADC signal pulse (from a μ -detector) belonging to a multi-particle transition. The dashed line corresponds to the average MIP detector response, which was used to generate the response matrix. The continuous line represents the forward folded solution which is the product of the unfolded arrival time distribution and the response matrix. *Middle:* Corresponding unfolded particle arrival time distribution. *Right:* Example of overall particle arrival time distributions in the distance interval $R = (250 - 300)$ m.

muonic shower fronts. The mean value of the distributions represents the most probable arrival time of the corresponding particle type. The shower front profile of the electromagnetic and the muonic component is shown in figure 2. The thicknesses of the shower disks of both components by means of the standard deviation of the corresponding arrival time distributions are depicted in figure 3. The time

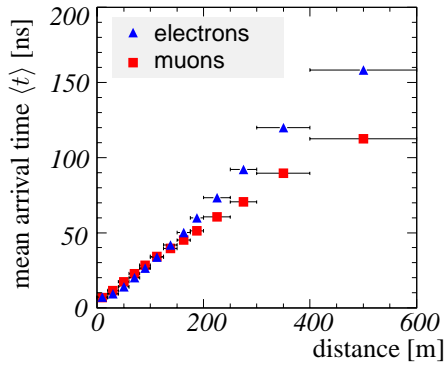


Figure 2: Mean arrival time of electrons and muons as a function of the core distance according to the mean values of the particle arrival time distributions.

profile indicates that for $R > 200$ m muons start to arrive earlier at the observation level than electrons. The relative difference in the average arrival time increases with increasing core distance as expected.

The difference in the average arrival time above $R = 200$ m allows the determination of an arrival time cut in order to separate electrons and muons. This time cut on the particle arrival time is defined as the average of the distributions' mean values. As the muons represent the early shower component, particles with an arrival time smaller than the arrival time cut are considered muons whereas particles with a later arrival time are considered electrons. The particle arrival time cut as a function of

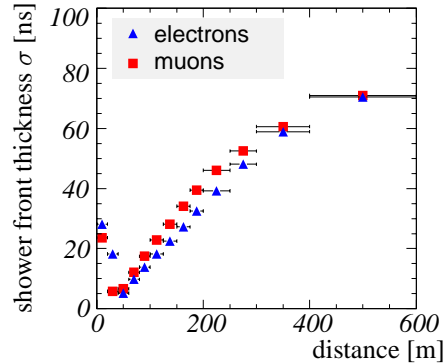


Figure 3: Thickness of the electromagnetic and muonic shower front as a function of the core distance in terms of the standard deviation of the particle arrival time distributions.

the core distance is shown in figure 4. Due to the large spread of the particle arrival times the muon selection obtained by this definition is not 100 %

clean, but will also contain misclassified early electrons. In order to determine the expected purity of the muon selection the arrival time cut was applied to the arrival time distributions and the muon purity was calculated as the ratio of the number of muons to the total number of particles before the arrival time cut. The purity of the muon selection is shown in figure 5. The error band in both pictures reflects the sum of statistical and systematic errors and is dominated by the systematic error. The systematic error is mainly caused by the uncertainty of the reconstructed arrival time of the shower core and the alignment of the unfolded particle arrival times relative to the shower core arrival time.

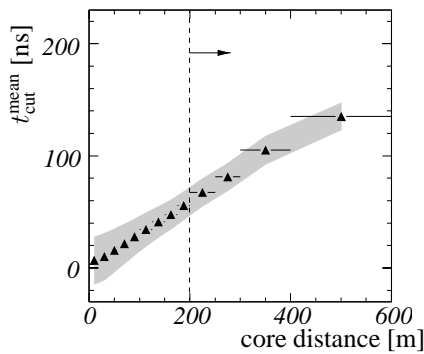


Figure 4: Separation cut values calculated from the mean values of the particle arrival time distributions with the systematic uncertainties represented by the error bands. The dashed lines represent the core distance above which a separation of electrons and muons according to their arrival times becomes feasible.

Discussion

The analysis of particle arrival times of the electromagnetic and muonic shower component with data from the KASCADE-Grande experiment has shown that muons have on average an earlier arrival time at the observation level than electrons. This difference in the arrival time can be used for an alternative method to determine the muon content in extensive air showers. Experiments without dedicated muon detectors but with time resolving data acquisition electronics are able to separate muons from electrons according to their arrival time to a certain extent.

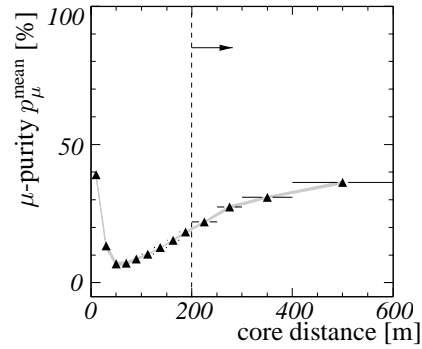


Figure 5: Muon purities calculated from the mean values of the particle arrival time distributions with the systematic uncertainties represented by the error bands. The dashed lines represent the core distance above which a separation of electrons and muons according to their arrival times becomes feasible.

References

- [1] T. Antoni et al., Nucl. Instr. Meth. A513 (2003), 429
- [2] M. Brüggemann, PhD Thesis (2007), Siegen University
- [3] A. Chiavassa et al. - KASCADE-Grande collaboration, 2003 *Proc. of 28th ICRC, Tsukuba, Japan* 989
- [4] A. Haungs et al. - KASCADE-Grande collaboration, 2003 *Proc. of 28th ICRC, Tsukuba, Japan* 985
- [5] G. Navarra et al., Nucl. Instr. Meth. A518 (2004), 207
- [6] J. van Buren et al. - KASCADE-Grande collaboration, 2007 *Proc. of 30th ICRC, Merida, Mexico*, these proceedings



Muon Production Height in the Air-Shower Experiment KASCADE-Grande

P. DOLL^a, W.D. APEL^a, J.C. ARTEAGA^a, F. BADEA^a, K. BEKK^a, M. BERTAINA^b, J. BLÜMER^{a,c}, H. BOZDOG^a, I.M. BRANCUS^d, M. BRÜGGEMANN^e, P. BUCHHOLZ^e, A. CHIAVASSA^b, F. COSSAVELLA^c, K. DAUMILLER^a, V. DE SOUZA^c, F. DI PIERRO^b, R. ENGEL^a, J. ENGLER^a, M. FINGER^c, D. FUHRMANN^f, P.L. GHIA^g, H.J. GILS^a, R. GLASSTETTER^f, C. GRUPEN^e, A. HAUNGS^a, D. HECK^a, J.R. HÖRANDEL^c, T. HUEGE^a, P.G. ISAR^a, K.-H. KAMPERT^f, D. KICKELBICK^e, H.O. KLAGES^a, Y. KOLOTAEV^e, P. LUCZAK^h, H.J. MATHES^a, H.J. MAYER^a, C. MEURER^a, J. MILKE^a, B. MITRICA^d, A. MORALES^a, C. MORELLO^g, G. NAVARRA^b, S. NEHLS^a, J. OEHLSCHLÄGER^a, S. OSTAPCHENKO^a, S. OVER^e, M. PETCU^d, T. PIEROG^a, S. PLEWNIA^a, H. REBEL^a, M. ROTH^a, H. SCHIELER^a, O. SIMAⁱ, M. STÜMPERT^c, G. TOMA^d, G.C. TRINCHERO^g, H. ULRICH^a, J. VAN BUREN^a, W. WALKOWIAK^e, A. WEINDL^a, J. WOCHOLE^a, J. ZABIEROWSKI^h.

^a Institut für Kernphysik, Forschungszentrum Karlsruhe, Germany

^b Dipartimento di Fisica Generale dell'Università Torino, Italy

^c Institut für Experimentelle Kernphysik, Universität Karlsruhe, Germany

^d National Institute of Physics and Nuclear Engineering, Bucharest, Romania

^e Fachbereich Physik, Universität Siegen, Germany

^f Fachbereich Physik, Universität Wuppertal, Germany

^g Istituto di Fisica dello Spazio Interplanetario, INAF Torino, Italy

^h Soltan Institute for Nuclear Studies, Lodz, Poland

ⁱ Department of Physics, University of Bucharest, Romania

doll@ik.fzk.de

Abstract: A large area ($128m^2$) Muon Tracking Detector (MTD), located within the KASCADE experiment, has been built with the aim to identify muons ($E_\mu > 0.8\text{GeV}$) and their directions in extensive air showers by track measurements under more than 18 r.l. shielding. The orientation of the muon track with respect to the shower axis is expressed in terms of the radial- and tangential angles. By means of triangulation the muon production height H_μ is determined. By means of H_μ , transition from light to heavy cosmic ray primary particle with increasing shower energy E_o from 1-10 PeV is observed.

Introduction

Muons have never been used up to now to reconstruct the hadron longitudinal development of EAS with sufficient accuracy, due to the difficulty of building large area ground-based telescopes [1]. Muons are produced mainly by charged pions and kaons in a wide energy range. They must not always be produced directly on the shower axis. The multiple Coulomb scattering in the atmosphere and in the detector shielding also change the muon direction. It is evident that the reconstruction of the longitudinal development of the muon component by means of triangulation [2, 3] provides a power-

ful tool for primary mass measurement and for the study of high-energy hadron interactions with the atmospheric nuclei, giving the information similar to that obtained with the Fly's Eye experiment, but in the energy range not accessible by the detection of fluorescent light. Muon tracking allows also the study of hadron interactions by means of the muon pseudorapidity [4]. Already in the past, analytical tools have been developed which describe the transformation between shower observables recorded on the observation level and observables which represent the longitudinal shower development [5]. Fig. 1 shows the experimental environment.

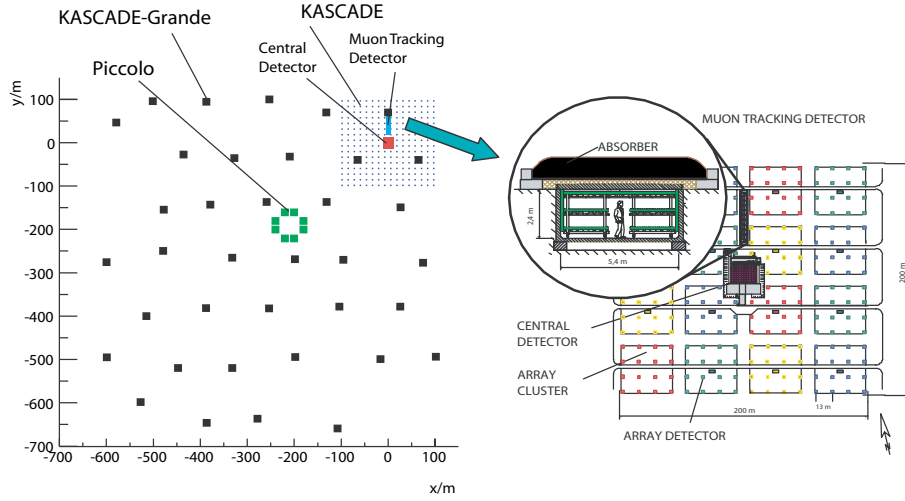


Figure 1: Schematic view of the KASCADE-Grande experiment with some details on the Muon Tracking Detector (MTD).

Muon Production Height over Electron and Muon Size

Usually, X_{max} is the atmospheric depth at which the electrons and photons of the air shower reach their maximum numbers and is considered to be mass A sensitive [6]. Concerning muons which stem dominantly from π^\pm decays, the corresponding height where most muons are created may also provide a mass A sensitive observable. For X_{max} , Matthews [7] in a phenomenological ansatz gives for the e.m. part the elongation rate of $85gcm^{-2}$ per decade ($\lg=\log_{10}$) which is in a good agreement with simulations. For the X_{max} value for nuclei ref. [7] reports: $X_{max}^A = X_{max}^p - X_o \ln(A)$ (X_o radiation length in air), therefore, X_{max} from iron showers is $\sim 150gcm^{-2}$ higher than X_{max} from proton showers at all energies. With the integral number of muons for a proton or nucleus A induced shower:

$$N_\mu \sim E_0^\beta \quad \text{or} \quad N_\mu^A \sim A(E_A/A)^\beta \quad (1)$$

and

$$X_{max} \sim \lg(E_0) \quad (2)$$

we assume that $\langle H_\mu \rangle$ exhibits a similar $\lg(N_e)$ and $\lg(N_\mu^{tr})$ dependence as X_{max} . Note however, $\langle H_\mu \rangle$, because of the long tails in the H_μ distribution towards small (gcm^{-2}) can be systematically

higher than the muon production height, where most of the muons are created in a shower. Some energetic muons may stem from the first interaction and survive down to the MTD detector plane. The elongation rate D_μ becomes

$$D_\mu = \delta \langle H_\mu \rangle / \delta \lg N_\mu^A \quad (3)$$

The almost mass A independent energy assignment in equation [4] was employed.

$$\lg E_0 [GeV] = 0.19 \lg(N_e) + 0.79 \lg(N_\mu^{tr}) + 2.33 \quad (4)$$

The shower development leads also to different fluctuations in those shower parameters.

For the following analysis the elongation rate D_μ was given the value $70gcm^{-2}$ per decade in $\lg(N_\mu^{tr})$. After subtracting from each track the 'energy' dependent penetration depth

$$H_\mu^A = H_\mu - 70gcm^{-2} \lg(N_\mu^{tr}) + 20gcm^{-2} \lg(N_e) \quad (5)$$

the remaining depth H_μ^A should be giving the mass A dependence.

The correction with the electron size $\lg(N_e)$ in equation [5] should be of opposite sign because of fluctuations to larger size for this variable (X_{max} also fluctuates to larger values).

Investigating in a closer look the distribution of the parameters involved in the correction for H_μ^A for

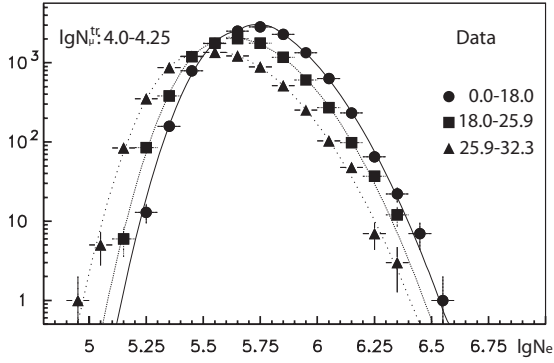


Figure 2: $\lg(N_e)$ size spectra for $\lg(N_\mu^{tr})=4.0-4.25$ and three zenith angle ranges.

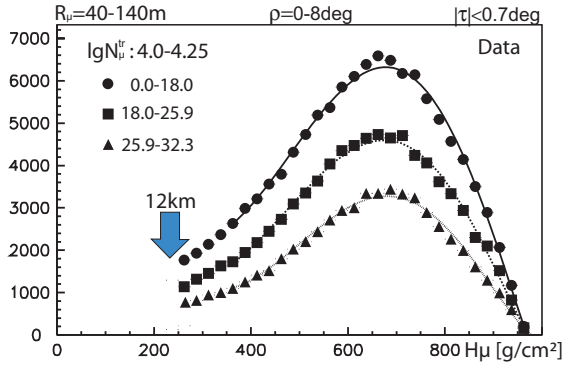


Figure 3: H_μ spectra for $\lg(N_\mu^{tr})=4.0-4.25$ and three zenith angle ranges.

the elongation rate, Fig. 2 shows how the electron size distributions for fixed muon number bin and three zenith angle bins vary with angle. In a similar way Fig. 3 shows muon production height distributions for the same shower parameters (below 12km were the errors are small). It is known from earlier studies, that the $\lg(N_e)$ parameter exhibits fluctuations to large values in agreement with simulations while the $\lg(N_\mu^{tr})$ parameter exhibits little fluctuations. In contrary, the H_μ parameter in Fig. 3 is fluctuating to smaller values (gcm^{-2}). Therefore, we may argue that the fluctuations in the corrections for H_μ for the elongation rate will cancel to some extent and, therefore, the resulting mass A dependent muon production height H_μ^A represents a stable mass A observable.

Fig. 4 shows the regions of different mass A dependent mean muon production height $\langle H_\mu^A \rangle$ in the 2 parameter space $\lg(N_e) - \lg(N_\mu^{tr})$. H_μ^A in Fig. 4 is the mean $\langle H_\mu^A \rangle$ per shower and any muon track in the MTD. The picture shows regions of distinct $\langle H_\mu^A \rangle$ in a color code with a $40gcm^{-2}$ step size. The borders between different regions are for some cases marked with lines which exhibit a slope in the $\lg(N_e) - \lg(N_\mu^{tr})$ plane. While in the middle of the distribution the slope confirms the previously employed slope $\lg(N_\mu^{tr}) = 0.74(\pm 0.01)\lg(N_e)$ for selecting light or heavy primary particles, modified slopes may be recognized for regions away from the middle of the ridge. The slope for the $600gcm^{-2}$ line comes close to the slope of the air-shower simulations employed in [8]. Note also that the number of tracks increase with energy and exhibit a specific mass A dependent rise, which is under study.

The lines obtain their slope from the muon number-energy relation in equation [1] combined with equation [4]. There, the exponent is according to ref. [7] connected to the amount of inelasticity κ (fraction of energy used up for π production) involved in the processes of the A-air collisions. A comparatively steeper slope $\beta = (1 - 0.14\kappa)$ [7], corresponds to an increased inelasticity. The correction in equation [5] depending on $\lg(N_e)$ and $\lg(N_\mu^{tr})$ was found appropriate to get the slope of the H_μ^A profile in the 2 parameter $\lg(N_e) - \lg(N_\mu^{tr})$ presentation (Fig. 4). Differences between 2 lines amount to $40gcm^{-2}$. Differences between two different models in ref. [8] amount to about $20gcm^{-2}$ on the H_μ^A scale.

Sorting the $\lg(N_e) - \lg(N_\mu^{tr})$ events by their range in H_μ^A and employing for the same event the mass A independent equation [4] for $\lg E_o [GeV]$, energy spectra are obtained and given in Fig. 5. Sofar no explicit mass range assignment is given as would be motivated by the equation $X_{max}^A = X_{max}^p - X_o \ln(A)$. The spectra in Fig. 5 together with their preliminary error estimations are almost model independent. The preliminary spectra reveal distinct features. While low mass spectra show a rapid drop with increasing shower energy, medium mass and heavy mass spectra seem to overtake at large primary energy. Systematic errors dominate the low and high energy bins and are a subject of further investigation. In the present analysis the

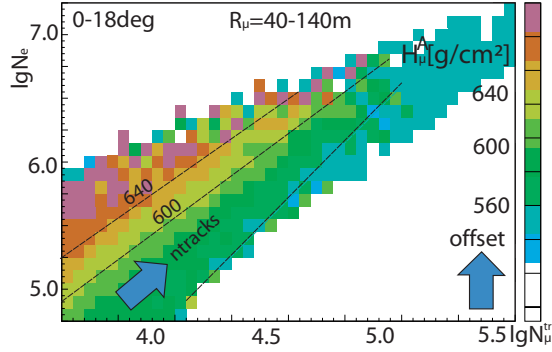


Figure 4: $lg(N_e) - lg(N_{\mu}^{tr})$ matrix with effective muon production height H_{μ}^A along the z-axis.

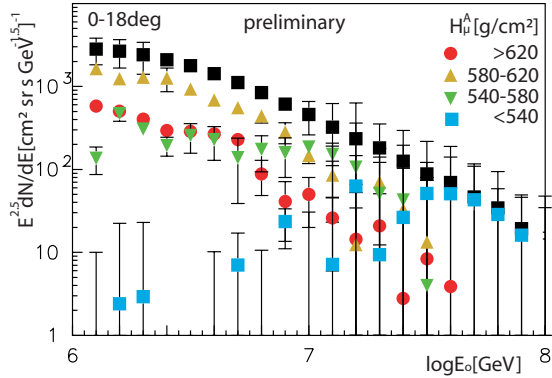


Figure 5: Energy spectra for different mass A groups which produce muons at different effective muon production height H_{μ}^A .

detection threshold of the MTD may be effective and a fraction of tracks may be missing leading to a light particle mass interpretation.

Conclusions

Triangulation allows to investigate H_{μ} . Future analysis of other shower angle bins and of larger and improved quality data sample will provide a more detailed information on the nature of high energy shower muons. Also muon multiplicities provide valuable parameters to derive the relative contributions of different primary cosmic ray particles. A natural extension towards even larger shower en-

ergies will be provided by KASCADE-Grande [9]. There is a common understanding that the high energy shower muons serve as sensitive probes to investigate [4] the high energy hadronic interactions in the EAS development. Very inclined muons which can be studied with tracks recorded by the wall modules of the MTD are currently of vital interest.

Acknowledgements

The support by the PPP-DAAD/MNiSW grant for 2007-2008 is kindly acknowledged.

References

- [1] P.Doll et al., Nucl.Instr.and Meth. A488 (2002) 517; J.Zabierowski and P.Doll., Nucl.Instr.and Meth. A484 (2002) 528.
- [2] M.Ambrosio et al., Nucl. Phys. (Proc.Suppl.)75A (1999) 312.
- [3] R.Obenland et al., (KASCADE Coll.), Proc. 29th ICRC 2005, Pune, India Vol.6,225.
- [4] J.Zabierowski et al., (KASCADE Coll.), Proc. 29th ICRC 2005, Pune, India Vol.6,357; J.Zabierowski et al., (KASCADE Coll.), Proc. 30th ICRC 2007, Merida, Mexico, these proceedings.
- [5] L.Pentchev and P.Doll, J.Phys.G: Nucl.Part.Phys. 27 (2001) 1459.
- [6] J.Linsley, Proc.15th ICRC, 12 (1977) 89; T.K.Gaisser et al., Proc. 16th ICRC, 9 (1979)258.
- [7] J.Matthews, Astropart.Phys.22 (2005) 387
- [8] T. Antoni et al., (KASCADE Coll.), Astropart. Phys. 24 (2005) 1.
- [9] A.Haungs et al., (KASCADE-Grande Coll.), Proc. ISVHECRI, Weihei, Nucl.Phys.B, in press.



Tests of hadronic interaction models with muon pseudorapidities measured with KASCADE-Grande

J. ZABIEROWSKI^a, W.D. APEL^b, J.C. ARTEAGA^a, F. BADEA^b, K. BEKK^b, M. BERTAINA^c, J. BLÜMER^{b,d}, H. BOZDOG^b, I.M. BRANCUS^e, M. BRÜGGEMANN^f, P. BUCHHOLZ^f, A. CHIAVASSA^c, F. COSSAVELLA^d, K. DAUMILLER^b, V. DE SOUZA^d, F. DI PIERRO^c, P. DOLL^b, R. ENGEL^b, J. ENGLER^b, M. FINGER^d, D. FUHRMANN^g, P.L. GHIA^h, H.J. GILS^b, R. GLASSTETTER^g, C. GRUPEN^f, A. HAUNGS^b, D. HECK^b, J.R. HÖRANDEL^d, T. HUEGE^b, P.G. ISAR^b, K.-H. KAMPERT^g, D. KICKELBICK^f, H.O. KLAGES^b, Y. KOLOTAEV^f, P. LUCZAK^a, H.J. MATHES^b, H.J. MAYER^b, C. MEURER^b, J. MILKE^b, B. MITRICA^e, A. MORALES^b, C. MORELLO^h, G. NAVARRA^c, S. NEHLS^b, J. OEHLSCHLÄGER^b, S. OSTAPCHENKO^b, S. OVER^f, M. PETCU^e, T. PIEROG^b, S. PLEWNIA^b, H. REBEL^b, M. ROTH^b, H. SCHIELER^b, O. SIMAⁱ, M. STÜMPERT^d, G. TOMA^e, G.C. TRINCHERO^h, H. ULRICH^b, J. VAN BUREN^b, W. WALKOWIAK^f, A. WEINDL^b, J. WOCHLE^b.

^a *Soltan Institute for Nuclear Studies, Lodz, Poland*

^b *Institut für Kernphysik, Forschungszentrum Karlsruhe, Germany*

^c *Dipartimento di Fisica Generale dell'Università Torino, Italy*

^d *Institut für Experimentelle Kernphysik, Universität Karlsruhe, Germany*

^e *National Institute of Physics and Nuclear Engineering, Bucharest, Romania*

^f *Fachbereich Physik, Universität Siegen, Germany*

^g *Fachbereich Physik, Universität Wuppertal, Germany*

^h *Istituto di Fisica dello Spazio Interplanetario, INAF Torino, Italy*

ⁱ *Department of Physics, University of Bucharest, Romania*

janzab@zpk.u.lodz.pl

Abstract: The Muon Tracking Detector in the KASCADE-Grande experiment allows the measurement of muon directions up to 700 m from the shower center. It means, that nearly all muons produced in a shower and surviving to the ground level are subject of investigation. It is important not only for studying mean muon production heights but also for investigations of EAS muon pseudorapidity distributions. These distributions are nearly identical to the pseudorapidity distributions of their parent mesons produced in hadronic interactions. Lateral distribution of muon pseudorapidity in extensive air showers (EAS) is a sensitive probe of hadronic interaction parameters embedded in the models. In this quantity lateral distribution of muon energy and lateral distribution of muon transverse momenta are hidden. Results of the analysis compared with the predictions of QGSJetII and FLUKA2002 models are discussed.

Introduction

The Muon Tracking Detector (MTD) [1] is one of the detector components in the KASCADE-Grande experiment [2] operated on site of the Research Center Karlsruhe in Germany by an international collaboration. The MTD with its detection acceptance of about $500 \text{ m}^2 \cdot \text{sr}$ measures in EAS tracks of muons, which energy exceeds 0.8 GeV, with the excellent angular resolution of ($\approx 0.35^\circ$).

The layout of the experiment is shown in Fig. 1.

Muons are very sensitive probe of the processes responsible for the development of an air shower in the atmosphere. They hardly interact and suffer only small deflection due to scattering in the air. Thus, in the directional information they conserve some of the kinematic parameters of their parent mesons - the most abundant products of hadronic interactions. Despite significant progress over the last decade, these interactions, at the en-

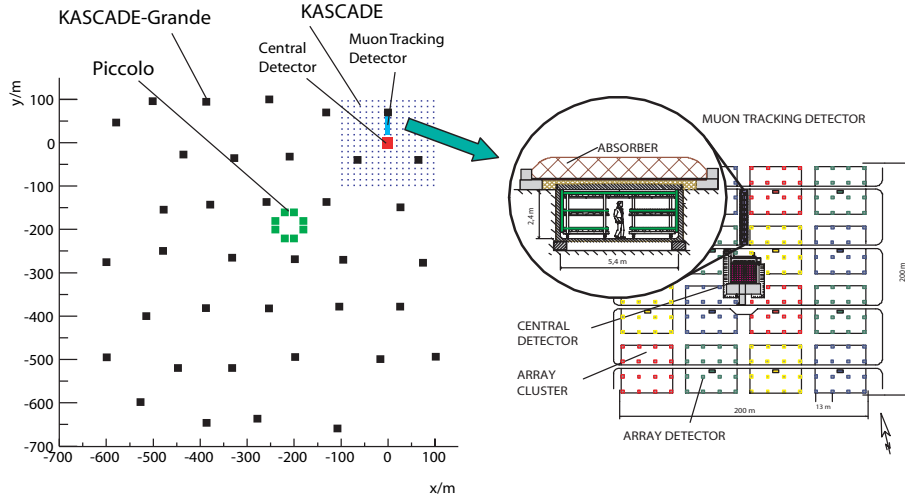


Figure 1: Layout of the KASCADE-Grande experiment distributed over the Research Center Karlsruhe. KASCADE is situated in the North-East corner of the Center; note the position of the Muon Tracking Detector.

ergies and kinematical regions relevant for the development of EAS, are still not well understood, mainly due to the lack of direct accelerator measurements. Therefore, tests of the models with the EAS data are the only accessible means to improve them.

Muon tracking

The muon tracking in KASCADE-Grande utilizes the concept of radial (ρ) and tangential (τ) angles (Fig. 2). The radial angle is a basic quantity in the determination of muon production heights [3]. A combination of both angles, as shown in [4], allow to determine the pseudorapidities of muons in EAS. Namely, a certain combination of τ and ρ is equal to the ratio of transversal to longitudinal momentum components of the muon with respect to the shower direction:

$$\zeta \equiv \sqrt{\tau^2 + \rho^2} = \frac{p_t}{p_{\parallel}} \quad (1)$$

Hence, the pseudorapidity η of muons with energy > 0.8 GeV (MTD threshold) can be expressed as follows:

$$\eta = \ln \frac{2 \times p_{\parallel}}{p_t} \approx -\ln \frac{\zeta}{2} \quad (2)$$

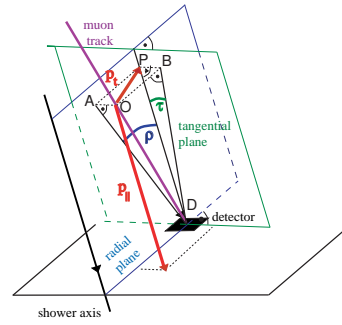


Figure 2: Definition of radial and tangential angles.

This muon pseudorapidity is highly correlated with pseudorapidity of their parent hadrons [5], thus being a powerful probe of high-energy hadronic interactions and can be used to test and improve existing hadronic interaction models.

Results and discussion

In KASCADE-Grande we have measured muon directions up to 600 m distance from the shower core. As simulations show, we track in this way nearly all muons surviving to the observation level [6]. A very good probe of the hadronic interaction is the lateral distribution of mean radial angle and, finally, of mean muon pseudorapidity. This

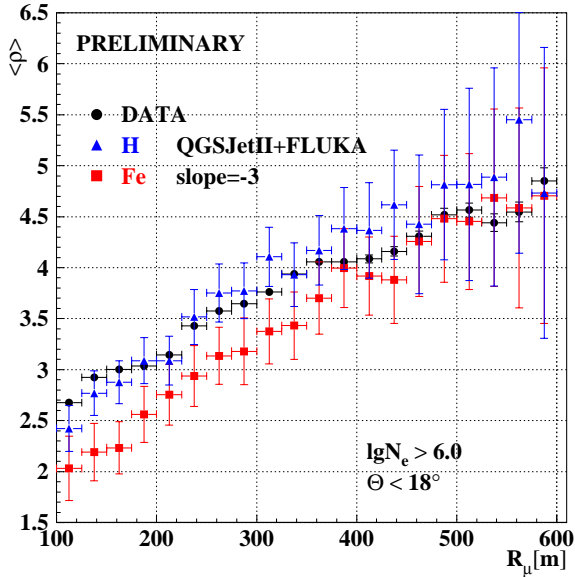


Figure 3: Lateral distribution of mean radial angle of EAS muons. Statistical errors only are shown.

is because with the MTD we examine the longitudinal development of the muonic shower component. At every given distance to the shower core we register muons from a certain window of production heights. Thus, lateral distribution of any measured muon parameter is a result of sliding this window over the whole shower development. The content of such a window is a result of hadronic interactions together with the propagation-related processes like multiple scattering and decays (of mesons and muons). Therefore, measured lateral distributions can be used to check how these distributions are predicted by hadronic interaction models.

In the following we shall analyze vertical air showers ($\theta \leq 18^\circ$) efficiently triggered by the Grande Array, what means, having electron size $\lg(N_e) \geq 6$. The measured experimental values are compared with the predicted ones for proton and iron primaries by Monte Carlo CORSIKA [7] simulations using QGSJetII and FLUKA2002 [8] as high and low energy hadronic interaction models, respectively. In Fig. 3 the lateral distribution of mean radial angles of muons registered in such showers is shown. Limiting the value of ρ to maximum 10° removes from the analysis long tails of radial angle distributions produced by low energy muons created close above the detector.

Moving away from the shower core one observes a rise of the mean radial angle value, i.e. at large distances more muons are detected which are produced deeper in the atmosphere. The value of radial angle is dominated by the transversal momentum of a muon so, the distribution in Fig. 3 reflects the lateral distribution of mean transversal momentum of survived EAS muons, what is confirmed by CORSIKA simulations.

As it is seen from the figure in the range 100 - 400 m data points lay either above or very close to the points obtained for the proton initiated showers. At the distances below 200 m there seems to be a mismatch between simulations and the experiment. Investigations below 100 m done with KASCADE Array data confirm this situation. Above 400 m one observes a bend in the distribution causing the points fall close to the iron simulation results. Due to the large statistical errors and not fully identical conditions in the experiment and in simulations in this region one cannot make any quantitative conclusions here, noting only that the rise of the mean values of ρ is maintained.

The lateral distribution of mean pseudorapidity of EAS muons which survived to the observation level is particularly well suited as a tool for testing interaction models. In this quantity such kinematical variables like muon energy and its transversal momentum are covered (pseudorapidity being proportional to the ratio of those two).

The results showing experimental data compared with the simulation results for proton and iron primaries are given in Fig. 4. As it is seen from equations (1) and (2) the value of η is dominated by the radial angle. Therefore, one observes the same relations between measured and simulated results as in the previously discussed distribution. The slope of the distribution is smaller in the measured data than in the simulated ones resulting in a growing discrepancy while approaching the shower core. Previous analyses done with KASCADE data for distances 40 - 140 m are in agreement with the present one showing the continuation into the closer distances with the same slope [9]. Also the measured mean pseudorapidity values are below the simulated ones for proton showers in KASCADE distances, as it starts to be seen below 200 m in Fig. 4. The argumentation for the better agree-

ment above 400 m is the same as in case of ρ distribution above.

There may be several reasons why simulations result in too high pseudorapidity value of measured muons. The model produces either muons with too high mean energy or too small mean transverse momentum. However, having in mind that the values are averaged for "survived" muons one can also assume, that slightly higher energy of muons at production would give them a chance not to decay and be registered, adding their relatively low pseudorapidities to the measured sample.

Similar results one would get enlarging the muon survival probability by producing them deeper in the atmosphere. Since the low energy (below 10 GeV) muons are dominating in the registered sample even slight increase in their number (number of survived ones - not necessarily one should increase the pion multiplicity in the interactions) would give the shift of the mean values towards agreement with the measurements.

Apart from the above indicated drawbacks of the data at distances over 400 m one should note, that they cannot fully account for generally better agreement between data and simulations in the remote region. As indicated in [6] at different distances to the shower core we are sensitive with the MTD to muons produced in different ranges of hadronic interaction energies. In the close-by distances (KASCADE range: 40 - 160 m) the majority of registered muons originate from mesons created at energies modelled by high-energy interaction model. With moving away from the shower core (KASCADE-Grande distances - up to 700 m) the input from the interactions governed in simulations by a low-energy model becomes more and more important.

Therefore, one can conclude that the largest discrepancies between measured and simulated results seen in Fig. 4 are likely to be due to the imperfections of high-energy hadronic interaction model, here QGSJetII.

Acknowledgements

The support by the PPP-DAAD/MNiSW grant for 2007-2008 is kindly acknowledged.

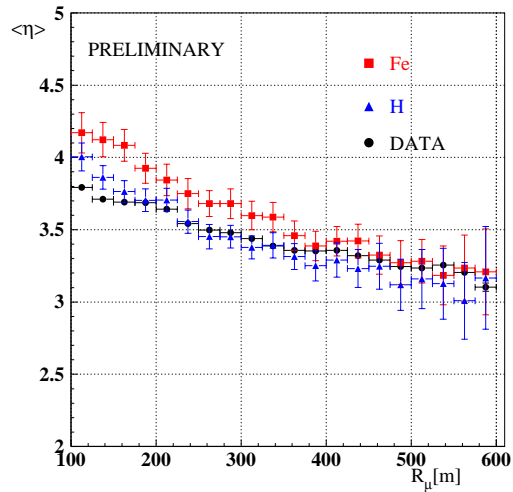


Figure 4: Lateral distribution of mean muon pseudorapidity measured in the MTD.

References

- [1] P.Doll et al., Nucl. Instr. and Meth. A 488, (2002) 517.
- [2] A.Haungs et al. KASCADE-Grande Coll., Proc of 28th ICRC, Tsukuba (2003) 2, 985.
- [3] P.Doll et al. KASCADE-Grande Coll., Proc. of 30th ICRC, Merida (2007), these proceedings.
- [4] J.Zabierowski, K. Daumiller and P. Doll, Nucl. Phys. B (Proc.Suppl.) 122, (2003), 275.
- [5] J.Zabierowski et al. KASCADE-Grande Coll., Nucl. Phys.B (Proc.Suppl.) 151,(2006) 291.
- [6] J.Zabierowski et al.KASCADE-Grande Coll., Proc 29th ICRC, Pune (2005) 6, 357.
- [7] D.Heck et al., FZKA Report 6019 (1998).
- [8] A.Fasso et al.,Proc CHEP2003, Paper MOMT005,eConf C0303241 (2003), arXiv:hep-ph/0306267.
- [9] A.Haungs et al. KASCADE-Grande Coll., Proc. 14th ISVHECRI, Weihai, Nucl. Phys. B (Proc.Supl), in press (2007).



Reconstruction of primary mass group energy spectra with KASCADE

H. ULRICH^a, W.D. APEL^a, J.C. ARTEAGA^a, F. BADEA^a, K. BEKK^a, M. BERTAINA^b, J. BLÜMER^{a,c}, H. BOZDOG^a, I.M. BRANCUS^d, M. BRÜGGEMANN^e, P. BUCHHOLZ^e, A. CHIAVASSA^b, F. COSSAVELLA^c, K. DAUMILLER^a, V. DE SOUZA^c, F. DI PIERRO^b, P. DOLL^a, R. ENGEL^a, J. ENGLER^a, M. FINGER^c, D. FUHRMANN^f, P.L. GHIA^g, H.J. GILS^a, R. GLASSTETTER^f, C. GRUPEN^e, A. HAUNGS^a, D. HECK^a, J.R. HÖRANDEL^c, T. HUEGE^a, P.G. ISAR^a, K.-H. KAMPERT^f, D. KICKELBICK^e, H.O. KLAGES^a, Y. KOLOTAEV^e, P. LUCZAK^h, H.J. MATHES^a, H.J. MAYER^a, C. MEURER^a, J. MILKE^a, B. MITRICA^d, A. MORALES^a, C. MORELLO^g, G. NAVARRA^b, S. NEHLS^a, J. OEHLISCHLÄGER^a, S. OSTAPCHENKO^a, S. OVER^e, M. PETCU^d, T. PIEROG^a, S. PLEWNIA^a, H. REBEL^a, M. ROTH^a, H. SCHIELER^a, O. SIMAⁱ, M. STÜMPERT^c, G. TOMA^d, G.C. TRINCHERO^g, J. VAN BUREN^a, W. WALKOWIAK^e, A. WEINDL^a, J. WOCHOLE^a, J. ZABIEROWSKI^h.

^a *Institut für Kernphysik, Forschungszentrum Karlsruhe, Germany*

^b *Dipartimento di Fisica Generale dell'Università Torino, Italy*

^c *Institut für Experimentelle Kernphysik, Universität Karlsruhe, Germany*

^d *National Institute of Physics and Nuclear Engineering, Bucharest, Romania*

^e *Fachbereich Physik, Universität Siegen, Germany*

^f *Fachbereich Physik, Universität Wuppertal, Germany*

^g *Istituto di Fisica dello Spazio Interplanetario, INAF Torino, Italy*

^h *Soltan Institute for Nuclear Studies, Lodz, Poland*

ⁱ *Department of Physics, University of Bucharest, Romania*

holger.ulrich@ik.fzk.de

Abstract: The KASCADE-Grande experiment was designed for the measurement of extensive air showers induced by cosmic rays of the knee region, i.e. with energies between 0.5 PeV and 1 EeV. Main focus of the experiment is the precise determination of energy and composition of the primary cosmic rays, thus clarifying the nature of the knee. Data of the preceding KASCADE experiment have been used in a composition analysis[1], proposing the knee to be caused by a steepening in the light-element spectra. Furthermore, the analysis identified insufficiencies of the simulations and the interaction models used therein in describing the considered data. In the following, an update on the analysis will be presented.

Introduction

Even though the majority of recent air shower experiments aims at the highest energy (well above 10^{19} eV), the much lower PeV-range is still of considerable interest. Here, at an energy of approx. 4 PeV, a sudden steepening of the energy spectrum occurs, which is referred to as the so-called *knee* of cosmic rays. Hypotheses for its origin range from astrophysical scenarios, like changing acceleration mechanisms or escape from the Galaxy, to particle physics models. For restricting or even rejecting different models, detailed knowledge about the

energy dependent chemical composition of cosmic rays is necessary.

At present, measurements in the knee region are only possible by the detection of extensive air showers (EAS) induced by primary cosmic-ray particles. While gaining statistical significance by this approach, any reconstructed properties of the primary particles have to rely on simulations and the description of high energy hadronic interactions used therein. By nature, these interaction models have to be phenomenological and differ in their predictions. In this sense any thorough anal-

ysis of EAS data offers the opportunity of testing and improving high energy interaction models.

The KASCADE experiment[2], precursor and now part of the KASCADE-Grande experiment[3], aims at these questions. By analyzing the KASCADE key observables (electron and muon shower size) a strong dependence of the result for the elemental abundances on the used interaction model was demonstrated[1]. In addition, an insufficient description of the data by the considered simulations could be revealed.

In the following, an update on this composition analysis is given with special emphasis on the influence of the low energy interaction model. Furthermore, the analysis was repeated for data of different zenith angle intervals, thus testing for consistency of the procedure. A brief discussion of the properties of simulations using the new EPOS[4] model finally concludes this article.

Outline of the analysis

Starting point for the analysis is the number of measured EAS depending on electron number $\lg N_e$ and muon number $\lg N_\mu^{tr}$ (muons with core distances between 40 m and 200 m), the so-called two-dimensional shower size spectrum. For showers inside the KASCADE array and with inclination less than 18° this spectrum is also shown in Fig. 3. The content N_j of each histogram cell j is

$$N_j = C \sum_{A=1}^{N_A} \int_{-\infty}^{+\infty} \frac{dJ_A}{d \lg E} p_A d \lg E. \quad (1)$$

C is a normalizing constant (time, aperture). The sum is carried out over all primary particle types of mass A . The functions $p_A = p_A(\lg N_{e,j}, \lg N_{\mu,j}^{tr} | \lg E)$ give the probability for an EAS of primary energy E and mass A to be measured and reconstructed with shower sizes $N_{e,j}$ and $N_{\mu,j}^{tr}$. The probabilities p_A include shower fluctuations, efficiencies, and reconstruction systematics and resolution. For reasons of clarity integration over solid angle and cell area is omitted in Eqn. 1, but taken into account.

With this notation the two-dimensional size spectrum is interpreted as a set of coupled integral equations. This set can be solved for the primary energy spectra $\frac{dJ_A}{d \lg E}$ by the application of

unfolding algorithms. In the analysis the particles H, He, C, Si, and Fe were chosen as representatives for five mass groups of primary cosmic ray particles. The corresponding probabilities p_A were determined by Monte Carlo simulations using COSRIKA[5] and a GEANT[6] based simulation of the experiment. Details of the procedure can be found in Ref.[1].

Using FLUKA instead of GHEISHA

In Ref.[1], the probabilities p_A were determined using the high energy interaction models QGSJet[7] (2001 version) and SIBYLL[8] 2.1 in the simulations. In both cases low energy interactions (< 80 GeV) were modeled with the GHEISHA[9] code. For the present analysis, GHEISHA was replaced by the FLUKA[10] package, and only the QGSJet 01 model was used. Differences between these simulations are rather small, with nearly energy and primary independent differences of $\Delta \lg N_e \approx 0.015$ and $\Delta \lg N_\mu^{tr} \approx 0.02$ (more electrons and less muons with FLUKA).

Because of these small differences of the simulation predictions, it is not surprising, that the results of the complete unfolding analysis differ for the FLUKA case only little from those of the GHEISHA case. As an example, the results for the energy spectra of H, He, and C obtained with GHEISHA and FLUKA are compared with each other in Fig. 1. The differences between the two solution sets are small, especially in comparison with methodical uncertainties (shaded bands in the figure). In case of the heavy elements (Si, Fe) the influence is somewhat larger, but still of same or smaller order than methodical uncertainties. To summarize, the overall picture of the solution seems to be affected insignificantly by using FLUKA instead of GHEISHA.

Analysing data of different zenith angle ranges

In the presented analysis only EAS with zenith angles smaller than 18° were considered so far. Apart from increasing statistics, the analysis of more inclined shower data could serve as a consistency

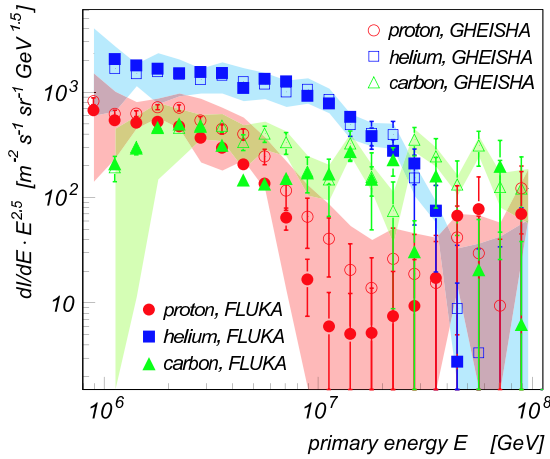


Figure 1: Results for the energy spectra of H, He, and C using QGSJet/FLUKA and QGSJet/GHEISHA based simulations. Shaded bands correspond to estimates of methodical uncertainties for the QGSJet/GHEISHA spectra.

check. Since the data could not be described satisfactorily by the simulations (see Ref.[1]), identical results compared to the vertical data set cannot be expected. Nevertheless, strong and large differences between the solution sets would indicate a severe problem in either the simulation code or the applied analysis technique. For this kind of cross-check the QGSJet/FLUKA analysis was repeated for two more data sets of EAS with higher inclination. In the first one considered zenith angles range from 18° to 25.9° , in the second from 25.9° to 32.3° .

The results for the all-particle spectrum coincide very well inside their statistical uncertainties, only for the underlying mass group spectra small differences can be detected. For lack of space, only the results for H and He are discussed in the following. The spectra for Helium derived from the three data sets coincide inside their statistical uncertainties, as can be seen in Fig. 2. In the same figure, obvious systematic differences can be observed for the proton spectra at energies above the proton knee. Here, the change of index decreases with increasing zenith angle, i.e. gets less pronounced.

The observed systematic deviations of the solution sets to each other are small and can be understood by the increasing shower fluctuations with increas-

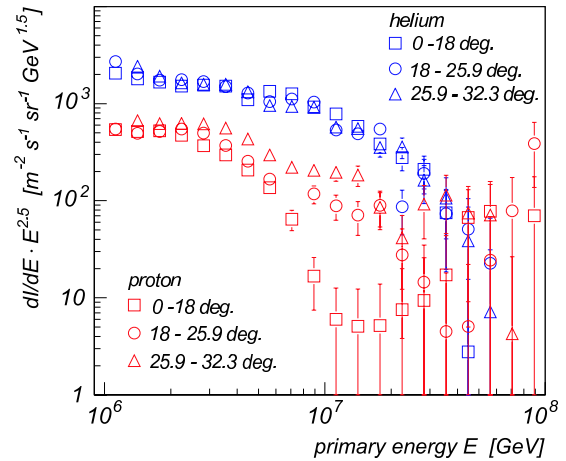


Figure 2: Energy spectra of H and He based on the analysis of EAS data originating from different zenith angle intervals. For reasons of clarity estimates of methodical uncertainties are omitted.

ing zenith angle and shifted energy threshold due to the fixed data range in $\lg N_e$ and $\lg N_\mu^{tr}$. Therefore, no strong or unexplainable differences are found, which would hint to severe problems in the simulation or the analysis. Thus, conclusions[1] drawn from the analysis of nearly vertical showers are not affected.

New interaction model: EPOS

The most recent release of CORSIKA made the new EPOS[4] model available for the simulation of high energy hadronic interactions in EAS. Using the combination EPOS/FLUKA in CORSIKA a set of EAS similar to the ones used in the presented analyses was generated. Of special interest is the energy dependence of the shower fluctuations $s_A(\lg N_e, \lg N_\mu^{tr} | \lg E)$, describing the probability for an EAS of primary mass A and energy $\lg E$ to exhibit electron size $\lg N_e$ and muon size $\lg N_\mu^{tr}$ at observation level. Figure 3 compares the positions of the maxima of these distributions for proton and iron induced EAS using EPOS, QGSJet 01, and SIBYLL 2.1. For orientation, the two-dimensional electron and muon size spectrum is also shown.

It can be seen from the figure, that for each model the lines, which correspond to the most probable

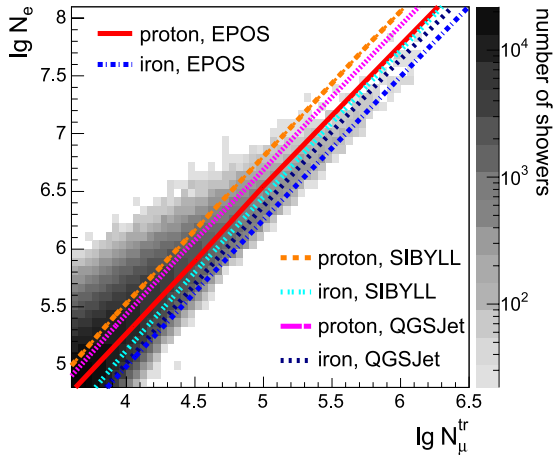


Figure 3: Predictions for the most probable values of proton and iron induced showers using QGSJet 01 and EPOS in the simulations. In addition the two-dimensional KASCADE shower size spectrum of $\lg N_e$ and $\lg N_\mu^{tr}$ is shown.

values of the shower sizes, belonging to different primary particle types are nearly parallel. Furthermore, the same holds for lines corresponding to QGSJet and SIBYLL simulations. A QGSJet line "could be shifted" into a SIBYLL line. For EPOS simulations, this is no longer the case. The most-probable-lines exhibit a different slope as compared to QGSJet and SIBYLL. It is interesting to note, that the iron-lines of EPOS and QGSJet lie on each other at small shower sizes (≈ 1 PeV). With increasing shower sizes, EPOS predictions for iron induced EAS resemble EAS induced by ultra-heavy primaries in the QGSJet framework.

A closer inspection reveals, that for high energies (around 10^{18} eV) the EPOS most-probable-line for proton induced EAS seems to cross the SIBYLL line for iron induced showers. This could alter any composition analysis at higher energies drastically.

Conclusions

In parallel to measurements and analyses with KASCADE-Grande[11], composition analyses with KASCADE data are ongoing. Besides the cross-check of the conducted composition analysis with data from different zenith angle intervals, the influence of the low interaction model (replac-

ing GHEISHA by FLUKA) has been investigated. It could be shown, that the influence of this replacement on the results of the analysis is small.

First simulations using the new hadronic interaction model EPOS have been carried out, indicating new and interesting properties of EAS predictions. Results of a complete unfolding analysis using EPOS will be published soon. Moreover, in the future this kind of analysis will give further information on the validity of hadronic interaction models and for their improvement.

References

- [1] T. Antoni et al., KASCADE Collab., *Astropart. Phys.* 24 (2005) 1-25.
- [2] T. Antoni et al KASCADE Coll., *Nucl. Instr. Meth. A* 513 (2003) 490-510.
- [3] G. Navarra et al., KASCADE-Grande Collab., *Nucl. Instr. Meth. A* 518 (2004) 207-209.
- [4] K. Werner, F.M. Liu and T. Pierog, *Phys. Rev. C* 74 (2006) 044902.
- [5] D. Heck et al., Forschungszentrum Karlsruhe, Report FZKA 6019 (1998).
- [6] GEANT - Detector Description and Simulation Tool, CERN Program Library Long Writeup W5013, CERN (1993).
- [7] N.N. Kalmykov and S.S. Ostapchenko, *Phys. Atom. Nucl.* 56 (1993) 346.
- [8] R. Engel et al., *Proc. 26th Int. Cosmic Ray Conf. Salt Lake City (USA)* 1 (1999) 415.
- [9] H. Fesefeldt, Report PITHA-85/02, RWTH Aachen (1985).
- [10] A. Fassò et al., FLUKA: status and prospective for hadronic applications, in: A. Kling et al. (Eds.), *Proc. Monte Carlo 2000 Conf., Lisbon, 23-26 October 2000*, 955, Springer, Berlin, 2001. Available from: <www.fluka.org>.
- [11] A. Haungs et al., KASCADE-Grande Collab., *Proc. of 30th ICRC, Merida* (2007), these proceedings.



Measurement of attenuation lengths of hadrons in air showers with KASCADE

D. HILDEBRAND^c, W.D. APEL^a, J.C. ARTEAGA^a, F. BADEA^a, K. BEKK^a, M. BERTAINA^b, J. BLÜMER^{a,c}, H. BOZDOĞ^a, I.M. BRANCUS^d, M. BRÜGGEMANN^e, P. BUCHHOLZ^e, A. CHIAVASSA^b, F. COSSAVELLA^c, K. DAUMILLER^a, V. DE SOUZA^c, F. DI PIERRO^b, P. DOLL^a, R. ENGEL^a, J. ENGLER^a, M. FINGER^c, D. FUHRMANN^f, P.L. GHIA^g, H.J. GILS^a, R. GLASSTETTER^f, C. GRUPEN^e, A. HAUNGS^a, D. HECK^a, J.R. HÖRANDEL^{c,j}, T. HUEGE^a, P.G. ISAR^a, K.-H. KAMPERT^f, D. KICKELBICK^e, H.O. KLAGES^a, Y. KOLOTAEV^e, P. LUCZAK^h, H.J. MATHES^a, H.J. MAYER^a, C. MEURER^a, J. MILKE^a, B. MITRICA^d, A. MORALES^a, C. MORELLO^g, G. NAVARRA^b, S. NEHLS^a, J. OEHLISCHLÄGER^a, S. OSTAPCHENKO^a, S. OVER^e, M. PETCU^d, T. PIEROG^a, S. PLEWNIA^a, H. REBEL^a, M. ROTH^a, H. SCHIELER^a, O. SIMAⁱ, M. STÜMPERT^c, G. TOMA^d, G.C. TRINCHERO^g, H. ULRICH^a, J. VAN BUREN^a, W. WALKOWIAK^e, A. WEINDL^a, J. WOCHLEA^a, J. ZABIEROWSKI^h.

^a Institut für Kernphysik, Forschungszentrum Karlsruhe, Germany ^b Dipartimento di Fisica Generale dell'Università Torino, Italy ^c Institut für Experimentelle Kernphysik, Universität Karlsruhe, Germany ^d National Institute of Physics and Nuclear Engineering, Bucharest, Romania ^e Fachbereich Physik, Universität Siegen, Germany ^f Fachbereich Physik, Universität Wuppertal, Germany ^g Istituto di Fisica dello Spazio Interplanetario, INAF Torino, Italy ^h Soltan Institute for Nuclear Studies, Lodz, Poland ⁱ Department of Physics, University of Bucharest, Romania ^j now at Radboud University Nijmegen, The Netherlands
hoerandel@ik.fzk.de

Abstract: Different methods are applied to derive the attenuation lengths of hadrons in air showers with the KASCADE experiment. A data set of unaccompanied hadrons is used (where only a hadron is registered with a calorimeter) as well as full air showers, where also the number of electrons and muons is registered with a field array. The different attenuation lengths obtained are discussed.

Introduction

The measurement of the attenuation lengths of hadrons in air showers provides a suitable experimental access to the properties of high-energy hadronic interactions.

Main detector for the present analysis is the $16 \times 20 \text{ m}^2$ hadron calorimeter of the KASCADE experiment [3]. An iron sampling calorimeter comprising of nine layers of liquid ionization chambers interspaced with absorbers of lead, iron, and concrete. It measures the energy, as well as point and angle of incidence for hadrons with energies $E_h > 50 \text{ GeV}$. It has been calibrated at an accelerator beam [9]. In addition, for a part of the analyses discussed here the electromagnetic and muonic

($E_\mu > 0.23 \text{ GeV}$) shower components are registered with a $200 \times 200 \text{ m}^2$ scintillator array [1].

Different methods are discussed to derive attenuation lengths. The values obtained are not a priori comparable to each other since they are based on different definitions. The first part deals with unaccompanied hadrons, i.e. only one hadron is registered with the calorimeter, followed by an analysis of hadrons in air showers.

Unaccompanied Hadrons

For the following analyses the actual vertical thickness X_0 of the atmosphere above the KASCADE experiment is needed. The average ground pressure during the observation time

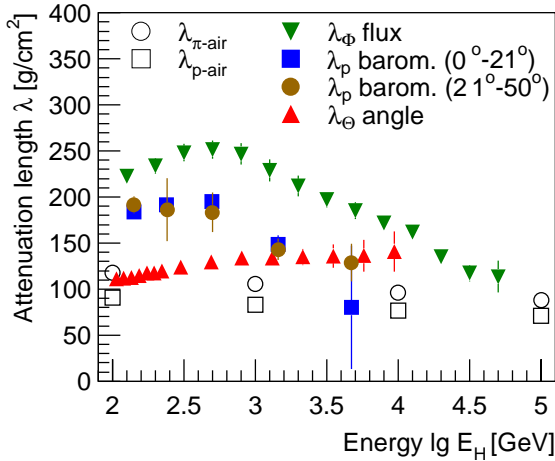


Figure 1: Attenuation lengths derived from the measurement of unaccompanied hadrons applying different methods, see text. For comparison, the open symbols represent the proton-air and pion-air interaction lengths according to QGSJET 01.

amounts to 1004 hPa, corresponding to an average $X_0=1023 \text{ g/cm}^2$.

The first method relates the flux observed above the atmosphere to unaccompanied hadrons measured at ground level. Simulations show, that unaccompanied hadrons mostly originate from primary protons [2]. Therefore, the flux of primary protons Φ_0 as measured above the atmosphere by satellite and balloon experiments [6] and the flux of unaccompanied hadrons Φ_H as measured by KASCADE [2] are used and an attenuation length λ_Φ is derived applying $\Phi_H = \Phi_0 \exp(-X_0/\lambda_\Phi)$. The values obtained range from $\approx 250 \text{ g/cm}^2$ at low energies to values around 100 g/cm^2 and are presented in Fig. 1 as function of hadron energy.

The following methods use the change of the measured hadron rate caused by variations of the absorber thickness. One possibility is to investigate the hadron rate as function of the zenith angle Θ of the hadrons, which implies a change in the absorber thickness $X = X_0/\cos(\Theta)$. This yields an attenuation length λ_Θ with $\Phi_H(\Theta) \propto \exp(-X/\lambda_\Theta)$. Fits to the measured data for different energy intervals yield values for λ_Θ as shown in Fig. 1. The values increase slightly as function of energy from $\approx 110 \text{ g/cm}^2$ to about 140 g/cm^2 .

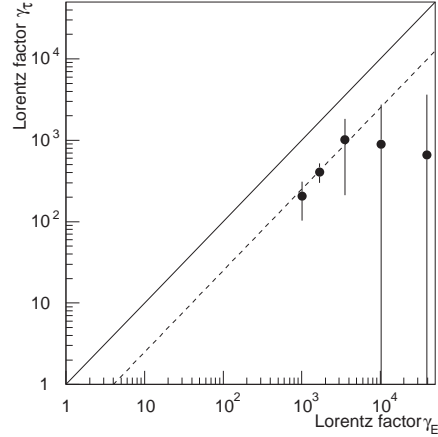


Figure 2: Lorentz factor γ_τ versus γ_E , see text. The solid line corresponds to $\gamma_\tau = \gamma_E$ and the dashed one to $\gamma_\tau = \gamma_E/4$.

The last method described uses a change in the absorber thickness caused by variations in the atmospheric ground pressure p . In addition, the measured rate of unaccompanied hadrons depends on the temperature T_{200} of the atmosphere, measured 200 m above KASCADE. The temperature effect is caused by the fact that for a given pressure (or column density) a higher temperature yields a smaller air density and thus more pions decay. Approximating the atmosphere as ideal gas a temperature change relates to a change of the height of an atmospheric layer. Motivated by CORSIKA [5] air shower simulations it is assumed that most pions in air showers are generated at an atmospheric depth of about 150 g/cm^2 , corresponding to $H_0 \approx 14 \text{ km}$. Applying the ideal gas law the production height is approximated as $H(T_{200}) = H_0(1 + 3.4 \cdot 10^{-3}(T_{200} - T_0))$ with $T_0 = 15^\circ\text{C}$.

The pressure and temperature dependencies of the observed rates are described by the relations $\Phi_H(p) \propto \exp(-p/\lambda_p)$ and $\Phi_H(T_{200}) \propto \exp(-H/l_0)$, respectively. The values λ_p and l_0 are determined through an iterative procedure in which the rates are normalized to a standard temperature and pressure. The data have been analyzed in two zenith angle intervals of $0^\circ - 21^\circ$ and $21^\circ - 50^\circ$. The results for λ_p are depicted in Fig. 1 as function of energy. The values for the two zenith angle ranges agree well with each other, and show a decrease from values around 190 g/cm^2 at low energies to about 100 g/cm^2 at higher energies.

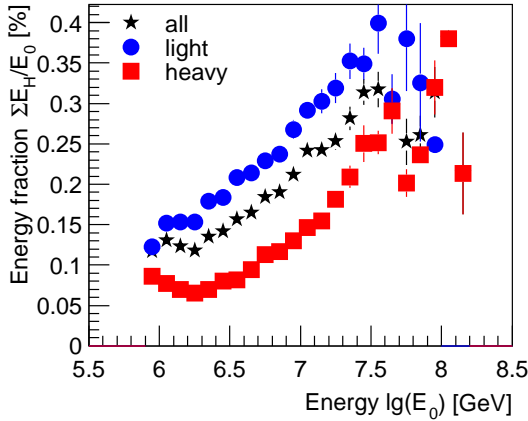


Figure 3: Fraction of energy $\Sigma E_H/E_0$ reaching the ground in form of hadrons as function of estimated primary energy E_0 for all data and for a selection of light and heavy primaries.

As a plausibility check, the temperature dependence has been used to estimate the charged pion life time. l_0 is taken as the decay length of pions, yielding for the life time $\tau = l_0/c$. With the life time of pions in the rest system $\tau_\pi = 2.2 \cdot 10^{-8}$ s the Lorentz factor of the registered hadrons can be estimated $\gamma_\tau = \tau/\tau_\pi$. Since the energy of the hadrons/pions is measured independently with the calorimeter, a second Lorentz factor can be estimated $\gamma_E = E_H/m_\pi$ with the rest mass of the pions $m_\pi = 140$ MeV. In an ideal case both values derived for γ should agree. However, a comparison of the values obtained for different energy bins, as shown in Fig. 2, exhibits that the quantities differ by a factor of about 4. On the other hand it is quite interesting to realize that such a simple approach delivers results within the expected order of magnitude.

The attenuation lengths obtained applying the different methods yield values between about 100 g/cm^2 and $\approx 250 \text{ g/cm}^2$. It is obvious that the different methods yield different attenuation lengths. In particular, they are not expected to agree with the interaction lengths for pions and/or protons.

Nevertheless, to give a hint towards the expected magnitude of the attenuation lengths in Fig. 1 also expectations according to a hadronic interaction model are shown. The open symbols represent the proton-air λ_{p-air} and pion-air $\lambda_{\pi-air}$ interac-

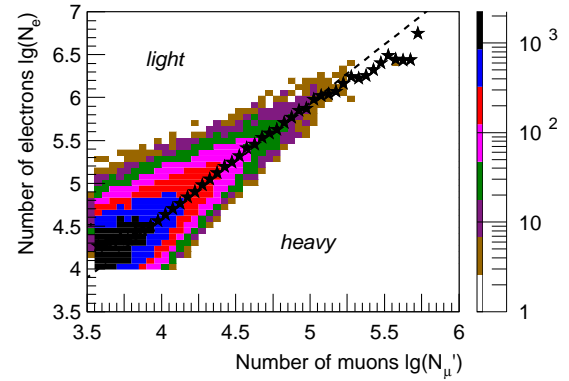


Figure 4: Number of electrons and muons for the measured showers.

tion lengths according to the model QGSJET 01 [8]. Over the three decades shown they decrease slightly with energy starting with $\lambda_{p-air} \approx 90$ and $\lambda_{\pi-air} \approx 120 \text{ g/cm}^2$ at 100 GeV. In the analyses presented, the measured hadrons are treated as surviving primary particles. However, in reality, the "unaccompanied hadrons" are mostly the debris of small air showers interacting in the upper atmosphere. Hadrons reaching ground level have undergone about two to five interactions. Thus, the measured attenuation lengths are larger as compared to the interaction lengths of the particles in the model.

Hadrons in Air Showers

The second part deals with hadrons in air showers. The primary energy E_0 of the shower inducing particle is roughly estimated based on the number of electrons N_e and muons N'_μ registered with the KASCADE field array: $\lg E_0 \approx 0.19 \lg N_e + 0.79 \lg N'_\mu + 2.33$. The "surviving energy" in form of hadrons ΣE_H is measured with the hadron calorimeter. Thus, a fraction $R = \Sigma E_H/E_0$ of hadronic energy reaching ground level can be inferred as function of primary energy as shown in Fig. 3. In the energy range investigated about 0.1% to 0.35% of the primary energy reach the observation level in form of hadrons. With an average elasticity $\epsilon \approx 0.25$ [7] and $R = \epsilon^N$ the average number of generations N in the shower can be estimated and it turns out that the registered hadrons have undergone about four to five interactions.

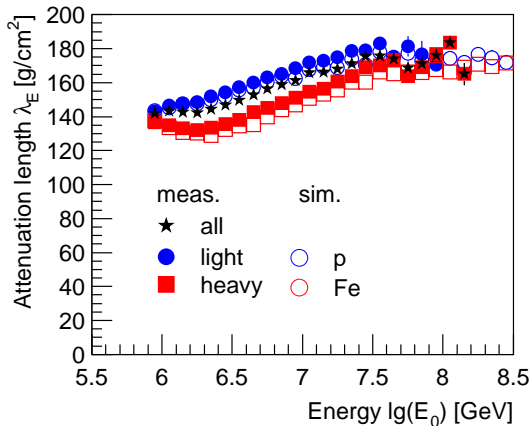


Figure 5: Attenuation length λ_E as function of estimated primary shower energy.

The two-dimensional distribution of the number of electrons and muons for the measured showers is depicted in Fig. 4. The asterisks represent the most probable values of the distribution. The dashed line, obtained by a fit to the most probable values is used to separate the registered data into a "light" and "heavy" sample. The energy fraction reaching observation level is shown in Fig. 3 as well for the light and heavy primaries. As expected from a simple superposition model, proton-like showers transport more energy to the observation level as compared to iron-like showers.

An attenuation length λ_E has been derived from the measured energy fraction assuming $\Sigma E_H = E_0 \exp(-X_0/\lambda_E)$. The results are presented as function of the estimated primary energy in Fig. 5. Values for the complete data set as well as for the light and heavy selection are shown. The values are compared to results obtained from full air shower simulations for primary protons and iron nuclei using the CORSIKA program with the hadronic interaction generators FLUKA [4] and QGSJET 01. It can be seen in the figure that the results for the light and heavy selections agree well with the values for primary protons and iron nuclei, respectively.

Instead of the primary energy the results can also be calculated as function of the hadronic energy sum at observation level. The values thus obtained can be compared to the previous results shown in Fig. 1. However, it should be pointed out that λ_E

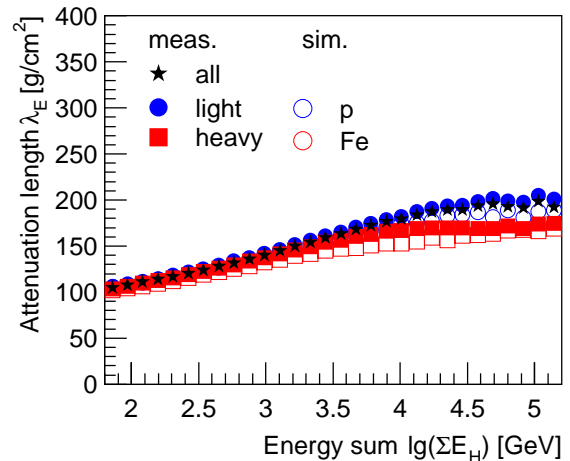


Figure 6: Attenuation length λ_E as function of the measured hadronic energy sum at observation level.

is yet another definition for an attenuation length. The results for all data, as well as for the light and heavy selection are presented in Fig. 6. Again, the measured attenuation lengths are compared to simulations for primary protons and iron nuclei and a reasonable agreement between measured and simulated values can be stated.

References

- [1] T. Antoni et al. *Nucl. Instr. & Meth. A*, 513:490, 2003.
- [2] T. Antoni et al. *Astrophys. J.*, 612:914, 2004.
- [3] J. Engler et al. *Nucl. Instr. & Meth. A*, 427:528, 1999.
- [4] A. Fassò et al. *FLUKA: Status and Prospective of Hadronic Applications*, page 955. Proc. Monte Carlo 2000 Conf., Lisbon, A. Kling, F. Barao, M. Nakagawa, P. Vaz eds., Springer (Berlin), 2001.
- [5] D. Heck et al. Report FZKA 6019, Forschungszentrum Karlsruhe, 1998.
- [6] J.R. Hörandel. *Astropart. Phys.*, 19:193, 2003.
- [7] J.R. Hörandel. *J. Phys. G: Nucl. Part. Phys.*, 29:2439, 2003.
- [8] N.N. Kalmykov et al. *Nucl. Phys. B (Proc. Suppl.)*, 52B:17, 1997.
- [9] S. Plewnia et al. *Nucl. Instr. & Meth. A*, 566:422, 2006.



Investigations of the lateral extension of radio emission in air showers by LOPES30 measurements

S. NEHLS^a, W.D. APEL^a, J.C. ARTEAGA^a, T. ASCH^b, J. AUFFENBERG^c, F. BADEA^a, L. BÄHREN^d, K. BEKK^a, M. BERTAINA^e, P.L. BIERMANN^f, J. BLÜMER^{a,g}, H. BOZDOĞ^a, I.M. BRANCUS^h, M. BRÜGGEMANNⁱ, P. BUCHHOLZ^j, S. BUITINK^j, H. BUTCHER^d, A. CHIAVASSA^e, F. COSSAVELLA^g, K. DAUMILLER^a, V. DE SOUZA^g, F. DI PIERRO^e, P. DOLL^a, R. ENGEL^a, H. FALCKE^{d,j}, H. GEMMEKE^b, P.L. GHIA^k, R. GLASSTETTER^c, C. GRUPENⁱ, A. HAUNGS^a, D. HECK^a, J.R. HÖRANDEL^j, A. HORNEFFER^j, T. HUEGE^a, P.G. ISAR^a, K.-H. KAMPERT^c, D. KICKELBICKⁱ, Y. KOLOTAEVⁱ, O. KRÖMER^b, J. KUIJPERS^j, S. LAFEBRE^j, P. LUCZAK^l, H.J. MATHES^a, H.J. MAYER^a, C. MEURER^a, J. MILKE^a, B. MITRICA^h, C. MORELLO^k, G. NAVARRA^e, A. NIGL^j, J. OEHLISCHLÄGER^a, S. OSTAPCHENKO^a, S. OVERⁱ, M. PETCU^h, J. PETROVIC^j, T. PIEROG^a, S. PLEWNIA^a, J. RAUTENBERG^c, H. REBEL^a, M. ROTH^a, H. SCHIELER^a, O. SIMA^m, K. SINGH^j, M. STÜMPERT^g, G. TOMA^h, G.C. TRINCHERO^k, H. ULRICH^a, J. VAN BUREN^a, W. WALKOWIAKⁱ, A. WEINDL^a, J. WOCHLE^a, J. ZABIEROWSKI^l, J.A. ZENSUS^f.

^a *Institut für Kernphysik, Forschungszentrum Karlsruhe, Germany*

^b *Inst. Prozessdatenverarbeitung und Elektronik, Forschungszentrum Karlsruhe, Germany*

^c *Fachbereich Physik, Universität Wuppertal, Germany*

^d *ASTRON, Dwingeloo, The Netherlands*

^e *Dipartimento di Fisica Generale dell'Università Torino, Italy*

^f *Max-Planck-Institut für Radioastronomie Bonn, Germany*

^g *Institut für Experimentelle Kernphysik, Universität Karlsruhe, Germany*

^h *National Institute of Physics and Nuclear Engineering Bucharest, Romania*

ⁱ *Fachbereich Physik, Universität Siegen, Germany*

^j *Dept. of Astrophysics, Radboud University Nijmegen, The Netherlands*

^k *Istituto di Fisica dello Spazio Interplanetario, INAF Torino, Italy*

^l *Soltan Institute for Nuclear Studies Lodz, Poland*

^m *Department of Physics, University of Bucharest, Romania*

steffen.nehls@ik.fzk.de

Abstract: The antenna field of LOPES uses inverted V-shaped dipole antennas to measure radio signals originating from extensive air showers (EAS). The LOPES antennas are measuring in coincidence with the air shower experiment KASCADE-Grande. For roughly one year data in the frequency range from 40–80 MHz were taken, having 30 linearly polarized antennas oriented to East-West. In this data set the East-West polarization only was measured in order to investigate in detail the lateral extension of the radio emission. By using an external source all antennas have an absolute amplitude calibration, i.e. a frequency dependent correction factor allows to reconstruct the electric field strength of the radio emission. For first analyses, in particular air showers with a high signal-to-noise ratio, data are used to investigate the lateral distribution, which shows an exponential decrease.

Introduction

The LOPES experiment was set up at the site of KASCADE-Grande [1] to confirm the principle of

radio detection of air showers [2] and the theory of geosynchrotron radiation [3] as dominant emission process in the frequency range below a few hundred Megahertz. The KASCADE-Grande experiment is measuring EAS in the energy range 10^{14} –

10^{18} eV. LOPES and KASCADE-Grande experiment are measuring in coincidence the radio emission of EAS, implemented by an external triggering for LOPES. The LOPES experiment uses inverted vee-shaped dipole antennas. For the detection of radio signals from 40 to 80 MHz was chosen in order to avoid most of the radio frequency interference (RFI) being present at the location.

In a first construction phase (LOPES10), 10 antennas were taking a sufficiently large data set for detailed investigations [2] of the relation between detected radio pulses and air shower reconstruction parameters, provided by KASCADE-Grande.

In a next construction phase (LOPES30), the number of antennas and the baseline were increased. In addition an absolute amplitude calibration was performed to reconstruct the electric field strength at each individual antenna. For both phases only the East-West polarization direction was measured. Meanwhile in a third phase dual polarization measurements are performed.

Calibration

The amplitude calibration uses a reference source (VSQ) of known electric field strength at a certain distance. Each LOPES30 radio antenna is calibrated at its location inside the KASCADE-Array and therefore this calibration includes all environmental effects, like ground characteristics, temperature effects, or setup systematics. The power to be received from the radio antenna in calibration mode is compared with the power recorded in the LOPES electronics P_M . With the relation:

$$V(\nu) = \left(\frac{4\pi r \nu}{c} \right)^2 \cdot \frac{P_M(\nu)}{G_r(GP)_{VSQ} \cos^2(\beta)} \quad (1)$$

The amplification factor $V(\nu)$ describes the frequency dependent behavior of each electronic channel for the signal transmission. The directivity pattern G_r of the LOPES antenna is obtained by a simulation assuming realistic conditions. To quantify polarization losses during a misalignment of the linearly polarized VSQ and linearly polarized LOPES antenna the angle β is introduced. For the VSQ only the product of gain and emitted power $(GP)_{VSQ}$ is known. In Figure 1 the determined amplification factors $V(\nu)$ for a vertical calibration for all 30 antennas are shown.

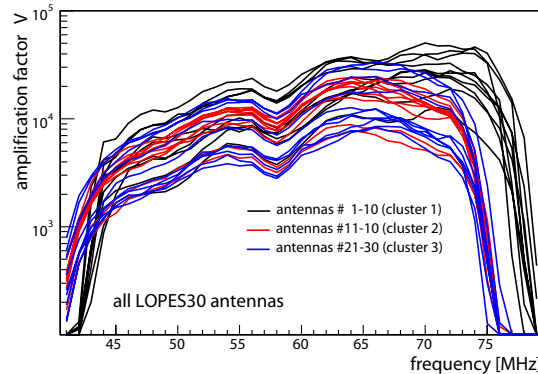


Figure 1: The frequency dependent amplification factors for all 30 antennas obtained by the amplitude calibration.

The earlier LOPES10 hardware can be distinguished (antennas 1–10) by their band pass range (43–76 MHz) from the other 20 antennas (42–74 MHz). The calibration results in a spread for the amplification factors of nearly one order of magnitude. This large spread illustrates the need for an absolute calibration and is corrected for in the analysis software. The uncertainty of the calibration method can be estimated from repeated measurement campaigns for a single antenna under all kinds of conditions, including the precision of achieving the same geometry in all measurements. It results in an uncertainty of approximately 25% for the power related amplification factor V , averaged over the effective frequency range.

Radio pulse investigations

LOPES30 in the described setup took data in the period from mid of November 2005 until beginning of December 2006, receiving 966.000 external triggers from KASCADE. The LOPES data acquisition system was able to process 860.000 of them, where the loss is mostly due to the dead-time of roughly 1.5 seconds.

The EAS observables, e.g. shower size, number of muons, arrival direction, and shower core position are reconstructed only with the KASCADE data and have to fulfill quality cuts, before further processing of the radio information. As the full data set consists mostly of low energetic showers the expected radio signal strength is relatively low.

Therefore, for a first radio pulse analysis a preselection of high energetic showers based on restrictions in the electron and muon number was done. Showers with shower size $N_e > 5 \cdot 10^6$ and truncated muon number [1] $N_\mu^{\text{tr}} > 5 \cdot 10^4$ where further investigated, giving 1200 candidate events.

The analysis of the candidate events performs a series of processing steps to determine the correlation quantity cc-beam pulse height. First the raw data is corrected for instrumental delays and afterwards a fast Fourier-transformation is applied. To suppresses radio frequency interference a mitigation of narrow band emitters is applied. Then the reconstructed geometry of the EAS from KASCADE is taken to apply a phase shift to each antenna data, what can be translated as a shift in time. Further the amplitude calibration is considered and a correction due to small instrumental phase shifts. The data are transformed back into the time domain, according to the observables from the EAS reconstruction. All time series $s_i(t)$ can now be superimposed interferometrically and with:

$$CC(t) = \pm \sqrt{\left| \frac{1}{N_{\text{pairs}} - 1} \sum_{i \neq j} s_i(t) \cdot s_j(t) \right|} \quad (2)$$

the so called cross correlation beam $CC(t)$ is calculated. With this kind of data processing the radio pulses recorded in the LOPES30 data can be identified. For a detailed description of the processing steps see [4].

Such cc-beam radio pulses are fitted with a Gaussian function to quantify the height, which is an averaged field strength for a mean distance to the shower axis of the selected radio antennas. As an estimation of the pulse height uncertainty the uncertainty of the Gaussian fit is used. For 849 candidates a radio pulse could be fitted (see Figure 2).

From Monte Carlo simulations an approximately linear dependence of primary energy E_0 with the electric field strength E is predicted. As the number of muons detected at ground scales roughly with the primary energy, in Figure 2 the radio pulse height is plotted against the truncated number of muons N_μ^{tr} . The used error bars are derived from the fit uncertainty.

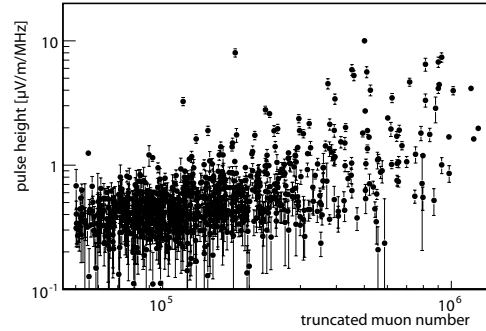


Figure 2: Relation of truncated muon number N_μ^{tr} and cc-beam pulse height.

| | Shower 1 | Shower 2 |
|---------------------------------------|---------------|---------------|
| $\log N_e$ | 7.26 | 7.27 |
| $\log N_\mu^{\text{tr}}$ | 5.95 | 5.91 |
| $\log E_{\text{est.}} [\text{eV}]$ | 17.4 | 17.4 |
| $\theta [\text{deg.}]$ | 24.0 | 23.8 |
| $\phi [\text{deg.}]$ | 2.3 | 4.9 |
| $CC_{\text{all}} [\mu\text{V/m/MHz}]$ | 6.8 ± 0.6 | 6.5 ± 0.8 |

Table 1: EAS observables for two similar shower.

There can be seen no significant correlation between those two quantities. Due to the strong dependence of the radio signal on the shower direction [5] (geomagnetic angle, zenith angle, and azimuth angle) and on the distance to the shower core, the correlation with the muon number is spread out and an unfolding of the dependences is needed. In a first step for this unfolding the lateral dependence will be investigated in more detail and discussed here for two events explicitly.

Lateral extension of radio signals

In the used data set there are two resembling showers, which can be used to directly compare the radio pulse height for certain distance ranges from the shower axis. The layout in Fig. 3 gives the shower core position in the KASCADE-Array and the originating direction indicated by an arrow. The reconstructed EAS observables are given in Table 1 in addition to the cc-beam of all antennas (CC_{all}) (see Fig. 4), we considered antennas

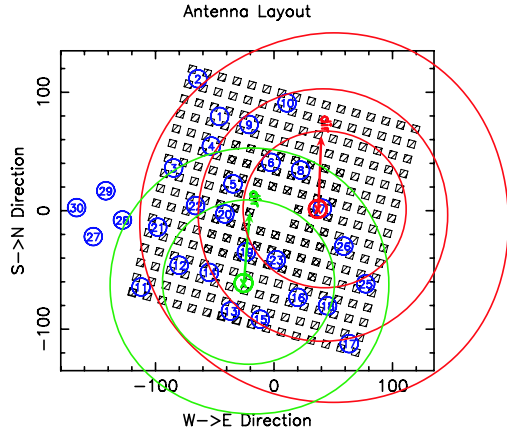


Figure 3: The radial distance ranges are illustrated by rings around the shower core, indicated with an encircled X. Green-left: 3 distance ranges; Red-right: 4 distance ranges. Ranges are from 0–50 m, 50–100 m, 100–150 m, 150–200 m.

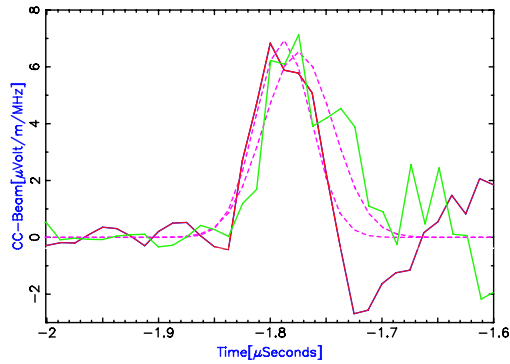


Figure 4: Combined cc-beam plot (solid lines, light and dark) with Gaussian fit (dashed lines) for complete antenna field.

within 0–50, 50–100, 100–150 m, and further out from the shower axis and the calculated cc-beams pulse heights are shown in Figure 5. The simulation and earlier data analyses predict an exponential decrease of the radio field strength E with increasing lateral distance R . Following the relation: $E \sim \exp(-R/R_0)$, the shown fit is performed for both events and radial distances larger than 50 m, resulting in a scaling parameter $R_0 = 101 \pm 43$ m. Due to increasing RFI from the surrounding detector stations close to the shower core, the cc-beam pulse height in the innermost ring can be systematically affected towards lower values, but both events have similar field strengths further out.

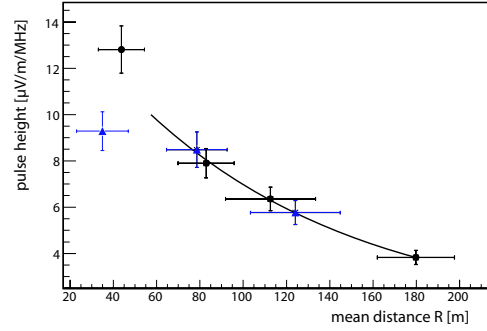


Figure 5: Lateral distribution of the radio pulse height for sub-sets of antennas. The events are fitted by an exponential function $\exp(-R/R_0)$.

Conclusions

The investigations of the lateral distribution of the radio emission with LOPES30 data are performed with absolute amplitude calibrated antennas. The spread of one order of magnitude in the amplification factor is corrected for in the analysis software and a systematic uncertainty of $\approx 13\%$ for measured field strengths remains.

Exemplarily two high energy events with high S/N ratio are investigated for their lateral distribution. The reconstruction of the cc-beam radio pulse height was done for distance ranges of round 50 m from the shower axis. The exponential decrease as predicted by the simulations is verified and a scaling parameter R_0 could be determined for the relation $E \sim \exp(-R/R_0)$ to $R_0 = 101 \pm 43$ m. A full analysis of the LOPES30 data set in terms of lateral behavior of the radio signal is currently in preparation.

References

- [1] T. Antoni et al., Nucl. Instr. Meth. A, Vol. 513, 490 (2003)
- [2] H. Falcke et al., Nature 435, 313 (2005)
- [3] T. Huege & H. Falcke, APh. Vol. 24, 116, (2005)
- [4] A. Horneffer et al., Int. J. Mod. Phys., Vol. A21S1, 168 (2006)
- [5] A. Haungs et al., Proc. ARENA conf., Newcastle, UK; Int. J. Phys.: Conf. Series (2006)



Operation of LOPES-30 for Polarization Measurements of the Radio Emission of Cosmic Ray Air Showers

P.G. ISAR^a, W.D. APEL^a, J.C. ARTEAGA^a, T. ASCH^b, J. AUFFENBERG^c, F. BADEA^a, L. BÄHREN^d, K. BEKK^a, M. BERTAINA^e, P.L. BIERMANN^f, J. BLÜMER^{a,g}, H. BOZDOĞA^a, I.M. BRANCUS^h, M. BRÜGGEMANNⁱ, P. BUCHHOLZ^j, S. BUITINK^j, H. BUTCHER^d, A. CHIAVASSA^e, F. COSSAVELLA^g, K. DAUMILLER^a, V. DE SOUZA^g, F. DI PIERRO^e, P. DOLL^a, R. ENGEL^a, H. FALCKE^{d,j}, H. GEMMEKE^b, P.L. GHIA^k, R. GLASSTETTER^c, C. GRUPENⁱ, A. HAUNGS^a, D. HECK^a, J.R. HÖRANDEL^j, A. HORNEFFER^j, T. HUEGE^a, K.-H. KAMPERT^c, D. KICKELBICKⁱ, Y. KOLOTAEVⁱ, O. KRÖMER^b, J. KUIJPERS^j, S. LAFEBRE^j, P. LUCZAK^l, H.J. MATHES^a, H.J. MAYER^a, C. MEURER^a, J. MILKE^a, B. MITRICA^h, C. MORELLO^k, G. NAVARRA^e, S. NEHLS^a, A. NIGL^j, J. OEHLSCHLÄGER^a, S. OSTAPCHENKO^a, S. OVERⁱ, M. PETCU^h, J. PETROVIC^j, T. PIEROG^a, S. PLEWNIA^a, J. RAUTENBERG^c, H. REBEL^a, M. ROTH^a, H. SCHIELER^a, O. SIMA^m, K. SINGH^j, M. STÜMPERT^g, G. TOMA^h, G.C. TRINCHERO^k, H. ULRICH^a, J. VAN BUREN^a, W. WALKOWIAKⁱ, A. WEINDL^a, J. WOCHLE^a, J. ZABIEROWSKI^l, J.A. ZENSUS^f.

^a *Institut für Kernphysik, Forschungszentrum Karlsruhe, Germany*

^b *Inst. Prozessdatenverarbeitung und Elektronik, Forschungszentrum Karlsruhe, Germany*

^c *Fachbereich Physik, Universität Wuppertal, Germany*

^d *ASTRON, Dwingeloo, The Netherlands*

^e *Dipartimento di Fisica Generale dell'Università Torino, Italy*

^f *Max-Planck-Institut für Radioastronomie Bonn, Germany*

^g *Institut für Experimentelle Kernphysik, Universität Karlsruhe, Germany*

^h *National Institute of Physics and Nuclear Engineering Bucharest, Romania*

ⁱ *Fachbereich Physik, Universität Siegen, Germany*

^j *Dept. of Astrophysics, Radboud University Nijmegen, The Netherlands*

^k *Istituto di Fisica dello Spazio Interplanetario, INAF Torino, Italy*

^l *Soltan Institute for Nuclear Studies Lodz, Poland*

^m *Department of Physics, University of Bucharest, Romania*

gina.isar@ik.fzk.de

Abstract: The LOPES-30 experiment, located at the site of the air shower experiment KASCADE-Grande at Forschungszentrum Karlsruhe, Germany, is an array of 30 dipole antennas set-up to investigate the pulsed radio emission from cosmic ray air showers in the Earth's atmosphere. After one year of measurements of the East-West polarization by all 30 antennas, recently, the LOPES-30 set-up was re-configured to perform dual-polarization measurements. Half of the antennas have been configured for measurements of the North-South polarization direction. By measuring at the same time both, the E-W and N-S polarization components of the radio emission, the geosynchrotron effect as the dominant emission mechanism in air showers can be verified. The status of the measurements, including the absolute calibration procedure of the antennas as well as a preliminary analysis of dual-polarized event examples are reported.

Introduction

The LOFAR (LOW Frequency ARray) PrototypE Station - LOPES experiment [1] is operating in

the 40-80 MHz frequency range. The KASCADE-Grande [2] experiment (an extension of the Karlsruhe Shower Core and Array DETECTOR KASCADE) provides the trigger information and well-

reconstructed parameters of the air shower properties in the energy range from a few PeV to 1 EeV. The LOPES-30 configuration is an extension of the initially installed 10 LOPES antennas (LOPES-10) by the addition of 20 dipole antennas, which have an absolute amplitude calibration providing a larger sensitive area and a large baseline to the radio signal at a single event basis. This provides the possibility for a detailed investigation of the lateral extension of the pulsed radio signal. Moreover, the antenna number is high enough for a new configuration sensitive to both, the East-West and North-South polarization directions.

The LOPES-POL Configuration

Since end of 2006, LOPES is performing polarization measurements. Half of the 30 antennas are configured for the East-West and North-South polarization measurements respectively, while five of them are configured as dual-polarization antennas at the same place, measuring at the same time both, the N-S and E-W polarization directions. The actual configuration is depicted in Fig.4.

Since December 2006, the LOPES antennas are triggered by the original KASCADE and in addition by the KASCADE-Grande array. Within this new additional trigger source, the LOPES experiment can therefore benefit from the extended detection area making possible the analysis of large events at large distances with a much better accuracy.

Motivation for Performing Polarization Measurements

For the initial measurements, all 30 antennas of the LOPES experiment were equipped with dipoles in E-W direction, measuring the single polarization of the radio emission only. Recently, for recording the full radio signal, LOPES-30 has been reconfigured to perform dual-polarization measurements.

The radio emission generated by the geosynchrotron mechanism is expected to be highly linearly polarized [3]. As predicted by the sophisticated Monte Carlo simulation for the radio emission, the signal is usually present in both polar-

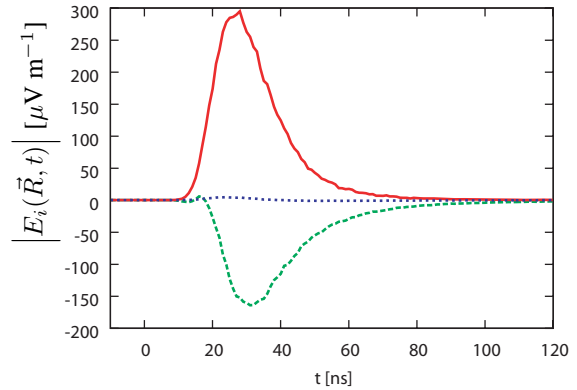


Figure 1: Raw simulated pulses in the individual linear polarization components of a 10^{17} eV vertical air shower. The solid line represent the E-W polarization component, dashed line N-S and dotted line the vertical component respectively.

ization components which strengths strongly depends on the position of the observer relative to the incoming air shower. In addition, the polarization is directly related with the shower azimuth for a given zenith angle. Knowledge of these polarization characteristics of the radio emission are mandatory for the interpretation of experimental measurements, which can directly verify the geomagnetic origin of the radio emission from atmospheric air showers.

Fig.1 shows a simulated raw (unlimited-bandwidth) pulse arriving at a distance of 200 m to the N-W from the center of a 10^{17} eV vertical shower. The N-S and E-W polarization components are of similar strength and arrive mostly synchronously, as expected for a linearly polarized pulse. For inclined air showers, a vertical polarized component can occur as well.

Polarization Sensitivity

The array of 30 digital radio antennas have an absolute amplitude calibration in order to estimate the electric field strength of the short radio pulse generated in air showers [5]. To perform the calibration, a commercial calibrated radio source is used as emitter and LOPES antennas are measuring within an artificially triggered event. For a cal-

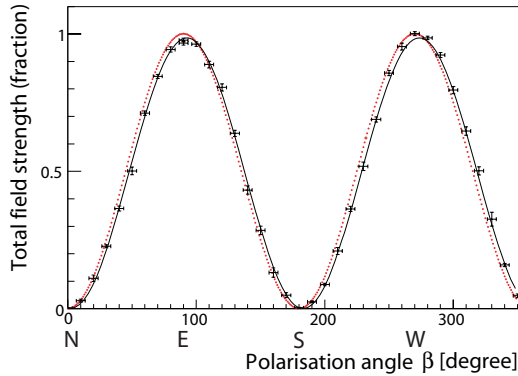


Figure 2: Fraction of the total field strength seen by the linearly polarized LOPES antenna (sensitive to E-W) as a function of the polarization angle β . Points: experimental data, solid line: data fit by a $\sin\beta$ -function, dotted line: theoretical $\sin\beta$ -distribution (normalized to the value at $\beta=270^\circ$).

ibration campaign, the reference source is placed at 11m above each LOPES antenna. It is a movable biconical reference antenna which is linearly polarized and has a nearly constant directivity near its principal axis.

Fig.2, respectively Fig.3 shows the fraction of the total field strength seen by a linearly dual-polarized LOPES antenna as a function of the angle β between the polarization axes of the reference source and the LOPES antenna. Each polarization direction is measured individually during the same campaign varying the polarization angle of the reference antenna in steps of 10 degrees by rotating the reference source in vertical position. The results obtained prove the expected polarization sensitivity (and insensitivity) of both, the E-W and N-S oriented LOPES antennas.

First Events

As an example, (see Fig.5) we display an event detected by LOPES in the new polarization configuration in December 2006. The KASCADE shower reconstruction results in a primary energy of $E_0 \approx 10^{18}$ eV, a geomagnetic angle (the angle between the shower axis and the Earth magnetic

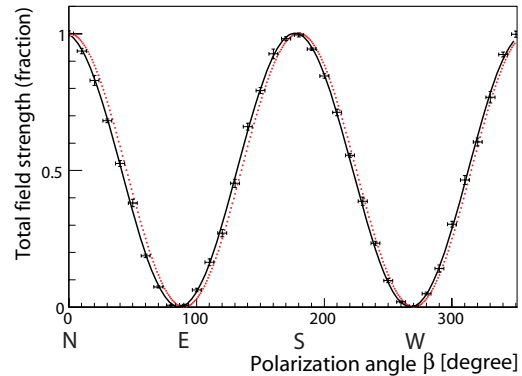


Figure 3: The same as Fig.2, but now for the antenna sensitive to the N-S polarization direction of the radio signal. The dotted curve is normalized to the value at $\beta=180^\circ$.

field) of 83° , an azimuth angle of 51° (i.e. coming from North-East), and a zenith angle of 66° . The shower shows clearly signals recorded in both polarization directions. The figure shows the value of the reconstructed CC-beam [6] which describes the average electric field strength for the mean distance from the shower axis.

As another example, (see Fig.6) we display an event detected in December 2006 with a primary energy of $E_0 \approx 3 \cdot 10^{17}$ eV, a geomagnetic angle of 77° , an azimuth angle of 333° (i.e. coming from North, North-West), and a zenith angle of 54° . The shower shows clearly signal recorded only in the E-W polarization direction without a significant signal contribution in the other N-S polarization direction.

These two selected events clearly show the capabilities of the LOPES experiment in recording the radio emission in both, the E-W and N-S polarization components. The new antenna configuration allows a full detection of the pulsed radio signal generated by the cosmic ray showers in the Earth's atmosphere.

Conclusions

In its current configuration, the LOPES experiment is performing polarization measurements; measur-

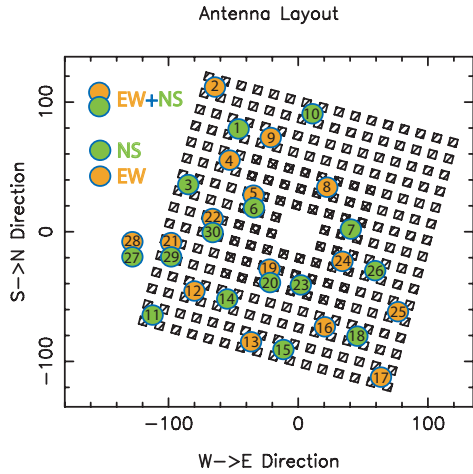


Figure 4: The antenna layout at the KASCADE array. The all antenna setup is divided in 15 E-W and 15 N-S polarized channels. Five antennas are sensitive to both polarization directions at the same time.

ing at the same time both, the E-W and N-S polarization components allows a much more detailed analysis of the radio events than with the East-West polarized measurements alone.

Providing calibrated data, the LOPES experiment allows a direct comparison with theoretical predictions for the first time. A direct verification of the geosynchrotron effect as the dominant emission mechanism in air showers is possible now.

References

- [1] H. Falcke et al., Nature 435, 313-316 (2005)
- [2] A. Haungs et al., 30th ICRC these Proc. (2007)
- [3] T. Huege & H. Falcke, Astropart.Phys. 24 116-136 (2005)
- [4] T. Huege, R. Ulrich and R. Engel, Astropart.Phys. 27 392-405 (2007)
- [5] S. Nehls et al., ARENA Proc. 2005, Int.J.Mod.Phys. A21S1, 187 (2006)
- [6] A. Horneffer et al., ARENA Proc. 2005, Int.J.Mod.Phys. A21S1, 168 (2006)
- [7] P.G. Isar et al., ARENA Proc. (2006)

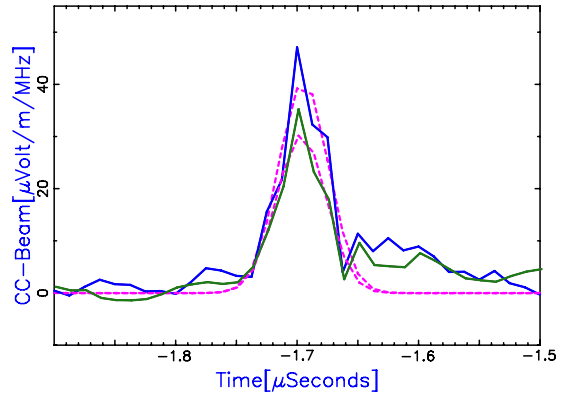


Figure 5: The Cross Correlation(CC)-beams for a dual-polarized event (E-W component: upper signal, N-S component: lower signal) of a primary energy of 10^{18} eV coming from North-East. The full lines indicate the CC-beams and the dotted lines the Gaussian fits respectively. One can clearly see very high radio signal recorded in both polarization directions.

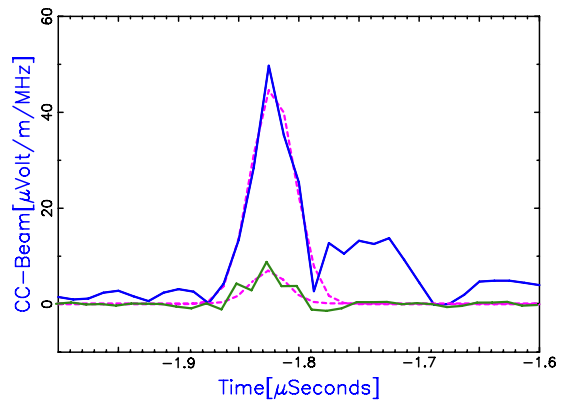


Figure 6: The same Cross Correlation(CC)-beams (see Fig.5) for a dual-polarized event of a primary energy of $3 \cdot 10^{17}$ eV coming from North, North-West. One can clearly see very high signal recorded in the E-W polarization direction only.



Update on radio detection of inclined air showers with LOPES-10

A. SĂFTOIU^h, W.D. APEL^a, J.C. ARTEAGA^a, T. ASCH^b, J. AUFFENBERG^c, F. BADEA^a, L. BÄHREN^d, K. BEKK^a, M. BERTAINA^e, P.L. BIERMANN^f, J. BLÜMER^{a,g}, H. BOZDOĞ^a, I.M. BRANCUS^h, M. BRÜGGEMANNⁱ, P. BUCHHOLZ^j, S. BUITINK^j, H. BUTCHER^d, A. CHIAVASSA^e, F. COSSAVELLA^g, K. DAUMILLER^a, V. DE SOUZA^g, F. DI PIERRO^e, P. DOLL^a, R. ENGEL^a, H. FALCKE^{d,j}, H. GEMMEKE^b, P.L. GHIA^k, R. GLASSTETTER^c, C. GRUPENⁱ, A. HAUNGS^a, D. HECK^a, J.R. HÖRANDEL^j, A. HORNEFFER^j, T. HUEGE^a, P.G. ISAR^a, K.-H. KAMPERT^c, D. KICKELBICKⁱ, Y. KOLOTAEVⁱ, O. KRÖMER^b, J. KUIJPERS^j, S. LAFEBRE^j, P. LUCZAK^l, H.J. MATHES^a, H.J. MAYER^a, C. MEURER^a, J. MILKE^a, B. MITRICA^h, C. MORELLO^k, G. NAVARRA^e, S. NEHLS^a, A. NIGL^j, J. OEHLSCHLÄGER^a, S. OSTAPCHENKO^a, S. OVERⁱ, M. PETCU^h, J. PETROVIC^j, T. PIEROG^a, S. PLEWNIA^a, J. RAUTENBERG^c, H. REBEL^a, M. ROTH^a, H. SCHIELER^a, O. SIMA^m, K. SINGH^j, M. STÜMPERT^g, G. TOMA^h, G.C. TRINCHERO^k, H. ULRICH^a, J. VAN BUREN^a, W. WALKOWIAKⁱ, A. WEINDL^a, J. WOCHOLE^a, J. ZABIEROWSKI^l, J.A. ZENSUS^f.

^a Institut für Kernphysik, Forschungszentrum Karlsruhe, Germany

^b Inst. Prozessdatenverarbeitung und Elektronik, Forschungszentrum Karlsruhe, Germany

^c Fachbereich Physik, Universität Wuppertal, Germany

^d ASTRON, Dwingeloo, The Netherlands

^e Dipartimento di Fisica Generale dell'Università Torino, Italy

^f Max-Planck-Institut für Radioastronomie Bonn, Germany

^g Institut für Experimentelle Kernphysik, Universität Karlsruhe, Germany

^h National Institute of Physics and Nuclear Engineering Bucharest, Romania

ⁱ Fachbereich Physik, Universität Siegen, Germany

^j Dept. of Astrophysics, Radboud University Nijmegen, The Netherlands

^k Istituto di Fisica dello Spazio Interplanetario, INAF Torino, Italy

^l Soltan Institute for Nuclear Studies Lodz, Poland

^m Department of Physics, University of Bucharest, Romania

allixme@gmail.com

Abstract: Inclined air showers are a particularly interesting target for observation with the radio technique. They are expected to be well detectable and allow analyses of angular correlations over a much broader range in geomagnetic angle than near-vertical events. We present an updated analysis of highly inclined ($> 50^\circ$ zenith angle), high energy ($N_\mu > 10^5$) air showers measured with LOPES-10 in coincidence with KASCADE-Grande. Data from the Grande rather than the KASCADE array are used for the reconstruction of the air shower events, giving us access to a broader range of core distances for an independent cross-check with the earlier analysis.

Introduction

It is a known fact that air showers generate radio waves while propagating through the atmosphere. Since the 1960s various mechanisms have been proposed. The last of them, dating back only to 2003, explains the radio emission from air show-

ers as a coherent geosynchrotron emission due to the deflection of charged particles, electrons and positrons, in the Earth's magnetic field [1, 2]. In order to shed more light on the features of the radio emission and confirm dominant mechanisms responsible for the emission, we must investigate in detail correlations of the measured field strength

with shower parameters. For this purpose we use the LOPES set-up, placed within the KASCADE-Grande array (KARlsruhe Shower Core and Array Detector and Grande array), which is a good tool to investigate shower radio emission in coincidence with shower parameters obtained from independent particle detectors in the energy range of $10^{16} - 10^{18}$ eV [3].

An air showers develops in the atmosphere and evolves due to multiple interactions. The electromagnetic component reaches a maximum high above the ground and afterwards decreases rapidly. Consequently, only a small number of electrons (comparing with the electron number at the shower maximum) reach the ground. But the number of electrons and positrons in the shower maximum is expected to be approximately proportional to the strength of the radio pulse detected by the antennas. Therefore, better knowledge of radio emission parameters may give extra information on shower development.

Also the radio detection technique is proposed as a tool for neutrino detection. High energy vertical neutrinos most likely pass through the Earth's atmosphere without any interaction, but as the zenith angle increases the probability that a neutrino may generate an electromagnetic shower increases. Radio emission can be observed for vertical, slightly inclined as well as highly inclined air showers with no principle limitations from the radio detection point of view. The antenna sensitivity poses much smaller problems when zenith angle increases in comparison with flat particle detectors for which the reconstruction becomes unreliable for zenith angles larger than 60° .

Data analysis

For the present study we have analyzed data recorded in 2004 by LOPES-10 which consists of 10 East-West polarization antennas placed inside the KASCADE array. The LOPES-10 data sets have been submitted to several selections in order to investigate different aspects. For this work we have selected only inclined events, zenith angle $> 50^\circ$, and high energy events, $N_\mu > 10^5$. By analyzing inclined events we are able to investigate angular correlations over a much broader geomag-

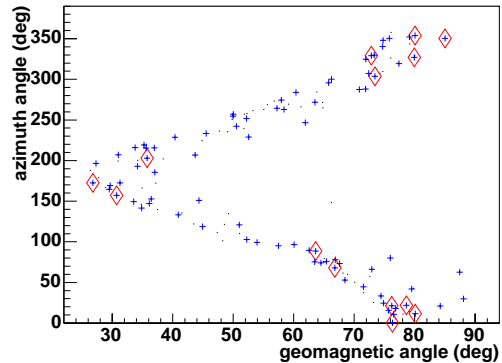


Figure 1: Azimuth angle as a function of geomagnetic angle for the 139 selected events with available radio data. Red rhombs - clear radio signal detected; blue crosses - reliable reconstruction with Grande, processed with optimized beam forming procedure; black dots - Grande reconstruction unreliable.

netic angle than vertical or near-vertical events. The geomagnetic angle is the angle between the shower axis and Earth's magnetic field.

A previous work on inclined showers [5] has reported correlations between measured field strength and shower parameters considering data in coincidence with the KASCADE array which covers an area of 200×200 m². The LOPES-10 antennas are also situated inside the KASCADE array, therefore only close events were processed. Now we extend the study and investigate events in coincidence with Grande data, keeping the zenith angle and energy cuts. This gives us the opportunity to investigate distant events of up to 800 m from the LOPES antennas that have been detected by the Grande stations on an area of ~ 0.5 km². For large showers triggering KASCADE with at least 10/16 clusters fired, data readout of both the LOPES antennas and the Grande array is triggered. In total, for 139 out of 149 selected high energy inclined events ($N_\mu > 10^5$ and zenith angle $> 50^\circ$) with Grande data, radio data was recorded with the LOPES array. The following analysis is performed with these 139 events.

Because we use KASCADE-Grande data as a starting point in the digital beam-forming of radio data

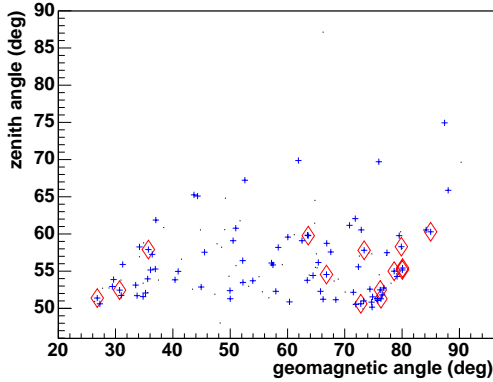


Figure 2: Zenith angle as a function of geomagnetic angle. Symbols are the same as in figure 1.

we have to establish which of the detected radio events have reliable reconstructed parameters (core coordinates, azimuth and zenith angles). Figure 1 shows the azimuth angle as a function of geomagnetic angle. Azimuth origin point (0°) is North. There are clear coherent events detected from North and South because the LOPES-10 antennas are more sensitive to the East-West polarization. For a shower coming from the East or West the emission is expected to be North-South polarized, therefore such a shower would not be detected with the LOPES-10 set-up. Also there are more events with azimuth angle corresponding to a northward direction than those coming from a southward direction. This effect is due to the fact that events coming from the North have larger geomagnetic angles, considering the orientation of the Northern Europe magnetic field.

Figure 2 shows the zenith angle as a function of geomagnetic angle for the same set of data as figure 1. Most detected events are in the range of $50^\circ - 60^\circ$. Above this limit, radio detection is possible but the shower parameters reconstruction becomes uncertain.

Optimized beam forming

The optimized beam forming procedure consists of varying the direction and core coordinates reconstructed for each event in the error range of

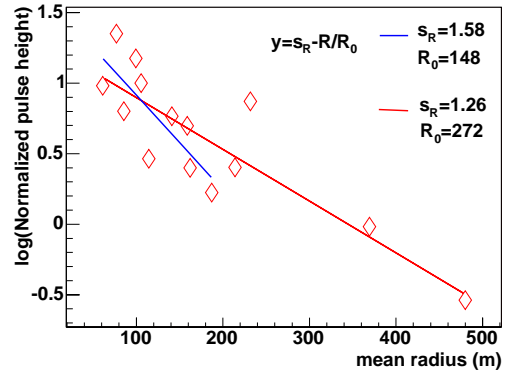


Figure 3: Dependence of radio pulse height (normalized by geomagnetic angle and muon number) on the mean distance from the shower axis to the antennas. The lines show results of a linear fit with a two parameter function: red line - parameter $R_0=272$ m, blue line - fit only for close events, mean distance < 200 m, parameter $R_0=148$ m.

Grande, 1.5° for the angle reconstruction and 20 m for the core coordinates reconstruction in order to improve beam parameters. All the events marked with blue crosses in figures 1 and 2 were submitted to the optimized beam forming procedure. For each of these events sets of 50 randomly varied parameters were generated in the Grande error range. For events with visible strong coherent signal the optimization lead to an important increase in the cross-correlation beam amplitude. For other 15 event the optimization improved the parameters only slightly, and did not clear the radio signal.

Correlations

The dependence of the radio pulse height on different parameters can be separated into: a dependence on the geomagnetic angle, a dependence on the distance to the shower axis and a dependence on the primary energy (\sim muon number) [4, 1, 2, 5]. To separate these parameters they are fitted separately in three iteration steps starting from the raw pulse height. In each fit the other dependencies are removed by dividing by the results of the fit from the previous iteration step. The correlations were made after optimized beam forming.

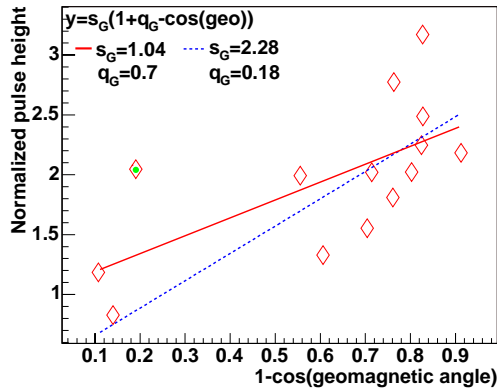


Figure 4: Dependence of the pulse height (normalized by muon number and distance) on the geomagnetic angle. Two linear fits were performed: red line - fit for all the clear radio events, blue dashed line without the event marked with the green dot. Parameters are shown in the plot.

Figure 3 shows the dependence of the pulse height, obtained after two iterations, corrected for muon number and geomagnetic angle, on the mean distance from the shower axis to the antenna set-up. There is a clear decrease with distance.

As shown in figure 4, there is a clear correlation of the pulse height, corrected for muon number and distance, with the geomagnetic angle which suggests that the emission is caused by the interaction of the shower with the Earth's magnetic field. The increase of the pulse height with geomagnetic angle supports the geosynchrotron theory. There is one event, marked with the green dot, which is still under investigation and therefore two fits were performed, one with the outlier and one without it.

Figure 5 shows a clear dependence of the pulse height, corrected for the geomagnetic angle and distance, on the muon number which is an approximate estimator of the primary particle energy. The dependence is fitted with a power law.

Conclusions

In this work we have extended previous studies of radio emission from inclined air showers to larger

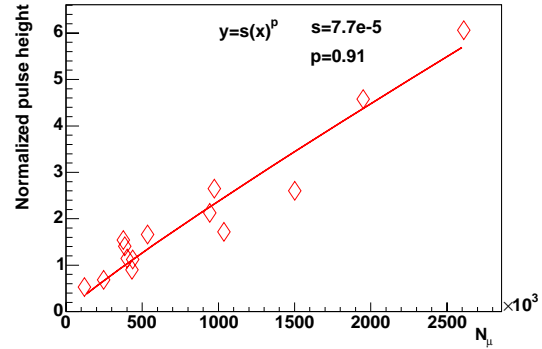


Figure 5: Dependence of the pulse height (normalized by geomagnetic angle and distance) on muon number, fitted with a power law.

distances by analyzing LOPES-10 data in coincidence with data recorded by the Grande array of the KASCADE-Grande experiment. The predicted features, increase of the pulse height with the primary energy, decrease of the pulse height with distance and the geomagnetic influence are confirmed. In addition, the data proves that very inclined events can be detected in the radio domain at large distances showing the capabilities of the radio technique for measuring very inclined air showers.

Acknowledgements

We express our thanks to the Romanian Ministry of Education of Research for the financial support of this study as part of the CEEX 05-D11-79 project.

References

- [1] T. Huege and H. Falcke, *Astron. Astrophys.*, 41, 19 (2003)
- [2] H. Falcke, P. Gorham, *Astropart. Phys.*, 19, 477 (2003)
- [3] H. Falcke et al., *Nature* 435, 313 (2005)
- [4] H.R. Allan, *Prog. in Elem. part. and Cos. Ray Phys.*, Vol. 10, 171 (1971)
- [5] J. Petrovic et al., *Astron. Astrophys.*, 462, 389 (2007)



Radio emission of air showers in electric fields

S. BUITINK^a, W.D. APEL^b, J.C. ARTEAGA^b, T. ASCH^c, J. AUFFENBERG^d, F. BADEA^b, L. BÄHREN^e, K. BEKK^b, M. BERTAINA^f, P.L. BIERMANN^g, J. BLÜMER^{b,h}, H. BOZDOG^b, I.M. BRANCUSⁱ, M. BRÜGGEMANN^j, P. BUCHHOLZ^j, H. BUTCHER^e, A. CHIAVASSA^f, F. COSSAVELLA^h, K. DAUMILLER^b, V. DE SOUZA^h, F. DI PIERRO^f, P. DOLL^b, R. ENGEL^b, H. FALCKE^{a,e}, H. GEMMEKE^c, P.L. GHIA^k, R. GLASSTETTER^d, C. GRUPEN^j, A. HAUNGS^b, D. HECK^b, J.R. HÖRANDEL^a, A. HORNEFFER^a, T. HUEGE^b, P.G. ISAR^b, K.-H. KAMPERT^d, D. KICKELBICK^j, Y. KOLOTAEV^j, O. KRÖMER^c, J. KUIJPERS^a, S. LAFEBRE^a, P. LUCZAK^l, H.J. MATHES^b, H.J. MAYER^b, C. MEURER^b, J. MILKE^b, B. MITRICAⁱ, C. MORELLO^k, G. NAVARRA^f, S. NEHLS^b, A. NIGL^a, J. OEHLISCHLÄGER^b, S. OSTAPCHENKO^b, S. OVER^j, M. PETCUⁱ, J. PETROVIC^a, T. PIEROG^b, S. PLEWNIA^b, J. RAUTENBERG^d, H. REBEL^b, M. ROTH^b, H. SCHIELER^b, O. SIMA^m, K. SINGH^a, M. STÜMPERT^h, G. TOMAⁱ, G.C. TRINCHERO^k, H. ULRICH^b, J. VAN BUREN^b, W. WALKOWIAK^j, A. WEINDL^b, J. WOCHOLE^b, J. ZABIEROWSKI^l, J.A. ZENSUS^g.

^a Dept. of Astrophysics, Radboud University Nijmegen, The Netherlands

^b Institut für Kernphysik, Forschungszentrum Karlsruhe, Germany

^c Inst. Prozessdatenverarbeitung und Elektronik, Forschungszentrum Karlsruhe, Germany

^d Fachbereich Physik, Universität Wuppertal, Germany

^e ASTRON, Dwingeloo, The Netherlands

^f Dipartimento di Fisica Generale dell'Università Torino, Italy

^g Max-Planck-Institut für Radioastronomie Bonn, Germany

^h Institut für Experimentelle Kernphysik, Universität Karlsruhe, Germany

ⁱ National Institute of Physics and Nuclear Engineering Bucharest, Romania

^j Fachbereich Physik, Universität Siegen, Germany

^k Istituto di Fisica dello Spazio Interplanetario, INAF Torino, Italy

^l Soltan Institute for Nuclear Studies Lodz, Poland

^m Department of Physics, University of Bucharest, Romania

s.buitink@astro.ru.nl

Abstract: The radio emission from cosmic ray air showers consists in large part of geosynchrotron radiation. Since the radiation mechanism is based on particle acceleration, atmospheric electric fields may play an important role. LOPES results show that electric fields under fair weather conditions do not alter the radio emission considerably, but during thunderstorms strongly amplified pulses are measured. We simulate the electric field influence on the shower development and radiated emission with CORSIKA and REAS2. We present results from LOPES data analysis and some first results from simulations.

Introduction

The secondary electrons and positrons of an extensive air shower (EAS) produce coherent radio emission in the atmosphere. Results from LOPES [1] show that the intensity of the radio emission is strongly correlated with the angle of the shower axis with the geomagnetic field, proving that the

dominant part of the emission is driven by the geomagnetic field. This mechanism can be understood in terms of transverse current emission [2] or geosynchrotron emission [3]. The latter description allows for detailed Monte Carlo simulations in which shower electrons and positrons are treated individually, which is done in [4].

Atmospheric electric fields may influence the emission mechanism, especially when the electric field force is of the same order of magnitude (or higher) as the Lorentz force from the geomagnetic field. The uncertainty introduced by this effect is one of the reasons why efforts to detect radio emission from cosmic ray air showers in the 1970's were abandoned [5]. In this work we discuss the mechanisms by which the electric field influences the emission. Results are shown from LOPES data analysis and Monte Carlo simulations with CORSIKA and REAS2.

Atmospheric electric fields

In fair weather, i.e. atmospheric conditions in which electrified clouds are absent, there is a downward electric field present with a field strength of $\sim 100 \text{ Vm}^{-1}$ at ground level. The field strength decreases rapidly with altitude. Clouds can typically gain field strengths of a few hundred Vm^{-1} . Nimbostratus clouds, which have a typical thickness of more than 2000m can have fields of the order of 10 kVm^{-1} . The largest electric fields are found inside thunderstorms and are typically 100 kVm^{-1} . In most clouds this field is directed vertically (either upwards or downwards, depending on the type of cloud), but thunderclouds contain complex charge distributions and can have local fields in any direction. Thunderclouds can have a vertical extent of $\sim 10 \text{ km}$ (values taken from [6]).

The atmospheric electric field acts on the radio emission from EAS in various ways. We distinguish two generations of electrons: the relativistic electrons from pair creation in the EAS (called shower electrons from here) and the non-relativistic electrons resulting from the ionization of air molecules by the EAS particles (called ionization electrons from here).

The electric force accelerates the shower electrons and positrons, producing radiation in more or less the same way as the magnetic field does. The total emitted power of a single electron or positron is proportional to the square of the Lorentz factor and the square of the applied perpendicular force: $P \propto \gamma^2 F_{\perp}^2$. The part of the electric force that is directed perpendicular on the particle orbit adds to

the Lorentz force, increasing (or decreasing, depending on geometry) F_{\perp} . The part of the electric force that is directed parallel to the particle orbit increases or decreases γ . Generally, the single particle pulses become stronger but narrower in time. Taking into account coherency effects, this does not automatically lead to amplification of the complete shower pulse. This effect (and the electric field emission mechanism in general) is discussed in detail in [7].

The ionization electrons are also accelerated in the electric field. A radio pulse will be emitted from the current that is produced in this way. When ionized electrons gain an energy of $\epsilon > \epsilon_c \approx 0.1 - 1 \text{ MeV}$ they can ionize new molecules. If the electric field is strong enough to accelerate ionization electrons to such energies a process called runaway breakdown [8] can occur. The critical field strength of $E_c \approx 100 - 150 \text{ kV/m}$, needed for this effect, is present only inside thunderclouds. The radiation pattern of the runaway breakdown is calculated in [9] for a vertical shower and resembles that of a current pulse. The pulse amplitude is calculated to be several orders of magnitude higher than the geosynchrotron emission from the EAS. Depending on the viewing geometry the pulses can have time widths of 100-300 ns.

Both mechanisms can be responsible for an amplification of the radio pulse from EAS. There are several ways to distinguish between them, including direction of emission, pulse time width and polarization.

LOPES data analysis

In 2004, the LOPES array consisted of 10 east-west aligned dipole antennas, co-located with the KASCADE experiment which provides triggers for LOPES and reconstructs the content, energy and direction of the air shower. When the data used in this paper was taken, LOPES measured only the polarization in the east-west plane. Details about the experimental setup and the reduction of the data can be found in [11].

Three sets of data were selected from the 2004 database of LOPES:

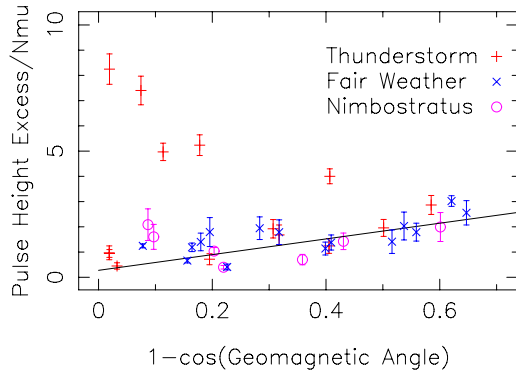


Figure 1: Pulse height, normalized with truncated muon number is plotted against geomagnetic angle. The black line indicates the geomagnetic dependence of the radio emission found in [1]. Pulse heights are given in arbitrary units.

1. Fair weather events which took place during periods with 0% cloud coverage (9455 events spread over the period March-September).
2. Events which took place while the sky was covered by nimbostratus clouds for more than 90% (2659 events spread over the period January-March).
3. Events during thunderstorms, which were identified by looking at lightning strike maps and the dynamic spectra of LOPES, on which the radio emission of lightning strikes show up as bright lines (3510 events taken from 11 thunderstorms in the period May-August).

The weather information is provided by the Karlsruhe weather station. Weather conditions at the LOPES site and the weather station are expected to differ only slightly. Together, all these events form only a very small fraction of the total LOPES database, because the weather information is not complete and even if it was, most weather conditions do not match the criteria of one of these selections. The selections include events for which a radio signal was not detected, i.e. not larger than the background noise by 3 sigma.

In Falcke et al.[1] it was shown that the strength of the radio signal correlates with the geomagnetic angle as $(1 - \cos \alpha)$ when it is normalized with the

truncated muon number. This dependence is indicated with a black line in Fig. 1. The events of our three selections that show a significant radio pulse are also plotted in Fig. 1. Events for which the geosynchrotron emission is dominant should be located near the black line. Events that lie a few sigma above this line have a radio signal that is amplified by an additional mechanism. Significant amplification is only observed for thunderstorm events [7].

Monte Carlo simulations

In order to simulate the radio pulse of an air shower in an electric field, two Monte Carlo codes are used, CORSIKA and REAS2. The CORSIKA [10] code, which tracks the evolution of an air shower, has been modified to include an acceleration due to the electric field. This will primarily affect the trajectories of the electrons and positrons. Since accelerated particles will emit bremsstrahlung photons with higher energies which will in turn create new electron-positron pairs this can affect the evolution of the electromagnetic part of the shower considerably.

To calculate the radio emission, particle data output on various levels in the atmosphere is needed. The shower is sampled in 50 layers for each of which four three-dimensional histograms are produced. One kind of histogram contains the particle energy, arrival time and lateral distance to the core and the other kind contains energy, and two angles describing the direction of the particle momentum. Both kinds are created for electrons and positrons.

As an example, Fig. 2 shows the shower evolution for two typical vertical showers of 10^{17} eV, one without electric field and one in a field of 100 kV/m (corresponding to the highest values reached inside thunderstorms). For both cases 10 showers were simulated after which one with a typical shower evolution was selected. The field is directed downwards, meaning it accelerates the shower positrons. When the field is switched on, the number of electrons decreases, while the number of positrons increases. The charge excess switches sign in this case. A field strength of 100 kV/m for the whole sky is unrealistically large and can be regarded as an upper limit.

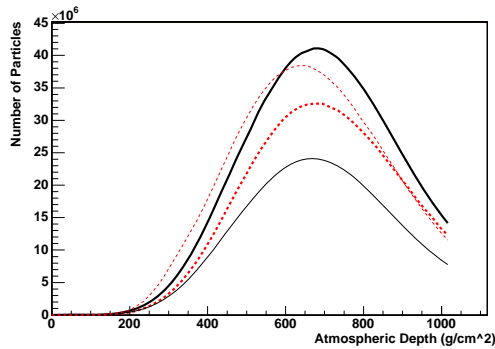


Figure 2: Shower evolution for absent electric field (black/solid) and a field of 100 kV/m (red/dotted). The number of electrons (thick lines) and positrons (thin lines) with energy above 50 keV in a layer are plotted against atmospheric depth.

The radio emission is calculated with REAS2 [12], which uses analytical trajectories for which the initial conditions are taken from the histograms. A new routine has been included in the REAS2 code which calculates analytical trajectories for particles in locally homogeneous magnetic and electric fields, for given field strengths and directions. Since particles are tracked only along a small part of their trajectory inside REAS2 the linear acceleration is not expected to be important at this point. The perpendicular acceleration, on the other hand, will directly affect the amount of radio emission. Fig. 3 shows simulated radio pulses for various electric fields. In this particular case the large electric field results in pulse amplification. This result is not general for different shower parameters and observer positions.

Conclusions

From analysis of LOPES data we find that the relation between the radio pulse and the geomagnetic angle is conserved under all weather conditions but thunderstorms. This means that radio detection of cosmic rays can be used for a reliable shower energy measurement in all but the most severe weather conditions. Currently we are simulating the electric field effects with CORSIKA and REAS2. A detailed description of the implementa-

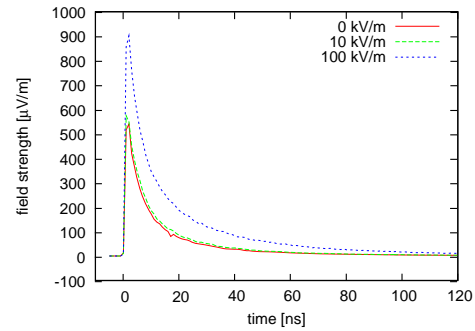


Figure 3: Radio pulses at 50 m to the east of the shower core for a 10^{17} eV shower in various electric fields.

tion of electric field routines into these codes and an analysis of simulation results will be the subject of a forthcoming paper.

References

- [1] H. Falcke et al., *Nature* 435, 313 (2005)
- [2] F. Kahn and I. Lerche, *Royal Society of London Proceedings A*, 289, 206 (1966)
- [3] T. Huege and H. Falcke, *Astronomy and Astrophysics*, 412, 19-34 (2003)
- [4] T. Huege and H. Falcke, *Astronomy and Astrophysics*, 430, 779-798 (2005)
- [5] R. Baggio, N. Mandolesi, G. Morigi and G. Palumbo, *Nuovo Cimento B*, 40, 289 (1977)
- [6] D. MacGorman and W. Rust, *The electrical nature of storms* (Oxford Univ. Press, New York, 1998)
- [7] S. Buitink et al., *Astronomy and Astrophysics*, 467, 385-394 (2007)
- [8] A. Gurevich et al., *Phys. Lett. A* 165, 463 (1992)
- [9] A. Gurevich et al., *Phys. Lett. A* 301, 320 (2002)
- [10] D. Heck, J. Knapp, J. Capdevielle, G. Schatz and T. Thouw, *FZKA Report 6019*, Forschungszentrum Karlsruhe (1998)
- [11] A. Horneffer et al., *Proc. SPIE* 5500-21, (2004)
- [12] T. Huege, R. Ulrich, R. Engel, *Astropart. Physics* 27, 392-405 (2007)



Trigger Strategy for Radio Detection of Atmospheric Air Showers with LOPES^{STAR}

T. ASCH^a, O. KRÖMER^a, W.D. APEL^b, J.C. ARTEAGA^b, J. AUFFENBERG^c, F. BADEA^b, L. BÄHREN^d, K. BEKK^b, M. BERTAINA^e, P.L. BIERMANN^f, J. BLÜMER^{b,g}, H. BOZDOĞ^b, I.M. BRANCUS^h, M. BRÜGGEMANNⁱ, P. BUCHHOLZ^j, S. BUITINK^j, H. BUTCHER^d, A. CHIAVASSA^e, F. COSSAVELLA^g, K. DAUMILLER^b, V. DE SOUZA^g, F. DI PIERRO^e, P. DOLL^b, R. ENGEL^b, H. FALCKE^{d,j}, H. GEMMEKE^a, P.L. GHIA^k, R. GLASSTETTER^c, C. GRUPENⁱ, A. HAUNGS^b, D. HECK^b, J.R. HÖRANDEL^j, A. HORNEFFER^j, T. HUEGE^b, P.G. ISAR^b, K.-H. KAMPERT^c, D. KICKELBICKⁱ, Y. KOLOTAEVⁱ, J. KUIJPERS^j, S. LAFEBRE^j, P. LUCZAK^l, H.J. MATHES^b, H.J. MAYER^b, C. MEURER^b, J. MILKE^b, B. MITRICA^h, C. MORELLO^k, G. NAVARRA^e, S. NEHLS^b, A. NIGL^j, J. OEHLSCHLÄGER^b, S. OSTAPCHENKO^b, S. OVERⁱ, M. PETCU^h, J. PETROVIC^j, T. PIEROG^b, S. PLEWNIA^b, J. RAUTENBERG^c, H. REBEL^b, M. ROTH^b, H. SCHIELER^b, O. SIMA^m, K. SINGH^j, M. STÜMPERT^g, G. TOMA^h, G.C. TRINCHERO^k, H. ULRICH^b, J. VAN BUREN^b, W. WALKOWIAKⁱ, A. WEINDL^b, J. WOCHELE^b, J. ZABIEROWSKI^l, J.A. ZENSUS^f.

^a *Inst. Prozessdatenverarbeitung und Elektronik, Forschungszentrum Karlsruhe, Germany*

^b *Institut für Kernphysik, Forschungszentrum Karlsruhe, Germany*

^c *Fachbereich Physik, Universität Wuppertal, Germany*

^d *ASTRON, Dwingeloo, The Netherlands*

^e *Dipartimento di Fisica Generale dell'Università Torino, Italy*

^f *Max-Planck-Institut für Radioastronomie Bonn, Germany*

^g *Institut für Experimentelle Kernphysik, Universität Karlsruhe, Germany*

^h *National Institute of Physics and Nuclear Engineering Bucharest, Romania*

ⁱ *Fachbereich Physik, Universität Siegen, Germany*

^j *Dept. of Astrophysics, Radboud University Nijmegen, The Netherlands*

^k *Istituto di Fisica dello Spazio Interplanetario, INAF Torino, Italy*

^l *Soltan Institute for Nuclear Studies Lodz, Poland*

^m *Department of Physics, University of Bucharest, Romania*

asch@ipe.fzk.de

Abstract: In the framework of LOPES (LOFAR PrototypE Station), a Self-Triggered Array of Radio detectors (*STAR*) is developed. The challenge of LOPES^{STAR} is to provide an independent self-trigger on radio emission of extensive air showers with primary energies above $5 \cdot 10^{17}$ eV.

Measurements are done with an external trigger and self-trigger in radio loud and quiet areas. Based on these data the self-trigger is optimised and higher level triggers are developed, as well as algorithms for reconstruction of shower observables. The methods and first results from LOPES^{STAR} are described.

Introduction

On site of the Forschungszentrum Karlsruhe (FZK) in a first step 10 and later additional 20 short dipole antennas with an inverted V-shape (LOPES30) with east/west polarisation were installed and triggered by KASCADE [1, 2].

To optimise these techniques and to provide an independent trigger system for radio emission of Ultra High Energy Cosmic Rays (UHECRs) the LOPES^{STAR} detector was developed. Two antenna clusters, each with 4 logarithmically periodic dipole antennas (LPDAs) and two polarisation channels – east/west & north/south (8 channels),

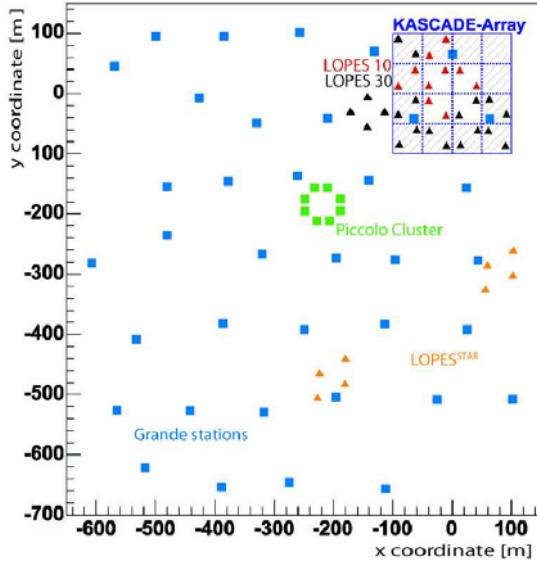


Figure 1: Layout of the KASCADE-Grande and LOPES experiment on site of the Forschungszentrum Karlsruhe.

were set up on the site of FZK within the area of the air-shower experiment KASCADE-Grande [3] (see fig. 1).

First self-triggered measurements have shown, that Radio Frequency Interferences (RFI) are dominating the trigger rate. To improve the self-trigger concept and to develop higher trigger levels an external trigger signal from KASCADE-Grande was provided. LOPES^{STAR} data are recorded whenever a coincidence configuration of seven KASCADE-Grande stations (blue squares in fig. 1) is registered. This corresponds to an energy threshold of $\approx 10^{16}$ eV and a trigger rate of ≈ 50 mHz.

Signal Chain

The pulsed, coherent radio emission of the cosmic ray shower can be observed by antennas when the UHECRs energy and the electric field strength are large enough [4]. The signal of each channel is raised by a low noise amplifier and transmitted to a 40 – 80 MHz bandpass filter. The Radio Frequency

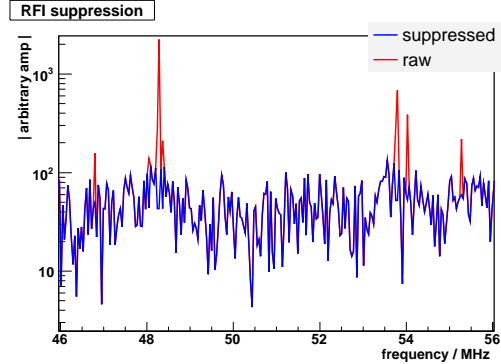


Figure 2: Example of RFI suppression of mono frequent components in the frequency space. The shown peaks corresponds to known TV transmitter.

(RF) signal is then split. One part can be used as input signal for the self-trigger analogue electronics while the other is digitised by a 12 bit ADC with a sampling frequency of 80 MHz and stored in ring buffers [5, 6]. Additionally, a timestamp from a GPS clock is stored with the ADC data if an event is triggered.

The digitisation of a 40 – 80 MHz bandpass signal with a sampling rate of 80 MHz fulfils the extended Nyquist Theorem. The n sub-sampled data have to be up-sampled by a factor k to $k \cdot n$ samples for analysis and reconstruction. For this purpose the signal is transformed to frequency domain, where also the suppression of mono frequent RFI (*RFI suppression*) is done (see fig. 2). By putting in $(k - 1) \cdot \frac{n}{2}$ zeros in the frequency space we achieve the factor k up-sampled spectra in the time domain [6, 7].

Basic Concept

The position of each antenna in the illustrated cluster in fig. 1 is part of a vertex of an equilateral triangle with a base length $b = 60$ m. This geometrical configuration of three LPDAs provides the coincidence constraint for the self-trigger. Most RFI sources are located at low elevations. The signals propagate dominantly in parallel to the earth's surface. For this RFI background the typical time difference t_{max} of two antennas is $\frac{h}{c} < t_{max} < \frac{b}{c}$, where h is the height of the triangle and c the speed

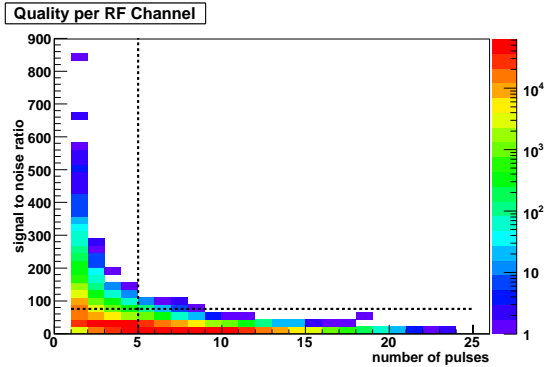


Figure 3: *Signal to noise ratio* versus the detected *number of pulses* with eight entries per event. The dashed lines indicate the Quality Cut.

of light. For zenith angles $\theta \leq 60^\circ$ most of the cosmic ray events are detected. The adjusted coincidence time $0 \leq t_c < t_{max}$ is used to suppress horizontal background.

New Approach

In a first step, a simple approach for the self-trigger analogue electronics was chosen. The sum of envelope signals of two polarisations of one antenna is compared with a fixed, but adjustable, threshold for all antennas. If this constraint per antenna is fulfilled within a given coincidence time t_c a trigger is generated and the data are stored.

The used fixed threshold, but also the addition of the envelope signals of one antenna were not effective to get a threshold equivalent to 10^{18} eV to obtain sufficient background suppression in triple coincidences. Therefore we developed a classification system to reject background and a new strategy to accept shower events.

Classification

The analysis is based on a 27d dataset triggered externally by KASCADE-Grande (2006-12-12 to 2007-01-07) in a four antenna array in the lower middle of KASCADE-Grande. More than 102,000 events are recorded with a primary energy $E > 10^{16}$ eV.

Events including one RF channel with a signal

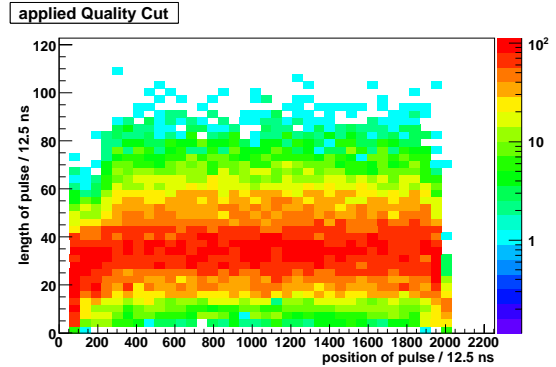


Figure 4: Shown is *length of pulses* versus *position of pulse* of all channels accepted by the Quality Cut.

larger than the range of the ADC are rejected for this analysis. *RFI suppression* is applied to all remaining RF channels. Four classification parameters are calculated: **signal to noise ratio** – The ratio of the peak value and noise in the squared 2048 point sub-sampled data. **number of pulses** – No. of pulses above a dynamically defined threshold counted on base of the sub-sampled data. **length of pulse** – The width of the peak of an envelope in the up-sampled data is calculated. **position of pulse** – The position of the peak in the time domain is calculated in the up-sampled data.

New Strategy

The distribution of the *signal to noise ratio* versus *number of pulses* is illustrated in fig. 3 and shows per event eight entries. As expected, the *number of pulses* is high if the *signal to noise ratio* is small. In this case the algorithm to count the pulses does not work efficiently, because the threshold is just above the noisy background. If the *signal to noise ratio* is > 100 the counted pulses are clearly visible pulses. On the other hand, the expected number of pulses are low, if more than five pulses are detected the broad band RFI is for this channel too high. The quality per RF channel is defined to be *good* by the cut *signal to noise ratio* > 75 AND *number of pulses* < 5 .

The *length of pulses* versus *position of pulse* of the accepted RF channels are plotted in fig. 4. RFI

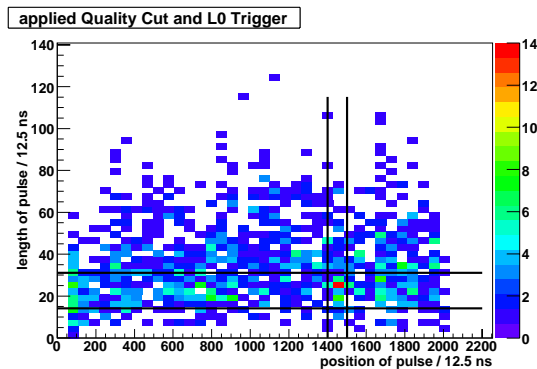


Figure 5: Applied are the Quality Cut and L0 trigger. The black lines indicate a part of further cuts.

signals are distributed randomly over the recorded time window. The maximum *length of pulse* corresponds to the mean length of RFI pulses $t_{\text{mean,RFI}} = 475$ ns at the antenna array. The decreasing mean length of pulses for low and high values of the recorded time are due to the used window function for Fourier transformation. Only 21,000 events (20%) of the given data sample are accepted for further analysis.

The Quality Cut acts like a monitor for each RF channel. The impact is directly visible in fig. 4. Each event which has at least one RF channel accepted by the Quality Cut is analysed by the following Level Zero (L0) trigger which verifies the coincidence of all RF channels. The envelope and a dynamic threshold of each polarisation per antenna (eight RF channels) are calculated. In the case of broad band RFI in several RF channels it is important to suppress these channels for the trigger decision.

The basic idea is to verify all possible coincidences of all RF channels of one triangle and to ensure that at least one RF channel per antenna is included. This also implies a comparison of different polarisations. The contribution of the signal strength in each polarisation is given by the geomagnetic angle (angle between shower axis and geomagnetic field) but is identical in both polarisations. 269 events (0.026%) of the given data sample are accepted by the L0 trigger. Due to the dynamic threshold per channel this mechanism is able to detect UHECR events in radio loud environments.

Applying the Quality Cut and L0 trigger on the data sample results to fig. 5. A suppression of RFI and random signals is visible. Due to the knowledge of the trigger delay and the expected time length of the observed radio signal the peak illustrated in fig. 5 corresponds to shower candidates. The black lines show a part of the final cuts to determine radio events. The cut is given by *number of pulses* = 1 AND *detected channels* > 2. Any event which includes one RF channel that fulfils this constraints is accepted and results to 12 out of 102,000 events. 5 of these events are in good agreement with the reconstructed shower direction by a plane fit compared with the reconstructed direction of KASCADE-Grande.

Conclusion

The detection of coherent radio emission of UHECR with an independent and self-triggered detector is the challenge of LOPES^{STAR}. On site of the Forschungszentrum Karlsruhe data are taken in coincidence with the air-shower experiment KASCADE-Grande. Based on this data sample a trigger strategy was developed. The data quality of each channel is monitored while a coincidence check is independent of the polarisation and noisy channels are suppressed. The introduced algorithm detected 12 shower candidates out of 102,000 triggered events. With the benefit of the KASCADE-Grande reconstruction 5 UHECR events with a reconstructed energy $E > 7 \cdot 10^{17}$ eV are detected.

References

- [1] T. Antoni et al., Nucl. Instr. Methods A, 513:490, 2003
- [2] A. Horneffer, PhD Thesis, University Bonn, 2006
- [3] G. Navarra et al., Nucl. Instr. Methods A, 518:207, 2004
- [4] T. Huege, H. Falcke, Astropart. Physics 24, 116-136, 2005
- [5] H. Gemmeke et al., Intern. Journal of Mod. Physics A, 21:242, 2006
- [6] T. Asch et al., Proc. VCI, 2007 *in print*
- [7] H. Nyquist, Proc. IEEE, Vol. 90, No. 2, 2002



REAS2: CORSIKA-based Monte Carlo simulations of geosynchrotron radio emission

T. HUEGE¹, R. ULRICH¹, R. ENGEL¹.

¹*Institut für Kernphysik, Forschungszentrum Karlsruhe, Postfach 3640, 76021 Karlsruhe, Germany*
tim.huege@ik.fzk.de

Abstract: Simulations of geosynchrotron radio emission from extensive air showers performed with the Monte Carlo code REAS1 used analytical parameterisations to describe the spatial, temporal, energy and angular particle distributions in air showers. The successor REAS2 replaces these parameterisations with precise, multi-dimensional histograms derived from per-shower CORSIKA simulations. REAS2 allows an independent selection between parameterisation and histogram for each of the relevant particle distributions, enabling us to study the changes arising from using a more realistic air shower model in detail. We describe the new simulation strategy and illustrate the effects introduced by the improved air shower model.

Introduction

From results of the LOPES experiment [1], radio emission from cosmic ray air showers is known to be dominated by a geomagnetic emission mechanism that can be described with the “geosynchrotron model” [2]. In the geosynchrotron process, relativistic secondary shower electrons and positrons are deflected in the earth’s magnetic field, thereby giving rise to strongly pulsed, coherent radio emission in the frequency range from ~ 10 to 100 MHz. In the recent years, the geosynchrotron model had evolved from analytic frequency-domain calculations [4] to time-domain Monte Carlo simulations based on an analytical description of the underlying extensive air shower, as implemented in the REAS1 simulation code [5]. Many general properties of the radio emission have been predicted since using REAS1 [6]. The successor to this code, REAS2, now features an implementation of the geosynchrotron model no longer based on analytically parameterised air shower properties, but using realistic, per-shower CORSIKA [3] simulations to model the spatial, temporal, energy and angular distributions of the shower particles. In this article, we describe the changes arising from the much more realistic air shower model and illustrate the potential of the

new simulation code for advanced studies of the radio pulse shape.

REAS2 air shower model

While the electromagnetic emission model has not changed between REAS1 and REAS2, REAS2 simulations are now based on very detailed particle information derived with CORSIKA on a per-shower basis. For each individual air shower, CORSIKA writes out separate information for electrons and positrons sampled in (usually) 50 layers between the point of first interaction and the observer position. Each layer encompasses

- one three-dimensional histogram of
 1. particle arrival time relative to that of an imaginary primary particle propagating with the speed of light from the point of first interaction
 2. lateral distance of the particle from the shower core
 3. particle energy
- and one three-dimensional histogram of
 1. angle of the particle momentum to the shower axis

2. angle of the particle momentum to the (radial) outward direction
3. particle energy.

These histograms give REAS2 access to a true four-dimensional distribution of particles in atmospheric depth, arrival time, lateral distance and energy, and in addition describe the angular distribution of particle momenta as a function of particle energy and atmospheric depth. The chosen separation of the distributions into two histograms ensures that the necessary amounts of data can be handled on standard PCs while making approximations of only minor significance for the simulation of the radio signal. (The most important drawback of this scheme is the loss of information on azimuthal asymmetries in the air shower.) Naturally, effects associated with air showers induced by different types of primary particles can be analysed in detail with this simulation strategy. The longitudinal evolution of the air shower is sampled on an additional, finer grid (usually) spaced with 5 g cm^{-2} distance.

REAS2 vs. REAS1 results

Incorporating the new CORSIKA-based air shower model and some additional enhancements, the REAS2 code provides a much more realistic determination of geosynchrotron radio emission than its predecessor REAS1. A particular merit of the chosen approach is that the transition from the REAS1 to the REAS2 air shower model can be performed in a gradual fashion, switching the different particle distributions (spatial, temporal, energy, and angular) from parameterised to histogrammed one at a time and analysing the changes arising in the radio signal. The corresponding effects and technical details have been discussed elsewhere [8]; here we only compare the end result of REAS2 simulations with those of REAS1 simulations for the typical reference case of a vertical 10^{17} eV proton-induced air shower. As presented in Fig. 1, the radio pulses calculated with REAS2 for an observer to the north of the shower core show only moderate changes in comparison with the REAS1-generated pulses. In particular, the pulses close to the core (75 m corresponds to the typical lateral distance in the LOPES experiment) get considerably nar-

rower, caused by the narrower arrival time distributions provided by CORSIKA in comparison with the parameterisation used in REAS1. Consequently, the frequency spectrum of the emission close to the core gets much flatter for the REAS2-calculated pulses (Fig. 2). Further away from the core (525 m corresponds to the distance range of interest for larger scale radio antenna arrays), the amplitude drops by a factor of ~ 2 , mainly as a consequence of the much broader angular distribution of particle momenta derived from CORSIKA. Interestingly, the overall field strength in the frequency band used by the LOPES experiment (40 to 80 MHz) does not change significantly between REAS1 and REAS2 (Fig. 2). A more sig-

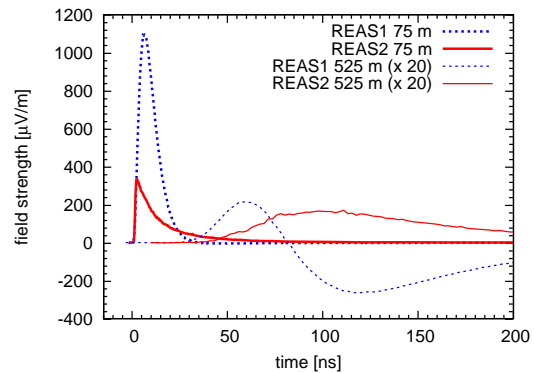


Figure 3: Comparison of REAS1 and REAS2-simulated radio pulses at 75 m and 525 m west of the shower core. The bipolar pulses present in the REAS1 simulations are no longer present.

nificant change becomes visible when studying the changes to the radio pulses for an observer west of the shower core, as depicted in Fig. 3. First, a significant drop in pulse amplitude close to the shower core can be identified. This leads to a pronounced east-west versus north-south asymmetry in the radio “footprint”, even for vertical air showers (cf. Fig. 4). At larger distances, a qualitative change in the pulse shape takes place: while REAS1-generated pulses in this region showed bipolar structures, the REAS2-calculated signals become universally unipolar. The bipolar pulse shapes in the REAS1 calculations can be considered artifacts of over-simplified particle distributions (e.g., in the momentum angles), and the REAS2 results describe the geosynchrotron emission much more realistically. Another important characteristic of

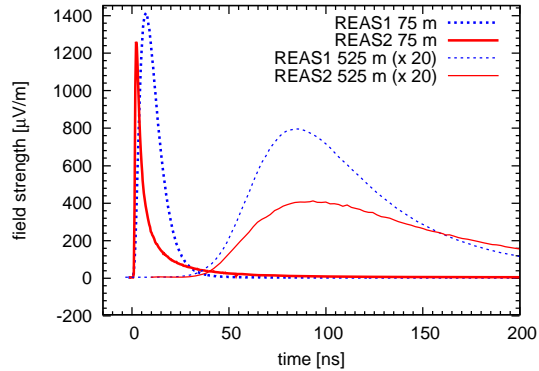


Figure 1: Comparison of REAS1 and REAS2-simulated radio pulses at 75 m and 525 m north of the shower core.

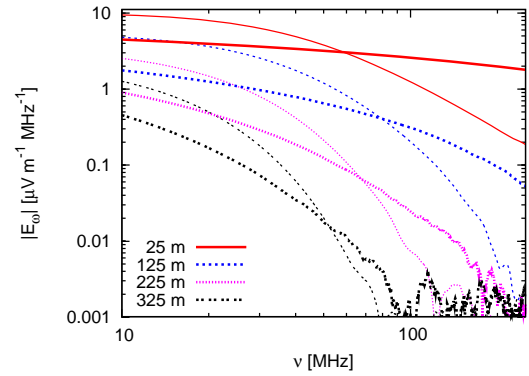


Figure 2: Comparison of frequency spectra for the REAS1 (thin) and REAS2 (thick) simulated radio pulses.

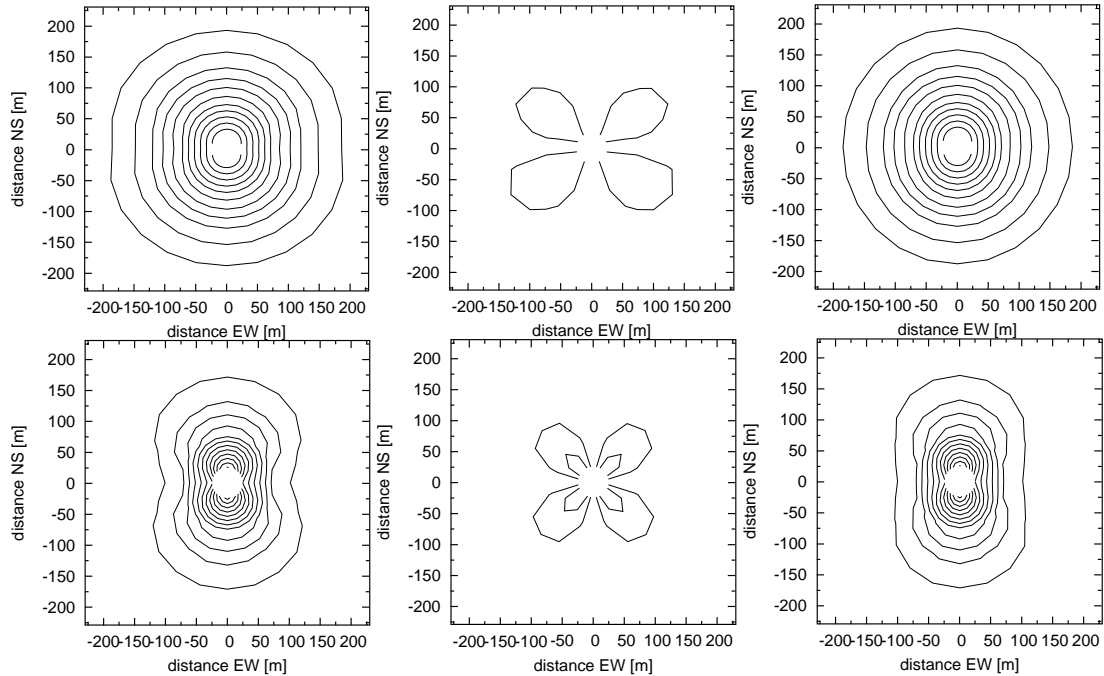


Figure 4: Contour plots of REAS1 (upper) and REAS2 (lower) air shower emission at $\nu = 60$ MHz. The columns (from left to right) show the total field strength, the north-south polarisation component and the east-west polarisation component. The vertical polarisation component (not shown here) does not contain any significant flux. Contour levels are $0.25 \mu\text{V m}^{-1} \text{MHz}^{-1}$ apart in E_ω , outermost contour corresponds to $0.25 \mu\text{V m}^{-1} \text{MHz}^{-1}$. White centre region has not been calculated.

geosynchrotron radiation is its mostly linear polarisation. The comparison of the individual polarisation components depicted in Fig. 4 demonstrates that the polarisation characteristics are identical between REAS1 and REAS2. At the same

time, the contour plots illustrate once more the newly arising east-west versus north-south asymmetry and confirm that the absolute field strengths in the centre of the LOPES band (60 MHz) do not change considerably.

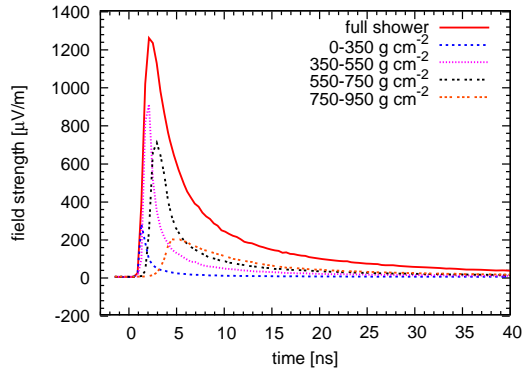


Figure 5: Contribution of different longitudinal shower evolution stages to the radio pulse at 75 m north from the shower core.

Pulse shape analyses

The highly detailed CORSIKA-based air shower model implemented in REAS2 allows advanced studies of the radio pulse shape. A particularly interesting question is how different phases in the longitudinal development of the air shower contribute to the radio pulses, as illustrated in Figs. 5 and 6. Close to the shower core, signals from all over the longitudinal shower evolution arrive approximately simultaneously at the observer. The pulse shape close to the shower core thus gives a direct estimate of the overall particle arrival time distribution. (This could change once the refractive index profile of the atmosphere is taken into account.) At larger distances, geometrical time delays become important; the pulse shape thus provides direct information on the shower evolution profile. Another interesting result is that the emission is dominated by the shower maximum (here at 640 g cm^{-2}) and the stage shortly before. The information content of the radio pulses can be exploited to estimate the primary particle energy and type from radio measurements on a shower-to-shower basis [7]. Analyses how different particle energy ranges or radial distance ranges contribute to the radio signal have also been performed [8].

Conclusions

With REAS2, a sophisticated Monte Carlo implementation of the geosynchrotron model based

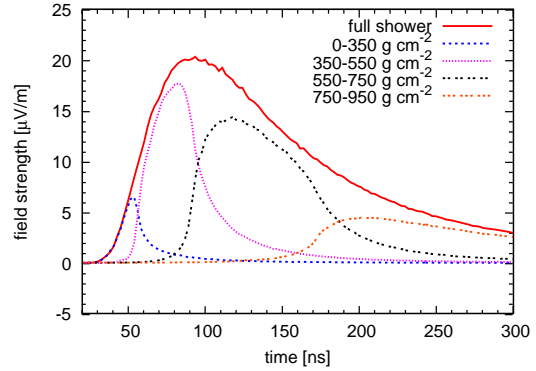


Figure 6: Contribution of different longitudinal shower evolution stages to the radio pulse at 525 m north from the shower core.

on a realistic, CORSIKA-based air shower model is now available. The transition from REAS1 to REAS2 has been carried out in a controlled way, and the changes arising are well-understood. In spite of the major model improvements, the changes are only moderate, in particular in the frequency range of current experiments. REAS2 can be used for in-depth studies of the information content of geosynchrotron radio pulses and as such is a powerful tool to unlock the full potential of the radio technique for cosmic ray measurements.

References

- [1] H. Falcke, W. D. Apel, A. F. Badea et al. *Nature*, 435:313–316, May 2005.
- [2] H. Falcke and P. W. Gorham. *Astropart. Physics*, 19:477–494, July 2003.
- [3] D. Heck, J. Knapp, J. N. Capdevielle, G. Schatz, and T. Thouw. FZKA Report 6019, Forschungszentrum Karlsruhe, 1998.
- [4] T. Huege and H. Falcke. *Astronomy & Astrophysics*, 412:19–34, December 2003.
- [5] T. Huege and H. Falcke. *Astronomy & Astrophysics*, 430:779–798, 2005.
- [6] T. Huege and H. Falcke. *Astropart. Phys.*, 24:116, 2005.
- [7] T. Huege, R. Ulrich, and R. Engel. (these proceedings).
- [8] T. Huege, R. Ulrich, and R. Engel. *Astropart. Physics*, 27:392–405, 2007.



Energy and composition sensitivity of geosynchrotron radio emission from EAS

T. HUEGE¹, R. ULRICH¹, R. ENGEL¹.

¹*Institut für Kernphysik, Forschungszentrum Karlsruhe, Postfach 3640, 76021 Karlsruhe, Germany*
 tim.huege@ik.fzk.de

Abstract: We analyse the sensitivity of geosynchrotron radio emission from inclined extensive air showers to the energy and mass of primary cosmic rays. We demonstrate that radio emission measurements at suitable lateral distances can infer both the number of electrons and positrons in the shower maximum and the atmospheric depth of the maximum on a shower-to-shower basis. Alternatively, measurements at a fixed lateral distance but in two different observing frequency bands yield comparable information. An RMS error of 5% in the determination of the number of electrons and positrons at shower maximum can be achieved. Through the determination of these quantities, geosynchrotron radiation provides access to the energy and mass of primary cosmic rays on a shower-to-shower basis.

Introduction

It is our current understanding that radio emission from extensive air showers is dominated by “geosynchrotron radiation” [3] emitted by secondary shower electrons and positrons being deflected in the earth’s magnetic field. The geosynchrotron model has by now been implemented in a sophisticated Monte Carlo code called REAS2 [5, 6], which itself relies on CORSIKA [1] for the simulation of the relevant extensive air shower (EAS) properties. In this article, we analyse the sensitivity of REAS2-simulated geosynchrotron radio emission on the primary cosmic ray energy and mass. The determination of these parameters on a shower-to-shower basis is one of the main goals of measuring radio emission from EAS, and we demonstrate that radio measurements of inclined showers indeed provide relatively direct access to these parameters.

Methodology

Results gathered so far point to inclined air showers with zenith angles above 45° as particularly promising targets for radio measurements of EAS [7]. Inclined air showers have a large radio “footprint” [4] and thus allow radio antennas to be spaced relatively far apart, an important prerequi-

site for the instrumentation of large effective areas at moderate cost. Concentrating on the energy range relevant to the Pierre Auger Observatory, we have thus performed an analysis of air showers with 60° and 45° zenith angles at primary particle energies of 10^{18} eV, 10^{19} eV and 10^{20} eV. For each of these zenith angles and energies, we have simulated 25 iron-induced and 25 proton-induced air showers. 25 gamma-induced air showers per zenith angle were simulated for 10^{18} eV and 10^{19} eV, but not for 10^{20} eV, where pre-showering in the geomagnetic field would have to be taken into account. The simulation chain consisted of a CORSIKA 6.502 run using the QGSJETII-03 and UrQMD1.3.1 interaction models, Argentinian magnetic field, fixed azimuth angle (showers coming from south), 10^{-6} optimised thinning, and an observer height 1400 m a.s.l. followed by a REAS2 simulation with antenna locations between 25 m and 925 m from the shower core (in ground-based coordinates); cf. also [5]. For each of the simulated radio events we then determined the peak amplitude of the electric field pulses filtered using idealised rectangle filters from 16 to 32 MHz, 32 to 64 MHz and 64 to 128 MHz, respectively. In the following, we discuss the 60° zenith angle case. The qualitative behaviour at 45° is completely analogue. Other shower azimuth angles do not change the qualitative behaviour either.

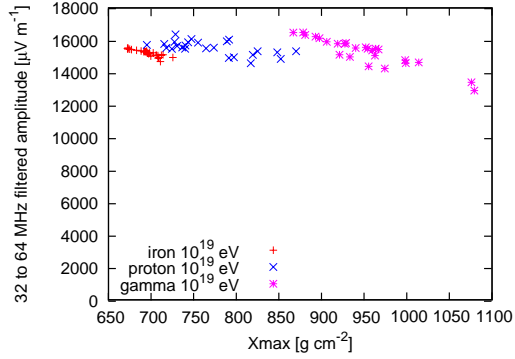


Figure 1: Peak radio field strengths of 10^{19} eV showers with 60° zenith angle as measured in the *flat region* 275 m north of the shower core.

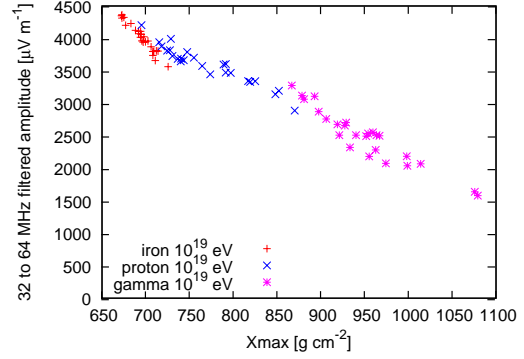


Figure 2: Peak radio field strengths of 10^{19} eV showers with 60° zenith angle as measured in the *steep region* 725 m north of the shower core.

Signal information content

The lateral slope of the radio signal is known to exhibit a dependence on the depth of the shower maximum (X_{\max}) and consequently, contains information on the primary particle energy and mass [4, 2]. To date, however, there had been no detailed investigation how this information content could be exploited in practice.

in analogy to the surface detector quantity $S(1000)$ of the Pierre Auger Observatory. This behaviour is illustrated for the 60° zenith angle case in Fig. 1: the electric field strength at 275 m north from the shower core is relatively constant regardless of primary particle type and shower X_{\max} . In contrast, at a distance of 725 m north as shown in Fig. 2, there is a clear dependence of signal strength on X_{\max} (hereafter called *steep region*).

A combination of measurements in these two regions can therefore differentiate between different types of primaries (Fig. 3).

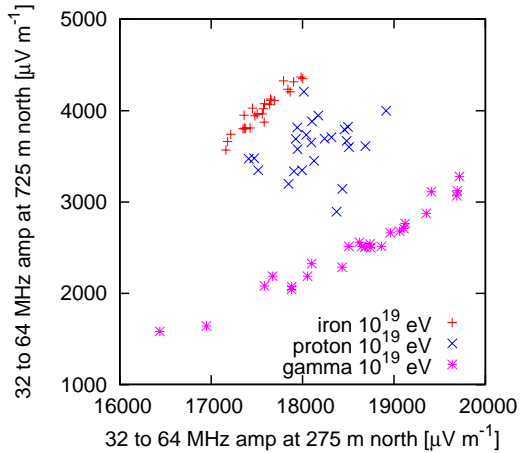


Figure 3: The ratio of field strengths in the *steep region* vs. the *flat region* of 10^{19} eV showers with 60° distinguishes between primary particle types.

The detailed analysis presented here reveals that for a given shower zenith angle, a suitable lateral distance exists where the radio signal is relatively independent of X_{\max} (hereafter called *flat region*),

Signal scaling with N_{\max}

When the measured radio field strength is divided by the number of electrons plus positrons in X_{\max} , hereafter called N_{\max} , it becomes clear that the radio signal scales linearly with N_{\max} . The reason for this is that most of the radio emission stems from the particles close to the shower maximum [5]. (The intensity of optical fluorescence light, in contrast, scales with the calorimetric energy deposited in the atmosphere by the shower.) The clean linear scaling is illustrated in Fig. 4, where the results from all energies and particle species yield an approximately constant electric field strength per N_{\max} in the *flat region*. The electric field strength per N_{\max} in the *steep region* is also constant over the different particle types and energies for a given X_{\max} .

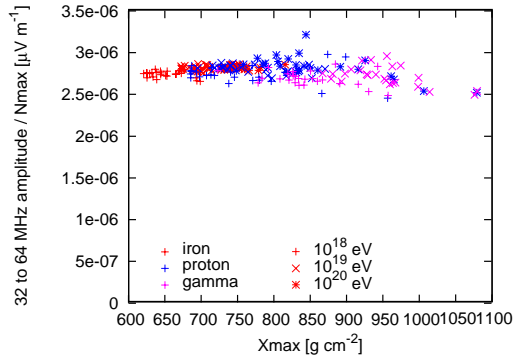


Figure 4: In the *flat region* at 275 m north, the radio pulse height per N_{\max} over all energies and particle types is approximately constant.

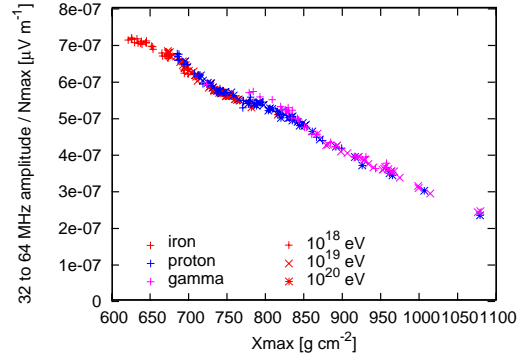


Figure 5: In the *steep region* at 725 m north, the radio pulse height per N_{\max} over all energies and particle types is constant for a given X_{\max} .

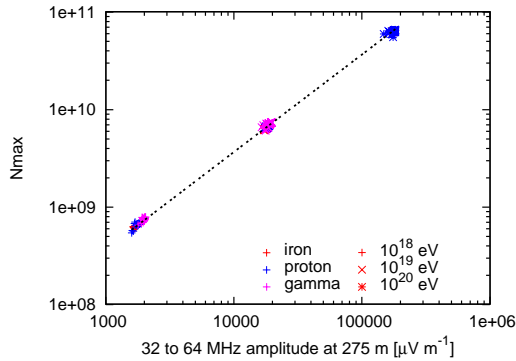


Figure 6: A measurement in the *flat region* at 275 m north directly yields the shower N_{\max} . The line denotes a linear functional dependence.

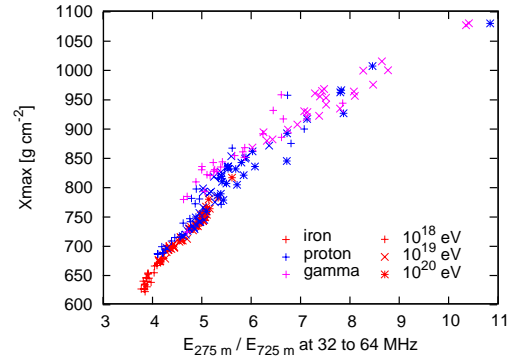


Figure 7: The ratio of peak field strengths in the *flat region* and *steep region* yields direct information on the shower X_{\max} .

Optimum parameter determination

Histogramming the distribution of electric field strengths per N_{\max} over all particle species and energies yields an RMS of only 5% in the *flat region* (Fig. 8). In spite of shower to shower fluctuations, radio measurements could thus determine the N_{\max} of individual EAS to very high precision. The position of the *flat region* for a given zenith angle is determined by the observing frequency band. As illustrated in Fig. 9, for 60° zenith angle and 32 to 64 MHz observing frequency, N_{\max} can be determined to highest precision around 275 m distance to the north (or south). At 16 to 32 MHz, 5% precision in the N_{\max} determination can be reached anywhere between around 200 m and 500 m from the core. Low frequencies are thus

particularly well suited for an energy determination of EAS primaries, if the technical difficulties involved with measurements at these frequencies can be overcome. In contrast, at 64 to 128 MHz the range for N_{\max} determination becomes much smaller and resides at smaller distances. (The peculiar steps in the 64 to 128 MHz RMS curve point to coherence effects starting to play a significant role at these high frequencies.) For the determination of X_{\max} using measurements in the *steep region*, a lateral distance should be chosen that shows a large RMS spread in electric field strength per N_{\max} . For 32 to 64 MHz and 60° zenith angle, 725 m constitutes a suitable compromise between a good handle on the X_{\max} value and detectable absolute signal levels. (The absolute signal strength drops quickly with lateral distance, cf. [4]).

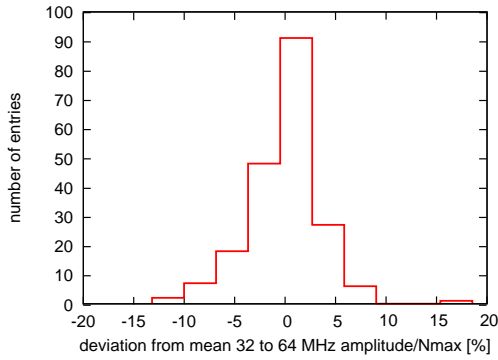


Figure 8: For 60° zenith angle showers, the RMS spread in peak field strength per N_{\max} in the *flat region* over all energies and particle types amounts to $\sim 5\%$. In principle, N_{\max} can thus be inferred with 5% uncertainty.

Conclusions

Simulations of geosynchrotron radio emission with the REAS2 Monte Carlo code reveal that information contained in the lateral profile of the radio signal can be exploited for a direct determination of N_{\max} and X_{\max} on a shower-to-shower basis. These quantities can in turn be related to the energy and mass of the primary cosmic ray particle.

For a given zenith angle and observing frequency band, distinct distance regimes denoted here as the *flat region* and the *steep region* can be identified. Measurements in the *flat region* directly yield the N_{\max} of the shower, with an RMS deviation of only 5%. A comparison of peak field strengths in the *steep region* and *flat region* for a given observing bandwidth provides a direct estimate of the shower X_{\max} . Alternatively, measurements at a fixed distance but in two different observing frequency bands provide comparable information.

The position of the *flat region* in case of 60° zenith angles for the observing frequency band from 32 to 64 MHz lies at approximately 275 m and would thus require an antenna spacing of that order. (The given number is valid for antenna positions along the shower axis; in the perpendicular direction the scales are smaller due to azimuthal asymmetries of the radio footprint.) If technical problems arising in measurements at lower frequencies such as 16 to 32 MHz can be overcome, antenna spacings of

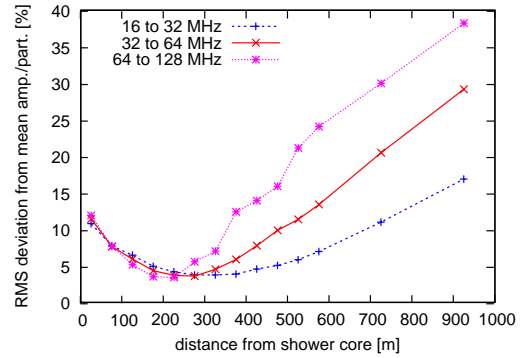


Figure 9: Determination of the RMS uncertainty in peak field strength per N_{\max} as a function of lateral (ground-coordinate) distance from the shower core. The *flat region* shifts to larger lateral distances at lower frequencies.

up to 500 m will allow measurements in the *flat region*. The qualitative behaviour at 45° zenith angle is analogue, yet at lower lateral distances. At larger zenith angles, the scales will be larger, but consistent simulations require the implementation of curved atmospheres for zenith angles much larger than 60° , which is currently being prepared.

References

- [1] D. Heck, J. Knapp, J. N. Capdevielle, G. Schatz, and T. Thouw. FZKA Report 6019, Forschungszentrum Karlsruhe, 1998.
- [2] T. Huege, W. D. Apel, A. F. Badea et al. In *Proc. of the 29th ICRC, Pune, India*, volume 7, page 107, 2005. astro-ph/0507026.
- [3] T. Huege and H. Falcke. *Astronomy & Astrophysics*, 412:19–34, December 2003.
- [4] T. Huege and H. Falcke. *Astropart. Phys.*, 24:116, 2005.
- [5] T. Huege, R. Ulrich, and R. Engel. *Astropart. Physics*, 27:392–405, 2007.
- [6] T. Huege, R. Ulrich, and R. Engel. In *Proceedings of the 30th ICRC, Merida, Mexico*, 2007. (these proceedings).
- [7] J. Petrovic, W. D. Apel, T. Asch, F. Badea et al. *Astronomy & Astrophysics*, 462:389–395, 2007.



Calculation of radio emission from high-energy air showers

N. N. KALMYKOV¹, A. A. KONSTANTINOV¹, R. ENGEL².

¹ *Scobel'syn Institute of Nuclear Physics, Moscow State University, Leninskie Gory 1, 119991 Moscow, Russia*

² *Institut für Kernphysik, Forschungszentrum Karlsruhe, 76021 Karlsruhe, Germany*

Ralph.Engel@ik.fzk.de

Abstract: Results of the simulation of radio signals from 10^{17} eV extensive air showers are reported. The simulations are based on a track-by-track electric field calculation using the EGSnrc Monte Carlo shower code. The lateral distribution of the predicted radio emission is compatible with the recent LOPES-10 experimental data at distances < 300 m. Perspectives of extending EAS radio emission calculations to the ultra-high energy range (up to 10^{20} eV) are also discussed.

Introduction

Radio emission accompanying extensive air showers (EAS) is considered as a promising alternative to traditional methods of high energy cosmic ray detection. Recently, first measurements from a new generation of radio antenna arrays, LOPES [1], which is co-located with the KASCADE air shower array [2], and CODALEMA [3], were published. The experimentally found, good correlation of the signal with the shower energy has also renewed the interest in theoretical predictions [1].

In general, there are two approaches of calculating the radio signal of an air shower.

The starting point of Askaryan's predictions in 1961 was the model of the motion of effective charges in EAS [4]. In [4] both electron excess and charge separation in the Earth's magnetic field were proposed as responsible for the EAS radio emission. In this picture a shower is considered as a continuous system of charges and currents. Evidently, the approach of calculating the radio emission for a system of charges and currents rather than individual particles has the potential of being numerically very efficient.

On the other hand, parametrizations of the overall charges and currents in EAS have not yet been developed. Therefore it is very useful to start with an approach that is based on following individual

particle trajectories using the Monte Carlo (MC) technique. In such an approach, shower properties can be included in the most accurate and simple way, which, however, requires very large computing time at primary energies above 10^{15} eV.

Using the MC approach, EAS radio emission has been theoretically investigated most intensively within the framework of the "geosynchrotron emission" model [5] proposed by Falcke and Gorham in 2003 [6]. In this model, it is assumed that the overall radio signal of air showers is dominated by the radio emission due to the deflection of particle trajectories in the magnetic field of the Earth. In the geosynchrotron model, simulations are performed in the time domain, i.e. the electric field contributions produced by shower particles are summed as function of the detection time [5, 7]. The refractive index of air is taken as unity.

In this paper, we follow a more general approach that does not explicitly distinguish between the geosynchrotron or Cherenkov radio signal. We calculate the radio signal of each shower particle in Fourier space (frequency domain). Signal contributions due to start and end points of particle trajectories and localized momentum changes in Coulomb scattering and bremsstrahlung are included as well as the continuous deflection in the Earth's magnetic field. The refractive index of air is naturally accounted for in the simulation.

Electric field calculation

In the EAS case, particle trajectories are mainly governed by elementary interactions with air and also the deflection of the particles in the Earth's magnetic field. The problem then is to calculate the radiation from a charged particle having a trajectory which cannot be described by an analytic function. An important constraint is that the sum over all particles should result in an expression similar to that of the continuous charges and currents approach.

As MC simulation is a linear procedure employing a "straight-step-by-straight-step" particle transportation, it is natural to calculate the electric field from a charged particle by considering the trajectory as a sum of many leaps of the velocity $\vec{\beta} = \vec{u}/c$:

$$\vec{E}_\omega(\Sigma_N) = \underbrace{\vec{E}_\omega(\vec{0} \rightarrow \vec{\beta}_1)}_{\text{birth of the particle}} + \dots + \underbrace{\vec{E}_\omega(\vec{\beta}_s \rightarrow \vec{\beta}_{s+1})}_{\text{deflection of the particle}} + \dots + \underbrace{\vec{E}_\omega(\vec{\beta}_N \rightarrow \vec{0})}_{\text{death of the particle}}. \quad (1)$$

Here N is the total number of adjoining individual trajectory segments at which the velocities $\vec{\beta}_s$ are being constant vectors, Fig.1. Internal terms in the series (1) may describe both discrete interactions of charged particles in air (including multiple Coulomb scattering and secondary particle creation below the simulation threshold) and their "smooth" deflection in the Earth's magnetic or electric fields.

In the case of discrete interactions, the electric field can be estimated within classical radiation theory rather than quantum theory due to $\omega\Delta t \ll 1$, where ω is the observation frequency and Δt is the time of interaction.

In the framework of the Fraunhofer approximation, the Fourier-component \vec{E}_ω of the electric field at a given frequency $\omega = 2\pi\nu$ produced by a sudden leap $\vec{\beta}_s \rightarrow \vec{\beta}_{s+1}$ of an electron velocity at the time moment $t_0^{(s+1)}$ is given by

$$\vec{E}_\omega(\vec{\beta}_s \rightarrow \vec{\beta}_{s+1}) = \frac{e}{8\pi^2\epsilon_0 c} \frac{e^{ikR_s}}{R_s} e^{i\omega(t_0^{(s+1)} - n\vec{e}_{R_s} \cdot \vec{\xi}_0^{(s+1)}/c)} \times$$

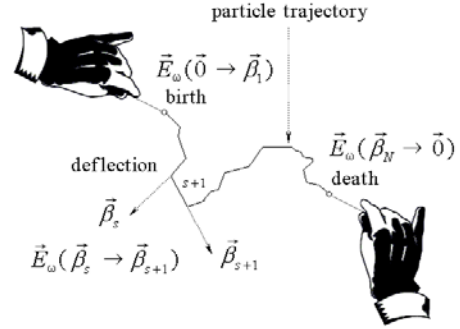


Figure 1: Illustration of the individual trajectory contributions considered in the calculation.

$$\times \left(\frac{\vec{\beta}_{s\perp}}{1 - n\vec{e}_{R_s} \cdot \vec{\beta}_s} - \frac{\vec{\beta}_{s+1\perp}}{1 - n\vec{e}_{R_s} \cdot \vec{\beta}_{s+1}} \right). \quad (2)$$

Here ϵ_0 is the permittivity of vacuum, c is the light speed in vacuum, $k = n\omega/c$, n is the refractive index of air, R is the distance between electron location and the observation point, \vec{e}_R is the unit vector in the direction of observation, $\vec{\xi}_0$ is the radius-vector of electron at the time t_0 and $\vec{\beta}_\perp$ is the transverse component of $\vec{\beta}$ with respect to \vec{e}_R .

In comparison, in the geosynchrotron model only the terms in the series (1) which are due to the particle deflections in the Earth's magnetic field are taken into account.

Modelling

Calculations of the EAS radio emission are carried out in the "particle-by-particle" manner in a special program written for this purpose. A photon is used as primary particle and MC shower modelling is performed just for the electromagnetic part of the shower using the EGSnrc code [9]. The density and optical properties of the Earth's atmosphere are taken to be uniform within slices of 9.5 g/cm^2 . The strength and declination of the Earth's magnetic field correspond to those for the LOPES experiment. The radiation field is calculated via (2) for all particle energies above the threshold 100 keV. The upper limit on step size of particle straight transport is equal to 1 m.

A straight-forward MC simulation of the full shower development is limited to energies up to

$\simeq 10^{15}$ eV. The situation may be improved by applying the “thinning” method [10], which is characterized by the parameter $\varepsilon_{th} = E_{th}/E_0$, where E_{th} is the energy at which the thinning process is started, E_0 is the energy of primary particle. The influence of thinning on the radio emission calculation quality has been studied in the $10^{12} - 10^{14}$ eV range. Unfortunately, the general conclusion is that thinning does not allow to increase the primary energy as much as would be needed to simulate showers at ultra-high energy. Namely, at the LOPES frequency range (40-80 MHz), the acceptable level ε_{th} reduces computing time by a factor of only 10-20 for a range of observation distances up to 200-300 m from a shower axis. The reason is that for radio emission the low energy particles (having energies much less than the critical energy of 81 MeV) are extremely important.

Results

In Fig.2 the longitudinal profile of one 10^{17} eV photon-initiated vertical shower is presented. The initial photon was injected at 30 km above the sea level. The simulated profile is similar to the average cascade curve at 10^{17} eV. Therefore it is reasonable to assume that the given shower is representative for a comparison of the predicted radio emission with experimental data at energies of about 10^{17} eV that is averaged over many showers. The comparison with LOPES-10 experimental data is plotted on Fig.3, where the simulated radio emission has been averaged over north, south, west and east directions. A correlation of radio signals with distance is found for the group of events selected out of 5 months of LOPES-10 measurements [8]. All selected showers have energies in the range $E_0 \simeq 5 \cdot 10^{16} - 6 \cdot 10^{17}$ eV and zenith angles $< 50^\circ$.

In the comparison, it has been taken into account that experimentally measured and theoretically calculated field strengths are not absolutely identical. In the simulation, the Fourier-component at a given frequency (2) is calculated, whereas in the experiment a field strength over the frequency range from 40 up to 80 MHz is measured. Such uncertainty introduces some fudge factor A , that does not influence essentially on the functional form

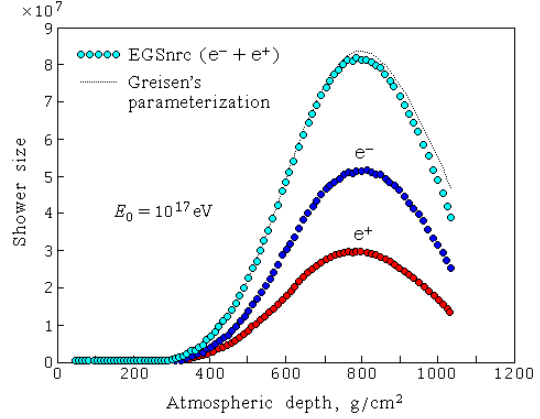


Figure 2: Number of charged particles of a 10^{17} eV photon-initiated vertical shower as a function of atmospheric depth. Thinning level $\varepsilon_{th} = 2 \cdot 10^{-7}$ or $E_{th} = 20$ GeV. The model results are compared to Greisen's parameterization for a radiation length of 36.8 g/cm^2 and an critical energy of 81 MeV.

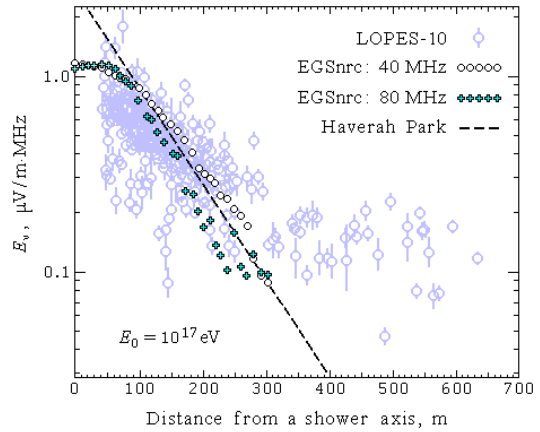


Figure 3: Lateral distribution of EAS radio emission. Results of the present work (EGSnrc), LOPES-10 experimental data [8] and Haverah Park experimental data approximation, taken from the same report [8], are compared.

of the lateral dependence of radio emission. In fact, we obtain that in the observed bandwidth of the LOPES experiment the field strength does not change substantially at the distances less than 300 m. On Fig.3 $A = 1$ has been adopted, but this value may have to be changed once the absolute calibration of the LOPES antennas is known.

It is seen that the calculated radio emission reproduces the experimentally found dependence on the lateral distance rather well. The deviation at larger lateral distances beyond 300 m is not unexpected. It is related to the detection threshold of the LOPES-10 array, since only showers with a detected radio signal were included in the LOPES data analysis. At large lateral distance, the detection probability falls below unity and showers without detected radio signal have to be included to allow a comparison with our calculation.

The parameterization of the data obtained with the old Haverah Park radio experiment [11] is also shown in the same figure. The presented approximation was fitted for the range $E_0 \simeq 10^{17} - 10^{18}$ of EAS with zenith angles $< 35^\circ$ [11] (the curve has been taken from [8]). The Haverah Park approximation (fitted for 55 MHz) corresponds to the field calculated at the range 100-300 m. Results differ significantly only for $R < 100$ m, where the exponential fit $\sim \exp(-R/(110 \text{ m}))$ seems not to be valid. Note that there is considerable uncertainty regarding the absolute calibration of the pioneering radio measurements of the 60ies and 70ies.

Conclusions

Calculation of radio emission from an air shower with $E_0 = 10^{17}$ eV has been performed. The lateral distribution of simulated radio signals is compatible with the recent LOPES-10 experimental data [8] and the old Haverah Park data [11].

The presented calculation should be considered just as a demonstration since 1 month and 50 processors have been required for its realization. At present time the real limit of the straight-forward MC simulation of EAS radio emission is $10^{15} - 10^{16}$ eV.

Our present hopes of calculating EAS radio emission at ultra-high energy are based on some specific features of the radio emission. It has been

mentioned that only two pure collective effects in the EAS development initiate their radio emission: an electron excess and a geomagnetic polarization. Thus, a full “particle-by-particle” shower modeling is something that is too detailed for efficient radio emission calculations.

The energy of the simulations could be considerably increased within the framework of the EAS macroscopic consideration, in which the shower is treated as a system of the electric moments and currents (due to an excess of electrons and systematic charge separating in the Earth’s magnetic field). Still MC simulations will be needed for calculating the overall shower properties and generating realistic shower-to-shower fluctuations.

Acknowledgments

A.A.K. would like to thank Dr. W.D. Apel for the support and advice he got while working on the KASCADE cluster. This work was supported by INTAS (grant 05-109-5459).

References

- [1] H. Falcke *et al.*, LOPES Collab., Nature 435, 313, 2005.
- [2] T. Antoni *et al.*, KASCADE Collab., NIM A513, 490, 2003.
- [3] D. Ardouin *et al.*, CODALEMA Collab., Astropart. Phys. 26, 341, 2006.
- [4] G. A. Askaryan, Sov. Phys. JETP. 41, 616 (1961).
- [5] T. Huege, H. Falcke, Astropart. Phys. 430, p. 779, 2005.
- [6] H. Falcke, P. W. Gorham, Astropart. Phys. 19, p. 477, 2003.
- [7] T. Huege, R. Ulrich, R. Engel, Astropart. Phys. 27, 392, 2007.
- [8] W. D. Apel *et al.*, LOPES Collab., Astropart. Phys. 26, 332, 2006.
- [9] <http://www.irs.inms.nrc.ca/EGSnrc/pirs701> .
- [10] A. M. Hillas, Proc. 17th Int. Cosmic Ray Conf. Paris. 8, p. 193, 1981.
- [11] H. R. Allan, Progress in elementary particle and cosmic ray physics. 10, p. 171, 1971.



Radio Detection of Neutrinos from Behind a Mountain

O. BRUSOVA¹, L. ANCHORDOQUI², T. HUEGE³, K. MARTENS¹.

¹*University of Utah, Department of Physics, 115S 1400E, Salt Lake City, UT 84112, USA*

²*Department of Physics, University of Wisconsin-Milwaukee, P.O. Box 413, Milwaukee, WI 53201, USA*

³*Institut für Kernphysik, Forschungszentrum Karlsruhe, Postfach 3640, 76021 Karlsruhe, Germany*

brusovao@physics.utah.edu

Abstract: We explore the sensitivity of a neutrino detector employing strongly directional high gain radio antennae to detect the conversion of neutrinos above 10^{16} eV in a mountain or the earth crust. The directionality of the antennae will allow both, the low threshold and the suppression of background. This technology would have the advantage that it does not require a suitable atmosphere as optical detectors do and could therefore be deployed at any promising place on the planet. In particular one could choose suitable topographies at latitudes that are matched to promising source candidates.

Introduction

Identifying the sources of the highest energy Cosmic Rays (CR) is a fundamental and unsolved problem in astroparticle physics. If they are accelerated in astrophysical objects, high energy neutrino emission should be associated with this acceleration [1]. Since these neutrinos would neither interact with intergalactic or interstellar media nor be deflected by magnetic fields, neutrino astronomy carries the hope of identifying these elusive sources of highest energy CRs.

Various detectors have been proposed for neutrino energies above 10^{16} eV, most of them relying on mountains to provide suitable target mass for ν_τ with the ensuing τ lepton decay providing a detectable air shower (AS) after the τ leaves the target [2]. As high energy neutrinos get absorbed in the earth, geometries for such events are restricted to within a few degrees of horizontal [3]. At energies above 10^{19} eV the τ decay length in vacuum exceeds 500 km, increasingly putting these decays out of the reach of detectors.

Optical detectors exploiting the fluorescence emission of horizontal showers as well scintillator telescopes have been proposed to measure the promising ν_τ signature [4]. Here we explore what could be a simpler and cheaper technology in the field:

Strongly directional (high gain, low threshold) radio antennas. All they require is a rigid mechanical support structure and like all the other detectors some electronics. But no optical components have to be calibrated and maintained, and the detector could be made largely insensitive to the local climate at a promising detector site. The challenge for our detector will lie in isolating the signal.

Geosynchrotron radio signals

AS produce geosynchrotron radio emission due to the deflection of secondary shower electrons and positrons in the earth's magnetic field [5]. In this study for the first time such radio signals are studied from horizontal showers. Using the REAS2 Monte Carlo code [6] we calculate the radio emission from 10^{15} eV and 10^{16} eV horizontal, π^+ induced AS propagating through a constant density atmosphere of 1.058×10^{-3} g cm⁻³, corresponding to approximately 1500 m above sea level. The magnetic field was set to a strength of 0.4 Gauss with an inclination of 60° , a conservative estimate for Central Europe and Northern America. The AS were simulated as propagating from north to south; the corresponding geomagnetic angle is thus 60° . This is the most conservative choice, as it effectively minimizes the field component perpendicular

lar to the propagation direction of the AS. Atmospheric curvature can be neglected here, as the AS need only a few kilometers to develop in the lower atmosphere. The AS simulations were carried out using CORSIKA 6.502 [7], with shower-to-shower fluctuations taken out by simulating 25 air showers per parameter set and then selecting a shower with a typical longitudinal evolution profile for the radio simulations.

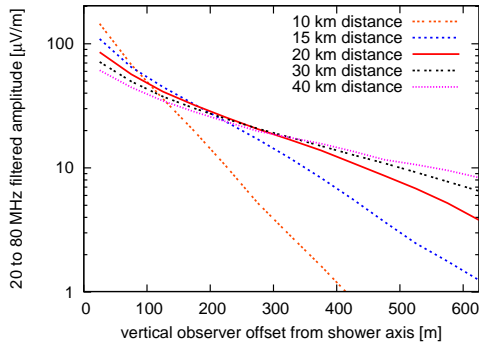


Figure 1: Lateral dependence of geosynchrotron radio emission field strengths of 10^{16} eV horizontal air showers for different observer distances from the τ decay point. 10^{15} eV values are lower by approximately a factor of 10.

One important question is which observer distance is suited best for radio observations of these horizontal AS. Figure 1 illustrates how the lateral profile of the radio signal spreads out as the distance from the starting point of the AS increases. Despite strong relativistic beaming of geosynchrotron radiation, the lateral slope changes significantly with the distance of the observer from the τ decay point. An observing distance of 20 km seems to constitute a good compromise: the signal in the center region is still strong while its lateral spread does not require too dense an array of antennae.

Also important is the selection of a suitable observation frequency band. This clearly depends on the actual noise situation at the selected observing site. In the absence of man-made radio interference, atmospheric and galactic noise set the limits. In Fig. 2 we show what signal-to-noise ratios (SNR, defined as peak power of the signal divided by power of the noise in the band of interest) can be expected for 10^{16} eV AS at 20 km observing distance and 225 m vertical observer off-

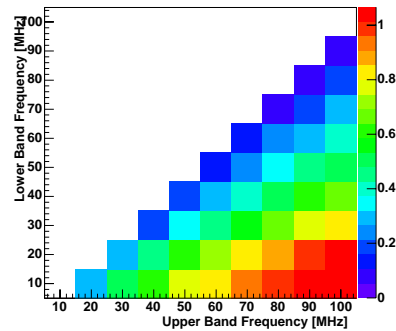


Figure 2: Expected SNR as a function of observing frequency band for 10^{16} eV showers initiated at 20 km distance and 225 m vertical observer offset from the shower axis, calculated for an isotropic radiator. 10^{15} eV values are lower by approximately a factor of 100.

set from the shower axis. The values are calculated for an isotropic radiator and a combination of day-time atmospheric noise and galactic noise based on measurements by the CCIR/ITU-R (International Telecommunication Union). As geosynchrotron emission has a steeply falling frequency spectrum, it is important to include low frequencies. As can be seen in Fig. 2 an observing bandwidth from 20 to 80 MHz would be desirable. Below 20 MHz, atmospheric noise gets very strong, and above 80 MHz FM radio transmitters could pose problems.

SNR of order unity are too low for self-triggered measurements of geosynchrotron radiation. Using directional antennae pointing at the target mass will significantly improve the SNR. For the envisioned broad-band measurements, logarithmic-periodic dipole antennae (LPDAs) can achieve antenna gains of 10 dBi. If three such antennae are phase coupled, effective gains of up to 16 dBi can be reached. This boosts the SNR into a region where measurements seem feasible up to axis offsets of ~ 300 m, as illustrated in Fig. 3.

For the specific relative geometry of AS and magnetic field explored here the lateral distribution of the radio signal is very different along the horizontal and the vertical axis. As multiple measurements along the vertical also allow to place additional constraints on the zenith angle of the

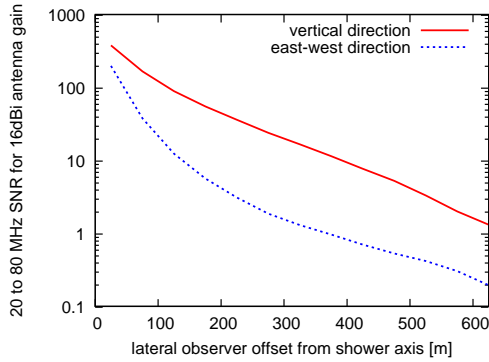


Figure 3: Expected SNR as a function of observing frequency band for 10^{16} eV showers at 20 km distance, calculated for an antenna with 16 dBi antenna gain. 10^{15} eV values are lower by approximately a factor of 100.

observed shower and as the signal falls off more slowly along the vertical axis, more than one antenna should be used along the vertical direction.

The SNR required for self-triggered operation of an antenna array depends on many factors such as the multiplicity of antennae used in coincidence and the required detection efficiencies. These issues would have to be addressed in a specific proposal for such a detector.

Neutrino event rates

A threshold close to 10^{16} eV for horizontal AS is well matched to the effective threshold beyond which τ leptons can escape from significant depth inside a rock mass: at 10^{15} eV the decay length of a τ (in vacuum) is only ~ 50 m. At 10^{17} eV this decay length will have grown to 5 km, which allows for τ from a reasonable amount of target mass to escape the rock before they decay, and on the other hand constrains the decay volume needed behind the rock to be reasonably small.

Using a modified ANIS [8] code we examine the probability that a ν_τ interacts in rock with the ensuing τ decay initiating an AS outside of the rock. In ANIS we use the option of CTEQ5 deduced cross-sections. A smooth approximation for the energy loss of the τ leptons in rock and air is included in the calculation. Depending on the energy of the incoming ν_τ , an equilibrium is reached at some point

inside the rock between ν_τ interactions producing new τ leptons and the decay of τ leptons that were produced in neutrino interactions further upstream. Our simulations show that for standard rock this equilibrium is reached after 1 km at 10^{15} eV, 2 km at 10^{16} eV, and 10 km at 10^{17} eV.

25 M ν_τ were injected at each of the energies mentioned above. From the above simulations of radio signals we infer an effective threshold of 8×10^{15} eV for AS detection to estimate how many neutrinos we might detect. Fig. 4 shows the distributions of decay vertices above that energy from the 10^{16} eV and 10^{17} eV simulations.

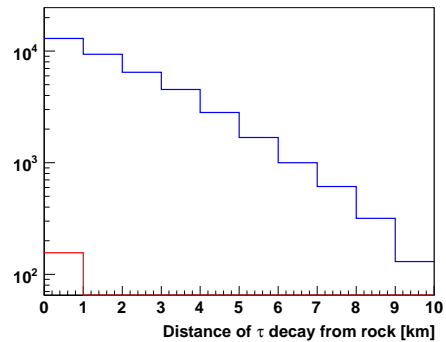


Figure 4: Distribution of decay vertices that result in showers with an energy above 8×10^{15} eV. The blue histogram is for a ν_τ energy of 10^{17} eV, the red one for 10^{16} eV.

Within the first 10 km after the mountain we see less than 200 decays for the lower ν_τ energy and about 40,000 for the higher one. At higher energies efficiency will be affected by τ decaying behind the detector “volume”. The detection efficiency for 10^{17} eV ν_τ is $\epsilon = 0.0016$. A detector element of two stations separated vertically by 200 m would allow to collect data over a vertical range of 400 m. Working with a 200m horizontal displacement between such detector elements one would hope to have a decent efficiency for threefold coincidences over an area of roughly $160,000 \text{ m}^2$ for two such elements, and each vertical expansion of the array by one additional element would add roughly $80,000 \text{ m}^2$. The exposure of an eight antenna array accumulated over one year would be $31,536,000 \text{ s} \times 320,000 \text{ m}^2 \approx 10^{17} \text{ cm}^2 \text{ s}$ for a pointlike source. As the LDPAs typically have

an opening angle of 65° , detectors situated 30 km from a 1.5 km high mountain range would cover a solid angle of 5.7×10^{-2} sr.

A source would only be seen if it is behind a target mass at the local horizon of the detector. The time any given source spends near the horizon depends on its declination. Figure 5 summarizes the total observation times that can be expected if the source can be followed within $\pm 1.5^\circ$ of the horizon and gives the azimuthal coverage required to follow the source along that segment of its path. If a source were to just rise or set vertically through a $\pm 1.5^\circ$ detector aperture, it would be visible for less than 1% of the total time. If the location was chosen to accommodate the requisite azimuthal coverage shown in Fig. 5, then one would expect to “see” the source about 15% of total time for a latitude of 45° . The proposed antennae will cover the requisite 30° in azimuth. Putting all this together, if we can measure ν_τ between 10^{16} eV and 10^{17} eV, with the efficiencies estimated above and linearly interpolated between the two energies, it would take an array of a little more than 130k antennae to observe one event per year from Galactic sources [9].

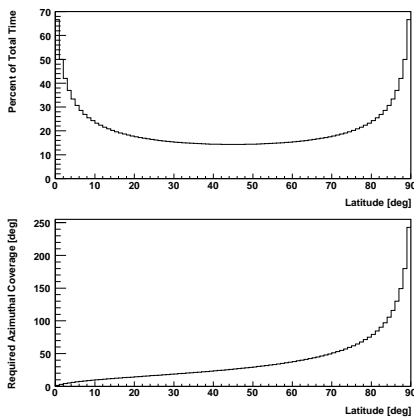


Figure 5: Upper panel: Percent of total time spent in a $\pm 1.5^\circ$ band around the horizon if the upper or lower culmination point is arranged to be 1.5° above or below the horizon. Lower panel: total number of degrees that have to be covered in azimuth in order to attain that maximal time.

To give an example of the sensitivity reach to the diffuse neutrino flux we consider, $\phi_{\nu_\tau} \simeq 10^{-3} (E_\nu/\text{GeV})^{-2.54} \text{ GeV}^{-1} \text{ cm}^{-2} \text{ s}^{-1} \text{ sr}^{-1}$,

which is expected if extragalactic cosmic rays (from transparent sources) begin dominating the observed spectrum at energies as low as $\sim 10^{17.6}$ eV [10], as suggested by recent HiRes data [11]. For such a ν_τ -flux, the expected number of events (with $E_\nu > 10^{17}$ eV) per year per eight antennae is about 0.003.

Conclusions

The energy range at which the detector works is well matched to the problem of ν_τ detection through τ decay in the atmosphere. 300 antennae is quite an undertaking for 1 event per year. Efforts are underway to better estimate the detector response around 10^{16} eV.

Acknowledgements

We thank O. Kroemer for very useful discussions.

References

- [1] F. Halzen and D. Hooper, Rept. Prog. Phys. **65**, 1025 (2002).
- [2] D. Fargion, Astrophys. J. **570**, 909 (2002).
- [3] K. Martens for the HiRes Collaboration, in these Proceedings (2007).
- [4] Z. Cao *et al.*, J. Phys. G **31**, 571 (2005); M. Iori *et al.*, arXiv:astro-ph/0602108.
- [5] T. Huege and H. Falcke, Astron. Astrophys. **412**, 19 (2003).
- [6] T. Huege, R. Ulrich and R. Engel, Astropart. Phys. **27**, 392 (2007).
- [7] D. Heck, J. Knapp, J. N. Capdevielle, G. Schatz, and T. Thouw. FZKA Report 6019, Forschungszentrum Karlsruhe, 1998.
- [8] A. Gazizov and M. P. Kowalski, Comput. Phys. Commun. **172**, 203 (2005).
- [9] M. D. Kistler and J. F. Beacom, Phys. Rev. D **74**, 063007 (2006).
- [10] M. Ahlers *et al.*, and T. J. Weiler, Phys. Rev. D **72**, 023001 (2005).
- [11] R. U. Abbasi *et al.* [HiRes Collaboration], Phys. Rev. Lett. **92**, 151101 (2004).



The LOFAR air shower front evolution library

S. LAFEBRE¹, T. HUEGE², H. FALCKE^{1,3}, J. KUIJPERS¹

¹*Institute for Mathematics, Astrophysics and Particle Physics, Radboud University, P.O. box 9010, 6500 GL Nijmegen, the Netherlands*

²*Institut für Kernphysik, Forschungszentrum Karlsruhe, P.O. box 3640, 76021 Karlsruhe, Germany*

³*ASTRON, P.O. box 2, 7990 AA Dwingeloo, the Netherlands*

s.lafebre@astro.ru.nl

Abstract: The LOFAR radio telescope, under construction in the Netherlands, is an excellent test case for the detection of extensive air showers through their radio signal. In order to fully understand the properties of these signals, we are building a library of CORSIKA simulations over a wide range of energies on the LOFAR BlueGene supercomputer. This library contains particle data throughout the atmosphere, as opposed to the lowest detection level only. The REAS2 code is used to calculate geosynchrotron radio emission from these simulations. We present parametrisations of various characteristics of the particles from showers in this library.

Introduction

Recently, the development of digital radio telescopes such as LOFAR [2] has initiated a wave of renewed interest in the coherent radio emission from cosmic ray air showers [1]. In order to better understand the radiation mechanism and its implications, a series of air shower simulations is being carried out, which produce histogrammed particle data suitable for simulations using the REAS2 code. The CORSIKA [5] based radio emission simulations employ a realistic description of the air shower properties on a shower to shower basis [7] and we intend to pursue this approach further by using a shower simulation library in support of the high energy cosmic ray programme with the LOFAR telescope.

Unfortunately, using existing air shower libraries is not an option: these commonly only consist of distributions of particles on the lowest observation level – usually the Earth's surface. Such libraries are not suited for radio emission simulations, however, since according to our current understanding this radiation is caused by geomagnetic deflection of secondary shower electrons and positrons [6]. Here, we summarise our efforts building our *air*

shower front evolution library, and present first results obtained from this library.

Setup

The calculation of synchrotron emission from air showers is not built into CORSIKA: an additional code, REAS2 [7] needs to be run on the particle distributions, which determines the radio footprint on the ground. To this end we use the same interface code as in [7], which outputs two three-dimensional histograms for electrons and positrons for 50 observation levels at equidistant atmospheric slant depths. For each level, these histograms contain 1) particle energy vs. particle arrival time vs. lateral particle distance from the shower core; and 2) particle energy vs. angle of momentum to the shower axis vs. angle of momentum to the (radial) outward direction.

An overview of the simulations we are carrying out is given in table 1. We use photons, protons and iron as primaries, with energies ranging from 10^{16} to $10^{20.5}$ eV (set by an optimistic estimate of the LOFAR detection limits) for six zenith angles $\cos\theta = 1, 0.9, \dots, 0.5$. The azimuthal angle is constant, as the effect on the particle dis-

Table 1: The number of shower simulations per primary particle energy. Every run is repeated six times, for zenith angles of $\cos\theta = 1.0, 0.9, \dots, 0.5$.

| $\log E/\text{eV}$ | Number of runs | | | Total |
|--------------------|----------------|-------|------|-------|
| | γ | p | Fe | |
| 16.0 | 100 | 190 | 40 | 330 |
| 16.5 | 100 | 190 | 40 | 330 |
| 17.0 | 100 | 190 | 40 | 330 |
| 17.5 | 156 | 190 | 40 | 386 |
| 18.0 | 225 | 190 | 40 | 455 |
| 18.5 | 325 | 190 | 40 | 555 |
| 19.0 | 450 | 190 | 40 | 680 |
| 19.5 | 450 | 190 | 40 | 680 |
| 20.0 | 56 | 190 | 40 | 286 |
| 20.5 | 125 | 190 | 40 | 355 |
| Total per θ | 2087 | 1900 | 400 | 4387 |
| Total | 12522 | 11400 | 2400 | 26322 |

tributions is assumed to be of minor importance because of the azimuthal symmetry of the created histograms; the angle can be set to different values in the radio code, without the need to rerun a shower simulation. We use 10^{-6} level thinning width adaptive weight limitation [8] to obtain a sufficiently high resolution in the particle distributions. The interaction models used are QGSJetII 03 and UrQMD 1.3.1 for high and low energy interactions, respectively.

In order to finish these $\sim 26\,000$ simulations within a reasonable time, we use a parallel supercomputer, *Stella* (Supercomputer Technology for Linked LOFAR Applications). This BlueGene/L machine consists of roughly 12 000 nodes. Some of the code had to be rewritten in order to run CORSIKA on this parallel architecture. To test the validity and reliability of the results obtained with this modified code, we ran a test batch of 1000 showers of 10^{16} eV protons with vertical incidence, both using the parallel version and standard CORSIKA on two different architectures: adding a third, independent architecture allowed us to get an unbiased idea of the differences to be expected. We then performed some statistical tests on the results to check validity.

One such test considered the longitudinal development of the showers. The sum of electrons and

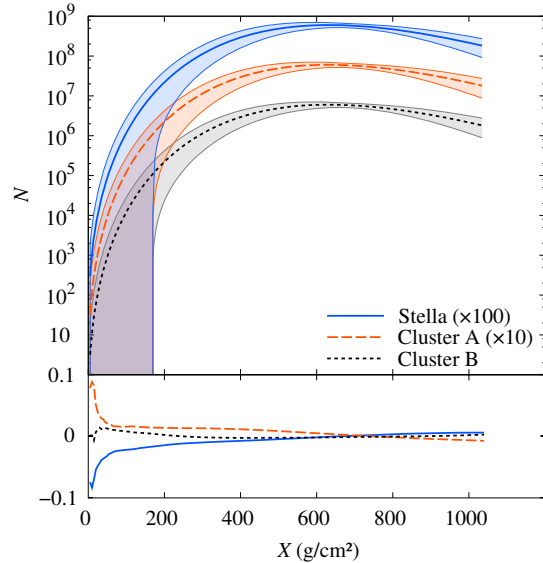


Figure 1: Averaged longitudinal profile of the sum of electrons and positrons for 1000 vertical proton-induced showers of 10^{16} eV, for *Stella* and two other architectures (labelled A and B). The coloured areas mark 1σ statistical errors. The lower panel shows the relative difference of each longitudinal profile compared to the other two.

positrons in the evolution of the shower N as a function of atmospheric depth X was averaged for all 1000 showers for each architecture's sample. The averaged longitudinal shower evolutions obtained in this manner are shown in the top panel in figure 1. The bottom panel of this figure shows the deviation of each distribution from the other two. The relatively large deviations for very low depths can be attributed to low number statistics, as the number of particles in the shower at these depths is no more than a few hundred. This is also reflected in the coloroued areas in the figure, which indicate 1σ statistical error levels from 1000 runs. It is clear that the deviations between architectures lie well within this area. Comparisons of other quantities, such as lateral and energy distributions, were also carried out. In none of these we could find any significant difference in the quantities involved or the statistical spread in them. We therefore conclude that our parallel code produces valid air shower simulations.

Results

The test sample of 3×1000 showers we obtained for validating our output can be used for an analysis of vertical air showers from protons at 10^{16} eV, given the large number of simulations we carried out for one single configuration. One of the air shower properties we investigated is the longitudinal profile $N(X)$.

A popular parametrisations to describe the longitudinal evolution of air showers was suggested by Greisen [4] and Gaisser & Hillas [3]. We can generalise both, however, to read

$$N_L(X) = N_{\max} \exp \left[\frac{\lambda}{X_{\max}} \left(\ln \frac{X}{X_{\max}} - \sum_{i=1}^n \epsilon_i \left(1 - \frac{X}{X_{\max}} \right)^i \right) \right], \quad (1)$$

where, in the case of 10^{16} eV proton showers, $\lambda \simeq 45 \pm 7$ g/cm² is a characteristic length parameter, $X_{\max} \simeq 6.4 \pm 0.8 \cdot 10^2$ g/cm² is the atmospheric depth at which the number of electrons and positrons $N(X)$ peaks, and $N_{\max} \simeq 6.5 \pm 0.5 \cdot 10^6$ is the number of particles at this depth. We determined optimal values for ϵ_i from the average of $N(X)$ in our sample of simulations, setting $i \leq 6$: using terms of even higher order does not decrease the variance reduction significantly anymore. The values we obtained are

$$\epsilon_i = [1.000, -0.013, 0.005, 0.053, 0.181, 0.207], \quad (2)$$

which is very close to the Gaisser–Hillas parametrisation, $\epsilon_i = [1, 0, 0, \dots]$. Using this parametrisation, $N(X)$ fits slightly better, even for *individual* showers, than either the Greisen or Gaisser–Hillas parametrisations. Note that this analysis was based on averaging in X : averaging of the shower age s might change these results.

Since the showers in our library contain histograms of particle distributions over the entire evolution of the shower, we can produce multidimensional representations of particle densities. As an example of such a representation, figure 2 shows the particle density $n = dN/dr^2$ as a function of X and the distance from the shower axis r . As expected, most of the particles in a 10^{16} eV shower exist in a

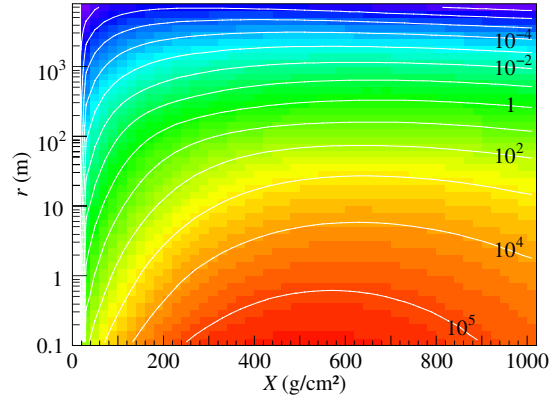


Figure 2: Two-dimensional structure of the average particle density n as a function of atmospheric depth X and distance from the shower axis r . The color scale and white contour lines represent particle densities in particles per m². Contour lines are spaced logarithmically at factors of ten.

narrow cylinder around the shower axis with a radius of a few meters. It is interesting to note that the maximum particle density is reached at different depths for different distances; also note that the reduction rate of the density with X varies with r .

A quantity that may influence the radio footprint of an air shower is the net charge of the shower. Air showers tend to develop a net negative charge as they evolve, through positrons interacting with atmospheric electrons. As this charge excess moves through the atmosphere at superluminal velocity, it gives rise to Čerenkov radiation in the radio domain. Currently, the relative role of this effect is uncertain. Looking into the charge excess may allow us to determine the relative importance of the effects compared to that of coherent synchrotron emission, which is thought to be dominant.

The charge excess q of electrons over photons as a function of shower depth X is defined as the ratio:

$$q(X) = \frac{n_{e^-}(X) - n_{e^+}(X)}{n_{e^-}(X) + n_{e^+}(X)}. \quad (3)$$

Figure 3 shows the relative average charge excess q as a function of X and r . Note the feature in the top right of this figure; its origin is unclear, but it is probably strongly correlated with the cutoff energy used (400 keV in these simulations): further study is required here. Contrary to the relative excess, the

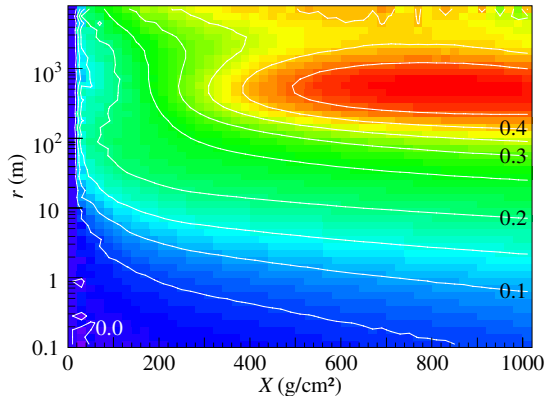


Figure 3: Two-dimensional structure of the average charge excess ratio q , as a function of atmospheric depth X and distance from the shower axis r . The color scale and white contour lines represent fractional charge excess value. Contour lines are spaced at intervals of 0.05.

absolute charge excess has much the same structure as the overall spatial structure of the air shower from figure 2, so that the largest absolute charge excess values are found near the shower core. Furthermore it should be noted that, because the particle distributions are folded over the azimuthal angle, any local excess due to charge separation from deflection in the Earth’s magnetic field is cancelled out. At this moment, the question whether the *local* charge excess due to this separation effect plays a larger role than the *overall* excess charge in the air shower is still open, as the average separation of positron-electron pairs is expected to be of the order of the radiation produced.

Conclusions & future work

Using a tailor-made CORSIKA version, we are running air shower simulations on a supercomputer. The library we are building with this CORSIKA version consists of over 26 000 air shower events, each containing particle histograms of the entire evolution of the air shower front instead of the particle flux on the ground only. On top of this output, we will run REAS2 to obtain the radio emission profile resulting from the geosynchrotron effect. We will use this library in support of the LOFAR project,

which can detect radio signatures from extensive air showers.

Though we have not started running REAS2 on the particle histograms we have produced so far, we have already done some analysis of a test sample of 3000 showers at 10^{16} eV. At this point, these results serve to prove that, even though we have not started analysis of the library itself, the amount of computation time available combined with full evolution data, will yield some interesting science.

Currently, nearly three quarters of the scheduled simulations have been finished on the Stella supercomputer. Once finished, the library will be made publicly available.

In the future, we hope to be able to summarise our analysis of the library, both in terms of particle distributions of the extensive air showers and the radio signals that arise from these showers, in a parametrisation of the radio pulses produced by the showers, as a function of all parameters involved.

Acknowledgements

We owe many thanks to Dieter Heck, Ralf Ulrich and Ralph Engel. We also thank Kjeld van der Schaaf and Hopko Meijering for support at Stella. This work is part of the research programme of the ‘Stichting voor Fundamenteel Onderzoek der Materie (FOM)’, which is financially supported by the ‘Nederlandse Organisatie voor Wetenschappelijk Onderzoek (NWO)’.

References

- [1] H. Falcke et al, *Nature* 435:313, 2005
- [2] H. Falcke et al, *ArXiv*, astro-ph/0610652, 2006
- [3] T. K. Gaisser and A. M. Hillas, In *Proc. 15th ICRC*, 353, 1978
- [4] K. Greisen, *Ann. Rev. of Nucl. and Part. Science*, 10:63, 1960
- [5] D. Heck, J. Knapp, et al, Technical Report 6019, Forschungszentrum Karlsruhe, 1998
- [6] T. Huege and H. Falcke, *A&A*, 412:19, 2003
- [7] T. Huege, R. Ulrich, and R. Engel, *Astropart. Phys.*, 27:392, 2007
- [8] M. Kobal and Pierre Auger Collaboration, *Astropart. Phys.*, 15:259, 2001



Measurement of the UHECR energy spectrum using data from the Surface Detector of the Pierre Auger Observatory

MARKUS ROTH¹, FOR THE AUGER COLLABORATION²

¹*Institut für Kernphysik, Forschungszentrum Karlsruhe, POB 3640, D-76021 Karlsruhe, Germany*

²*Observatorio Pierre Auger, Av. San Martín Norte 304, (5613) Malargüe, Mendoza, Argentina*

Markus.Roth@ik.fzk.de

Abstract: At the southern site of the Pierre Auger Observatory, which is close to completion, an exposure that significantly exceeds the largest forerunner experiments has already been accumulated. We report a measurement of the cosmic ray energy spectrum based on the high statistics collected by the surface detector. The methods developed to determine the spectrum from reconstructed observables are described. The energy calibration of the observables, which exploits the correlation of surface detector data with fluorescence measurements in hybrid events, is presented in detail. The methods are simple and robust, exploiting the combination of fluorescence detector (FD) and surface detector (SD) and do not rely on detailed numerical simulation or any assumption about the chemical composition. Besides presenting statistical uncertainties, we address the impact of systematic uncertainties.

Introduction

The Pierre Auger Observatory [1] is designed to measure the extensive air showers produced by the highest energy cosmic rays ($E > 10^{18.5}$ eV) with the goal of discovering their origins and composition. Two different techniques are used to detect air showers. Firstly, a collection of telescopes is used to sense the fluorescence light produced by excitation of nitrogen induced by the cascade of particles in the atmosphere. The FD provides a nearly calorimetric, model-independent energy measurement, because the fluorescence light is produced in proportion to energy dissipation by a shower in the atmosphere [2, 3]. This method can be used only when the sky is moonless and dark, and thus has roughly a 10% duty cycle [4]. The second method uses an array of detectors on the ground to sample particle densities as the air shower arrives at the Earth's surface. The surface detector has a 100% duty cycle [5]. A subsample of air showers detected by both instruments, dubbed hybrid events, are very precisely measured [6] and provide an invaluable energy calibration tool. Hybrid events make it possible to relate the shower energy (FD) to the ground parameter $S(1000)$.

Analysis procedure

The parameter $S(1000)$ characterises the energy of a cosmic ray shower detected by the SD array and is the signal in units of VEM that would be produced in a tank at a distance of 1000 m from the shower axis. One VEM is the signal produced by a single relativistic muon passing vertically through the centre of a water tank. A likelihood method is applied to obtain the lateral distribution function, where the shower axis, $S(1000)$ and the curvature of the shower front are determined [7]. The selection criteria are such to ensure the rejection of accidental triggers (physics trigger) and the events are well contained in the SD array (quality trigger), i.e. we require that all six nearest neighbours of the station with the highest signal be active. In this way we guarantee that the core of the shower is contained inside the array and enough of the shower is sampled to make an $S(1000)$ measurement. The present data set is taken from 1 January, 2004 through 28 February, 2007 while the array has been growing in size. To ensure an excellent data quality we remove periods with problems due to failures in data acquisition, due to lightning and hardware difficulties. We select events only if the

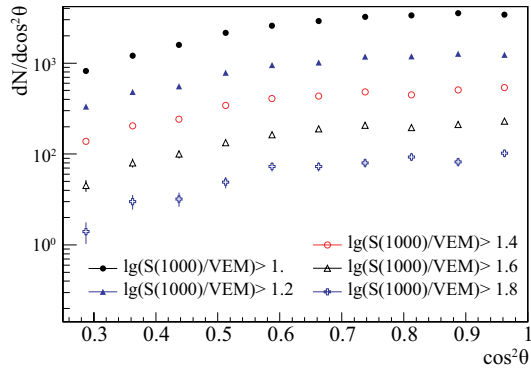


Figure 1: Integral number of events vs $\cos^2 \theta$ for the indicated minimum value of $S(1000)$.

zenith angle is less than 60° and the reconstructed energy is above 3 EeV. For this analysis, the array is fully efficient for detecting such showers, so the acceptance at any time is solely determined by the geometric aperture of the array [8]. The integrated exposure amounts up to about $5165 \text{ km}^2 \text{ sr yr}$, which is a factor of more than 3 larger than the exposure obtained by the largest forerunner experiment AGASA [9]. Moreover the present acceptance exceeds the one given in [10] by a factor of about 3. For a given energy the value of $S(1000)$ decreases with zenith angle, θ , due to attenuation of the shower particles and geometrical effects. Assuming an isotropic flux for the whole energy range considered, i.e. the intensity distribution is uniform when binned in $\cos^2 \theta$, we extract the shape of the attenuation curve from the data. In Figure 1 several intensities, $I_i = I(> S_i(1000))$, above a given value of $\lg S_i(1000)$ are shown as a function of $\cos^2 \theta$. The choice of the threshold $\lg S(1000)$ is not critical since the shape is nearly the same within the statistical limit. The fitted attenuation curve, $CIC(\theta) = 1 + a x + b x^2$, is a quadratic function of $x = \cos^2 \theta - \cos^2 38^\circ$ as displayed in Figure 2 for a particular constant intensity cut, $I_0 = 128$ events, with $a = 0.94 \pm 0.06$ and $b = -1.21 \pm 0.27$. The cut corresponds to a shower size of about $S_{38^\circ} = 47 \text{ VEM}$ and equivalently to an energy of about 9 EeV. Since the average angle is $\langle \theta \rangle \simeq 38^\circ$ we take this angle as reference and convert $S(1000)$ into S_{38° by $S_{38^\circ} \equiv S(1000)/CIC(\theta)$. It may be regarded as the signal $S(1000)$ the shower would have pro-

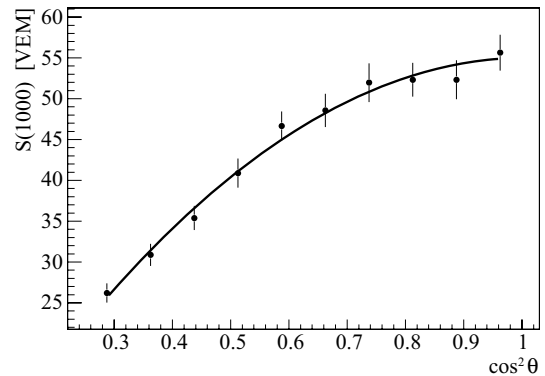


Figure 2: Derived attenuation curve, $CIC(\theta)$, fitted with a quadratic function.

duced had it arrived at $\theta = 38^\circ$. The reconstruction accuracy of the parameter $S(1000)$, $\sigma_{S(1000)}$, comprises 3 contributions and these are taken into account in inferring S_{38° and its uncertainty $\sigma_{S_{38^\circ}}$: a statistical uncertainty due to the finite size of the detector and the limited dynamic range of the signal detection, a systematic uncertainty due to the assumptions of the shape of the lateral distribution and finally due to the shower-to-shower fluctuations [11]. To infer the energy we have to establish the relation between S_{38° and the calorimetric energy measurement, E_{FD} . A set of hybrid events of high quality is selected based on the criteria reported in [6] without applying the cut on the field of view, which appears to have a negligible effect for the topic addressed here. A small correction to account for the energy carried away by high energy muons and neutrinos, the so-called *invisible energy*, depends slightly on mass and hadronic model. The applied correction is based on the average for proton and iron showers simulated with the QGSJet model and sums up to about 10% and its systematic uncertainty contributes 4% to the total uncertainty in FD energy [3]. Moreover the SD quality cuts described above are applied. The criteria include a measurement of the vertical aerosol optical depth profile (VAOD(h)) [12] using laser shots generated by the central laser facility (CLF) [13] and observed by the FD in the same hour of each selected hybrid event. The selected hybrid events were used to calibrate the SD energy. The following procedure was adopted. For each hybrid event, with measured FD energy E_{FD} , the SD energy estimator S_{38° was determined from the

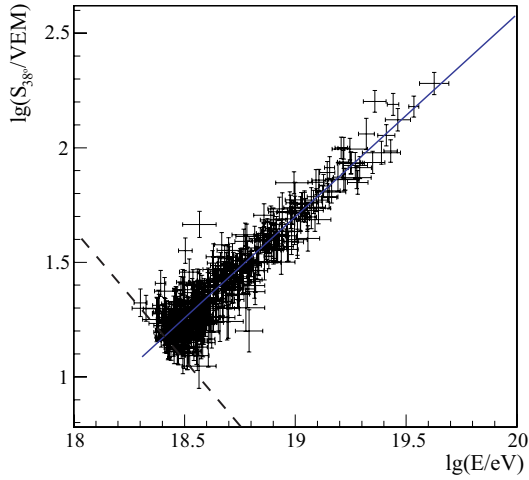


Figure 3: Correlation between $\lg E_{FD}$ and $\lg S_{380}$ for the 387 hybrid events used in the fit. The full line is the best fit to the data. Events below the dashed line were not included in the fit.

measured $S(1000)$ by using the constant intensity method described above. For each event the uncertainty in S_{380} is estimated by summing in quadrature three contributions: the uncertainty in the constant intensity parametrization, $\sigma_{S_{380}}(CIC)$, the angular accuracy of the event, $\sigma_{\cos\theta}$, and the uncertainty in the measured $S(1000)$, $\sigma_{S(1000)}$. The fluorescence yield used to estimate the energy E_{FD} is taken from [14]. An uncertainty in the FD energy, $\sigma_{E_{FD}}$, was also assigned to each event. Several sources were considered. The uncertainty in the hybrid shower geometry, the statistical uncertainty in the Gaisser-Hillas fit to the profile of the energy deposits and the statistical uncertainty in the invisible energy correction were fully propagated. The uncertainty in the VAOD measurement was also propagated to the FD energy on an event-by-event basis, by evaluating the FD energy shift obtained when changing the VAOD profile by its uncertainty. These individual contributions were considered to be uncorrelated, and were thus combined in quadrature to obtain $\sigma_{E_{FD}}$. The data appear to be well described by a linear relation $\lg E_{FD} = A + B \cdot \lg S_{380}$ (see Figure 3). A linear least square fit of the data was performed. To avoid possible biases, low energy events, below the dashed line, which is orthogonal to the best fit line and intersects it at $\lg(S_{380} = 15 \text{ VEM})$, were not included in the fit.

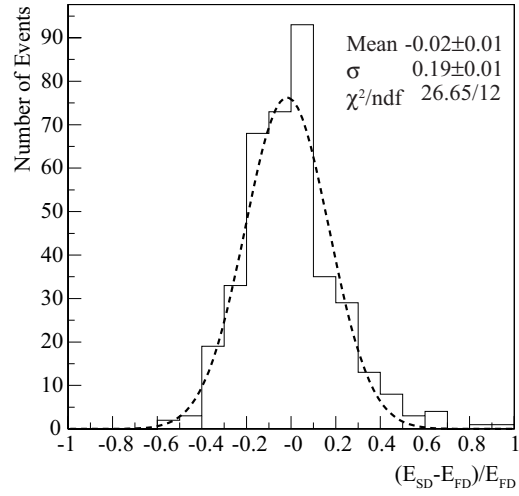


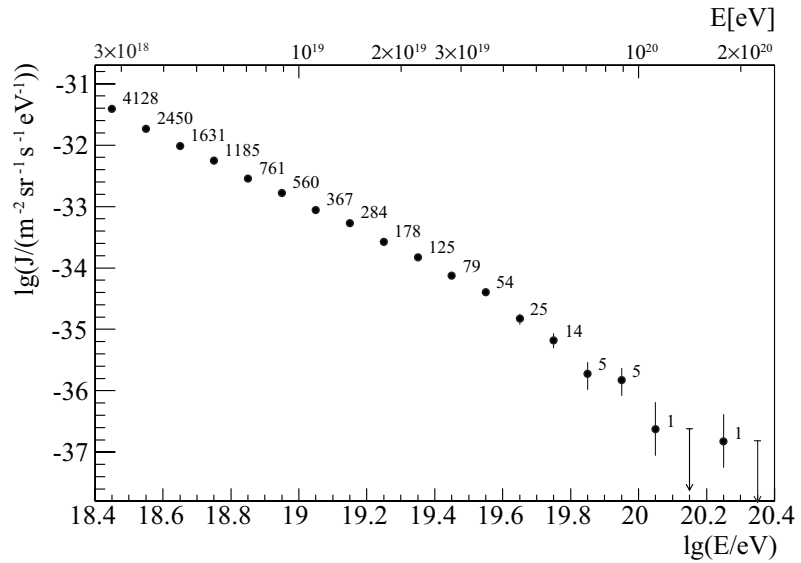
Figure 4: Fractional difference between the FD and SD energy for the 387 selected hybrid events.

An iterative procedure was used to determine the dashed line, and it was checked that the results of the fit were stable. The best fit yields $A = 17.08 \pm 0.03$ and $B = 1.13 \pm 0.02$ with a reduced χ^2 of 1.3 for $\lg E_{SD} = A + B \cdot \lg S_{380}$ in [eV]. The relative statistical uncertainty in the derived SD energy, $\sigma_{E_{SD}}/E_{SD}$, is rather small, e.g. of the order of 5% at 10^{20} eV. The energy spectrum J is displayed in Figure 5 together with its statistical uncertainty. The individual systematic uncertainties in determining E_{SD} coming from the FD sum up to 22%. For illustrative purposes we show in Figure 6 the difference of the flux with respect to an assumed flux $\propto E^{-2.6}$. The largest uncertainties are given by the absolute fluorescence yield (14%), the absolute calibration of the FD (9.5%) and the reconstruction method (10%). The uncertainty due to the dependence of the fluorescence spectrum on pressure (1%), humidity (5%) and temperature (5%) are taken into account as well as the wavelength dependent response of the FD, the aerosol phase function, invisible energy and others, which are well below 4% (see [4] for details).

Discussion and outlook

When inferring the energy spectrum from SD data we utilise the constant intensity method to calibrate the SD data. The systematic uncertainties

Figure 5: Auger spectrum J as a function of energy. Vertical error bars represent the statistical uncertainty only. The statistical and systematic uncertainties in the energy scale are of the order of $\approx 6\%$ and $\approx 22\%$, respectively.



have been scrutinised and the resulting spectrum is given. Several activities are on-going to reduce the systematic uncertainties of the energy estimate, e.g. the detector calibration uncertainty and the uncertainty of the fluorescence yield. Reducing these

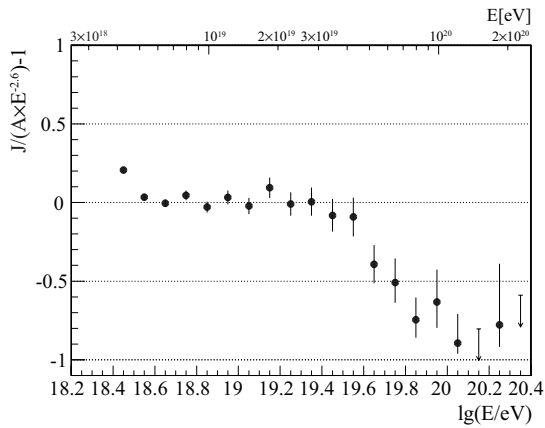


Figure 6: Fractional difference between the derived spectrum and an assumed flux $\propto E^{-2.6}$ as a function of energy.

uncertainties will make it desirable to deconvolve the energy spectrum using the estimate of the energy resolution. The presented spectrum is compared with a spectrum derived on basis of hybrid data only in T. Yamamoto et al. [15]. Astrophysical implications are also discussed there.

References

- [1] J. Abraham [Pierre Auger Collaboration], NIM 523 (2004) 50.
- [2] M. Risse and D. Heck, Astropart. Phys. 20 (2004) 661.
- [3] H. Barbosa et al., Astropart. Phys. 22 (2004) 159.
- [4] B. Dawson [Pierre Auger Collaboration] these proceedings, (2007), #0976.
- [5] T. Suomijarvi [Pierre Auger Collaboration] these proceedings, (2007) #0299.
- [6] L. Perrone [Pierre Auger Collaboration] these proceedings (2007), #0316.
- [7] D. Barnhill [Pierre Auger Collaboration], Proc. 29th ICRC, Pune (2005), 7, 291.
- [8] D. Allard [Pierre Auger Collaboration], Proc. 29th ICRC, Pune (2005), 7, 71.
- [9] M. Takeda et al., Astropart. Phys. 19 (2003) 447.
- [10] P. Sommers [Pierre Auger Collaboration], Proc. 29th ICRC, Pune (2005) 7, 387.
- [11] M. Ave [Pierre Auger Collaboration] these proceedings, (2007), #0297.
- [12] S. Ben-Zvi [Pierre Auger Collaboration] these proceedings, (2007) #0399.
- [13] B. Fick et al., JINST, 1 (2006) 11003.
- [14] M. Nagano, K. Kobayakawa, N. Sakaki, K. Ando, Astropart. Phys. 22 (2004) 235.
- [15] T. Yamamoto [Pierre Auger Collaboration] these proceedings, (2007) #0318.



Study of the Cosmic Ray Composition above 0.4 EeV using the Longitudinal Profiles of Showers observed at the Pierre Auger Observatory

MICHAEL UNGER¹ FOR THE PIERRE AUGER COLLABORATION²

¹*Forschungszentrum Karlsruhe, Postfach 3640, 76021 Karlsruhe, Germany*

²*Observatorio Pierre Auger, Av. San Martin Norte 304, 5613 Malargüe, Argentina*

Michael.Unger@ik.fzk.de

Abstract: The Pierre Auger Observatory has been collecting data in a stable manner since January 2004. We present here a study of the cosmic ray composition using events recorded in hybrid mode during the first years of data taking. These are air showers observed by the fluorescence detector as well as the surface detector, so the depth of shower maximum, X_{\max} , is measured directly. The cosmic ray composition is studied in different energy ranges by comparing the observed average X_{\max} with predictions from air shower simulations for different nuclei. The change of $\langle X_{\max} \rangle$ with energy (elongation rate) is used to derive estimates of the change in primary composition.

Introduction

Ultra-high-energy cosmic rays are presumed to be of extragalactic origin. With increasing energies, and thus Larmor radii, the galactic charged particles can not be confined in our Galaxy and the galactic cosmic ray accelerator candidates are expected to reach their maximum energy well below 10^{18} eV. Moreover, there are no experimental signs of an anisotropy of the cosmic ray arrival direction at these energies.

The transition between galactic and extragalactic cosmic rays is therefore believed to happen between 10^{18} and 10^{19} eV where a spectral break in the cosmic ray flux known as the 'ankle' or 'dip' is observed. The exact position and nature of the transition is still disputed and it seems clear that a combined precise measurement of the particle flux and composition in this energy range is needed to be able to distinguish between different models of the extragalactic cosmic ray component (see [1] for recent discussions on this subject).

For fluorescence detectors (FDs), the observable most sensitive to the composition is the slant depth position X_{\max} at which the maxi-

mum of the longitudinal shower profile occurs. Its average value $\langle X_{\max} \rangle$ at a certain energy E is related to the mean logarithmic mass $\langle \ln A \rangle$ via

$$\langle X_{\max} \rangle = D_p [\ln (E/E_0) - \langle \ln A \rangle] + c_p, \quad (1)$$

where D_p denotes the 'elongation rate' [2] of a proton, and c_p is the average depth of a proton with reference energy E_0 . Both, D_p and c_p , depend on the nature of hadronic interactions. The width of the X_{\max} distribution is another composition sensitive parameter, since heavy nuclei are expected to produce smaller shower-to-shower fluctuations than protons.

Data Analysis

In this analysis we use hybrid events collected by the Pierre Auger Observatory between the 1st of December 2004 and the 30th of April 2007. These are showers observed by at least one FD and with at least one triggered tank recorded by the surface detector.

In order to ensure a good X_{\max} resolution at the 20 g cm^{-2} level [3], the following quality cuts were applied to the data: The reconstructed X_{\max} should lie within the observed

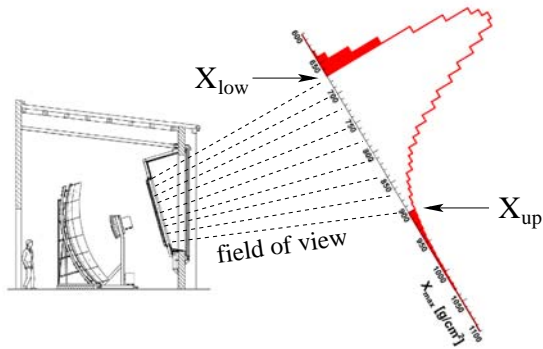


Figure 1: Illustration of the effect of the field of view of the fluorescence detector on the selected X_{\max} distribution. Filled areas indicate slant depths, which are de-selected by the quality cuts.

shower profile and the reduced χ^2 of a fit with a Gaisser-Hillas function [4] should not exceed 2.5. Moreover, insignificant shower maxima are rejected by requiring that the χ^2 of a linear fit to the longitudinal profile exceeds the Gaisser-Hillas fit χ^2 by at least four. Finally, the estimated uncertainties of the shower maximum and total energy must be smaller than 40 g cm^{-2} and 20%, respectively.

In addition, a set of fiducial volume cuts is applied to allow for an unbiased measurement of the X_{\max} -distribution: Energy dependent cuts on the zenith angle and the maximum tank-core distance ensure a single-tank trigger probability near one for protons and iron at all energies.

In order to minimise systematic uncertainties from the relative timing between the fluorescence and surface detectors, the minimum viewing angle under which a shower was observed is required to be larger than 20° . This cut also removes events with a large fraction of direct Cherenkov light.

Moreover, a minimisation of the effect of the field of view boundaries of the FDs is of utmost importance: The current fluorescence detectors cover an elevation range from $\Omega_1 = 1.5^\circ$ to $\Omega_2 = 30^\circ$ and therefore the observable heights for vertical tracks are between $R \tan \Omega_1 < h_v < R \tan \Omega_2$, where R denotes the distance of the

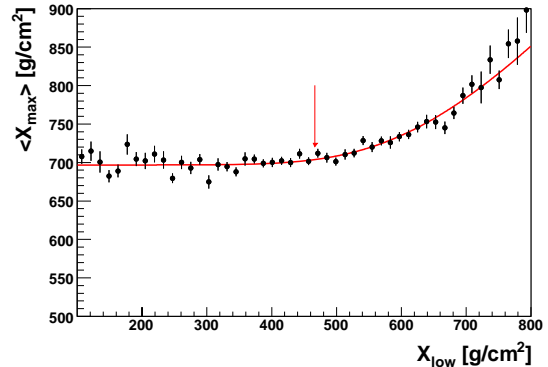


Figure 2: Dependence of the average measured X_{\max} on the upper viewable slant depth boundary for showers with energies between 10^{18} and $10^{18.25}$ eV. The arrow indicates the cut corresponding to an estimated contained event fraction of $> 95\%$.

shower core to the fluorescence detector. That is, the farther away from a fluorescence detector a track is detected, the smaller becomes the observable upper slant depth boundary X_{up} . Similarly the lower slant depth boundary X_{low} becomes larger for near showers.

Since in the quality selection it is required that the X_{\max} is detected within the field of view, these slant depth boundaries can severely bias the selected X_{\max} -distributions, as it is sketched in Fig. 1. This bias can be avoided by selecting only tracks with geometries corresponding to an $X_{\text{up}}-X_{\text{low}}$ range, which is large enough to contain most of the parent X_{\max} -distribution. Therefore, we investigate the dependence of $\langle X_{\max} \rangle$ on the field of view boundaries and place fiducial volume cuts at the X_{up} and X_{low} values, where the $\langle X_{\max} \rangle$ starts to be constant. An example of this procedure is shown in Fig. 2.

Systematic Uncertainties

The effect of atmospheric uncertainties on the measurement of the shower maximum is discussed in detail in [5]. The dominating contribution is the long-term validity of the monthly average molecular profiles

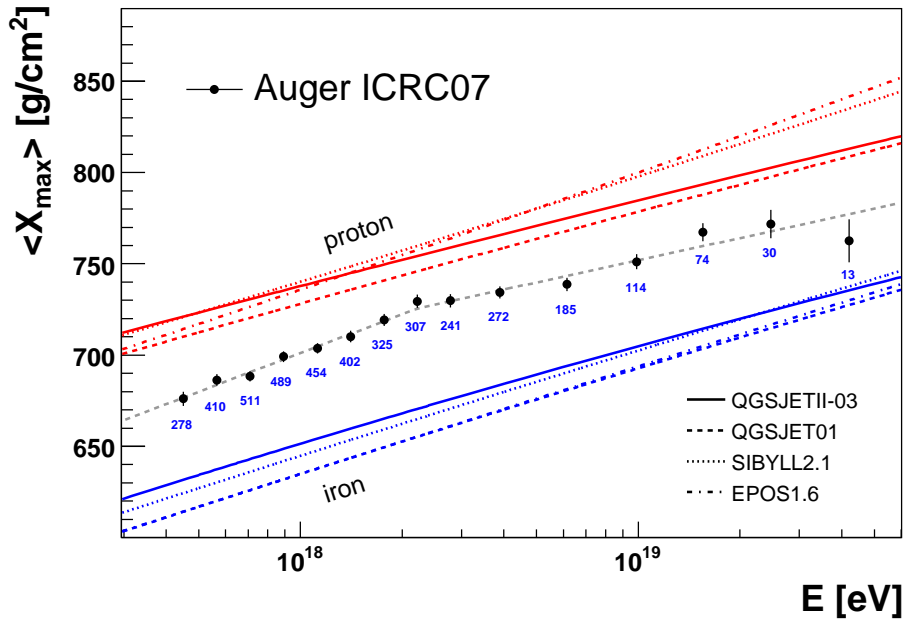


Figure 3: $\langle X_{\max} \rangle$ as a function of energy compared to predictions from hadronic interaction models. The dashed line denotes a fit with two constant elongation rates and a break-point. Event numbers are indicated below each data point.

used in this analysis, which we estimate to be $\leq 6 \text{ g cm}^{-2}$. Using a full detector and atmosphere simulation [6], the profile reconstruction algorithm [7] was found to be unbiased within 5 g cm^{-2} at all energies. The effect of multiple-scattered fluorescence and Cherenkov light was estimated to contribute about 5 g cm^{-2} by comparing different light collection algorithms.

Re-reconstructing showers with the geometry determined from the surface detector data alone yields an upper bound on the geometrical uncertainty of $\leq 6 \text{ g cm}^{-2}$.

The geometrical bias due to the camera alignment uncertainty is below 3 g cm^{-2} and the residual acceptance difference [8] between proton and iron showers contributes around 10 g cm^{-2} at lowest energies vanishing rapidly to zero above 10^{18} eV .

The total uncertainty is thus around $\leq 15 \text{ g cm}^{-2}$ at low energies and $\leq 11 \text{ g cm}^{-2}$ above 10^{18} eV . Note that in addition the

current uncertainty of the FD energy scale of 22% [3] needs to be taken into account.

Results

After all cuts are applied, 4329 events remain for the composition analysis. In Fig. 3 the mean X_{\max} as a function of energy is shown along with predictions from air shower simulations [10,11]. As can be seen, our measurement favours a mixed composition at all energies.

A simple linear fit, $\langle X_{\max} \rangle = D_{10} \cdot \lg(E/\text{eV}) + c$, yields an elongation rate of 54 ± 2 (stat.) $\text{g cm}^{-2}/\text{decade}$, but does not describe our data very well ($\chi^2/\text{Ndf} = 24/13$, $P < 3\%$). Allowing for a break in the elongation rate at an energy E_b leads to a satisfactory fit with $\chi^2/\text{Ndf} = 9/11$, $P = 63\%$ and $D_{10} = 71 \pm 5$ (stat.) $\text{g cm}^{-2}/\text{decade}$ below $E_b = 10^{18.35} \text{ eV}$ and $D_{10} = 40 \pm 4$ (stat.) $\text{g cm}^{-2}/\text{decade}$ above this energy. This fit is indicated as a dashed gray line in Fig. 3.

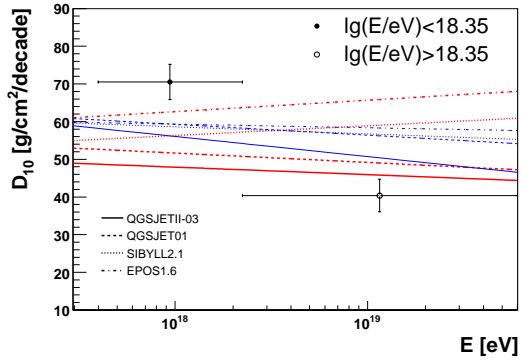


Figure 4: Comparison of the measured elongation rate, D_{10} , below (solid circle) and above (open circle) $10^{18.35}$ eV to predictions of air shower simulations (red: protons, blue: iron).

Due to the uncertainties of hadronic interaction at highest energies, the interpretation of these elongation rates is, however, ambiguous (cf. Fig. 4). Using the QGSJETII elongation rates the data suggests a moderate lightening of the primary cosmic at low energies and an almost constant composition at high energies, whereas the EPOS elongation rate is clearly larger than the measured one at high energies, which would indicate a transition from light to heavy elements. These ambiguities will be partially resolved by the analysis of the X_{\max} fluctuations as an additional mass sensitive parameter.

A comparison with previous measurements [9] is presented in Fig. 5. The results of all three experiments are compatible within their systematic uncertainties. It is worthwhile noting that although the data presented here have been collected during the construction of the Pierre Auger Observatory, their statistical precision already exceed that of preceding experiments.

References

[1] V. Berezhinsky et al., Phys. Rev. D **74** (2006) 043005; T. Stanev, astro-ph/0611633; A. M. Hillas, astro-ph/0607109, D. Allard et al., Astropart. Phys. **27**, (2007), 61.

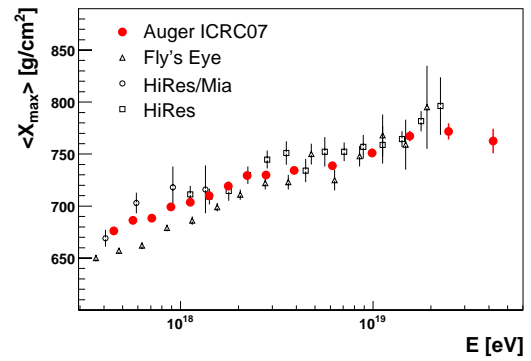


Figure 5: $\langle X_{\max} \rangle$ as a function of energy compared to previous experiments.

[2] J. Linsley, Proc. 15th ICRC, 12 (1977) 89; T.K. Gaisser et al., Proc. 16th ICRC, 9 (1979) 258; J. Linsley and A.A. Watson, Phys. Rev. Lett., **46** (1981) 459.

[3] B. Dawson [Pierre Auger Collaboration], these proceedings, #0976

[4] T.K. Gaisser and A.M. Hillas, Proc. 15th ICRC (1977), **8**, 353.

[5] M. Prouza [Pierre Auger Collaboration], these proceedings, #0398

[6] L. Prado et al., Nucl. Instrum. Meth., A545 (2005), 632.

[7] M. Unger, R. Engel, F. Schüssler, R. Ulrich, these proceedings, #0972

[8] H.O. Klages [Pierre Auger Collaboration], these proceedings, #0065

[9] D.J. Bird et al. [Fly's Eye Collaboration], Phys. Rev. Lett., **71** (1993) 3401; T. Abu-Zayyad et al. [HiRes-MIA Collaboration], Astrophys. J., **557** (2001) 686; R.U. Abbasi et al. [HiRes Collaboration], Astrophys. J., **622** (2005) 910.

[10] N.N. Kalmykov et al., Nucl. Phys. B (Proc. Suppl.) (1997), **7**; R. Engel et al., Proc. 26th ICRC (1999), 415; S. Ostapchenko, Nucl. Phys. Proc. Suppl., **151** (2006), 143; T. Pierog et al., these proceedings, #0905 and astro-ph/0611311.

[11] T. Bergmann et al., Astropart. Phys., **26**, (2007), 420.



Test of hadronic interaction models with data from the Pierre Auger Observatory

RALPH ENGEL¹, FOR THE PIERRE AUGER COLLABORATION²

¹ *Forschungszentrum Karlsruhe, P.O. Box 3640, 76021 Karlsruhe, Germany*

² *Observatorio Pierre Auger, Av. San Martín Norte 304, (5613) Malargüe, Mendoza, Argentina*

Ralph.Engel@ik.fzk.de

Abstract: The Pierre Auger Observatory allows the measurement of both longitudinal profiles and lateral particle distributions of high-energy showers. The former trace the overall shower development, mainly of the electromagnetic component close to the core where the latter reflect the particle densities in the tail of the shower far away from the core and are sensitive to both the muonic and electromagnetic components. Combining the two complementary measurements, predictions of air shower simulations are tested. In particular the muon component of the tank signals, which is sensitive to hadronic interactions at high energy, is studied with several independent methods. Implications for the simulation of hadronic interactions at ultra-high energy are discussed.

Introduction

During the last decade, air shower simulation codes have reached such a high quality that there is good overall agreement between the predicted and experimentally observed shower characteristics. The largest remaining source of uncertainty of shower predictions stems from our limited knowledge of hadronic interactions at high energy. Hadronic multiparticle production has to be simulated at energies exceeding by far those accessible at man-made accelerators and in phase space regions not covered in collider experiments. Therefore it is not surprising that predictions for the number of muons or other observables, which are directly related to hadron production in showers, depend strongly on the adopted hadronic interaction models [1].

In this work we will employ universality features of the longitudinal profile of the electromagnetic shower component to combine fluorescence detector and surface array measurements of the Pierre Auger Observatory. Using the measured shower depth of maximum, X_{\max} , the muon density at ground is inferred without assumptions on the primary cosmic ray composition. This allows a direct test of the predictions of hadronic interaction models.

Parameterisation of surface detector signal using universality

Universality features of the longitudinal profile of showers have been studied by several authors [2]. Here we exploit shower universality features to predict the surface detector signal expected for Auger Cherenkov tanks due to the electromagnetic and muonic shower components at 1000 m from the shower core. In the following only a brief introduction to the method of parameterising the muonic and electromagnetic tank signals is given. A detailed description is given in [3].

A library of proton and iron showers covering the energy range from 10^{17} to 10^{20} eV and zenith angles between 0° and 70° was generated with CORSIKA 6.5 [4] and the hadronic interaction models QGSJET II.03 [5] and FLUKA [6]. For comparison, a smaller set of showers was simulated with the combinations QGSJET II.03/GHEISHA [7] and SIBYLL 2.1/FLUKA [8, 9]. Seasonal models of the Malargüe molecular atmosphere were used [10]. The detector response is calculated using look-up tables derived from a detailed GEANT4 simulation [11].

Within the library of showers, the predicted surface detector signal for the electromagnetic component of a shower at the lateral distance of 1000 m

is found to depend mainly on the energy and the distance between the shower maximum and the ground (distance to ground, $DG = X_{\text{ground}} - X_{\text{max}}$). Here the signal of electromagnetic shower component is defined as that of all shower particles except muons and decay products of muons. The signal at 1000 m depends only slightly on the mass of the primary particle (13% difference between proton and iron primaries) and the applied interaction model ($\sim 5\%$). The functional form, however, is universal. The situation is similar for the expected tank signal due to muons and their decay products. In this case the shower-to-shower fluctuations are larger and the difference between proton and iron showers amounts to 40%.

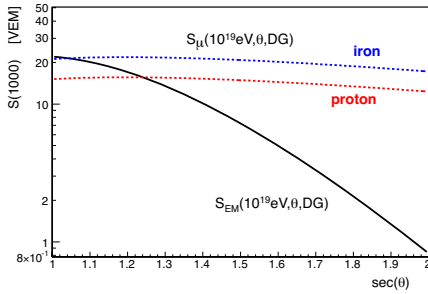


Figure 1: Electromagnetic and muon contributions to the detector signal as a function of zenith angle. Results of QGSJET II/FLUKA simulations are shown for 10^{19} eV showers.

After accounting for geometrical effects such as the projected tank surface area, the proton-iron averaged electromagnetic shower signal is parameterised in dependence on the energy E , distance to shower maximum DG , and zenith angle θ . The difference between proton and iron shower profiles is included in the calculation of the systematic uncertainties later. Similarly the universal shape of muon signal profile is parameterized simultaneously for all model primaries, taking the overall normalisation from proton showers simulated with QGSJET II/FLUKA. The expected detector signal at 1000 m can then be written as

$$S_{\text{MC}}(E, \theta, X_{\text{max}}) = S_{\text{em}}(E, \theta, DG) + N_{\mu}^{\text{rel}} S_{\mu}^{\text{QGSJET II, P}}(10^{19} \text{ eV}, \theta, DG), \quad (1)$$

where N_{μ}^{rel} is the number of muons relative to that of QGSJET proton showers at 10^{19} eV and

$S_{\mu}^{\text{QGSJET II, P}}$ is the muon signal predicted by QGSJET II for proton primaries. The relative importance of the electromagnetic and muonic detector signal contributions at different angles is shown in Fig. 1.

Constant-intensity-cut method

Within the current statistics, the arrival direction distribution of high-energy cosmic rays is found to be isotropic, allowing us to apply the constant intensity cut method to determine the muon signal contribution. Dividing the surface detector data into equal exposure bins, the number of showers with $S(1000)$ greater than a given threshold should be the same for each bin

$$\left. \frac{dN_{\text{ev}}}{d \sin^2 \theta} \right|_{S(1000) > S_{\text{MC}}(E, \theta, \langle X_{\text{max}} \rangle, N_{\mu}^{\text{rel}}} = \text{const.} \quad (2)$$

Using the independently measured mean depth of shower maximum $\langle X_{\text{max}} \rangle$ [12] the only remaining free parameter in Eq. (2) is the relative number of muons N_{μ}^{rel} . For a given energy E , N_{μ}^{rel} is adjusted to obtain a flat distribution of events in $\sin^2 \theta$.

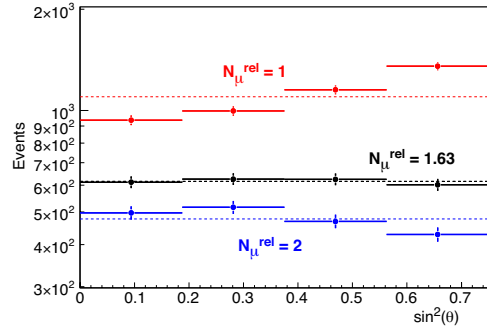


Figure 2: Sensitivity of the constant-intensity-cut method to the muon number for $E = 10^{19}$ eV.

The sensitivity of this method to the muon number parameter in Eq. (1) is illustrated in Fig. 2. The best description of the data above 10^{19} eV requires $N_{\mu}^{\text{rel}} = 1.63$. However, this result was obtained by using the measured mean depth of shower maximum [12] in Eq. (1). Shower-to-shower fluctuations in X_{max} and the reconstruction resolution cannot be neglected and have been estimated with a Monte Carlo simulation. Accounting for

fluctuations and reconstruction effects, the relative number of muons at 10^{19} eV is found to be $1.45 \pm 0.11(\text{stat})_{-0.09}^{+0.11}(\text{sys})$.

Knowing the muon number and the measured mean depth of shower maximum, the signal size at $\theta = 38^\circ$ can be calculated

$$S_{38}(10^{19}\text{eV}) = 37.5 \pm 1.7(\text{stat})_{-2.3}^{+2.1}(\text{sys}) \text{ VEM}. \quad (3)$$

This value of S_{38} is a measure of the energy scale of the surface detector which is independent of the fluorescence detector. It is within the systematic uncertainties of the energy determination from fluorescence detector measurements, including the uncertainty of the fluorescence yield [13]. It corresponds to assigning showers a $\sim 30\%$ higher energy than done in the fluorescence detector-based Auger shower reconstruction ($E = 1.3E_{\text{FD}}$).

Hybrid event and inclined shower analysis

Hybrid events that trigger the surface detector array and the fluorescence telescopes separately are ideally suited to study the correlation between the depth of shower maximum and the muon density at 1000 m. However, the number of events collected so far is much smaller. For each individual event the reconstructed fluorescence energy and depth of maximum are available and the expected $S(1000)$ due to the electromagnetic component can be calculated directly. The difference in the observed signal is attributed to the muon shower component and compared to the predicted muon signal.

For this study, high-quality hybrid events were selected for which the shower maximum was in the field of view of a telescope, $\theta < 60^\circ$, and the Mie scattering length was measured. Furthermore the distance between the telescope and the shower axis was required to be larger than 10 km and the Cherenkov light fraction was limited to less than 50%. The surface detector event had to satisfy the T5 selection cuts which are also applied in [13].

In Fig. 3, we show the muon signal derived from these hybrid events as function of distance to ground. The relative number of muons at 10^{19} eV is found to be

$$N_{\mu}^{\text{rel}}|_{E=1.3E_{\text{FD}}} = 1.53 \pm 0.05$$

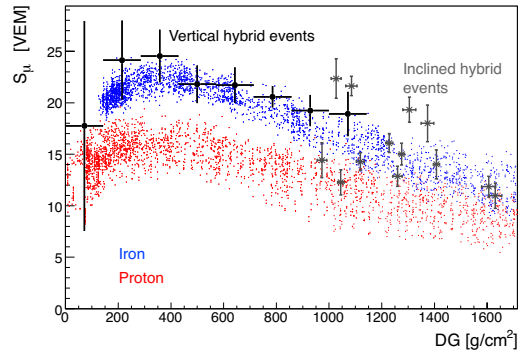


Figure 3: Reconstructed and predicted muon tank signal contribution in dependence on the distance to ground for vertical and inclined hybrid events. The muon profiles expected from QGSJET II simulations are indicated by the red (proton showers) and blue (iron showers) points for the energy scale $E = 1.3E_{\text{FD}}$.

$$N_{\mu}^{\text{rel}}|_{E=E_{\text{FD}}} = 1.97 \pm 0.06, \quad (4)$$

consistent with the analysis above.

A similar study has been performed for inclined hybrid events ($60^\circ < \theta < 70^\circ$). Within the limited statistics, good agreement between muon numbers of the inclined and the vertical data sets is found, see Fig. 3.

In Fig. 4 we compare the results of the different methods applied for inferring the muon density at 1000 m from the shower core. The relative number of muons is shown as function of the adopted energy scale with respect to the Auger fluorescence detector energy reconstruction. Only the constant-intensity-cut method is independent of the energy scale of the fluorescence detector. Very good agreement between the presented methods is found.

Discussion

Assuming universality of the electromagnetic shower component at depths larger than X_{max} , we have determined the muon density and the energy scale with which the data of the Auger Observatory can be described self-consistently. The number of muons measured in data is about 1.5 times bigger

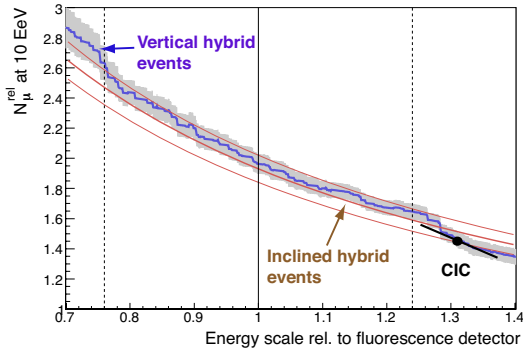


Figure 4: Comparison of the results on the relative muon multiplicity at 10^{19} eV from different methods.

than that predicted by QGSJET II for proton showers. Consistent results were obtained with several analysis methods.

The QGSJET II and SIBYLL 2.1 predictions for iron showers correspond to relative muon numbers of 1.39 and 1.27, respectively. Therefore, interpreted in terms of QGSJET II or SIBYLL 2.1, the derived muon density would correspond to a primary cosmic ray composition heavier than iron, which is clearly at variance with the measured X_{\max} values. The discrepancy between air shower data and simulations reported here is qualitatively similar to the inconsistencies found in composition analyses of previous detectors, see, for example, [14, 15, 16].

Finally it should be mentioned that the results of this study depend not only on the predictions of the hadronic interaction models but also on the reliability of the model used for calculating the electromagnetic interactions (EGS4 in this study [17]).

References

- [1] J. Knapp, D. Heck, S. J. Sciutto, M. T. Dova, and M. Risse, *Astropart. Phys.* 19 (2003) 77–99 and astro-ph/0206414.
- [2] P. Billoir, lecture given at CORSIKA School, <http://www-ik.fzk.de/corsika/corsika-school>, 2005; M. Giller, A. Kacperczyk, J. Malinowski, W. Tkaczyk, and G. Wieczorek, *J. Phys.* G31 (2005) 947–958; F. Nerling, J. Blümer, R. Engel, and M. Risse, *Astropart. Phys.* 24 (2006) 421–437 and astro-ph/0506729; D. Gora *et al.*, *Astropart. Phys.* 24 (2006) 484–494 and astro-ph/0505371; A. S. Chou [Pierre Auger Collab.], Proc. of 29th ICRC (Pune), India, 3-11 Aug 2005, p. 319.
- [3] F. Schmidt, M. Ave, L. Cazon, A. Chou, these proceedings #0752, 2007.
- [4] D. Heck, J. Knapp, J. Capdevielle, G. Schatz, and T. Thouw, *Wissenschaftliche Berichte FZKA 6019*, Forschungszentrum Karlsruhe, 1998.
- [5] S. Ostapchenko, *Phys. Rev.* D74 (2006) 014026 and hep-ph/0505259.
- [6] A. Fasso, A. Ferrari, J. Ranft, and R. P. Sala, in Proc. of Int. Conf. on Advanced Monte Carlo for Radiation Physics, Particle Transport Simulation and Applications (MC 2000), Lisbon, Portugal, 23-26 Oct 2000, A. Kling, F. Barao, M. Nakagawa, L. Tavora, P. Vaz eds., Springer-Verlag Berlin, p. 955, 2001.
- [7] H. Fesefeldt, preprint PITHA-85/02, RWTH Aachen, 1985.
- [8] R. S. Fletcher, T. K. Gaisser, P. Lipari, and T. Stanev, *Phys. Rev.* D50 (1994) 5710.
- [9] R. Engel, T. K. Gaisser, P. Lipari, and T. Stanev, in Proceedings of the 26th ICRC (Salt Lake City) vol. 1, p. 415, 1999.
- [10] B. Keilhauer, J. Blümer, R. Engel, H. O. Klages, and M. Risse, *Astropart. Phys.* 22 (2004) 249 and astro-ph/0405048.
- [11] P.L. Ghia and I.L.Henry-Yvon [Pierre Auger Collab.], these proceedings #0300, 2007.
- [12] M. Unger [Pierre Auger Collab.], these proceedings #0594, 2007.
- [13] M. Roth [Pierre Auger Collab.], these proceedings #0313, 2007.
- [14] T. Abu-Zayyad *et al.* (HiRes-MIA Collab.), *Phys. Rev. Lett.* 84 (2000) 4276 and astro-ph/9911144.
- [15] M.T. Dova, M.E. Mancenido, A.G. Mariazzi, T.P. McCauley and A.A. Watson, *Astropart. Phys.* 21 (2004) 597 and astro-ph/0312463.
- [16] A.A. Watson, *Nucl. Phys. Proc. Suppl.* 136 (2004) 290 and astro-ph/0408110.
- [17] W.R. Nelson, Report SLAC-265, Stanford Linear Accelerator Center, 1985.



HEAT – Enhancement Telescopes for the Pierre Auger Southern Observatory

H. O. KLAGES¹, FOR THE PIERRE AUGER COLLABORATION

¹*Forschungszentrum Karlsruhe, Institut für Kernphysik, P.O.Box 3640, D76021 Karlsruhe, Germany
hans.klages@ik.fzk.de*

Abstract: The southern part of the Pierre Auger Observatory (PAO) is nearing completion in the province of Mendoza, Argentina. Since 2004 the instrument is used to take air shower data at the highest energies [1]. The energy threshold of the 3000 km² surface array of 1600 particle detectors for high quality air shower reconstruction is about $3 \cdot 10^{18}$ eV. The 24 Auger fluorescence telescopes (FD), located in four “eye” stations at the edge of the detector array, enable precise air shower measurements even at primary energies below 10^{18} eV. The Auger Collaboration has decided to further expand its energy range down to 10^{17} eV after completion of the southern observatory around the end of 2007 by three additional fluorescence telescopes with an elevated field of view from 30° to 60° above the horizon. It is foreseen to use these High Elevation Auger Telescopes (HEAT) in combination with the existing telescopes at one of the four existing FD sites (Coihueco) as well as in hybrid mode using the shower particle data from a new infill detector area of about 25 km² with fourfold sampling density – close to HEAT and in the field of view of the new telescopes. This SD infill array (AMIGA) will also be equipped with large area muon detectors [2]. In addition, it will be a perfectly suited test area for the development of novel detection techniques for air showers at ultrahigh energies [3].

Introduction

Cosmic rays with energies in the range between 10^{17} eV and $5 \cdot 10^{18}$ eV are of special interest for the determination of the details of the transition from galactic to extragalactic cosmic rays. The precise shape of the energy spectrum and the possible changes in primary composition must be well known to enable stringent tests of models for the acceleration and transport of both, galactic and extragalactic, cosmic rays. More elaborated arguments can be found in a separate contribution to this conference [4].

The fluorescence technique for the detection of air showers encounters difficulties at energies below 10^{18} eV. The signal strength in fluorescence photons per unit path length is (at air shower maximum) roughly proportional to the primary energy. Therefore, the effective distance range of air shower detection gets smaller at lower energies. Only relatively close-by showers will trigger the DAQ. At these small distances the height of observation by the FD telescopes is limited. In addition, lower energy air showers reach their maximum of development at higher altitudes.

This height cutoff effect naturally gets even worse for air showers incident at larger zenith angles.

The maximum of shower development will thus quite often fall outside the field of view of the existing FD telescopes of the Auger Observatory, which is limited to about 30° above the horizon. For an unambiguous reconstruction of the shower profiles this leads to severe cuts in the triggered data, which may be dependent on primary mass. The telescope detection efficiency for showers, which hit the ground at a certain distance from the “eye”, also depends on the shower-detector geometry. Showers approaching the telescopes will have a higher trigger probability due to the angular dependence of the scattered Cherenkov light. Also, the efficiency for successful reconstruction of the shower profile and X_{\max} will be increased as is illustrated in figure 1. Therefore, it is clear that for lower energies the fluorescence telescopes benefit from a larger elevation range.

The Auger Collaboration will combine several of their existing telescopes with three additional telescopes tilted by about 30°, therefore covering elevation angles up to 60° above horizon, but else these will be very similar to the existing systems.

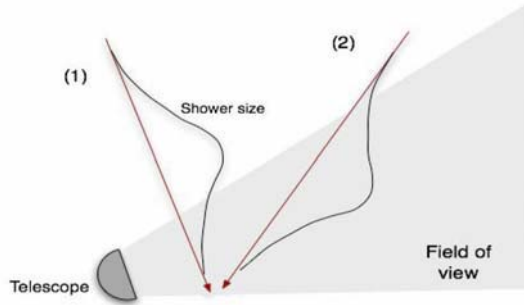


Figure 1: Severe effects of a limited field of view of fluorescence telescopes. Showers approaching the “eye” have higher reconstruction efficiency.

Auger FD and the HEAT Telescopes

The Auger Collaboration has installed 24 fluorescence telescopes at the southern observatory site in Argentina. The telescopes are taking data in four FD buildings (45 km apart from each other at the edges of the array) overlooking the 3000 km² array of 1600 particle detector tanks.

Each telescope has a field of view of 30° x 30°. The Schmidt optics of the telescopes has an effective aperture of about 3 m². The signal/noise ratio is improved by the use of UV transmitting filter glass (M-UG6) for the entrance windows. The high sensitivity of the Auger telescopes enables the detection of showers with $E > 10^{19}$ eV up to distances of more than 40 km. Therefore, most of the highest energy events are detected in stereo mode by at least two telescopes simultaneously.

The strength of the Auger experiment is the operation in Hybrid mode. More than 10% of all events are detected by the surface detector system (SD) and at least one (FD) telescope. These events are especially valuable in two different ways. The FD information allows the independent energy calibration of well measured SD events at higher energies. On the other hand, the FD traces for low energy events can be reconstructed much better, if at least one of the SD detector tanks has triggered and its timing information can be used for the event reconstruction. In this “brass hybrid mode” the energy threshold of reconstruction is much lower than for the surface detector alone, where at least five tanks must trigger for good reconstruction quality of all shower parameters.

Therefore, the energy range below $10^{18.5}$ eV is the domain of the Auger FD telescopes. The three new HEAT telescopes will show their full strength also in the hybrid mode.

An SD infill area of 25 km² with fourfold surface detector density close to the HEAT telescopes will raise the hybrid trigger rate considerably and lower the combined threshold for high quality data. The additional large area muon detectors in this area (AMIGA) will further enhance the high capabilities of the PAO South experiment for the determination of the mass distribution of the primary cosmic ray particles.

The installation and commissioning of these two enhancement systems will fit perfectly in the time span between the end of detector commissioning in Argentina and the start of installations for the PAO North experiment in Colorado.

Properties of the HEAT Telescopes

In the context of design studies for the Auger North experiment planned for a Colorado site it became obvious to the FD study group that the quality of the fluorescence telescopes operating in Argentina is very satisfying. Apparently there is no need for major design changes. Therefore, it was decided to keep the main design parameters like the structure of the PMT cameras and the layout for the telescope optics unchanged.

These decisions lead to new requirements for the mechanics of the HEAT telescopes. The existing 24 telescopes are operated in four solid concrete FD buildings. The new systems will be installed in moveable individual enclosures. As several obsolete electronic circuits will have to be replaced anyhow, new designed readout electronics will be used for HEAT, also as baseline design and prototypes for the PAO North FD telescopes.

The three telescope shelters are made from steel structures with lightweight insulating walls. They are design to withstand large wind and snow loads according to the local conditions and legal regulations. Each shelter is built on a heavy platform, a strong steel frame filled with concrete. These platforms can be tilted by 30° using commercial hydraulic drives and heavy duty bearings. The large weight of the ground plates is necessary to reduce wind induced vibrations of the shelters. All critical installations are connected to these solid ground plates only, not to the shelter walls.

Additional fixing bolts and improvements of the mechanical support structures are foreseen in order to ensure the stability of the alignment of the optical system, which is critical both for the telescope pointing and for the optical resolution.

HEAT “Downward” Operation

In the horizontal (“down”) position, installation, commissioning, and maintenance of the hardware are performed. These operations for HEAT are very similar as for the existing telescopes. Also the absolute calibration of the telescopes will be performed only in the horizontal position of the shelters. Possible changes in telescope properties due to the tilting of the whole system will be monitored by a high accuracy relative calibration system based on pulsed LEDs with measurements in both orientations and careful tracing of any gain variations due to e.g. the change of the orientation of the PMTs in the earths magnetic field. Data taking on cosmic ray air showers or laser shots will be possible both in the “up” and in the “down” position. In the “down” orientation the telescopes will cover the same field of view as some of the existing telescopes at the Coihueco building, which is located at a distance of less than 200 m from the HEAT area. A comparison of the reconstruction results for air shower data (or laser scattering events) taken simultaneously by the old and the new telescopes enables a direct determination of the Auger telescope resolution e.g. in energy and X_{\max} as is demonstrated by a set of simulated events in figure 2.

HEAT Tilting Operation

The whole system of ground plate, enclosure and telescope will be tilted by 30° using a hydraulic drive and two heavy bearings. The stability of the mechanics and optics during the tilting will be monitored precisely by multiple sensors for the tilt angle of some of the elements like mirrors, PMT cameras, corrector ring lenses, etc. as well as by vibration sensors to detect wind induced effects and by several other measuring devices for the control of distances between mirrors and the PMT camera, or the corrector ring, respectively. All mechanical monitoring data will be readout and stored by the Slow Control System of HEAT,

which else is similar to the system operating in the already existing four FD buildings.

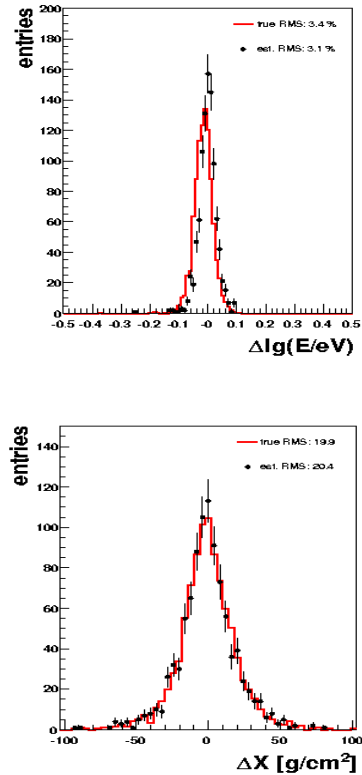


Figure 2: Telescope resolution study simulating a “double-downward” measurement campaign for the energy range above 10^{18} eV.

HEAT “Standard” Operation

With the HEAT enclosures in the “up” position, the combined telescopes cover an elevation range from the horizon to about 60° . As can be seen in the example of a simulated close-by shower event in figure 3 the extended field of view will enable the reconstruction of low energy showers and resolve ambiguities in the X_{\max} determination. HEAT will act as an independent fifth “eye” of the PAO South experiment. The combined shower data of the FD and the HEAT telescopes will lead to better resolutions for the determination of air shower energy and X_{\max} . This effect is present at all energies, but especially in the energy range below 10^{18} eV. The results of the corresponding Monte Carlo simulations are shown in figure 4.

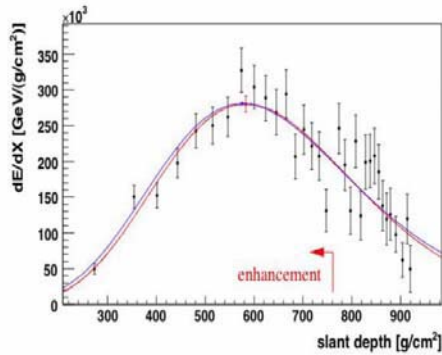


Figure 3: “Data” and reconstruction for a simulated shower with $E = 10^{17.25}$ eV at $R = 1.2$ km. The data measured by the HEAT telescopes (left of the red arrow) would enable the reconstruction.

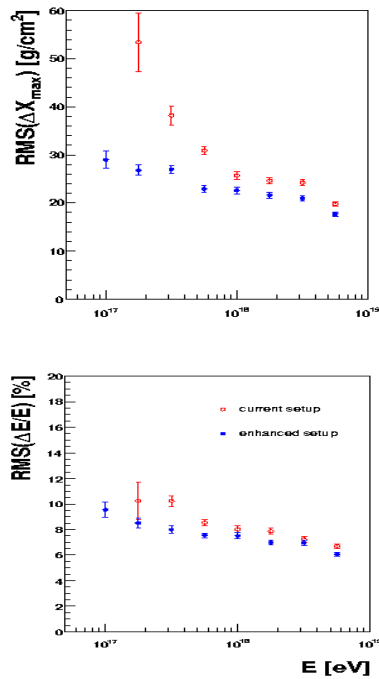


Figure 4: Enhanced reconstruction quality of the Auger FD system by the HEAT telescopes (MC).

By using the additional information of the “brass hybrid triggers”, the combination of the HEAT telescopes with the denser infill array of AMIGA will enable “bias-free” measurements of the air shower elongation rate down to about 10^{17} eV.

The fourfold SD detector density will effectively remove the dependence of the single tank trigger efficiency on the primary CR mass at this energy. The improved quality at low energies can also be seen in the increased trigger and reconstruction efficiencies for nearby showers. The hybrid count rates of the combined HEAT and infill SD array will be sufficient to measure the important parameters for the cosmic ray spectrum and composition above 10^{17} eV with good statistical quality within three years of operation.

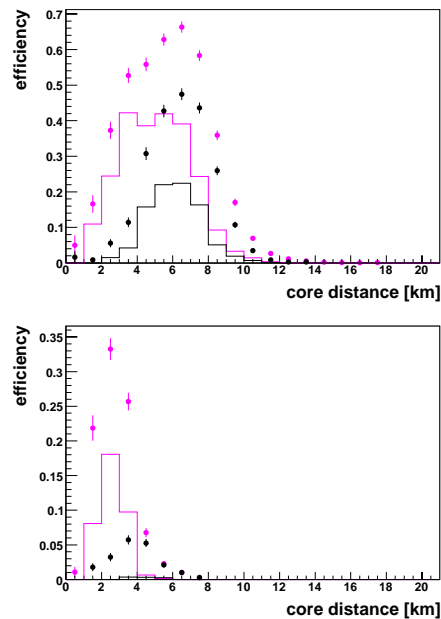


Figure 5: FD trigger probability (dots) and reconstruction efficiency (solid lines) for near showers. Top: at $10^{17.5}$ eV and bottom: at $10^{17.0}$ eV. Black: old FD telescopes, pink: FD + HEAT telescopes.

References

- [1] J. Abraham [Pierre Auger Collaboration] NIM 523 (2004), 50
- [2] A. Etchegoyen, [Pierre Auger Collaboration] these proceedings (2007), #1307
- [3] A. M. van den Berg, [Pierre Auger Collaboration] these proceedings (2007), #0176
- [4] G. Medina Tanco, [Pierre Auger Collaboration] these proceedings (2007), #0991



Longitudinal Shower Profile Reconstruction from Fluorescence and Cherenkov Light

M. UNGER, R. ENGEL, F. SCHÜSSLER AND R. ULRICH

Forschungszentrum Karlsruhe, Postfach 3640, 76021 Karlsruhe, Germany

Michael.Unger@ik.fzk.de

Abstract: Traditionally, longitudinal shower profiles are reconstructed in fluorescence light experiments by treating the Cherenkov light contribution as background. Here we will argue that, due to universality of the energy spectra of electrons and positrons, both fluorescence and Cherenkov light can be used simultaneously as signal to infer the longitudinal shower development. We present a new profile reconstruction method that is based on the analytic least-square solution for the estimation of the shower profile from the observed light signal and discuss the extrapolation of the profile with a Gaisser-Hillas function.

Introduction

During its passage through the atmosphere of the earth an extensive air shower excites nitrogen molecules of the air, which subsequently radiate isotropically ultraviolet fluorescence light. Since the amount of emitted light is proportional to the energy deposited, the longitudinal shower development can be observed by appropriate optical detectors such as HiRes [1], Auger [2] or TA [3].

As part of the charged shower particles travel faster than the speed of light in air, Cherenkov light is emitted in addition. Therefore, in general a mixture of the two light sources reaches the aperture of the detector.

In the traditional method [4] for the reconstruction of the longitudinal shower development the Cherenkov light is iteratively subtracted from the measured total light. The drawbacks of this ansatz are the lack of convergence for events with a large amount of Cherenkov light and the difficulty of propagating the uncertainty of the subtracted signal to the reconstructed shower profile.

It has already been noted in [5] that, due to the universality of the energy spectra of the secondary electrons and positrons within an air shower, there exists a non-iterative solution

for the reconstruction of a longitudinal shower profile from light detected by fluorescence telescopes.

Here we will present the analytic least-square solution for the estimation of the shower profile from the observed light signal in which both, fluorescence and Cherenkov light, are treated as signal.

Scattered and Direct Light

The non-scattered, i.e. direct fluorescence light emitted at a certain slant depth X_i is measured at the detector at a time t_i . Given the fluorescence yield Y_i^f [6, 7] at this point of the atmosphere, the number of photons produced at the shower in a slant depth interval ΔX_i is

$$N_\gamma^f(X_i) = Y_i^f w_i \Delta X_i,$$

where w_i denotes the energy deposited at slant depth X_i (cf. Fig. 1). These photons are distributed over a sphere with surface $4\pi r_i^2$, where r_i denotes the distance of the detector. Due to atmospheric attenuation only a fraction T_i of them can be detected. Given a light detection efficiency of ε , the measured fluorescence light flux y_i^f can be written as

$$y_i^f = d_i Y_i^f w_i \Delta X_i, \quad (1)$$

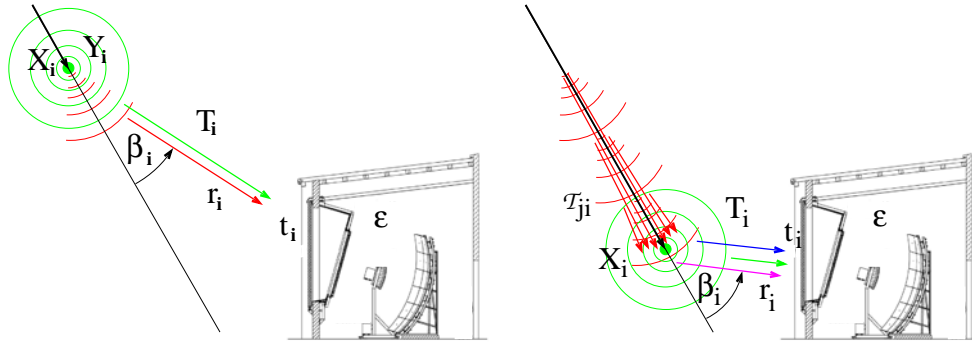


Figure 1: Illustration of the isotropic fluorescence light emission (circles), Cherenkov beam along the shower axis and the direct (left) and scattered (right) Cherenkov light contributions.

where the abbreviation $d_i = \frac{\varepsilon T_i}{4\pi r_i^2}$ was used. For the sake of clarity the wave length dependence of Y , T and ε will be disregarded in the following but be discussed later.

The number of Cherenkov photons emitted at the shower is proportional to the number of charged particles above the Cherenkov threshold energy. Since the electromagnetic component dominates the shower development, the emitted Cherenkov light, N_γ^C , can be calculated from

$$N_\gamma^C(X_i) = Y_i^C N_i^e \Delta X_i,$$

where N_i^e denotes the number of electrons and positrons above a certain energy cutoff, which is constant over the full shower track and not to be confused with the Cherenkov emission energy threshold. Details of the Cherenkov light production like these thresholds are included in the Cherenkov yield factor Y_i^C [5, 8, 9, 10].

Although the Cherenkov photons are emitted in a narrow cone along the particle direction, they cover a considerable angular range with respect to the shower axis, because the charged particles are deflected from the primary particle direction due to multiple scattering. Given the fraction $f_C(\beta_i)$ of Cherenkov photons emitted at an angle β_i with respect to the shower axis [8, 10], the light flux at the detector aperture originating from direct Cherenkov light is

$$y_i^{\text{Cd}} = d_i f_C(\beta_i) Y_i^C \Delta X_i N_i^e. \quad (2)$$

Due to the forward peaked nature of Cherenkov light production, an intense

Cherenkov light beam can build up along the shower as it traverses the atmosphere (cf. Fig. 1). If a fraction $f_s(\beta_i)$ of the beam is scattered towards the detector it can contribute significantly to the total light received. In a simple one-dimensional model the number of photons in the beam at depth X_i is just the sum of Cherenkov light produced at all previous depths X_j attenuated on the way from X_j to X_i by \mathcal{T}_{ji} :

$$N_\gamma^{\text{beam}}(X_i) = \sum_{j=0}^i \mathcal{T}_{ji} Y_j^C \Delta X_j N_j^e.$$

Similar to the direct contributions, the scattered Cherenkov light received at the detector is then

$$y_i^{\text{Cs}} = d_i f_s(\beta_i) \sum_{j=0}^i \mathcal{T}_{ji} Y_j^C \Delta X_j N_j^e. \quad (3)$$

Finally, the total light received at the detector at the time t_i is obtained by adding the scattered and direct light contributions.

Shower Profile Reconstruction

The aim of the profile reconstruction is to estimate the energy deposit and/or electron profile from the light flux observed at the detector. At first glance this seems to be hopeless, since at each depth there are the two unknown variables w_i and N_i^e , and only one measured quantity, namely y_i . Since the total energy deposit

is just the sum of the energy loss of electrons, w_i and N_i^e are related via

$$w_i = N_i^e \int_0^\infty f_e(E, X_i) w_e(E) dE, \quad (4)$$

where $f_e(E, X_i)$ denotes the normalized electron energy distribution and $w_e(E, X_i)$ is the energy loss of a single electron with energy E . As it is shown in [9, 5, 10], the electron energy spectrum $f_e(E, X_i)$ is universal in shower age $s_i = 3/(1 + 2X_{\max}/X_i)$, i.e. it does not depend on the primary mass or energy, but only on the relative distance to the shower maximum, X_{\max} . Eq. (4) can thus be simplified to

$$w_i = N_i^e \alpha_i.$$

where α_i is the average energy deposit per electron at shower age s_i . With this one-to-one relation between the energy deposit and the number of electrons, the shower profile is readily calculable from the equations given in the last section. For the solution of the problem, it is convenient to rewrite the relation between energy deposit and light at the detector in matrix notation: Let $\mathbf{y} = (y_1, y_2, \dots, y_n)^T$ be the n -component vector (histogram) of the measured photon flux at the aperture and $\mathbf{w} = (w_1, w_2, \dots, w_n)^T$ the energy deposit vector at the shower track. Using the ansatz

$$\mathbf{y} = \mathbf{C} \cdot \mathbf{w} \quad (5)$$

the elements of the *Cherenkov-fluorescence matrix* \mathbf{C} can be found by a comparison with the coefficients in equations (1), (2) and (3):

$$C_{ij} = \begin{cases} 0, & i < j \\ c_i^d + c_{ii}^s, & i = j \\ c_{ij}^s, & i > j, \end{cases} \quad (6)$$

where

$$c_i^d = d_i (Y_i^f + f_C(\beta_i) Y_i^C / \alpha_i) \Delta X_i$$

and

$$c_{ij}^s = d_i f_s(\beta_i) \mathcal{T}_{ji} Y_j^C / \alpha_j \Delta X_j.$$

The solution of Eq. (5) can be obtained by inversion, leading to the energy deposit estimator $\hat{\mathbf{w}}$:

$$\hat{\mathbf{w}} = \mathbf{C}^{-1} \cdot \mathbf{y}.$$

Due to the triangular structure of the Cherenkov-fluorescence matrix the inverse can be calculated fast even for matrices with large dimension. As the matrix elements in (6) are always ≥ 0 , \mathbf{C} is never singular.

The statistical uncertainties of $\hat{\mathbf{w}}$ are obtained by error propagation:

$$\mathbf{V}_w = \mathbf{C}^{-1} \mathbf{V}_y (\mathbf{C}^T)^{-1}.$$

It is interesting to note that even if the measurements y_i are uncorrelated, i.e. their covariance matrix \mathbf{V}_y is diagonal, the calculated energy loss values \hat{w}_i are not. This is, because the light observed during time interval i does not solely originate from w_i , but also receives a contribution from earlier shower parts w_j , $j < i$, via the 'Cherenkov beam'.

Wavelength Dependence

Until now it has been assumed that the shower induces light emission at a single wavelength λ . In reality, the fluorescence yield shows distinct emission peaks and the number of Cherenkov photons is proportional to $\frac{1}{\lambda^2}$. In that case, also the wavelength dependence of the detector efficiency and the light transmission need to be taken into account. Assuming that a binned wavelength distribution of the yields is available ($Y_{ik} = \int_{\lambda_k - \Delta\lambda}^{\lambda_k + \Delta\lambda} Y_i(\lambda) d\lambda$), the above considerations still hold when replacing c_i^d and c_{ij}^s in Eq. (6) by

$$\tilde{c}_i^d = \Delta X_i \sum_k d_{ik} (Y_{ik}^f + f_C(\beta_i) Y_{ik}^C / \alpha_i)$$

and

$$\tilde{c}_{ij}^s = \Delta X_j \sum_k d_{ik} f_s(\beta_i) \mathcal{T}_{jik} Y_{jk}^C / \alpha_j,$$

where

$$d_{ik} = \frac{\varepsilon_k T_{ik}}{4 \pi r_i^2}.$$

The detector efficiency ε_k and transmission coefficients T_{ik} and \mathcal{T}_{jik} are evaluated at the wavelength λ_k .

Shower Age Dependence

Due to the age dependence of the electron spectra $f_e(E, s_i)$, the Cherenkov yield factors Y_i^C and the average electron energy deposits α_i depend on the shower maximum, which is not known before the profile has been reconstructed. Fortunately, these dependencies are small: In the age range of importance for the shower profile reconstruction ($s \in [0.8, 1.2]$) α varies only within a few percent [10] and Y^C by less than 15% [5]. Therefore, a good estimate of α and Y^C can be obtained by setting $s = 1$. After the shower profile has been calculated with these estimates, X_{\max} can be determined and the profiles can be re-calculated with an updated Cherenkov-fluorescence matrix.

Gaisser-Hillas Fit

The knowledge of the complete profile is required for the calculation of the Cherenkov beam and the shower energy. If due to the limited field of view of the detector only a part of the profile is observed, an appropriate function for the extrapolation to unobserved depths is needed. A possible choice is the Gaisser-Hillas function [11] which was found to give a good description of measured longitudinal profiles [12]. It has only four free parameters: X_{\max} , the depth where the shower reaches its maximum energy deposit w_{\max} and two shape parameters X_0 and λ .

The best set of Gaisser-Hillas parameters \mathbf{p} can be obtained by minimizing the error weighted squared difference between the vector of function values \mathbf{f}_{GH} and $\hat{\mathbf{x}}$, which is

$$\chi_{\text{GH}}^2 = [\hat{\mathbf{w}} - \mathbf{f}(\mathbf{p})]^T \mathbf{V}_{\mathbf{w}}^{-1} [\hat{\mathbf{w}} - \mathbf{f}(\mathbf{p})]$$

This minimization works well if a large fraction of the shower has been observed below and above the shower maximum. If this is not the case, or even worse, if the shower maximum is outside the field of view, the problem is under-determined, i.e. the experimental information is not sufficient to reconstruct all four Gaisser-Hillas parameters. This complication can be overcome by weakly constraining X_0 and λ to

their average values $\langle X_0 \rangle$ and $\langle \lambda \rangle$. The new minimization function is then the modified χ^2

$$\chi^2 = \chi_{\text{GH}}^2 + \frac{(X_0 - \langle X_0 \rangle)^2}{V_{X_0}} + \frac{(\lambda - \langle \lambda \rangle)^2}{V_{\lambda}},$$

where the variance of X_0 and λ around their mean values are in the denominators.

In this way, even if χ_{GH}^2 is not sensitive to X_0 and λ , the minimization will still converge. On the other hand, if the measurements have small statistical uncertainties and/or cover a wide range in depth, the minimization function is flexible enough to allow for shape parameters differing from their mean values. These mean values can be determined from air shower simulations or, preferably, from high quality data profiles which can be reconstructed without constraints.

References

- [1] T. Abu-Zayyad et al. [HiRes Collaboration]. *Nucl. Instrum. Meth.*, A450:253, 2000.
- [2] J. Abraham et al. [Pierre Auger Collaboration]. *Nucl. Instrum. Meth.*, A523:50, 2004.
- [3] H. Kawai et al. [Telescope Array Collaboration]. *Proc. 29th ICRC*, 8:141, 2005.
- [4] R. M. Baltrusaitis et al. [Fly's Eye Collaboration]. *Nucl. Instrum. Meth.*, A240:410, 1985.
- [5] M. Giller et al. *J. Phys. G*, 30:97, 2004.
- [6] M. Nagano et al. *Astropart. Phys.*, 22:235, 2004.
- [7] F. Kakimoto et al. *Nucl. Instrum. Meth.*, A372:527, 1996.
- [8] A. M. Hillas. *J. Phys. G*, 8:1461, 1982.
- [9] A. M. Hillas. *J. Phys. G*, 8:1475, 1982.
- [10] F. Nerling et al. *Astropart. Phys.*, 24:421, 2006.
- [11] T. K. Gaisser and A. M. Hillas. *Proc. 15th ICRC*, 8:353, 1977.
- [12] Z. Cao et al. [HiRes Collaboration]. *Proc. 28th ICRC*, page 378, 2003.



Comparison of preshower characteristics at Auger South and North

P. HOMOLA¹, M. RISSE², R. ENGEL³, D. GÓRA^{1,4}, J. PEKALA¹, B. WILCZYŃSKA¹, H. WILCZYŃSKI¹

¹*H. Institute of Nuclear Physics PAN, Radzikowskiego 152, 31-342 Kraków, Poland*

²*University of Wuppertal, Department of Physics, Gausstr. 20, 42097 Wuppertal, Germany*

³*Forschungszentrum Karlsruhe, Institut für Kernphysik, 76021 Karlsruhe, Germany*

⁴*Universität Karlsruhe, Institut für Experimentelle Kernphysik, 76128 Karlsruhe, Germany*

Piotr.Homola@ifj.edu.pl

Abstract: Due to geomagnetic cascading, the properties of air showers initiated by photons above 10^{19} eV depend strongly on the arrival direction and on the geographical location of the experimental site. This offers the possibility of a complementary search for such ultra-high energy photons with observatories located at sites with significantly different local geomagnetic field. In this paper we compare the characteristics of photon showers at the southern and northern sites of the Pierre Auger Observatory. The complementarity of the shower features seen by the two sites is demonstrated. We study how this complementarity can be used to search for ultra-high energy photons.

Introduction

Substantial fluxes of cosmic-ray photons at ultra-high energy (UHE), above 10^{19} eV, are predicted by non-acceleration (top-down) models of cosmic-ray origin (for example, see [2]). At a smaller level, UHE photons are also expected to be produced in acceleration (bottom-up) models [4]. So far, upper limits on the photon flux were set (see [15] and references therein). The large exposure expected to be collected during the next years, in particular by the Pierre Auger Observatory [12], will enormously increase the sensitivity for detecting UHE photons [13].

Contrary to the case of hadron primaries, UHE photons around 10^{20} eV can interact with the geomagnetic field before entering the atmosphere [10] producing a bunch of lower energy particles. This process is commonly called geomagnetic cascading or preshower and leads to a dramatic change of the air shower development for primary photons (see [7] and references therein). The probability of magnetic e^+e^- pair production (“photon conversion”) and, in case of conversion, the synchrotron emission by the produced electrons depend on the particle energy and on the transverse component of the local magnetic field [3, 6]. This implies

the dependence of the expected properties of the photon-induced shower on the primary arrival direction within the local coordinate system and on the geographic location of the experiment [10].

In this work we study how the preshower characteristics affects the properties of air showers for the conditions of the southern part of the Auger Observatory (“Auger South”) situated in Malargue (Argentina) at 69.2° W, 35.2° S and its northern part (“Auger North”) planned in Colorado (USA) at 102.7° W, 37.7° N. The geomagnetic field vector differs significantly between these two sites: at Auger South, the magnetic field of $\sim 24.6 \mu T$ points upward to $\theta \sim 55^\circ$, $\phi \sim 87^\circ$ while at Auger North, the magnetic field of $\sim 52.5 \mu T$ points downward from $\theta \sim 25^\circ$, $\phi \sim 262^\circ$.¹ It is also considered how the different properties of photon-showers at the two sites can be used to perform a complementary search for UHE photons.

While the study is performed for the specific case of the two Auger sites, the general findings hold for any two sites with sufficiently different local magnetic field conditions.

¹ Azimuth is defined in this work counterclockwise from geographic East. For instance, $\phi = 0^\circ$ means East, $\phi = 90^\circ$ North etc.

Conversion of an UHE energy photon at Auger South and North

A key parameter to characterize the fate of an UHE photon in the Earth's magnetic field is the conversion probability P_{conv} . Given the local differential probability of a photon to convert into an electron pair, P_{conv} results from an integration along the particle trajectory. Small values of P_{conv} indicate a large probability of the UHE photon to enter the atmosphere without conversion and to keep its original identity. In turn, UHE photons would almost surely undergo geomagnetic cascading for values of P_{conv} close to unity.

P_{conv} depends on the experimental site, the photon energy, and the direction of the particle trajectory in the local coordinate system of zenith θ and azimuth ϕ , $P_{\text{conv}} = f(\text{site}, E, \theta, \phi)$. Thus, for a chosen site and a fixed primary photon energy, sky maps within the local coordinate system $P_{\text{conv}} = f(\theta, \phi)$ can be produced to study the pattern of UHE photon conversion. As an example, in Figure 1 two such sky maps are shown for two different geographical locations, Auger South and Auger North, and for one primary energy of 100 EeV. One can see significant differences in P_{conv} between the two sites for a given direction in terms of local coordinates. As expected, small conversion probabilities are found for sky regions around the pointing direction of the local magnetic field vector.

It is clear from Fig. 1 that cuts on the local shower arrival direction can be introduced to select regions of the sky where P_{conv} is larger (or smaller) at one site compared to the other site. A possible photon signal could then show up with *different* signatures at the two sites for the *same* selection cuts.

Air showers initiated by converted and unconverted photons

It is well known that unconverted photon showers, contrary to converted, have a considerably delayed development due to the LPM effect [9, 11]. Additionally, event-by-event fluctuations can be extraordinarily large due to a positive correlation of the suppression of the cross-section with air density. To demonstrate how this effect can be seen at

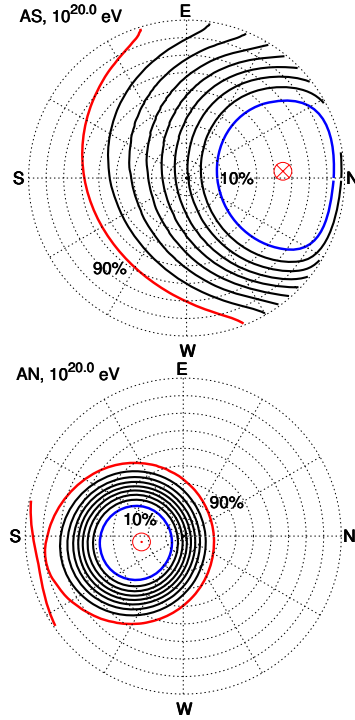


Figure 1: Exemplary sky maps of conversion probabilities at $\lg(E/\text{eV})=20.0$ for Auger South (AS, top) and Auger North (AN, bottom). Contour lines are given for the conversion probability with a step-size of 10%. Azimuthal directions are labeled (“E” for East etc.). Zenith angles are given as concentric circles of 10° steps ($\theta = 0^\circ$ in the center). The pointing direction of the local magnetic field vector at ground is indicated for a specific site.

two different locations, detailed simulations were carried out with CONEX [14, 1], which reproduces well CORSIKA [5] results. All the primaries were simulated at energies of 10^{20} eV with two different local arrival directions and two different observation sites: Auger North and South. 1000 photon events per each combination of site and arrival direction were simulated, and hadron showers (simulated with QGSJET 01 model [8]) were added for comparison. The resulting distributions of depth of shower maximum X_{max} are shown in Figure 2. In the upper panel all the primaries arrived from geographic North at 45° zenith. For this particular direction the photon conversion probability is large at Auger North ($> 99.9\%$) and small

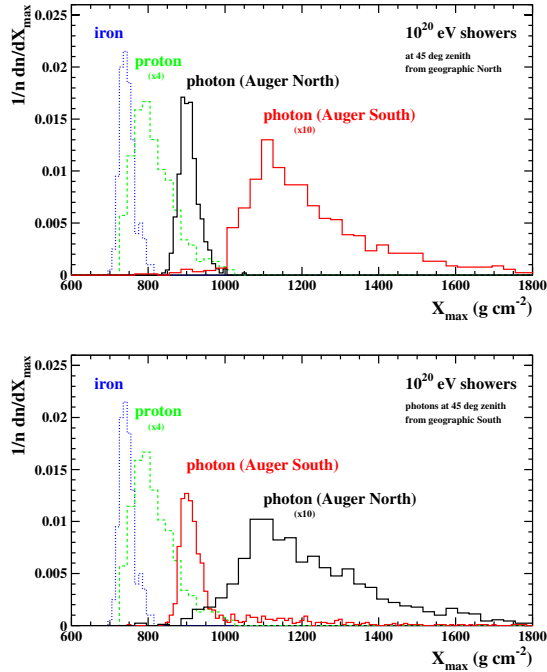


Figure 2: *Upper panel:* X_{\max} distributions of different primaries arriving from local geographic North). *Lower panel:* same as in upper panel, but the photon simulations were performed with the azimuth changed by 180° (photons arriving from local geographic South). If indicated, distributions were scaled.

at Auger South (0.4%). Consequently, most of the photons at Auger North convert and have a depth of shower maximum $200\text{--}300\text{ g cm}^{-2}$ smaller than the (mostly unconverted) photon showers at Auger South. As expected, also fluctuations are much smaller at Auger North in this example. The opposite behavior can be seen for the arrival direction with the azimuth changed by 180° (lower panel of Fig. 2). As expected from Figure 1, the X_{\max} distribution of photons at Auger South is now peaked at smaller values, while the distribution at Auger North is dominated by the large X_{\max} values from unconverted events.

From the above example it is clear that for the same local directions, the expected features of photon showers can be very different at two different sites.

There are other shower observables, especially from ground arrays, that were shown (or are expected) to differ between converted and unconverted photons. However, as discussed in Ref. [7], a study of X_{\max} distributions provides us with most relevant information for investigating possible complementary features of both sites.

UHE photon scenarios and their observation at Auger South and North

The complementarity between the preshower characteristics at Auger North and South can be taken as an advantage when searching for the presence of the photon component in the cosmic-ray flux at highest energies. Photons can manifest themselves at Earth within different scenarios. One of such scenarios, a diffuse photon signal, is considered below as an example. The other possibilities, e.g. a signal from a source region or the absence of photons are discussed in Ref. [7].

An isotropic primary flux with the all-particle energy power law spectrum with index -2.84 is assumed. Such a spectrum is consistent with the first estimate from the Auger South Observatory [16]. We assume protons and photons as primaries and the input fraction of photons as a function of primary energy follows the results from a topological defect model in [4]. For each Auger site, we simulated ~ 1000 events above $\lg(E/\text{eV}) = 19.6$ with zenith angles between $30\text{--}75^\circ$ and random azimuth. We accounted for a detector resolution of 25 g cm^{-2} in X_{\max} and 10% in primary energy. The zenith angle range was chosen similar to that in the analysis of Auger data for the first photon limit [13]. For other details and specifications the reader is referred to Ref. [7].

In Figure 3 we show average X_{\max} as a function of energy. We restricted the azimuth range in this plot to the local *northern* sky by requiring an azimuth between $30\text{--}150^\circ$. In this region of the sky, photon conversion starts at Auger North at smaller energies than at Auger South.

As expected, there are considerably fewer events with large X_{\max} (e.g. exceeding 1000 g cm^{-2}) at Auger North, for the same overall cuts applied to the data at both sites. Additionally, the larger average X_{\max} at Auger South is accompanied by sig-

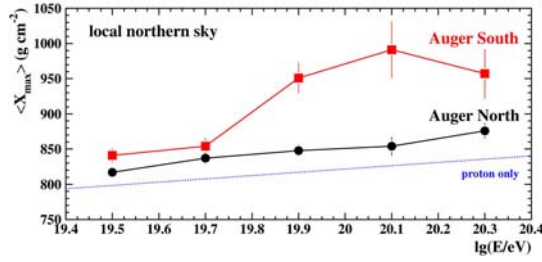


Figure 3: Average X_{\max} vs. energy for the local northern sky (for definition see the text) at Auger North and at Auger South. For comparison, values corresponding to a pure proton flux are also shown using the model QGSJET 01 (dotted blue line).

nificantly increased shower fluctuations (for a reference plot see Ref. [7]). An observation of such different characteristics at Auger North and South would be an unambiguous confirmation of a photon signal detection.

The above conclusions are not changed for the cosmic ray spectrum with the GZK cut-off. For a discussion and a quantitative example of applying a simple cut-off to the power law energy spectrum the reader is referred to Ref. [7].

Conclusion

The difference of conversion probabilities is a convenient and effective parameter to estimate the complementarity between two sites for searching for UHE photons. Regarding the two sites of the Pierre Auger Observatory, Auger North and Auger South, significant differences in the preshower features of UHE photons exist. These differences in the preshower characteristics result in different rates of (un-)converted photons from the same (both in local and astronomical coordinates) regions of the sky. Air showers initiated by converted and unconverted photons can be well distinguished by current experiments. The main difference is related to the position of depth of shower maximum X_{\max} , which is typically $\sim 200\text{--}300 \text{ g cm}^{-2}$ smaller for converted photons.

For a variety of UHE photon flux scenarios (diffuse photon flux; photons from source regions; absence of photons), the different preshower characteristics

at the experimental sites can be used for a complementary search for UHE photons. Most important, a possible detection of UHE photons at Auger South may be confirmed in an unambiguous way at Auger North by observing the well predictable change in the signal from UHE photon showers.

Acknowledgements

This work was partially supported by the Polish Ministry of Science and Higher Education under grants No. N202 090 31/0623 and PAP/218/2006 and in Germany by the DAAD under grant No. PPP 323. MR acknowledges support from the Alexander von Humboldt foundation.

References

- [1] T. Bergmann et al. *astro-ph/0606564*, 2006.
- [2] P. Bhattacharjee and G. Sigl. *Phys. Rep.*, 327:109, 2000.
- [3] T. Erber. *Rev. Mod. Phys.*, 38:626, 1966.
- [4] G. Gelmini et al. *astro-ph/0506128*, 2005.
- [5] D. Heck et al. *Reports FZKA 6019 & 6097*. Forschungszentrum Karlsruhe, 1998.
- [6] P. Homola et al. *Comp. Phys. Comm.*, 173:71, 2005.
- [7] P. Homola et al. *Astropart. Phys.*, 27:174, 2007.
- [8] N.N. Kalmykov et al. *Nucl. Phys. B (Proc. Suppl.)*, 52:17, 1997.
- [9] L.D. Landau and I.Ya. Pomeranchuk. *Dokl. Akad. Nauk SSSR*, 92:535 & 735, 1953.
- [10] B. McBreen and C.J. Lambert. *Phys. Rev. D*, 24:2536, 1981.
- [11] A.B. Migdal. *Phys. Rev.*, 103:1811, 1956.
- [12] J. Abraham et al., P. Auger Collaboration. *Nucl. Instrum. Meth. A*, 523:50, 2004.
- [13] J. Abraham et al., P. Auger Collaboration. *Astropart. Phys.*, 27:155, 2007.
- [14] T. Pierog et al. *Nucl. Phys. B (Proc. Suppl.)*, 151:159, 2006.
- [15] M. Risse and P. Homola. *Mod. Phys. Lett. A*, 22:749, 2007.
- [16] P. Sommers for the P. Auger Collaboration. *Proc. 29th Intern. Cosmic Ray Conf., Pune.*, 7:387, 2005.



Variation of the shower lateral spread with air temperature at the ground

B. WILCZYŃSKA¹, R. ENGEL², P. HOMOLA¹, B. KEILHAUER³, H. KLAGES², J. PEKALA¹, H. WILCZYŃSKI¹.

¹*Institute of Nuclear Physics PAN, Radzikowskiego 152, 31-342 Kraków, Poland*

²*Forschungszentrum Karlsruhe, Institut für Kernphysik, 76021 Karlsruhe, Germany*

³*Universität Karlsruhe, Institut für Experimentelle Kernphysik, 76128 Karlsruhe, Germany*

Barbara.Wilczynska@ifj.edu.pl

Abstract: The vertical profile of air density at a given site varies considerably with time. Well understood seasonal differences are present, but sizeable effects on shorter time scales, like day-to-day or day-to-night variations, are also present. In consequence, the Molière radius changes, influencing the lateral distribution of particles in air showers and therefore may influence shower detection in surface detector arrays. In air shower reconstruction, usually seasonal average profiles of the atmosphere are used, because local daily measurements of the profile are rarely available. Therefore, the daily fluctuations of the atmosphere are not accounted for. This simplification increases the inaccuracies of shower reconstruction. We show that a universal correlation exists between the ground temperature and the shape of the atmospheric density profile, up to altitudes of several kilometers, hence providing a method to reduce inaccuracies in shower reconstruction due to weather variation.

Introduction

In experimental studies of highest energy cosmic rays, the atmosphere serves both as the target in which primary cosmic rays interact and the medium in which extensive air showers develop. Therefore, as precise as possible knowledge of properties of the atmosphere is very important. In particular, the vertical profile of air density is of primary importance.

It was shown in [3, 4, 5] that the time variability of the vertical profile of air density (and consequently, atmospheric depth) is very important. Systematic, site-specific seasonal variation of the atmospheric profile is observed. In addition, irregular variation is observed on shorter time scales like day-to-day or day-to-night. Variation of the atmospheric density implies a variation of the Molière radius and in consequence, the lateral spread of air shower particles varies accordingly. Therefore, uncertainties of the profile of air density influence air shower detection in surface detector arrays. A trigger bias may result from inaccurate accounting for lateral spread of shower particles. Thus it is important to

account for atmospheric variation as accurately as possible to avoid errors in shower reconstruction.

In this paper we use UK Met Office data [1] to study the vertical profile of air density. These data contain temperature and pressure profiles measured by radiosondes at a worldwide network of balloon launching stations. In the following we present an analysis of data collected in years 2002–2004 at the station in Salt Lake City (USA) and at the station in Mendoza (Argentina), located near the site of the southern Pierre Auger Observatory.

Lateral particle distribution

The lateral particle distribution in a shower is determined by the Molière radius, which is inversely proportional to air density. This distribution observed at the ground level is shaped mainly in a lowest layer of the atmosphere, about two cascade units thick, above the ground.

The vertical distribution of air density, and consequently the Molière radius, varies a lot from the model distribution usually assumed in air shower studies. It was shown in [5] that this variation is

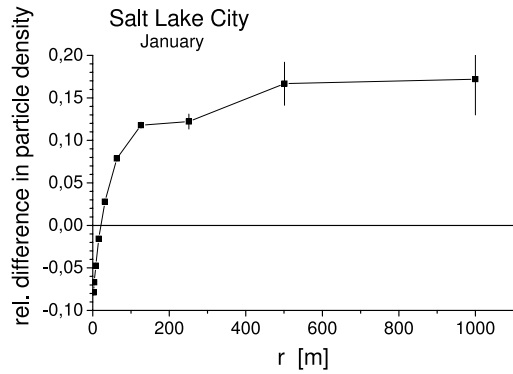


Figure 1: Relative difference in lateral distribution of particle density in a vertical 10^{19} eV proton shower simulated using atmospheric profiles in two extreme January days at Salt Lake City.

especially large in winter. As an example, January atmospheric profiles at Salt Lake City were used to simulate shower development. Showers simulated using different atmospheric profiles differ considerably in lateral particle distribution. Lateral distributions of a 10^{19} eV proton shower were simulated with CORSIKA [2] using atmospheric profiles of extremely warm and cold days in January. The relative difference of the lateral particle density is shown in Figure 1. This difference can be as large as 15% at large distances from the shower axis. Although it may be treated as an upper limit rather than a typical value, one should note that the 15% variation in particle density due to weather effects alone is a very large difference. This example demonstrates the need for a profile of atmospheric density as accurate as possible.

Local daily soundings of the atmosphere are rarely available at air shower detector sites, so that one has to use some average profiles of air density in everyday shower reconstruction. Neglecting the daily variation of the atmosphere introduces inaccuracies in shower reconstruction. Therefore, an important question is whether one can approximate the true atmospheric profile based on some easily available data, like temperature and pressure at ground level, when the radiosounding is not available. This is the subject of the current study.

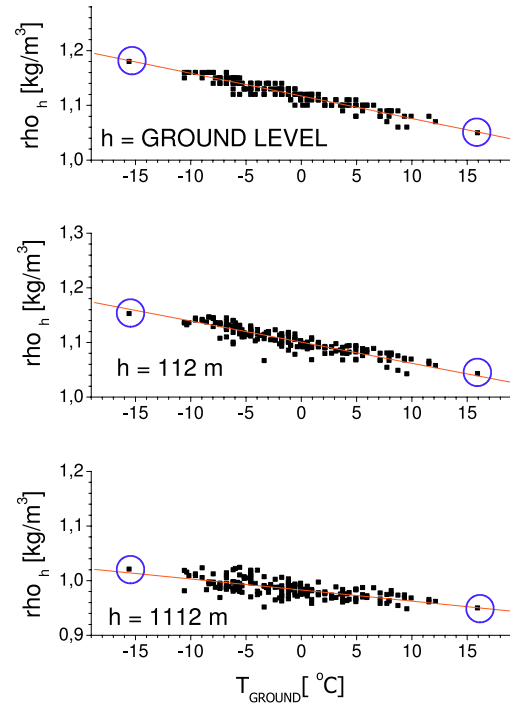


Figure 2: Example of correlation of air density at two different altitudes above ground, with temperature at the ground level. The circles mark the extremely warm and cold days used to prepare Fig.1.

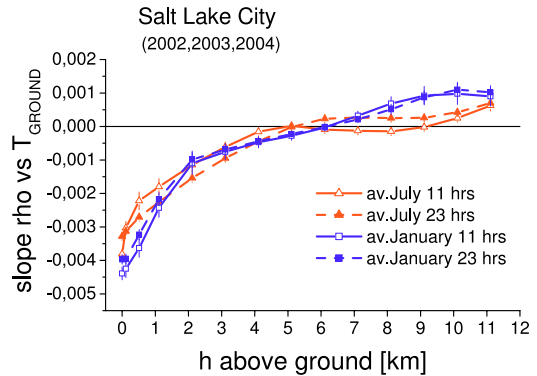


Figure 3: Slope of the correlation shown in Fig.2 as a function of altitude, at different times of day in summer and winter at Salt Lake City.

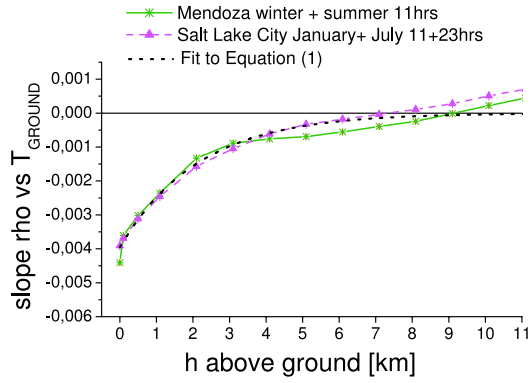


Figure 4: Comparison of the correlation slopes at Salt Lake City and Mendoza. The dotted line represents the fits of Eq.1.

Air density correlation with ground temperature

A correlation exists between air temperature *at the ground level* and air density *at altitudes above ground*, as shown in Fig.2. This correlation can be well approximated by a linear relation. The spread of the data points reflects the influence of atmospheric pressure variation on air density. Thus the variation of temperature appears to be more important.

The slope of the linear correlation of Fig.2 is shown in Fig.3 as a function of altitude above ground. The correlation appears to be quite independent of seasons or time of day. It is strongest at the ground level and fades away with increasing altitude. A similar pattern of air density correlation with the ground temperature is observed in Mendoza. Dependences of the correlation slope on altitude at Salt Lake City and at Mendoza are compared in Fig.4.

The slope of the correlation presented in Fig.4 can be well parameterized by an exponential function

$$\alpha(h) = A \exp(-h/B) \quad (1)$$

where h is the altitude above ground. The fitted values of the parameters for Salt Lake City are: $A = -0.0040 \pm 0.0002 \text{ kg/m}^3/\text{°C}$, $B = 2.15 \pm 0.25 \text{ km}$ and for Mendoza: $A = -0.0040 \pm 0.0002 \text{ kg/m}^3/\text{°C}$, $B = 2.21 \pm 0.23 \text{ km}$. These fits are

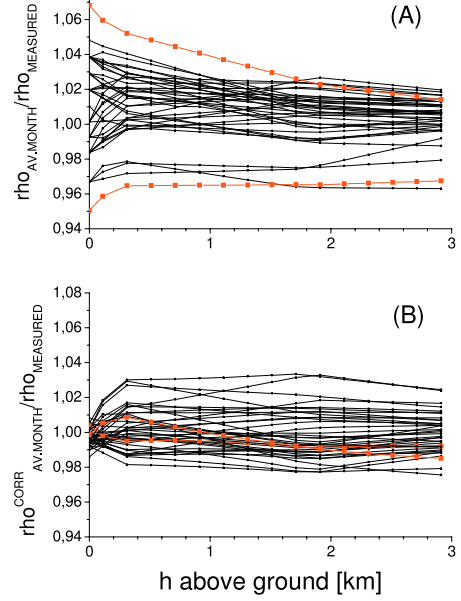


Figure 5: (A) Ratios of the average monthly profile of air density to profiles actually measured in many January days at Salt Lake City; (B) Ratios of the corrected average profile to daily measurements.

shown in Fig.4 by the dotted lines (the two lines overlap). Therefore one can conclude that the correlation of air density *at a given altitude above ground* with temperature *at the ground level* is universal, with very little dependence on site location, season or time of day. If so, this correlation may be used to refine extensive air shower studies.

Correction to the profile of air density

Results of the previous section indicate that the actual profile of air density $\rho(h)$ can be approximated using an average (e.g. monthly) profile $\rho^{\text{avg}}(h)$, with a correction depending on a deviation of the ground temperature T_G from the average T_G^{avg} :

$$\rho^{\text{corr}}(h) = \rho^{\text{avg}}(h) + \alpha(h)(T_G - T_G^{\text{avg}}) \quad (2)$$

where $\alpha(h)$ is the slope of the linear correlation of air density with ground temperature given by Eq.1.

The actual daily profiles of air density over Salt Lake City are compared with the average monthly

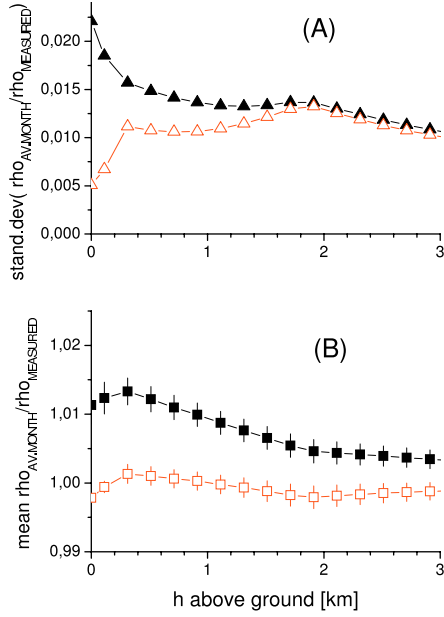


Figure 6: (A) Standard deviation and (B) mean of ratios shown in Fig.5 as a function of altitude. The filled symbols pertain to uncorrected density profiles of Fig.5A, while the open symbols concern the corrected profiles of Fig.5B.

profile. In Fig.5A ratios of the average to the daily measured ones are plotted. A relatively large spread (several percent), especially near the ground level, is seen. In Fig.5B the ratios of $\rho^{\text{corr}}(h)$ to the actually measured ones are plotted. It is evident that the correction of Eq. 2 considerably reduces the dispersion of the density ratios at low altitudes. This means that at low altitudes $\rho^{\text{corr}}(h)$ approximates the actual profile considerably better than the monthly average does. This is illustrated in Fig.6, in which the mean and standard deviation of the sets of curves plotted in Fig.5 are shown as a function of altitude. The correction effectively works only at low altitudes, as the correlation shown in Fig.4 vanishes with increasing altitude. Nevertheless, we note that the lateral distribution of shower particles at the ground level is determined mainly by the Molière radius over lowest two cascade units, i.e. over lowest ~ 750 m above ground, in case of the Pierre Auger Observatory.

Conclusion

The observed correlation of ground temperature with air density at altitudes up to several kilometers above ground provides a method to approximate the true profile of atmospheric density. For shower reconstruction it is always best to use the local daily measurement of the atmospheric profile. However, when the actual measurement of the profile is not available for a given day, an approximation of the daily profile can be derived from an average (e.g. monthly) profile, adjusted with a correction depending only on temperature at the ground. Since the temperature reading at ground is always available, this correction helps to reduce inaccuracies in shower reconstruction, especially in surface arrays of detectors.

Acknowledgements

This work was partially supported by the Polish Ministry of Science and Higher Education under grants No. N202 090 31/0623 and PAP/218/2006 and in Germany by the DAAD under grant No. PPP323. One of the authors (BK) is supported by the DFG under grant No. KE 1151/1.

References

- [1] British Atmospheric Data Centre. <http://badc.nerc.ac.uk/data/radiosglobe/radhelp.html>.
- [2] D. Heck et al. *Reports FZKA 6019 and 6097, Forschungszentrum Karlsruhe*, 1998.
- [3] B. Keilhauer et al. *Astropart. Phys.*, 22:249, 2004.
- [4] B. Wilczynska et al. *Proc. 29th ICRC, Pune*, 7:203, 2005.
- [5] B. Wilczynska et al. *Astropart. Phys.*, 25:106, 2006.



Simulation study of shower profiles from ultra-high energy cosmic rays

V. SCHERINI¹, F. SCHÜSSLER², R. ENGEL², K.-H. KAMPERT¹, M. RISSE¹, M. UNGER².

¹*Bergische Universität Wuppertal, Wuppertal, Germany*

²*Forschungszentrum Karlsruhe, Karlsruhe, Germany*

scherini@physik.uni-wuppertal.de

Abstract: The identification of the primary particle type can provide important clues about the origin of ultra-high energy (UHE) cosmic rays above 10^{18} eV. The depth of shower maximum of the air shower profile offers a good discrimination between different primaries. This observable is usually extracted from a fit to the longitudinal shower profile. Recently it has been used to obtain a limit to photons from data taken by the Pierre Auger Observatory. In this paper we study the fit quality that is obtained with different functional forms for simulated shower profiles of nuclear and photon primaries. The impact of the functional form on the extrapolation to non-observed parts of the profile is commented on. We also investigate to what extent additional profile parameters such as the width of the profile or a reconstructed “first interaction” of the cascade can be exploited to improve the discrimination between the primaries.

Introduction

Determining the composition of the UHE cosmic rays above the knee region is one of the challenges in cosmic rays detection. In particular the Fluorescence Detector of the Pierre Auger Observatory is observing directly the longitudinal shower development in the atmosphere. The detected light intensity, including the Fluorescence and Cherenkov direct and scattered contributions, and taking into account the atmospheric effects, is proportional to the energy deposited at each depth.

The so called longitudinal shower profile, in shower size or energy deposit, as a function of atmospheric slant depth can be reconstructed with good accuracy and the non-observed part extrapolated. As a matter of fact the shower profile can be well described by a trial function (GH) originally proposed by Gaisser and Hillas [1]:

$$GH(X) = \frac{dE}{dX} \Big|_{X_{max}} \left(\frac{X - X_0}{X_{max} - X_0} \right)^{\frac{(X_{max} - X_0)}{\lambda}} \cdot \exp \frac{(X_{max} - X)}{\lambda} \quad (1)$$

where X_{max} is the position of shower maximum in slant depth, $\frac{dE}{dX} \Big|_{X_{max}}$ is the energy deposit at shower maximum.

X_0 and λ are strongly correlated and connected with the starting point and width of the curve, but cannot directly be interpreted as the first interaction point and interaction length, as already pointed out in [2].

The observable X_{max} has good discriminating power between the different primaries inducing the cascade. The average value of the simulated distribution for photons differs from that of hadrons by about 200 gcm^{-2} at 10 EeV. This evidence was used to set a limit to the photon fraction of the total flux [3] and for a recent update see [4].

Composition sensitivity of profile shape

The basic idea of this study is the search of further sensitive observables to enhance the discrimination power between different primaries. Photon selection could be contaminated by late developing hadron cascades, in particular from deeply fluctuating protons.

In Fig. 1 the energy deposit as a function of slant depth for some example profiles is plotted (dashed blue line for photons, thick red line for protons).

The protons have been chosen to have a deep value of the shower maximum, compatible with the photon average distribution.

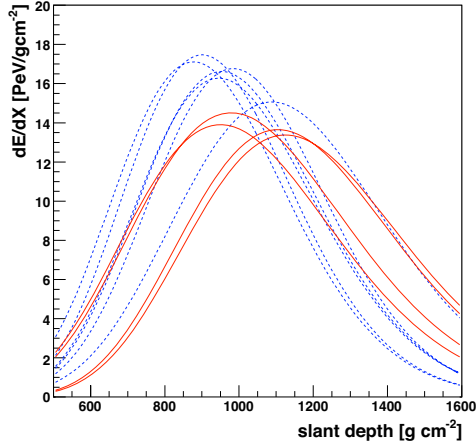


Figure 1: Example of $\frac{dE}{dX}$ profiles of simulated showers induced by photons (dashed blue line) and protons (thick red line) at 10 EeV. The proton profiles have been chosen to have a value of X_{max} compatible with photons.

A dedicated study has been performed on a set of simulated CORSIKA [5] showers induced by different primary particles. The sample consists of 750 protons, 500 iron nuclei, and 800 photons at an energy of 10 EeV (FLUKA [6] and QGSJET1 [7] as low and high-energy hadronic interaction models). The possibility to exploit the information of the profile shape, like for instance the width, has been investigated.

Other proposed trial functions, like a gaussian [8, 9] and double gaussian [10] in shower age, have been included in the fitting routine and tested on the same set of simulated events. Finally, a detailed study on the parameters correlations and the Principal Component Analysis (PCA) have been performed. Results are presented in the following sections.

CORSIKA profile and Gaisser-Hillas fit

The longitudinal profile of each event is recorded in the CORSIKA output file, together with the result of a 6-parameter Gaisser-Hillas fit. The definition of λ , see Eq. 1, is replaced here by a quadratic function of the atmospheric depth.

This fit is found to be robust for deriving X_{max} but less efficient in adapting the shape of the GH curve to the data points. This may be connected with the limited number of profile points, especially in the falling side of the shower development.

A more effective 4-parameters constrained fit with the GH function has been implemented as in [11]. The X_{max} value agrees to CORSIKA better than 1 g cm^{-2} . In Tab. 1 the average slant X_{max} and the RMS values of the distribution for iron, proton and photon showers are summarised. The average X_{max} value for photons differs from that of hadrons by $\sim 200 \text{ g cm}^{-2}$.

Table 1: Average and RMS of the X_{max} distribution for the simulated primaries at 10 EeV.

| | $\langle X_{max} \rangle [\text{g cm}^{-2}]$ | RMS $[\text{g cm}^{-2}]$ |
|--------|--|--------------------------|
| Iron | 695 | 22 |
| Proton | 780 | 67 |
| Photon | 969 | 59 |

Other trial functions and PCA analysis

The longitudinal profile can be translated into shower age s by means of the following transformation:

$$s(X) = \frac{3X}{X + 2X_{max}} \quad (2)$$

that aligns the profiles at $s(X_{max}) = 1$ and is scale-free. The shower starting point is in this case set to 0, but could be re-introduced as the fourth fit parameter substituting X with $(X - X_1)$. The normalised profile can be then fitted by the following gaussian function in age (AG):

$$AG(s) = \exp\left(-\frac{1}{2\sigma^2}(s-1)^2\right) \quad (3)$$

where the free parameters are σ and X_{max} , together with $\frac{dE}{dX}|_{X_{max}}$.

Following [10] we can employ a double gaussian (2G) with two different widths corresponding to the shower development before and after the shower maximum. The free parameters are in this case again four.

In Fig. 2 the average relative residuals, as a function of shower age, obtained with the tested analytical fit functions are plotted for the proton sample. In Tab. 2 the mean and RMS values of the σ of the gaussian for the simulated iron, proton and photon showers are summarised. The correlation between the width of the gaussian AG and the depth of shower maximum is shown in Fig. 3. A later development of the cascade is associated with a narrower profile width. Similar average values and the same correlation are found between the rising edge σ and the X_{max} for the 2G fit, in agreement with the previously cited works.

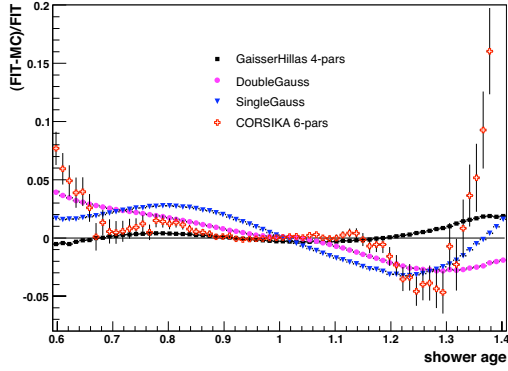


Figure 2: Average relative residuals to the tested analytical functions for protons at 10 EeV: 4-parameters GH fit (black squares), single gaussian (blue triangles), double gaussian (pink bullets), and 6-parameters CORSIKA (red crosses).

Using X_1 as a free parameter in the fitting process we observe a correlation with σ that can be represented, both for hadrons and photons, by a straight line. This correlation is shown in Fig. 4 for the simulated sets of iron, proton and photon

Table 2: Average and RMS values of the σ distributions for the simulated primaries at 10 EeV.

| | $\langle \sigma \rangle$ [g cm^{-2}] | RMS [g cm^{-2}] |
|--------|---|----------------------------|
| Iron | 0.22 | 0.006 |
| Proton | 0.20 | 0.015 |
| Photon | 0.16 | 0.011 |

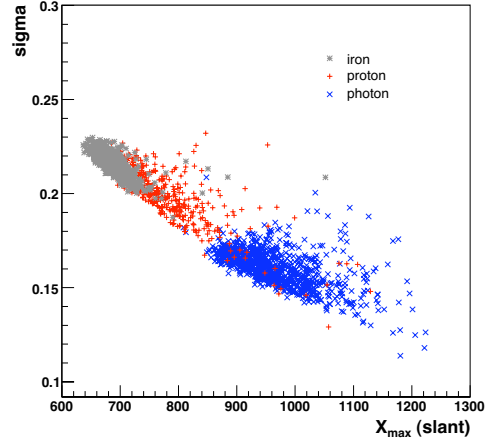


Figure 3: Correlation between the width of the gaussian (AG) and depth of shower maximum for showers initiated by iron, proton and photon primaries, respectively marked as grey stars, red crosses and blue \times .

primaries, respectively marked by grey stars, red crosses and blue \times .

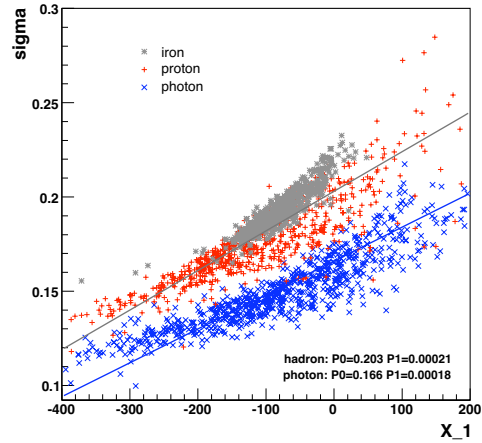


Figure 4: Correlation between σ and X_1 for the gaussian fit, same color code as Fig. 3.

The possibility to exploit the information carried by the σ has been quantified applying the Principal Component Analysis (PCA).

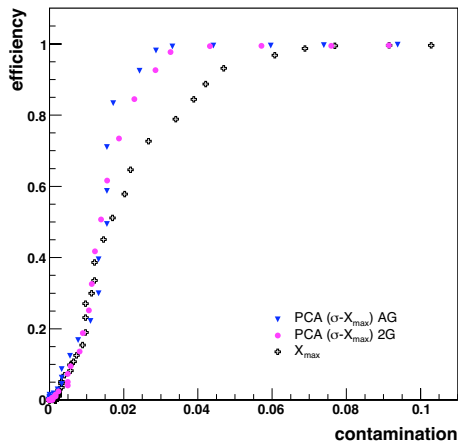


Figure 5: Efficiency for accepted photons as a function of hadron contamination in the PCA-transformed variable (combined σ and X_{max}) for the single gaussian (blue triangles) and for the double gaussian (pink bullets) compared to the X_{max} cut (black crosses for AG).

In Fig. 5 the efficiency of a cut for accepted photons in the PCA transformed variable is plotted as a function of the hadron contamination. Blue triangles refer to the single gaussian fit and pink bullets to the double gaussian fit. The photon-hadron separation power of a cut in the PCA variable compared to a X_{max} cut on the data set (black crosses for the AG) is clearly enhanced in both cases. Other PCA tests, on the variables from the GH and gaussian fits, gave less evident results.

Conclusions

We have verified that the depth of shower maximum, X_{max} , has a very good discriminating power between cosmic rays primary particles. The quality of the different fitting functions and the correlation between the fit free parameters have been checked.

The possibility to exploit further information, as for instance the width of the shower profile or the shower starting point, has been investigated. The hadron-photon separation power of a simple X_{max} cut has been quantified and compared to the one

achievable combining other sensitive observables. The PCA analysis shows that the best cut is the one that combines X_{max} with the single gaussian σ . An enhancement of the hadron-photon separation power is found, both for AG and 2G fits.

Other PCA tests, e.g. adding another variable from the GH or gaussian fits, gave less evident results. Further tests on those observable are planned especially for the Pierre Auger Fluorescence Detector including its full detector simulation.

Acknowledgements

The authors would like to thank the Karlsruhe and Wuppertal groups for support. Moreover Dieter Heck, Lorenzo Perrone and Julian Rautenberg for helpful suggestions.

References

- [1] T. K. Gaisser and A. M. Hillas. volume 8 of *International Cosmic Ray Conference*, page 353, 1977.
- [2] HIRES collaboration. *Astroparticle Physics*, 16:1–11, 2001.
- [3] Pierre Auger Collaboration. *Astropart. Phys.*, 27:155–168, 2007.
- [4] D. Barnhill, M. Healy, M. Risse, C. Roucelle, V. Scherini, B. Smith, and C. Wileman. 0602, At this Conference.
- [5] D. Heck et al. *Report FZKA 6019*, 1998.
- [6] A. Fassò, A. Ferrari, J. Ranft, and B. E. Sala. *CERN-2005-10, INFN/TC_05/11, SLAC-R-773*.
- [7] N. N. Kalmykov and S. S. Ostapchenko. *Physics of Atomic Nuclei*, 56:346–353, 1993.
- [8] HIRES Collaboration. volume 2 of *International Cosmic Ray Conference*, page 490, 2001.
- [9] C. Song, Z. Cao, B. R. Dawson, B. E. Fick, P. Sokolsky, and X. Zhang. *Astroparticle Physics*, 14:7–13, 2000.
- [10] M. Giller, A. Kacperczyk, J. Malinowski, W. Tkaczyk, and G. Wieczorek. *Journal of Physics G Nuclear Physics*, 31:947–958, 2005.
- [11] M. Unger et al. 0972, At this Conference.



Contribution of atmospheric scattering of light to shower signal in a fluorescence detector

J. PEKALA¹, D. GÓRA^{1,2}, P. HOMOLA¹, M. RISSE³, B. WILCZYŃSKA¹, H. WILCZYŃSKI¹.

¹*Institute of Nuclear Physics PAN, Radzikowskiego 152, 31-342 Kraków, Poland*

²*Universität Karlsruhe, Institut für Experimentelle Kernphysik, 76128 Karlsruhe, Germany*

³*University of Wuppertal, Department of Physics, 42097 Wuppertal, Germany*

Henryk.Wilczynski@ifj.edu.pl

Abstract: The light emitted by an extensive air shower undergoes scattering on molecules and aerosols in the atmosphere. The scattering effect not only attenuates the light, but also contributes to the signal recorded by a detector. Hence, this effect directly influences the determination of shower energy. In routine analyses so far only contributions from direct and singly-scattered Cherenkov photons have been accounted for. Monte Carlo simulations were used in this work to study single and multiple scattering of fluorescence photons as well as multiple scattering of Cherenkov photons, for various shower geometries and varying distributions of aerosols in the air. The resulting contribution of scattered photons to the signal recorded in a fluorescence detector was obtained. A parameterization of this additional contribution is provided that can be used in shower reconstruction in the fluorescence technique of cosmic ray detection.

Introduction

The effect of scattering of light in the air results in attenuation of light emitted by an air shower before it arrives to a detector. However, it may also contribute to the signal received by the detector when light scatters several times before finally getting to the detector. Since the intensity of the scattered light does not relate directly to current number of particles in a shower, the scattered light is a background for a "useful" unscattered fluorescence light.

In routine air shower analyses so far, only the background due to direct and singly scattered Cherenkov light is subtracted from the signal recorded by a fluorescence detector. A contribution to the signal coming neither from multiply scattered Cherenkov photons, nor from scattered (singly and multiply) fluorescence light, is subtracted. Failure to account for this additional background signal results in overestimation of shower energy in the fluorescence method of shower detection.

The aim of this work is to quantify the contribution from scattered fluorescence and multiply scattered

Cherenkov photons to the shower signal recorded by a fluorescence detector and to provide means to amend the existing shower reconstruction procedure so that a correction for the multiple scattering contribution can be applied.

Simulation set

Simulations of scattering, and tracing of scattered photons were done using the Hybrid_fadc program [2]. The original program was modified [6], so that multiple scattering of both fluorescence and Cherenkov photons can be simulated separately. Wavelength-dependent Rayleigh scattering on molecules and Mie scattering on aerosols are simulated.

An extensive set of simulations was made. Simulation runs were performed for various shower energies, different shower-detector distances and different shower inclinations. Also, a variable distribution of aerosols in the atmosphere, with different aerosol concentration at the ground and different scale height of the distribution were tested. In addition, a possible dependence of the scattering effect on the molecular atmosphere distribution (i.e.

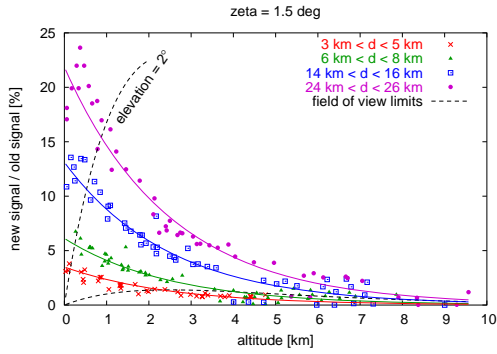


Figure 1: Contribution of scattered light to shower signal versus altitude above ground for selected shower-detector distances. The solid lines are fits of Eq.1. The dashed lines show limits of a detector field of view (elevation 2° – 30°).

variable vertical distribution of air mass) and on location of a detector at different altitudes above sea level were checked.

Two distributions of Cherenkov photon emission from a shower were also used: a simple exponential distribution [1] and a more realistic two-exponent one [5].

Contributions to the signal in a detector were recorded, coming from direct fluorescence and direct and singly scattered Cherenkov light, which are accounted for in routine shower reconstruction algorithms. These are collectively called in this paper the "old signal". In addition, the newly analysed contributions from multiply scattered Cherenkov and scattered (singly and multiply) fluorescence photons, called here the "new signal", were recorded.

Contribution of scattering

The results of simulations are quantified in terms of variable $M = \text{"new signal"}/\text{"old signal"}$, i.e. in percentage of the total shower signal used in shower reconstruction so far. It was shown in [6] that the contribution of scattered fluorescence light and multiply scattered Cherenkov light to the shower "image spot" falls with altitude of shower front above the ground. The "image spot" is the solid angle within which 90% of the signal is received.

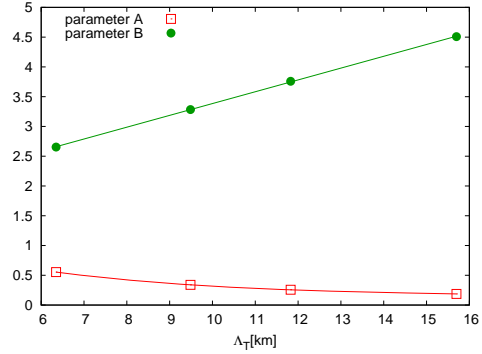


Figure 2: Dependence of the A and B parameters on the total horizontal attenuation length (see the text for details).

It is important to note that pixellization of the field of view of a fluorescence detector must be taken into account. The angular size of the image spot depends on the shower-detector distance and for distant showers has a radius of about half of a degree. On the other hand, the radius of a detector pixel size is usually larger than 0.5° . Since the angular distribution of the scattered light is much wider than that of the direct fluorescence [6], the relative contribution of the scattered component depends on the solid angle, from which signal is collected in the detector. For example, in fluorescence telescopes of the Pierre Auger Observatory the signal is collected from a solid angle with a radius larger than 1° [3]. Therefore, for distant showers this solid angle is larger than the image spot of the shower, and in consequence the contribution from multiple scattering is increased.

The scattering contribution to shower signal can be well parameterized by

$$M = A\zeta d \exp(-h/B) \quad (1)$$

where ζ is the radius of the signal collection angle in the detector, d – the shower-detector distance, h is the altitude of the shower front above the ground; A and B are parameters of the fit. As shown in Fig.1, Eq.1 very well describes the contribution from scattering. For low altitudes this contribution can exceed 20% for distant showers. If the detector field of view is limited at low elevations, the distant showers are not observed at very low altitudes. For example, only the region to the right

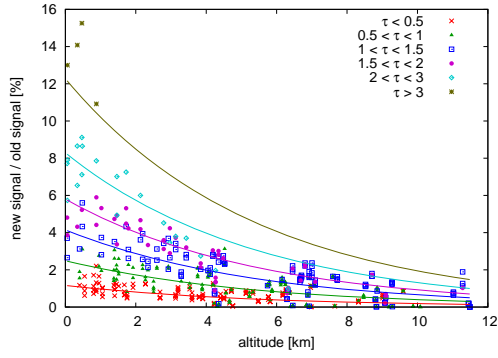


Figure 3: Contribution of multiple scattering for all values of the total horizontal attenuation length, in groups of the optical depth τ along the shower-detector line of sight. The lines are fits of Eq.2 with mean values of the respective τ intervals.

from "elevation=2°" dashed curve in Fig.1 can be observed in the Auger fluorescence detectors.

The A and B parameters of Eq.1 depend on distribution of aerosols. We show this dependence as a function of the total horizontal attenuation length Λ_T (for the wavelength of 361 nm) which can be easily measured experimentally. Fig.2 shows the dependence of A and B on Λ_T :

$A = a_1 \exp(-\Lambda_T/a_2) + a_3$, with $a_1 = 1.77 \pm 0.03\%$, $a_2 = 4.37 \pm 0.06\text{km}$, $a_3 = 0.14 \pm 0.01\%$;
 $B = b_1 \Lambda_T + b_2$, with $b_1 = 0.198 \pm 0.004$, $b_2 = 1.40 \pm 0.03\text{km}$.

Alternatively, the scattering contribution can be expressed as a function of the optical depth τ of the shower-detector line of sight:

$$M = F\zeta\tau \exp(-h/G) \quad (2)$$

with $F = 3.32 \pm 0.01\%$, $G = 5.43 \pm 0.03\text{km}$.

The contribution of the multiple scattering to the shower signal was found to be rather insensitive to details of vertical air mass distribution. Simulations were performed using the US Standard Atmosphere Model, as well as seasonal atmospheric profiles for the southern site of the Auger Observatory. The differences between them are important for determination of depth of shower maximum. However, local differences of air density among these models appear to be rather insignificant for the scattering effect. Similarly, variation of the de-

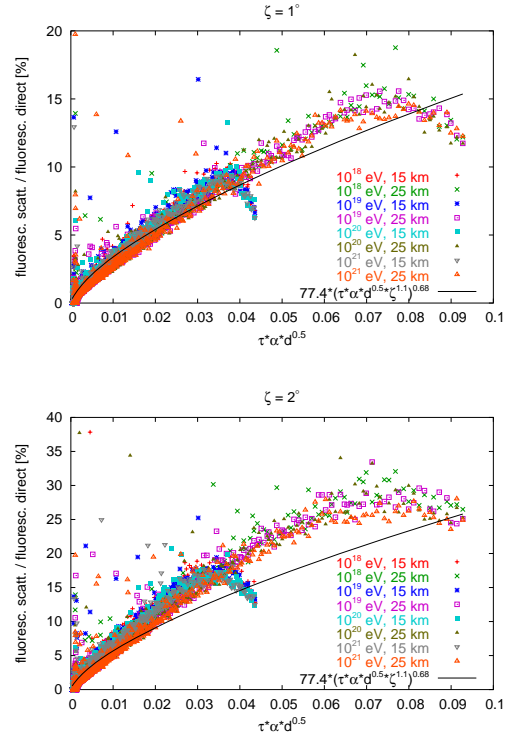


Figure 4: Comparison of fluorescence light scattering with results of [7] for $\zeta = 1^\circ$ and $\zeta = 2^\circ$. The data points are results of this work, the lines represent the fit given in [7].

detector altitude above sea level by a few hundred meters does not affect the scattering contribution. We note that the air density depends on altitude above sea level, while the distribution of aerosols – on altitude above ground, so that the Rayleigh and Mie scattering effects might contribute differently. Nevertheless, the total scattering contribution to shower signal does not appear to be noticeably sensitive to the detector altitude.

Similarly, different distributions of Cherenkov emission from the shower, proposed in [1, 5] result in similar scattering contributions to the shower signal.

Comparison with other results

Some studies of the scattering contribution can be found in the literature. In Ref.[7] scattering of flu-

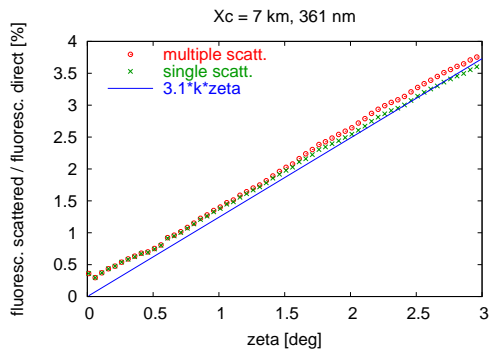


Figure 5: Comparison of Rayleigh scattering of fluorescence light with results of [4]. The data points are results of this work, the line represents the fit given in [4]

orescence light was studied assuming a uniform fluorescence light intensity along the shower track. To make the comparison, scattering of fluorescence light only was extracted from our simulations. The comparison shown in Fig.4 demonstrates a reasonable agreement in the range of small scattering contributions.

Another study was made in Ref.[4] of Rayleigh scattering only of fluorescence photons in a constant-density atmosphere. Since the air density in a real atmosphere falls approximately exponentially with altitude, positions of shower front low above the horizon were selected from our simulations, to study light propagation in a near-constant air density. A comparison of the Rayleigh scattering only of fluorescence light with the results of [4] is shown in Fig.5. One can conclude therefore that a comparison of results of [7] and [4] with corresponding subsets of our results shows a satisfactory agreement.

Conclusion

A comprehensive study of multiple scattering contribution to shower signal as recorded by a fluorescence detector was made. This contribution is parameterized as a function of the signal collection angle ζ in the detector, the shower-detector distance, the shower front altitude above ground and the total horizontal attenuation length (Eq.1),

or as a function of ζ , optical depth and altitude (Eq.2). The scattering contribution varies along the shower track, and may exceed 10% for distant showers low above the horizon. Failure to account for the multiple scattering effect may result in a *systematic* overestimation of the shower energy by a few percent.

Since the contribution to the signal received by a detector varies along the shower track, it may change the shape of the shower longitudinal profile, and in consequence, the reconstructed depth of shower maximum is affected. This change, however, is generally small, a few g/cm^2 .

The parameterization of the scattering contribution presented in this paper can be readily implemented into existing algorithms of shower reconstruction in the fluorescence detection technique.

Acknowledgements

This work was partially supported by the Polish Ministry of Science and Higher Education under grants No. N202 011 31/0401, N202 090 31/0623 and PAP/218/2006.

References

- [1] R. M. Baltrusaitis et al. *Nucl. Instr. Meth. A*, 240:410, 1985.
- [2] B. Dawson. *private communication*, 1998.
- [3] V. de Souza et al. *Proc. 29th ICRC, Pune*, 7:21, 2005.
- [4] M. Giller and A. Smialkowski. *Proc. 29th ICRC, Pune*, 7:195, 2005.
- [5] F. Nerling et al. *Astropart. Phys.*, 24:421, 2006.
- [6] B. Pekala et al. *Proc. 29th ICRC, Pune*, 7:207, 2005.
- [7] M. Roberts. *J. Phys. G: Nucl. Part. Phys.*, 31:1291, 2005.



New statistical parameters for mass composition studies with energy above 10^{17} eV

F. CATALANI¹, J.A. CHINELLATO¹, V. DE SOUZA², J. TAKAHASHI¹.

¹ Instituto de Física Gleb Wataghin, Universidade Estadual de Campinas, Brasil

² Institut für Experimentelle Kernphysik, Universität Karlsruhe, 76021 Karlsruhe, Germany

vtor.de.souza@gmail.com

Abstract: The determination of the mass composition of the ultra high energy cosmic rays is essential to many open questions in astroparticle physics. However the identification of the cosmic ray primary particle is a complex task due to several difficulties such as the large fluctuations in the shower development and the low number of experimental measurables. We present a proposal for composition studies applying multivariate analysis to make use of all the possible parameters to improve primary particle identification. Several measurable features of the CR shower longitudinal profile such as the N_{max} , X_{max} , asymmetry, kurtosis, and skewness were combined using linear discriminant analysis (LDA). Studies were done using cosmic ray showers simulated by the CONEX code considering gamma, proton, helium, carbon and iron as primary particles.

Introduction

The mass composition of ultra high energy cosmic rays (UHECR) plays a fundamental role in the understanding of their origin, acceleration and propagation mechanisms. In the energy region of cosmic ray spectra around 10^{15} , known as the spectra knee, the most probable source for these particles are the galactic supernovae. However, for higher energies there are no known sources inside our galaxy that could be capable of accelerating particles to such energies. Thus, the natural conclusion is that they must be of extragalactic origin. Within this scenario, the exact energy point where transition from the galactic to extragalactic component occurs varies with different models that predict different chemical composition for the CR in this high energy region. For example, in a model that considers that the transition occurs at the ankle energies around 10^{18} eV [4], the chemical composition of the spectra will be mostly populated by heavy nuclei such as iron. On the other hand, models that considers a dip scenario the transition occurs around 10^{17} eV and the extragalactic component is composed basically by protons (it admits a small fraction of helium nuclei) [3]. Thus, the determination of the chemical composition of cosmic

rays above 10^{17} eV is essential to solve this problem.

At lower energies, the composition of the cosmic ray spectra is achieved by studying, on a statistical basis, the variation of some experimental observable and considering that different primary particles will develop different shower parameters. For example, in the case of fluorescence detector, the position in the atmosphere where the shower is maximum (X_{max}) is different for proton initiated or iron initiated showers, thus it is used as a composition estimator. With ground array detectors, composition studies are done comparing the ratio between the hadronic and electromagnetic component of the shower. However, in the energy range above 10^{17} eV, the shower development and the process of detection are constrained by large fluctuations that makes the the primary particle identification more difficult. In this region of the CR spectra, composition measurements are still inconclusive [8]. While the HiRes Collaboration [1] measured an unchanging light composition above 10^{18} eV and a change from heavy to light composition in the range $10^{17} - 10^{18}$ eV, the AGASA experiment [9] measured an upper limit of the iron fraction of 35% in the range $10^{19} - 10^{19.5}$ eV and 76% in the range $10^{19.5} - 10^{20}$ eV.

In a previous paper [6] we have presented a method for chemical composition studies based on the application of a statistical method known as Linear Discriminant Analysis to enhance the separation between proton and iron primary particle cosmic ray showers. We made use of several features of the longitudinal development of the CR shower such as the N_{max} , X_{max} , asymmetry, kurtosis, and skewness rather than using only the depth of the shower maximum (X_{max}), to improve primary particle identification. The method was tested using simulated showers of proton, iron and photons generated by the Monte Carlo CORSIKA CR shower simulation code. In this paper, we extend our studies testing the same method to simulated showers generated by the CONEX code, and verify how the method improves the separation for other primary particles, comparing proton, helium, carbon and iron nuclei.

Shower Longitudinal Profile

We simulated showers of photon, proton, helium, carbon and iron primaries with energy of 10^{18} eV using the CONEX program [7]. CONEX is a hybrid Monte Carlo(MC) program that combines a MC treatment together with the solution of cascade equations. The hadronic interaction model used was QGSJETII [11] and the shower longitudinal development was sampled in vertical steps of 5 g/cm^2 . The gamma showers have been simulated with the pre-shower effect. For each primary particle species we have simulated and analyzed 2000 showers.

Figure shows the distribution of shower maximum depth X_{max} for the different primary particles. From left to right, we have the distributions of iron, carbon, proton and gamma sequentially. It is clear that the X_{max} parameter shows some discrimination capability, specially between hadrons and gamma initiated showers. However it does poorly between the different hadrons with small shifts in the mean of the distribution and large overlaps. We have included in our studies, CR showers initiated by helium nuclei, but they are not included in the plots due to the fact that we observed no separation between proton and helium showers distributions. To quantify the separation capability between two

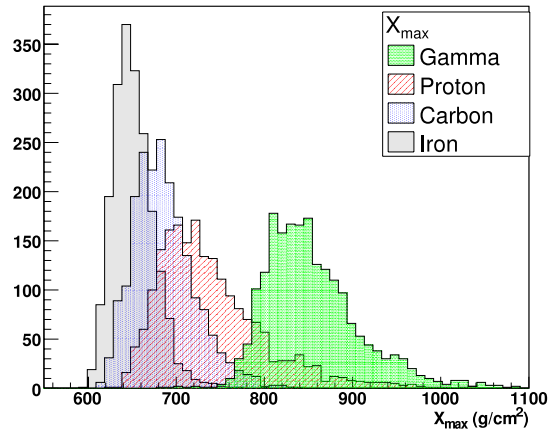


Figure 1: Distribution of the shower maximum depth X_{max} for simulated showers initiated by gamma, proton, carbon and iron showers

distributions, hence the discrimination between the different primary particles, we have chosen to use the merit factor (MF) statistical parameter that is defined as:

$$MF = \frac{\bar{A} - \bar{B}}{\sqrt{\sigma_A^2 + \sigma_B^2}}, \quad (1)$$

where \bar{A} and \bar{B} are the distributions averages, and σ_A and σ_B the respective standard deviations. The distributions shown in figure yields a separation merit factor of 1.4 between proton and gamma initiated showers, 0.7 between proton and carbon initiated showers and 1.3 between proton and iron initiated showers. These values are similar to the values obtained in [6], where we have used showers simulated by the CORSIKA code. Also, in the same work, we have presented a study that shows the dependence of the merit factor with the number of events in the distributions and with the relative number of events between the distributions. For a distribution of 2000 events we have shown that the error in the merit factor is below 5%. We have also evaluated the separation capability of other shower parameters such as the N_{max} , the number of particles in the shower maximum, sigma, a measure of the width of the shower, asymmetry (a direct measure of the difference between the parts of the shower below and above X_{max}),

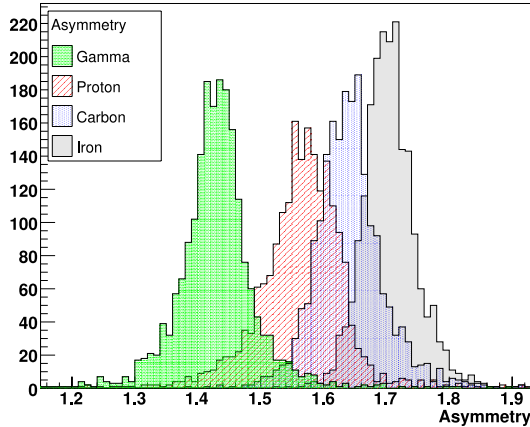


Figure 2: Distribution of the shower longitudinal profile asymmetry for simulated showers initiated by gamma, proton, carbon and iron showers

skewness and kurtosis, that correspond to the third and fourth momentum of the distribution. Figure shows the distribution of the asymmetry of the different shower profiles. With this parameter, we achieve a separation merit factor of 2.1 between proton and iron showers and 2.0 between proton and photon showers, which is a better separation than the X_{max} parameter. However, this should not be true in the case of real data where the limited field of view of the fluorescence detector and the smaller sampling of the longitudinal profile should affect more the variance of parameters such as asymmetry, skewness and kurtosis.

Linear discriminant analysis

We have studied the separation capability of all the different shower profile parameters mentioned above, and have combined them using a statistical method for event discrimination known as Linear Discriminant Analysis (LDA) [10]. LDA is a statistical discrimination method used to find a function of linear combinations of variables that maximizes the separation between two or more classes of objects or events. It accomplishes that by considering a Gaussian probability density function for each population and maximizing the difference between the mean of the distribution of the two

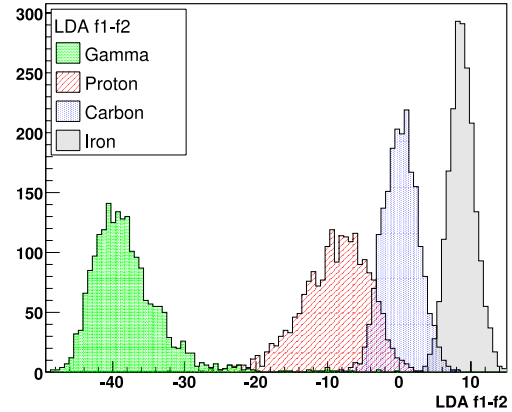


Figure 3: Distribution of LDA parameter $f1 - f2$ for gamma, proton, carbon and iron showers.

groups normalized by the effective variance of both distributions. The ratio of the variability between different groups is determined through the covariance matrix of the pooled (overall) events. In this analysis, we have used all six parameters of the shower longitudinal profile to obtain a discriminant coefficient calculated using the proton and the iron populations. The same linear coefficients were used to calculate the discrimination parameters for all the showers including the ones initiated by carbon and gamma.

Training datasets with 500 simulated showers for proton and iron showers were used to determine a set of discriminant coefficients. To discriminate the primaries of the simulated events, two linear discriminants $f1$ and $f2$ for each dataset points were calculated using the coefficient previously obtained. The discriminant of larger values indicates which population the new data point should be classified. We used the difference between the two LDA discriminants ($f1 - f2$) to obtain the best separation between the two populations. The same discriminant coefficients, calculated using the proton and iron showers were then applied to helium and carbon initiated showers. The final distribution of $f1 - f2$ parameters for all 4 different shower types are shown in figure .

We have calculated the separation merit factor between the different distributions. For proton and

iron showers, the distributions in figure 3 yields a separation merit factor of 3.7, while the separation between proton and gamma initiated showers provides a merit factor of 5.3, and proton and carbon yields a merit factor of 1.8.

Conclusions

It is clear that the chemical composition of the cosmic ray spectra at the high energy region is essential for understanding the origin and propagation of particles at such high energies. With the increase of data available in this region of the CR spectra, from experiments such as the Pierre Auger Observatory [2] and future experiments such as EUSO [5], it is important to develop new methods and techniques to improve chemical composition determination. We studied different features of the cosmic ray shower longitudinal profile to determine a better set of parameters that can be used to improve chemical composition of the high energy cosmic ray spectra. To combine the separation capability of all the parameters the statistical method linear discrimination analysis was applied resulting in a new parameter that provided better separation efficiency between the different shower types. To quantify the separation between the different shower distributions, we have defined a merit factor parameter. For shower initiated by proton and iron, with energy of 10^{18} eV, we have achieved a separation merit factor of 3.7, that can be compared to the separation merit factor of 1.3 obtained by using only the shower X_{max} parameter. This result is different and better than the result we have obtained using the showers simulated by the CORSIKA code, in which we had obtained a separation of 2.6 between the proton and the iron. For proton and gamma initiated showers, we have achieved a separation merit factor of 5.7, that can be compared to the separation obtained using only the X_{max} parameter of 1.4. The studies were performed on complete showers simulated using the CONEX code. Results are very similar to the results obtained by simulated showers using the CORSIKA code, with a slightly better separation efficiency between the different CR shower types. Further studies, including truncated shower profiles simulating the limited range of view of real fluorescence detectors show that the separation ca-

pability reduces, but still yields a better separation when compared to using only the X_{max} parameter.

Acknowledgments

This work is partially supported by the Brazilian science funding agencies FAPESP and CNPq, to which we are grateful.

References

- [1] Abbasi R.U. et al. *The Astrophysical Journal*, 622, 2005.
- [2] Abraham J. et. al. *Astroparticle Physics*, 27:155, March 2007.
- [3] Allard D. et al. *Astroparticle Physics*, 2007.
- [4] Aloisio R. et al. *Astroparticle Physics*, 27:76, 2007.
- [5] Ameri M. et al. *Nuclear Instruments and Methods in Physics Research A*, 567:107, November 2006.
- [6] Catalani F. et al. Statistical methods applied to composition studies of ultrahigh energy cosmic rays. *to be published in Astroparticle Physics*, astro-ph 0703582, 2007.
- [7] Pierog T. et al. *Nuclear Physics B - Proceedings Supplements*.
- [8] Watson A. et al. *Nuclear Physics B - Proceedings Supplements*, 151, January 2006.
- [9] Shinozaki K. and Teshima M. Agasa results. *Nuclear Physics B - Proceedings Supplements*, 136, January 2004.
- [10] Johnson R.A. and Wichern D. W. *Applied Multivariate Statistical Analysis*.
- [11] Ostapchenko S. *Nuclear Physics B - Proceedings Supplements*, 151, January 2006.



A MC simulation of neutrino showers and their detection with the Pierre Auger Observatory

D. GÓRA^{1,2}, M. ROTH³, A. TAMBURRO¹

¹*Institut für Experimentelle Kernphysik Universität Karlsruhe, D-76021 Karlsruhe, Germany*

²*Institute of Nuclear Physics PAN, ul. Radzikowskiego 152, 31-342 Kraków, Poland*

³*Forschungszentrum Karlsruhe, D-76021 Karlsruhe, Germany*

Dariusz.Gora@ik.fzk.de

Abstract: In this paper we present a study about the possibility to detect neutrino induced extensive air showers at the Pierre Auger Observatory. The Monte Carlo simulations performed take into account the details of the neutrino propagation inside the Earth, the air as well as the surrounding mountains, which are modelled by a digital elevation map. Details on the sensitivity with respect to the incoming direction as well as the aperture, the acceptance and the total observable event rates, on the basis of various assumptions of the incoming neutrino flux, and an upper limit for ultra high energy neutrinos, above 0.1 EeV, are given.

Introduction and method

The Pierre Auger Observatory has the capability to detect neutrino induced showers. Especially, if a ν_τ interacts close to the Earth's surface, the so-called Earth skimming neutrinos, it can produce a tau lepton which can emerge from the Earth, decay and produce extended air showers. If the decay vertex of a tau lepton is close enough to the surface array, it can be detected and distinguished from very inclined showers induced by a proton or nuclei due to the presence of the electromagnetic component. As shown in Fig. 1A, the Southern site (SO) is surrounded by a large amount of rock (the Andes mountains). This is the natural target for Earth skimming neutrinos which leads to a significant enhancement of the tau lepton flux with respect to calculations done with the simple spherical model of the Earth. In case of the Northern site (NO) the mountains which might enhance the tau lepton flux are far away, Fig. 1B, so that the influence of the mountains is not very pronounced. However due to a larger area of the detector (the planned area is about 3.5 times larger than SO) the rate is supposed to be

about three times larger than the one for the Southern site. In order to simulate the neutrino propagation through the Earth and the τ lepton decay, an extended version of the ANIS code was used [1]. First, for a fixed energy of the tau neutrinos, 200.000 events were generated with a zenith angle in the range between $90^\circ - 95^\circ$ and azimuth between $0^\circ - 360^\circ$ at the top of the atmosphere. Then tau neutrinos are propagated to the detector in small steps. At each step of propagation the probability of a ν_τ nucleon interaction is calculated according to the parameterization of the cross section based on the CTEQ5 [2] parton distribution function. The propagation of tau leptons through the Earth was simulated with the energy loss model (continuous energy loss approach) given by Dutta et al. in Ref. [4]: $\beta(E_\tau) \equiv 1.2 \times 10^{-6} + 0.16 \times 10^{-6} \ln(E_\tau/10^{10}) \text{ cm}^2 \text{ g}^{-1}$. The factor β parameterizes the τ lepton energy loss through bremsstrahlung, pair production, and photonuclear interactions. The computations were done by using digital elevation maps (DEM) [5] and then they were repeated by using the spherical model of the Earth (SP), with its radius set to 6371 km (sea level). As a result, the flux of the emerging τ leptons, i.e. the

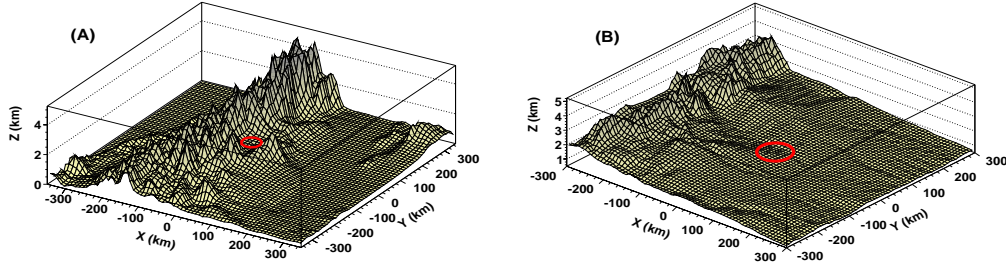


Figure 1: (A) Topography of the Southern site according to CGIAR-CSI data [5]. The center of the map corresponds to the center of the Auger array (latitude $\phi_{SO} = 35.25^\circ$ S, longitude $\lambda_{NO} = 69.25^\circ$ W); (B) Topography of the Northern site where the center of the map corresponds to $\phi_{NO} = 37.75^\circ$ N, $\lambda_{NO} = 102.75^\circ$ W. The Southern and Northern site positions are marked by a circle.

energy and the decay vertex position, was calculated inside a given detector volume. For the Southern site the geometrical size of the detector was set to $50 \times 60 \times 10 \text{ km}^3$ and the detector was positioned at 1430 m above sea level. For the Northern site the geometrical size of the detector was set to $100 \times 100 \times 10 \text{ km}^3$ at 1300 m above sea level. A DEM with resolution of 500(5000) m was used for the NO(SO). In case of the computations with the simple spherical model of the Earth, the same size of the detector was assumed, but with the position of the detector set to 10 m above sea level. In order to calculate the acceptance, the trigger efficiency $T_{eff}(E_\tau, h_{10})$ shown in Fig. 2B according to the results obtained in Ref. [3], was used. The parameter, h_{10} , corresponds to the height of the shower at 10 km from the tau decay point. In this work the acceptance for a given initial neutrino energy E_ν is given by

$$A(E_\nu) = N_{gen}^{-1} \times \sum_{i=1}^{N_\tau} \sum_{j=1}^{N_{\theta,\phi}} P_{i,j}(E_\nu, E_\tau, \theta) \times T_{eff}(E_\tau, h_{10}) \times A_j(\theta) \times \Delta\Omega, \quad (1)$$

where N_{gen} is the number of generated neutrino events, N_τ is the number of emerging τ leptons from the Earth with energy E_τ^f larger than threshold energy of the detector (E_{th}) for which the decay vertex position is above ground and inside the detector volume, $N_{\theta,\phi}$ is the number of tau leptons coming from a given direction inside the detector volume,

$P(E_\nu, E_\tau, \theta)$ is the probability that a neutrino with energy E_ν crossing the distance ΔL would produce a τ lepton with an energy E_τ^i (this probability was used as "weight" of the event), $\Delta\Omega$ is the space angle. In case of aperture calculations the Eq. (1) was used, but the $T_{eff}(E_\tau, h_{10})$ was set to 1. Finally the total observable rates (number of expected events) on basis of three neutrino fluxes, shown in Fig. 2D, are calculated according to $N = \Delta T \times \int_{E_{th}}^{E_{max}} A(E_\nu) \times \Phi(E_\nu) \times dE$ where $\Phi(E_\nu)$ is the isotropic neutrino flux and ΔT the observation time.

Results

In Fig. 2A the calculated aperture and acceptance are shown for a threshold energy of the detector of $E_\tau > 0.1 \text{ EeV}$. In case of the Southern site the two computations with the DEM and SP show clear differences: for example, at the energy of 0.3 EeV, the DEM calculations lead to an aperture of about 10% larger than the one obtained with the SP calculation, and to an aperture about 2 times larger at the energy of 10 EeV. In other words the effect on the aperture is energy dependent and it increases by increasing the energy of the initial neutrino. The observed differences are due to the increase of the neutrino cross section with energy. The initial neutrino interacts with the mountains surrounding the Auger site and pro-

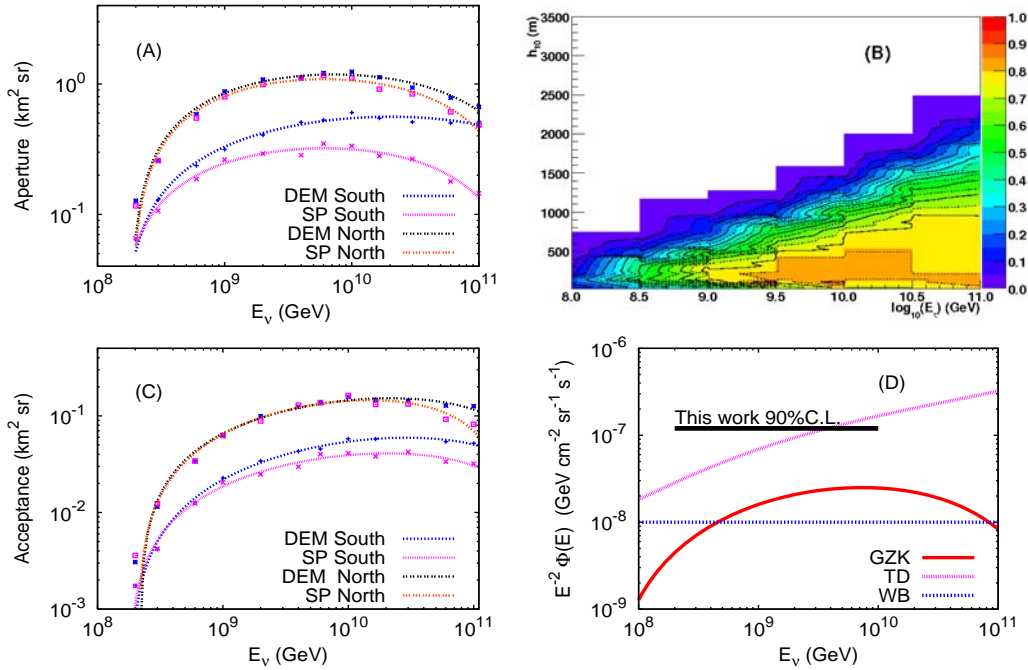


Figure 2: (A) The effective aperture for the Pierre Auger Observatory. Here the computations including the topography of the Auger site (DEM) and with the simple spherical model of the Earth (SP), are shown; (B) The trigger efficiency (including the muon decay channel) as a function of the height h_{10} , see Ref. [3] for more details; (C) The effective acceptance for the Pierre Auger Observatory; (D) Tau neutrino and anti-neutrino fluxes from different theoretical models. In addition the flux limit at 90% C.L. (thick black line) for E^{-2} flux of tau neutrino is shown for one year of operation.

duces a τ lepton. For higher energies of the initial neutrino, the produced lepton in the mountains can reach the detector from larger distances. In case of the Northern site the calculated aperture with the DEM is almost the same as the aperture with the SP computations. Only for initial neutrino energies larger than a few EeV we can observe that the DEM computations give larger values for the aperture, within 10%, than the SP computations. In case of the acceptance calculations, Fig. 2C, the observed differences between DEM and SP computation are smaller. This is due to the fact that the energy and the zenith angle distribution of the emerging τ leptons are different in case of the DEM and SP calculations. Thus, even if we use the same trigger probability presented in Fig. 2B, the capability to detect neutrino induced showers is not the same

in the case of DEM and SP calculations and this effect levels out the differences seen in the aperture. Indeed we have to notice that the acceptance for the Northern site is biased by the assumption of the same trigger efficiency as the one for the Southern site. In case of the Northern site the larger spacing of surfaces detectors as compared to the Southern site is planned. Since the area of the Northern site is not flat, there are many small hills, which can "shadow" tanks, so that the expected efficiency will be rather smaller than the one for the Southern site.

In Tab. 1 the rate (number of events per year) for the different injected neutrino fluxes, and based on our acceptance and aperture calculation, are listed. The WB rate is obtained for the Waxman-Bahcall bound [6], $\Phi(E_{\nu_\tau + \bar{\nu}_\tau}) = 1 \times 10^{-8} E^{-2}$ (GeV s⁻¹ cm⁻² sr⁻¹). Other

| | | WB | | | GZK | | | TD | | |
|------------|----|-----------------------------------|----------------------------------|------------|-----------------------------------|----------------------------------|------------|-----------------------------------|----------------------------------|------------|
| | | N_{DEM} (yr^{-1}) | N_{SP} (yr^{-1}) | k (%) | N_{DEM} (yr^{-1}) | N_{SP} (yr^{-1}) | k (%) | N_{DEM} (yr^{-1}) | N_{SP} (yr^{-1}) | k (%) |
| N_{Aper} | SO | 3.39 | 2.27 | 56 | 4.85 | 3.27 | 43 | 24.8 | 16.20 | 53 |
| | NO | 8.22 | 7.72 | 6 | 11.80 | 11.10 | 7 | 58.94 | 54.95 | 7 |
| N_{Acc} | SO | 0.21 | 0.18 | 17 | 0.33 | 0.28 | 18 | 1.80 | 1.46 | 23 |
| | NO | 0.59 | 0.58 | 2 | 0.97 | 0.95 | 2 | 5.05 | 4.93 | 2 |

Table 1: Expected event rate in (yr^{-1}) for the Southern (SO) and the Northern (NO) site based on aperture (N_{Aper}) and acceptance calculations (N_{Acc}). The precision on the listed values is about 4%.

rates are calculated for the GZK [7] flux and Topological Defects (TD) [8]. The GZK flux refers to the possible scenario of cosmogenic neutrinos, which are those produced from an initial flux of UHE protons. The TD case is an example of exotic model. To quantify the influence of the topography of the Auger Observatory on the calculated rate, we define the factor $k = (N_{DEM} - N_{SP})/N_{SP}$, where N_{DEM} is the rate calculated with the DEM and N_{SP} the one calculated with the spherical model of the Earth. As one can see from Tab. 1 the rates for the Southern site are about 50% larger, in case of our aperture calculations, and about 20% larger, in case of our acceptance calculations, than the rate calculated with the simple spherical model of the Earth. For the Northern site the calculated rates are about 7% and 2% larger than the rate for the SP computations, in case of our aperture and the acceptance calculations, respectively.

Finally as an exercise the limit for an injected spectrum $K*\Phi(E)$ with a known shape $\Phi(E) \propto E^{-2}$ is calculated using the same method as the one applied to the Auger data [9]. The 90% C.L. on the value of K according to Ref. [10] is $K_{90\%} = 2.44/N_{WB}$. Assuming a negligible background, zero neutrino events have been observed by the Auger Observatory. In such a case the upper limit for tau neutrinos is $1.2 \pm 0.6 \times 10^{-7} \text{ GeV km}^{-2} \text{ yr}^{-1} \text{ sr}^{-1}$, where the uncertainty is coming from the poor knowledge of the ν cross-section, the tau lepton energy loss and the tau lepton polarization. This limit is valid in the energy range from 0.1 EeV up to about 10 EeV, where the 90% of the expected events are located.

To conclude, in this work we show a study about the possibility to detect neutrino induced extensive air showers at the Pierre Auger Observatory taking into account the actual topography of the Auger Observatory. We find an enhancement (about 20% wrt a spherical Earth) on the neutrino rate for skimming tau neutrinos for the Southern site. In addition our calculated limit, proves the sensitivity of the Auger Observatory to GZK neutrinos.

Acknowledgments. We acknowledge the financial support from the HHNG-128 grant of the Helmholtz association and the Ministry of Science and Higher Education under Grants No. N202 090 31/0623 and PAP/218/2006.

References

- [1] D. Góra, M. Roth and A. Tamburro, *Astropart. Phys.* 26 (2007) 402.
- [2] H. Lai, et al., hep-ph/9903282.
- [3] O. Blanch and P. Billoir, GAP-2005-017.
- [4] S.I. Dutta et al., *Phys. Rev. D* 72 (2005) 013005.
- [5] Consortium for Spatial Information (CGIAR-CSI), <http://srtm.csi.cgiar.org/>
- [6] J.N. Bahcall, E. Waxman, *Phys. Rev. D* 64 (2001) 0230002.
- [7] R. Engel, D. Seckel, T. Stanev, *Phys. Rev. D* 64 (2001) 093010.
- [8] P. Bhattacharjee and G. Sigl, *Phys. Rept.* 327 (2000) 109.
- [9] O. Blanch [Pierre Auger Collaboration] these proceedings, (2007) #0603.
- [10] G.J. Feldman and R.D. Cousins, *Phys. Rev. D* 57 (1998) 3873.

Investigation of backgrounds for horizontal neutrino showers at ultra-high energy

O. TAȘCĂU¹, R. ENGEL², K.-H. KAMPERT¹, M. RISSE¹.

¹ *Bergische Universität Wuppertal, Germany*, ² *Forschungszentrum Karlsruhe, Germany*
andorada@physik.uni-wuppertal.de

Abstract: A possible signature of a neutrino-induced air shower is a near-horizontal event developing very deeply in the atmosphere at depths exceeding a few thousand g/cm^2 . Making use of high-statistics shower libraries we study the background to such events from high-energy muons produced in primary proton events, which may propagate deeply into the atmosphere before initiating a subcascade. The rates of background events are compared with various flux models of ultra-high energy neutrino production.

Introduction

The Pierre Auger Observatory is one of the detectors able to detect neutrino showers and, in the relevant energy range, Auger is equivalent to tens of km^3 of water. The detection of neutrinos is not the main aim of the Auger Observatory, but it can be considered as a very rich by-product for many reasons. We are investigating if we can extract a ν signal above the hadronic background. If no signal is observed, this will put severe constraints on models which predict high-energy neutrino production.

Why are we interested in neutrinos? Mainly because: 1) Neither the GZK cutoff nor magnetic fields operate on ν . Therefore the reconstructed directions should point directly to the source, with the intrinsic angular precision of the detector. 2) The existence of detectable fluxes of neutrinos with energies in excess of 10^{18} eV is in principle one of the signatures of Topological Defect theories. 3) At around 10^{17} eV we are close to the highest energies accessible to the large future neutrino telescope projects and give some indications, several years before such detectors become operational, on the validity of the models used in the design of such projects (detecting mainly predicted neutrinos produced in AGNs).

Above 10^{15} eV the Earth becomes opaque to ν and only down-going or Earth-skimming EeV neutrinos can be detected. The challenge lies in the identification of these showers in the background of

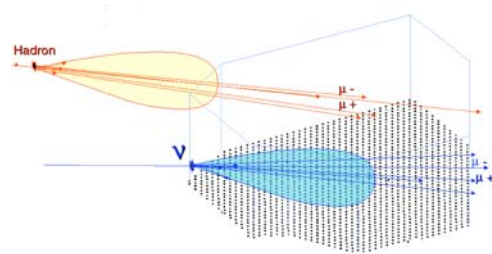


Figure 1: "Old" and "young" cosmic ray showers.

down-going cosmic rays and atmospheric muons. Inclined showers in the atmosphere are expected to play a crucial role for the detection of EeV neutrinos. The background for the detection of inclined showers produced by neutrinos is mainly due to showers induced by protons and nuclei. The first ones are expected to develop high in the atmosphere so that when the shower front reaches ground level it has very different properties from 'ordinary' showers that are observed in the vertical direction. They are called "old showers". Deep-inclined showers induced by neutrinos can develop close to ground level so that their shower front looks like a typical vertical proton cosmic ray shower. Another type of background to inclined showers induced by ν is given by deep showers induced otherwise.

The electromagnetic part of cosmic ray showers gets practically absorbed in the first $2000 g/cm^2$

and, to a very good approximation, only muons generated in highly inclined showers reach the ground. The lower energy muons actually decay in flight and can contribute a small electromagnetic component that follows closely that of the muons. As a result, the average energy of the muons reaching ground increases rapidly as the zenith angle increases. The shower front that reaches ground level for inclined showers is very different from vertical showers. Most of the inclined shower fronts practically only contain energetic muons and their density patterns have lost the cylindrical symmetry because of the Earth's magnetic field which is separating the negative muons from the positive ones, in inverse proportion to their energy.

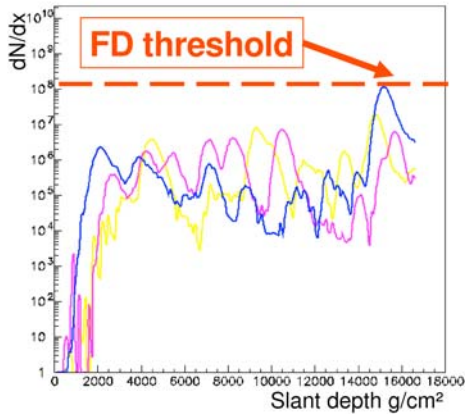


Figure 2: Example of light curves for individual muons which maybe produced in a proton induced shower at 10^{19} eV and $\theta = 87^\circ$.

Different muon's behavior in a shower

For a better understanding of the muon behavior, individual muon induced showers were generated with the CORSIKA code and made available in a library in Wuppertal University. The shower particle profiles and the energy deposits were investigated in order to check if there are events which exceed the threshold given by the fluorescence detector (FD). Such cases would be considered background events.

The source of this potential neutrino background changes with the energy, in function of the critical energy ϵ_c of the parent particle. The critical energy delimits the competition between decay and interaction length of the particle and is calculated in terms of the particle rest energy mc^2 , the mean life τ and, by adopting the isothermal atmosphere

Table 1: The "prompt" and "conventional" muon flux generated in air showers.

| The charm contribution gives the "prompt" flux | | | | |
|--|----------------------|-------------------|-----------------------------------|------------------------------------|
| Particle | Struct. | $c\tau$ | ϵ_c (GeV) ⁽¹⁾ | η ₀ ⁽²⁾ |
| D^+, D^- | $cd, \bar{c}\bar{d}$ | 317 μm | $3.8 \cdot 10^7$ | 17.2 |
| D^0, \bar{D}^0 | $c\bar{u}, \bar{c}u$ | 124 μm | $9.6 \cdot 10^7$ | 6.8 |
| D_s^+, D_s^- | $c\bar{s}, \bar{c}s$ | 149 μm | $8.5 \cdot 10^7$ | 5.2 |
| Λ_c^+ | udc | 62 μm | $2.4 \cdot 10^8$ | 4.5 |
| π and K contribution gives the "conventional" flux | | | | |
| π^+, π^- | $ud, \bar{u}\bar{d}$ | 7.8 m | 115 | 100 |
| K^+, K^- | $u\bar{s}, \bar{u}s$ | 3.7 m | 855 | 63.5 |
| Λ^0 | uds | 7.9 cm | $9.0 \cdot 10^4$ | 0.1 |
| μ^+, μ^- | lepton | 659 m | 1.0 | 100 |

(1) According to ϵ_c , with $h_0 = 6.4$ km.

(2) For inclusive decays yielding leptons.

approximation, a scale constant h_0 , so we obtain:

$$\epsilon_c = \frac{mc^2}{c\tau} h_0.$$

Comparing the critical energies we find that above 1-10 TeV, the semileptonic decay of very short lived charmed particles (mainly D-mesons and Λ_c^+ -hyperons) is the dominant source. These constitute the so called "prompt" flux, while the low energy products (from pions and kaons) are giving the "conventional" flux. The main contribution for the prompt flux comes from $D^- \rightarrow K + \mu + \nu$ and $\Lambda_c^- \rightarrow \Lambda_0 + \mu + \nu$.

Estimation of event rates

Several groups were investigating the prompt flux, and the debate over the years provided us several models. We are taking into account three of these, including the extremes. The flux estimations vary by several orders of magnitude due to different models used to calculate the charm cross section and energy spectra. This huge model dependence is due to the need to extrapolate charm production data obtained at accelerator energies, which are

several orders of magnitude below the relevant cosmic rays collisions. The most conservative model was studied in several papers based on Thunman et al. [7](TIG), using state-of-the-art models to simulate charm particle production through perturbative QCD processes in high energy hadron-hadron interactions, and investigations of a possible non-perturbative mechanism for the case of an intrinsic charm quark component in the nucleon. The next model considered is Gondolo et al. [2](GGV) and it is considered an improvement of the TIG values, being compatible with the results from Pasquali et al. [6] which used a complementary analysis. They used higher K factors for the parton distribution functions (PDF's) as function of energy, making a full simulation of the cascades, while PRS used approximative analytic solution to the cascade equations in the air. The most exotic model we took into account is the one presented by Zas et al. [8] (ZHV), which pushes the charm production to 10%, thus obtaining a very high charm flux. Each paper cited here used several parameters and methods, obtaining results which may differ by 2 orders of magnitude. However, in our interval of interest, we chose, for a simple estimate, the following values of the E^3 -weighted-flux of the muons F_μ : for TIG, 10^{-5} , for GGV, 10^{-3} and for ZHV, $10^{-1} \text{ GeV}^3/\text{cm}^2 \text{ sr s}$.

All the prompt fluxes presented here are vertical fluxes. At the energies $< 10^{16}$ eV, the horizontal flux has a slower cutoff than the vertical one, and, in our interval, we assume that the horizontal flux is 10 times higher than the vertical one, using the estimations given by Martin et al in [4].

The estimate of the rate of the potential backgrounds for the neutrino showers detected by Auger is given by dN_μ/dt in the following form:

$$D \int d\Omega \int d\epsilon_\mu \frac{dN_\mu}{dt d\Omega d\epsilon_\mu} \int dV * P_{non-int} * P_{int} \quad (1)$$

The background light introduces a duty cycle which limits its acceptance both for cosmic ray and neutrino detection. In this equation we take into account the duty cycle D for the fluorescence detector in Auger which is considered 10%. The solid angle in which the considered showers may arrive is $\int_{80^\circ}^{90^\circ} \int_0^{360^\circ} \sin(\theta) d\theta d\phi$

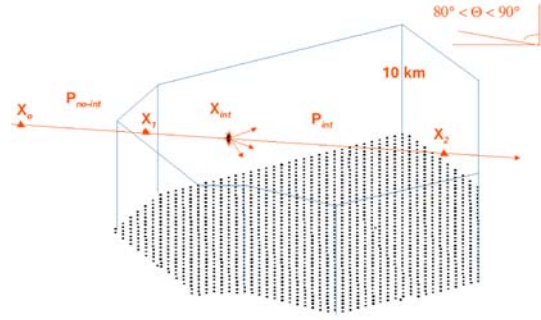


Figure 3: The interaction should take place in the sensitive area of Auger.

We consider events only with the interaction is in the sensitive volume. The probability for this is given by $P_{int} = 1 - e^{-\frac{x_2-x_1}{\lambda_{int}}}$ while the one to enter the volume without interaction is $P_{non-int} = e^{-\frac{x_1-x_0}{\lambda_{int}}}$, with x_1 , x_0 and x_2 as in the figure, where a symbolic Auger volume is shown, for a 10 km height.

The integral prompt muon flux in our energy range (in GeV) $\int d\epsilon_\mu$ is $\int_{10^8}^{10^{11}} \frac{F_\mu}{E_\mu^3} dE_\mu$. We denote

$$D \int d\Omega \int d\epsilon_\mu \frac{dN_\mu}{dt d\Omega d\epsilon_\mu} = C \quad (2)$$

and dN_μ/dt becomes:

$$C \int dA_\perp P_{non-int} \int_{l_1}^{l_2} \frac{dP_{int}(x_{int})}{dx_{int}} \rho(x_{int}) dl \quad (3)$$

where $\rho(x_{int}) dl = dx_{int}$ and A_\perp is the transversal area for the line elements of the trajectories inside the considered volume.

For the case $x_{int} - x_1 \ll \lambda_{int}$ we can approximate $e^{-\frac{x_{int}-x_1}{\lambda_{int}}} \approx 1$ and, for the moment, we do not include the energy loss. We consider $\rho = -\frac{dXv}{dh}$; $Xv = X_0 e^{-\frac{h}{h_0}}$; $\int \rho dl = x$ and we get

$$\frac{dN_\mu}{dt} = C \int dA \frac{1}{\lambda_{int}} \int_{X_2}^{X_1} dXv \quad (4)$$

with $h_0=8.4$ km and $X_0=1030 \text{ g/cm}^2$ and A , the fiducial surface of Auger South.

$M_{Auger} = \int dA \int_{X_2}^{X_1} dXv = 1.64 \cdot 10^{10} \text{ tons}$ is the mass of the air above the Auger South sur-

face, in a layer of 10 km thickness. The interaction length $\lambda_{int} = \frac{m_{air}}{N_a \cdot \sigma_{\mu-air}}$ is calculated using $m_{air}=14.54$ g/mol, $N_a = 6.023 \cdot 10^{23}$ mol⁻¹ and the cross section $\sigma_{\mu-air}$, taken from the CORSIKA simulations.

Results

Table 2 summarises the results of the calculated event rates according to previous section. The

Table 2: Possible FD background from HE muon-induced showers (events/year).

| θ | TIG [7] | GGV [2] | ZHV [8] |
|-----------|---------------------|---------------------|---------|
| 80° – 90° | $1.4 \cdot 10^{-5}$ | $1.4 \cdot 10^{-3}$ | 0.14 |
| 60° – 90° | $4 \cdot 10^{-5}$ | $4 \cdot 10^{-3}$ | 0.4 |

Table 3: FD hadronic background to ν FD signal

| ν /year/model ⁽¹⁾ | TIG [7] | GGV [2] | ZHV [8] |
|----------------------------------|---------|---------|---------|
| 0.043 / GZK-WB | 0.1% | 10 % | 100% |
| 0.67 / NH | 0.006% | 0.6% | 60 % |

(1) According to [5] for 60° – 90°

background values are computed also for $\theta = 60^\circ - 90^\circ$ in order to compare them with the neutrino signal predicted by Miele et al. [5], including here the conservative value obtained assuming the GZK flux for Waxman-Bahcall scenario for cosmogenic neutrinos (GZK-WB) and the extreme one given by the exotic model for generating UHECR with large associated neutrino fluxes, named New Hadrons (NH).

Conclusions

High energy muons from heavy flavor decay can induce young horizontal showers similar to the ν signatures. The theoretical uncertainties are huge, so the predicted possible background values spread over several orders of magnitude. muon energy loss is neglected is rather important. This calculation neglected the energy loss, therefore, the

estimated muon-induced event rates are upper limits. For the most exotic perspective, ZHV [8], the background rates almost rule out the ν detection, but, in turn, one could think about an interesting capability to detect charm, once the appropriate tools to recognize the charm signature are there. However, this is possible due to the assumption of a 10% charm production, which is not supported by the Akeno data [8]. For the other two considered models, the predicted background rates are sufficiently low, opening an interesting window to study high energy neutrinos with Auger.

While the present estimate was performed for the FD, further sensitivity to ν 's is provided by the surface array of Auger Observatory.

Another possible background source would be photon induced showers which due to the LPM effect develop very deep in the atmosphere. Related investigations are ongoing.

Acknowledgements

Financial support given by the German Ministry for Research and Education (BMBF), under the grant 05 CU5PX1/6, is gratefully acknowledged.

References

- [1] C. G. C. Costa. *High Energy Ph.* 0010306, 2001.
- [2] G. Gelmini, P. Gondolo, and G. Varieschi. *Phys. Rev. D* 61 056011, 2000.
- [3] D. Heck, J. Knapp, J. N. Capdevielle, G. Schatz, and T. Thouw. *FZKA* 6019, 1998.
- [4] A. D. Martin, M. G. Ryskin, and A. M. Stasto. *Hep. Ph.* 0302140, 2003.
- [5] G. Miele, O. Pastor, and O. Pisanti. *Phys. Lett. B* 634, pages 137–142, 2006.
- [6] L. Pasquali and M. H. Reno. *Phys. Rev. D*, 59, page 034020, 1999.
- [7] M. Thunman, B. Ingelman, and P. Gondolo. *Astropart. Phys.* 5, pages 309–332, 1995.
- [8] E. Zas, F. Halzen, and R. A. Vasquez. *Astropart. Phys.* 1, page 297, 1993.

The UHECR spectrum measured at the Pierre Auger Observatory and its astrophysical implications

T. YAMAMOTO¹ FOR THE PIERRE AUGER COLLABORATION²

¹ *KICP, Enrico Fermi Institute, University of Chicago, Chicago IL USA*

² *Pierre Auger Observatory, Av. San Martín Norte 304, (5613) Malargüe, Argent*
yamamoto@oddjob.uchicago.edu

Abstract: The Southern part of the Pierre Auger Observatory is nearing completion, and has been in stable operation since January 2004 while it has grown in size. The large sample of data collected so far has led to a significant improvement in the measurement of the energy spectrum of UHE cosmic rays over that previously reported by the Pierre Auger Observatory, both in statistics and in systematic uncertainties. We summarize two measurements of the energy spectrum, one based on the high-statistics surface detector data, and the other of the hybrid data, where the precision of the fluorescence measurements is enhanced by additional information from the surface array. The complementarity of the two approaches is emphasized and results are compared. Possible astrophysical implications of our measurements, and in particular the presence of spectral features, are discussed.

Measurement of the UHECR energy spectrum from hybrid data of the Pierre Auger Observatory

LORENZO PERRONE¹, FOR THE THE PIERRE AUGER COLLABORATION²

¹ *Università del Salento and INFN Lecce, I-73100 Lecce, Italy*

² *Observatorio Pierre Auger, Av. San Martín Norte 304, Malargüe, (5613) Mendoza, Argentina*
lorenzo.perrone@le.infn.it

Abstract: More than two years of fluorescence detector data collected in coincidence with at least one station of the surface detector array (“hybrid data”) are used to measure the flux and energy spectrum of cosmic rays above about 10^{18} eV. The hybrid measurement extends towards lower energies the spectrum measured with the surface detector data only, and provides a cross-check with an independent data set. The determination of the fluorescence detector aperture and of its live-time, which is the major aspect of this measurement, is illustrated in detail. Our current estimate of the corresponding systematic uncertainties are given.

Measurement of the UHECR spectrum above 10^{19} eV at the Pierre Auger Observatory using showers with zenith angles greater than 60°

P. FACAL SAN LUIS, FOR THE PIERRE AUGER COLLABORATION

Universidad de Santiago de Compostela and IGFAE, Campus Sur, 15782, Santiago, Spain
facal@fpaxp1.usc.es

Abstract: We report a measurement of the cosmic ray energy spectrum obtained using the inclined events detected with the Pierre Auger Observatory. Showers with zenith angles between 60° and 80° recorded in the period between 1 January 2004 and 28 February 2007 are analysed. Showers are first reconstructed in arrival direction and then fitted to density maps of the muon numbers obtained from 10^{19} eV simulated proton showers for different arrival directions, in order to obtain the core position and an overall normalisation factor N_{19} which is used as an energy estimator. The parameter N_{19} is shown to be correlated with the shower energy measured with the fluorescence technique for a sub-sample of good quality hybrid showers. This correlation, measured with hybrid events, is then used to determine the energy of all the showers.

Studies of clustering in the arrival directions of cosmic rays detected at the Pierre Auger Observatory above 10 EeV

SILVIA MOLLERACH¹, FOR THE PIERRE AUGER COLLABORATION

Pierre Auger Observatory, av. San Martín Norte 304, (5613) Malargüe, Argentina

¹ *Depto de Física, Centro Atómico Bariloche, CNEA and CONICET, Argentina*

mollerach@cab.cnea.gov.ar

Abstract: If clustering of the arrival directions of ultra high energy cosmic rays is discovered, this would provide important information about their origin, composition, and the galactic and extragalactic magnetic fields. We present here the analysis of the autocorrelation function of the data from the Pierre Auger Observatory as a function of the angular scale and the energy threshold. We compare our results with the signals found by previous experiments.

A search for possible anisotropies of cosmic rays with $0.1 < E < 10$ EeV in the region of the Galactic Centre

E.M SANTOS¹ FOR THE PIERRE AUGER COLLABORATION²

¹*CBPF, R. Xavier Sigaud, 150, 22290-180, Rio de Janeiro, RJ, Brazil*

²*Pierre Auger Observatory, Av. San Martín Norte 304, (5613) Malargüe, Argentina*

emoura@cbpf.br

Abstract: We present updated results for anisotropy searches in the direction of the Galactic Center (GC) at energies in the ranges: $0.1 < E < 1$ EeV and $1 < E < 10$ EeV. We use data from the Pierre Auger Observatory up to March, 2007. Present analyzes are therefore based on a substantially larger data set than our previous published results. A limit on the flux coming from a hypothetical point-like neutron source at the GC for $1 < E < 10$ EeV was imposed, and searches for extended excesses were also performed.

Search for large-scale anisotropies with the Auger Observatory

E. ARMENGAUD, FOR THE PIERRE AUGER COLLABORATION

Pierre Auger Observatory, Av. San Martín Norte 304, (5613) Malargüe, Argentina

armengau@in2p3.fr

Abstract: We use more than two years of data from the Pierre Auger Observatory to search for anisotropies on large scales in different energy windows. We account for various systematics in the acceptance, in particular due to the array growth and weather variations. We present the results of analyses and consistency checks looking for patterns in the right ascension modulation of the cosmic ray distribution. No significant anisotropies of this kind are observed.

Search for correlation of UHECRs and BL Lacs in Pierre Auger Observatory data

DIEGO HARARI¹, FOR THE PIERRE AUGER COLLABORATION²

¹*Departamento de Física, Centro Atómico Bariloche, CNEA and CONICET, Argentina*

²*Pierre Auger Observatory, Av. San Martín Norte 304, (5613) Malargüe, Argentina*

harari@cab.cnea.gov.ar

Abstract: Several analyses of the data collected by other experiments have found an excess of cosmic rays in correlation with subclasses of BL Lacs. Data from the Pierre Auger Observatory do not support previously reported excesses. The number of events correlated with BL Lac positions is compatible with that expected for an isotropic flux.

Search for Coincidences in Time and Arrival Direction of Auger Data with Astrophysical Transients

LUIS ANCHORDOQUI¹, FOR THE PIERRE AUGER COLLABORATION²

¹ *Department of Physics, University of Wisconsin-Milwaukee, P.O. Box 413, Milwaukee, WI 53201, USA*

² *Pierre Auger Observatory, Av. San Martín Norte 304, (5613) Malargüe, Argentina*

anchordo@uwm.edu

Abstract: The data collected by the Pierre Auger Observatory are analyzed to search for coincidences between the arrival directions of high-energy cosmic rays and the positions in the sky of astrophysical transients. Special attention is directed towards gamma ray observations recorded by NASA's Swift mission, which have an angular resolution similar to that of the Auger surface detectors. In particular, we check our data for evidence of a signal associated with the giant flare that came from the soft gamma repeater 1806-20 on December 27, 2004.

Search for Gamma Ray Bursts using the single particle technique at the Pierre Auger Observatory

X. BERTOU¹ FOR THE PIERRE AUGER COLLABORATION²

¹ *Centro Atómico Bariloche (CNEA), (8400) San Carlos de Bariloche, Río Negro, Argentina*

² *Av. San Martín Norte 304 (5613) Malargüe, Prov. de Mendoza, Argentina*

bertou@cab.cnea.gov.ar

Abstract: The Pierre Auger Observatory, with an array of currently more than 1200 Cherenkov detectors filled with 12 m³ of water, can detect the putative high energy emission of a GRB (photons down to a few hundreds of MeV) by the so-called "single particle technique", through a coherent increase in the average background particle rates over the whole array, due to secondary particles in the photon-induced showers. We present a search for bursts on data collected since September 2005, as well as a search for excesses in coincidence with bursts observed by satellites.

Composition-sensitive parameters measured with the surface detector of the Pierre Auger Observatory

M.D. HEALY¹ FOR THE PIERRE AUGER COLLABORATION²

¹ *University of California, Los Angeles, Los Angeles, CA 90095, USA*

² *Observatorio Pierre Auger, Av. San Martín Norte 304, (5613) Malargüe, Argentina*

healymd@physics.ucla.edu

Abstract: A key step towards the understanding of the origin of ultra-high energy cosmic rays is their mass composition. Primary photons and neutrinos produce markedly different showers from nuclei, while showers of different nuclear species are not easy to distinguish. To maximise the discrimination with the Pierre Auger Observatory ideally all mass-sensitive observables should be combined, but the 10% duty cycle of the fluorescence detector limits the use of direct measurements of shower maximum at the highest energies. Therefore, we investigate mass-sensitive observables accessible with the surface detectors alone. These are the signal risetime in the Cherenkov stations, the curvature of the shower front, the muon-to-electromagnetic ratio, and the azimuthal signal asymmetry. Risetime and curvature depend mainly on the depth of the shower development in the atmosphere, and thus on primary energy and mass. The muon content of a shower depends on the primary energy and the number of nucleons, while asymmetry about the shower core is due to geometric effects and attenuation, which are dependent on the primary mass. The mass sensitivity of these variables is demonstrated and their application for composition studies is discussed.

Search for Ultra-High Energy Photons with the Pierre Auger Observatory

M. HEALY¹ FOR THE PIERRE AUGER COLLABORATION²

¹ *University of California, Los Angeles, Los Angeles, CA 90095, USA*

² *Av. San Martín Norte 304 (5613) Malargüe, Prov. de Mendoza, Argentina*

bes@ast.leeds.ac.uk

Abstract: Data taken at the Pierre Auger Observatory are used to search for air showers initiated by ultra-high energy (UHE) photons. Results of searches are reported from hybrid observations where events are measured with both fluorescence and array detectors. Additionally, a more stringent test of the photon fluxes predicted with energies above 10^{19} eV is made using a larger data set measured using only the surface detectors of the observatory.

Constraints on top-down models for the origin of UHECRs from the Pierre Auger Observatory data

D. SEMIKOZ¹, FOR THE PIERRE AUGER COLLABORATION²

¹ *APC, 10, rue Alice Domon et Leonie Duquet, 75205 Paris, France*

² *Pierre Auger Observatory, av. San Martín Norte 304 (5613) Malargüe, Argentina*

dmitri.semikoz@apc.univ-paris7.fr

Abstract: Taking into account the Pierre Auger Observatory limits on the photon fraction among the highest energy cosmic rays, we show that the models based on the decay of super-heavy dark matter in the halo of our Galaxy are essentially excluded from being the sources of UHECRs unless their contribution becomes significant only above ~ 100 EeV. Some top-down models based on topological defects are however compatible with the current data and may be best constrained in future by the high-energy neutrino flux limit.

Limits to the diffuse flux of UHE tau neutrinos at EeV energies from the Pierre Auger Observatory

O. BLANCH BIGAS^{1,2}, FOR THE PIERRE AUGER COLLABORATION³

¹ *LPNHE, IN2P3 - CNRS - Universités Paris VI et Paris VII, 4 place Jussieu, Paris, France*

² *Ministerio de Educación y Ciencia, Spain*

³ *Pierre Auger Observatory, Av. San Martín Norte 304, (5613) Malargüe, Argentina*

blanch@lpnhe.in2p3.fr

Abstract: With the Pierre Auger Observatory we have the capability of detecting ultra-high energy neutrinos by searching for very inclined showers with a significant electromagnetic component. In this work we discuss the discrimination power of the instrument for earth skimming tau neutrinos with ultra-high energies. Based on the data collected since January 2004 an upper limit to the diffuse flux of neutrinos at EeV energies is presented and systematic uncertainties are discussed.

The sensitivity of the surface detector of the Pierre Auger Observatory to UHE Earth-skimming and down-going neutrinos

JAIME ALVAREZ-MUÑOZ¹, FOR THE PIERRE AUGER COLLABORATION²

¹ *Dept. Física de Partículas & IGFAE, Univ. Santiago de Compostela, 15782 Santiago, SPAIN*

² *Av. San Martín Norte 304 (5613) Malargüe, Prov. de Mendoza, ARGENTINA*

jaime@fpaxp1.usc.es

Abstract: The Pierre Auger Observatory is sensitive to ultra-high energy neutrinos in the EeV range and above. In this work we describe the complete chain needed to compute the neutrino acceptance of the surface detector. We firstly address the computation of the probability that an ultra-high energy neutrino produces an air shower. Subsequently we present the simulations to deduce the detector response to those showers. Finally, we discuss the identification of neutrinos based on searching for highly-inclined showers with a significant electromagnetic component at ground.

Reconstruction accuracy of the surface detector array of the Pierre Auger Observatory

M. AVE FOR PIERRE AUGER COLLABORATION¹

¹ *Pierre Auger Observatory, Av San Martín Norte 304, (5613) Malargüe, Argentina*
ave@cfcg.uchicago.edu

Abstract: The reconstruction of extensive air showers (arrival direction, core position and energy estimation) by the surface detector of the Pierre Auger Observatory is discussed together with the corresponding accuracy. We determine the angular reconstruction accuracy as a function of the station multiplicity by using two different approaches. We discuss statistical and systematic uncertainties in the determination of the signal at 1000 m from the core, $S(1000)$, which is used to estimate the primary energy.

Hybrid Performance of the Pierre Auger Observatory

B.R. DAWSON¹, FOR THE PIERRE AUGER COLLABORATION²

¹ *Department of Physics, University of Adelaide, Adelaide 5005, Australia*

² *Observatorio Pierre Auger, Av. San Martín Norte 304, (5613) Malargüe, Mendoza, Argentina*
bruce.dawson@adelaide.edu.au

Abstract: A key feature of the Pierre Auger Observatory is its hybrid design, in which ultra high energy cosmic rays are detected simultaneously by fluorescence telescopes and a ground array. The two techniques see air showers in complementary ways, providing important cross-checks and measurement redundancy. Much of the hybrid capability stems from the accurate geometrical reconstruction it achieves, with accuracy better than either the ground array detectors or a single telescope could achieve independently. We have studied the geometrical and longitudinal profile reconstructions of hybrid events. We present the results for the hybrid performance of the Observatory, including trigger efficiency, energy and angular resolution, and the efficiency of the event selection.

Systematic study of atmosphere-induced influences and uncertainties on shower reconstruction at the Pierre Auger Observatory

MICHAEL PROUZA¹, FOR THE PIERRE AUGER COLLABORATION²

¹ *Nevis Institute and Department of Physics, Columbia University, New York, N.Y., U.S.A.*

² *Observatorio Pierre Auger, Av. San Martín Norte 304, 5613 Malargüe, Argentina*
prouza@nevis.columbia.edu

Abstract: A wide range of atmospheric monitoring instruments is employed at the Pierre Auger Observatory : two laser facilities, elastic lidar stations, aerosol phase function monitors, a horizontal attenuation monitor, star monitors, weather stations, and balloon soundings. We describe the impact of analyzed atmospheric data on the accuracy of shower reconstructions, and in particular study the effect of the data on the shower energy and the depth of shower maximum (X_{\max}). These effects have been studied using the subset of “golden hybrid” events — events observed with high quality in the fluorescence and surface detector — used in the calibration of the surface detector energy spectrum.

Selection and reconstruction of very inclined air showers with the Surface Detector of the Pierre Auger Observatory

D. NEWTON¹ FOR THE PIERRE AUGER COLLABORATION²

¹ *Departamento de Física de Partículas, Universidad de Santiago de Compostela, Spain*

² *Av. San Martín Norte 304, (5613) Malargüe, Prov. De Mendoza, Argentina*
dnewton@fpmacth1.usc.es

Abstract: The water-Cherenkov tanks of the Pierre Auger Observatory can detect particles at all zenith angles and are therefore well-suited for the study of inclined and horizontal air showers ($60^\circ < \theta < 90^\circ$). Such showers are characterised by a dominance of the muonic component at ground, and by a very elongated and asymmetrical footprint which can even exhibit a lobular structure due to the bending action of the geomagnetic field. Dedicated algorithms for the selection and reconstruction of such events, as well as the corresponding acceptance calculation, have been set up on basis of muon maps obtained from shower simulations.

3D Reconstruction of Extensive Air Showers from Fluorescence Data

S. ANDRINGA¹, M. PATO¹ AND M. PIMENTA¹, FOR THE PIERRE AUGER COLLABORATION

¹*Laboratório de Instrumentação e Física de Partículas,
Av. Elias Garcia, 14, 1º, 1000-149 Lisboa, Portugal
sofia@lip.pt*

Abstract: A new method to reconstruct the 3-dimensional structure of extensive air showers, seen by fluorescence detectors, is proposed. The observation of the shower is done in 2-dimensional pixels, for consecutive time bins. Time corresponds to a third dimension. Assuming that the cosmic ray shower propagates as a plane wave front moving at the speed of light, a complex 3D volume in space can be associated to each measured charge (per pixel and time bin). The 3D description in space allows a simultaneous access to the longitudinal and lateral profiles of each shower. In the case that several eyes observe the same shower, the method gives a straight-forward combination of all the information. This method is in an early phase of development and is not used for the general reconstruction of the Auger data.

Performance of the Pierre Auger Observatory Surface Detector

T.SUOMIJÄRVI¹, FOR THE PIERRE AUGER COLLABORATION²

(1) *Institut de Physique Nucleaire, Université Paris-Sud, IN2P3-CNRS, Orsay, France*
(2) *Observatorio Pierre Auger, Av. San Martín Norte 304, (5613) Malargüe, Argentina*
tiina@ipno.in2p3.fr

Abstract: The Surface Detector of the Pierre Auger Observatory will consist of 1600 water Cherenkov tanks sampling ground particles of air showers produced by energetic cosmic rays. The arrival times are obtained from GPS and power is provided by solar panels. The construction of the array is nearly completed and a large number of detectors has been operational for more than three years. In this paper the performance of different components of the detectors are discussed. The accuracy of the signal measurement and the trigger stability are presented. The performance of the solar power system and other hardware, as well as the water purity and its long-term stability are discussed.

Weather induced effects on extensive air showers observed with the surface detector of the Pierre Auger Observatory

CARLA BLEVE¹, FOR THE PIERRE AUGER COLLABORATION²

¹*School of Physics and Astronomy, University of Leeds, Leeds, LS2 9JT, United Kingdom*
²*Observatorio Pierre Auger, Av. San Martín Norte 304, (5613) Malargüe, Mendoza, Argentina*
C.Bleve@leeds.ac.uk

Abstract: The rate of events measured with the surface detector of the Pierre Auger Observatory is found to be modulated by the weather conditions. This effect is due to the increasing amount of matter traversed by a shower as the ground pressure increases and to the inverse proportionality of the Molière radius to the air density near ground. Air-shower simulations with different realistic profiles of the atmosphere support this interpretation of the observed effects.

Testing the surface detector simulation for the Pierre Auger Observatory

P. L. GHIA¹, FOR THE PIERRE AUGER COLLABORATION²

¹ *Istituto di Fisica dello Spazio Interplanetario, INAF, Torino and Laboratori Nazionali del Gran Sasso, INFN, Assergi, Italy*
² *Pierre Auger Observatory, Av. San Martín Norte 304, (5613) Malargüe, Argentina*
piera.ghia@lngs.infn.it

Abstract: The building block of the surface detector of the Pierre Auger Observatory is a water Cherenkov tank. The response to shower particles is simulated using a dedicated program based on GEANT4. To check the simulation chain, we compare the simulated signals produced by cosmic muons at various zenith angles with experimental data from a special Cherenkov detector equipped with a muon hodoscope. The signals from muon-decay electrons and the evolution of the charge with water level are also studied.

The Absolute, Relative and Multi-Wavelength Calibration of the Pierre Auger Observatory Fluorescence Detectors

R. KNAPIK¹, P. BAULEO, B.R. BECKER, J. BRACK, R. CARUSO, C. DELLE FRATTE, A. DOROFEEV, J. HARTON, A. INSOLIA, J.A.J. MATTHEWS, A. MENSNIKOV, F. ORTOLANI, P. PETRINCA, A. PICHEL, S. RIGGI, M. ROBERTS, J. RODRIGUEZ MARTINO, A.C. ROVERO, M. SCUDERI, A. TAMASHIRO, D. TORRESI, V. TUCI AND L. WIENCKE FOR THE PIERRE AUGER COLLABORATION²

¹*Colorado State University Fort Collins, Colorado, USA*

²*Av. San Martin Norte 304 (5613) Malargue, Prov. de Mendoza, Argentina*

knapik@lamar.colostate.edu

Abstract: Absolute calibration of the Pierre Auger Observatory fluorescence detectors uses a 375 nm light source at the telescope aperture. This end-to-end technique accounts for the combined effects of all detector components in a single measurement. The relative response has been measured at wavelengths of 320, 337, 355, 380 and 405 nm, defining a spectral response curve which has been normalized to the absolute calibration. Before and after each night of data taking a relative calibration of the phototubes is performed. This relative calibration is used to track both short and long term changes in the detector's response. A cross check of the calibration in some phototubes is performed using an independent laser technique. Overall uncertainties, current results and future plans are discussed.

Online Monitoring of the Pierre Auger Observatory

J. RAUTENBERG¹ FOR THE AUGER COLLABORATION²

¹*Bergische Universität Wuppertal, 42097 Wuppertal, Germany*

²*Av. San Martin Norte 304 (5613) Malargüe, Prov. de Mendoza, Argentina*

julian.rautenberg@uni-wuppertal.de

Abstract: The data taking of the different components of the Pierre Auger Observatory, i.e. the surface detectors (SD) and the fluorescence telescopes (FD) has to be supervised by a shift crew on site to guarantee a smooth operation. A monitoring tool has been developed to support the shifter in judging and supervising the status of the detector components, the electronics and the data-acquisition (DAQ). Data are collected online for this purpose in the regular measuring time as well as in dedicated modes e.g., for calibration or atmospheric surveys. While for some components like SD this information is directly transmitted to the DAQ on the central campus, for others it is stored in a database locally, e.g for FD within the four remote housings of the telescopes. These databases are replicated to the central server on the campus via a wireless long distance link. A web-interface implemented on a dedicated server can dynamically generate graphs and particular developed visualisations to be accessible not only for the shifter, but also for experts remotely from anywhere in the world. In addition, in case of special occurrences an alarm is triggered automatically. This tool does also offer a unique opportunity to monitor the long term stability of some key quantities and the data quality. The concept and its implementation will be presented.

Measurement of Aerosols at the Pierre Auger Observatory

S.Y. BENZVI, F. ARQUEROS, R. CESTER, M. CHIOSSO, B.M. CONNOLLY, B. FICK, A. FILIPČIČ, B. GARCÍA, A. GRILLO, F. GUARINO, M. HORVAT, M. IARLORI, C. MACOLINO, M. MALEK, J. MATTHEWS, J.A.J. MATTHEWS, D. MELO, R. MEYHANDAN, M. MICHELETTI, M. MONASOR, M. MOSTAFÁ, R. MUSSA, J. PALLOTTA, S. PETRERA, M. PROUZA, V. RIZI, M. ROBERTS, J.R. RODRIGUEZ ROJO, D. RODRÍGUEZ-FRÍAS, F. SALAMIDA, M. SANTANDER, G. SEQUEIROS, P. SOMMERS, A. TONACHINI, L. VALORE, D. VERBERIČ, E. VISBAL, S. WESTERHOFF, L. WIENCKE, D. ZAVRTANIK, M. ZAVRTANIK, FOR THE PIERRE AUGER COLLABORATION¹

¹*Pierre Auger Observatory, Av. San Martín Norte 304 (5613) Malargüe, Argentina*
sybenzvi@phys.columbia.edu

Abstract:

The air fluorescence detectors (FDs) of the Pierre Auger Observatory are vital for the determination of the air shower energy scale. To compensate for variations in atmospheric conditions that affect the energy measurement, the Observatory operates an array of monitoring instruments to record hourly atmospheric conditions across the detector site, an area exceeding 3,000 km². This paper presents results from four instruments used to characterize the aerosol component of the atmosphere: the Central Laser Facility (CLF), which provides the FDs with calibrated laser shots; the scanning backscatter lidars, which operate at three FD sites; the Aerosol Phase Function monitors (APFs), which measure the aerosol scattering cross section at two FD locations; and the Horizontal Attenuation Monitor (HAM), which measures the wavelength dependence of aerosol attenuation.

New method for atmospheric calibration at the Pierre Auger Observatory using FRAM, a robotic astronomical telescope

SEGEV BENZVI, MARTINA BOHÁČOVÁ, BRIAN CONNOLLY, JIŘÍ GRYGAR, MIROSLAV HRABOVSKÝ, TATIANA KÁROVÁ, DUŠAN MANDÁT, PETR NEČESAL, DALIBOR NOSEK, LIBOR NOŽKA, MIROSLAV PALATKA, MIROSLAV PECH, MICHAEL PROUZA, JAN ŘÍDKÝ, PETR SCHOVÁNEK, RADOMÍR ŠMÍDA, PETR TRÁVNÍČEK, PRIMO VITALE, AND STEFAN WESTERHOFF
FOR THE PIERRE AUGER COLLABORATION¹

¹*Pierre Auger Observatory, Av. San Martín Norte 304, 5613 Malargüe, Argentina*
travnick@fzu.cz

Abstract: FRAM - F/(Ph)otometric Robotic Atmospheric Monitor is the latest addition to the atmospheric monitoring instruments of the Pierre Auger Observatory. An optical telescope equipped with CCD camera and photometer, it automatically observes a set of selected standard stars and a calibrated terrestrial source. Primarily, the wavelength dependence of the attenuation is derived and the comparison between its vertical values (for stars) and horizontal values (for the terrestrial source) is made. Further, the integral vertical aerosol optical depth can be obtained. A secondary program of the instrument, the detection of optical counterparts of gamma-ray bursts, has already proven successful. The hardware setup, software system, data taking procedures, and first analysis results are described in this paper.

Astrophysics Motivation behind the Pierre Auger Southern Observatory Enhancements

G. MEDINA TANCO¹, FOR THE PIERRE AUGER COLLABORATION²

¹*Instituto de Ciencias Nucleares, Universidad Nacional Autonoma de Mexico, A.P. 70-543, Ciudad Universitaria, D.F. 04510, Mexico.*

²*Pierre Auger Observatory, Av. San Martín Norte 304, (5613) Malargüe, Argentina*
gmtanco@nucleares.unam.mx

Abstract: The Pierre Auger Collaboration intends to extend the energy range of its southern observatory in Argentina for high quality data from 0.1 to 3 EeV. The extensions, described in accompanying papers, include three additional fluorescence telescopes with a more elevated field of view (HEAT) and a nested surface array with 750 and 433 m spacing respectively and additional muon detection capabilities (AMIGA). The enhancement of the detector will allow measurement of cosmic rays, using the same techniques, from below the second knee up to the highest energies observed. The evolution of the spectrum through the second knee and ankle, and corresponding predicted changes in composition, are crucial to the understanding of the end of Galactic confinement and the effects of propagation on the lower energy portion of the extragalactic flux. The latter is strongly related to the cosmological distribution of sources and to the composition of the injected spectrum. We discuss the science motivation behind these enhancements as well as the impact of combined HEAT and AMIGA information on the assessment of shower simulations and reconstruction techniques.

AMIGA, Auger Muons and Infill for the Ground Array

A. ETCHEGOYEN¹, FOR THE PIERRE AUGER COLLABORATION².

¹*Departamento de Física (Tandar), Centro Atómico Constituyentes, Comisión Nacional de Energía Atómica and UTN-FRBA,*

²*Observatorio Pierre Auger, Av. San Martín Norte 304 (5613) Malargüe, Prov. Mendoza, Argentina*
etchevoy@tandar.cnea.gov.ar

Abstract: The Pierre Auger Observatory is planned to be upgraded so that the energy spectrum of cosmic rays can be studied down to 0.1 EeV and the muon component of showers can be determined. The former will lead to a spectrum measured by one technique from 0.1 EeV to beyond 100 EeV while the latter will aid identification of the primary particles. These enhancements consist of three high elevation telescopes (HEAT) and an infilled area having both surface detectors and underground muon counters (AMIGA). The surface array of the Auger Observatory will be enhanced over a 23.5 km² area by 85 detector pairs laid out as a graded array of water-Cherenkov detectors and 30 m² buried muon scintillator counters. The spacings in the array will be 433 and 750 m. The muon detectors will comprise highly segmented scintillators with optical fibres ending on multi-anode phototubes. The AMIGA complex will be centred 6.0 km away from the fluorescence detector installation at Coihueco and will be overlooked by the HEAT telescopes. We describe the design features of the AMIGA enhancement.

Radio detection of high-energy cosmic rays at the Pierre Auger Observatory

A.M. VAN DEN BERG¹ FOR THE PIERRE AUGER COLLABORATION²

¹*Kernfysisch Versneller Instituut, University of Groningen, NL-9747 AA, Groningen, The Netherlands*

²*Av. San Martín Norte 304, (5613) Malargüe, Prov. de Mendoza, Argentina*
berg@kvi.nl

Abstract: The southern Auger Observatory provides an excellent test bed to study the radio detection of extensive air showers as an alternative, cost-effective, and accurate tool for cosmic-ray physics. The data from the radio setup can be correlated with those from the well-calibrated baseline detectors of the Pierre Auger Observatory. Furthermore, human-induced radio noise levels at the southern Auger site are relatively low. We have started an R&D program to test various radio-detection concepts. Our studies will reveal Radio Frequency Interferences (RFI) caused by natural effects such as day-night variations, thunderstorms, and by human-made disturbances. These RFI studies are conducted to optimise detection parameters such as antenna design, frequency interval, antenna spacing and signal processing. The data from our initial setups, which presently consist of typically 3 - 4 antennas, will be used to characterise the shower from radio signals and to optimise the initial concepts. Furthermore, the operation of a large detection array requires autonomous detector stations. The current design is aiming at stations with antennas for two polarisations, solar power, wireless communication, and local trigger logic. The results of this initial phase will provide an important stepping stone for the design of a few tens kilometers square engineering array.

Education and Outreach for the Pierre Auger Observatory

G. SNOW¹ FOR THE PIERRE AUGER COLLABORATION²

¹*Department of Physics and Astronomy, University of Nebraska, Lincoln, NE 68588-0111 USA*

²*Av. San Martín Norte 304 (5613) Malargüe, Prov. de Mendoza, Argentina*
gsnow@unlhep.unl.edu

Abstract: The scale and scope of the physics studied at the Auger Observatory offer significant opportunities for original outreach work. Education, outreach, and public relations of the Auger collaboration are coordinated in a task of its own whose goals are to encourage and support a wide range of efforts that link schools and the public with the Auger scientists and the science of cosmic rays, particle physics, and associated technologies. This report focuses on the impact of the collaboration in Mendoza Province, Argentina, as: the Auger Visitor Center in Malargüe that has hosted over 29,000 visitors since 2001, the Auger Celebration and a collaboration-sponsored science fair held on the Observatory campus in November 2005, the opening of the James Cronin School in Malargüe in November 2006, public lectures, school visits, and courses for science teachers. As the collaboration prepares the proposal for the northern Auger site foreseen to be in southeast Colorado, plans for a comprehensive outreach program are being developed in parallel, as described here.

Air fluorescence yield dependence on atmospheric parameters

P. PRIVITERA¹ FOR THE AIRFLY COLLABORATION

¹*University of Roma Tor Vergata and INFN, Via della Ricerca Scientifica 1, 00133, Rome, Italy*
priviter@roma2.infn.it

Abstract: The fluorescence detection of ultra high energy cosmic rays requires a detailed knowledge of the fluorescence light emission from nitrogen molecules over a wide range of atmospheric parameters, corresponding to altitudes typical of the cosmic ray shower development in the atmosphere. We have made a precise measurement of the fluorescence light spectrum excited by MeV electrons in air. The relative intensities of the fluorescence bands and their pressure, temperature and humidity dependence are reported.

Energy dependence of air fluorescence yield

M. AVE¹ FOR THE AIRFLY COLLABORATION

¹*University of Chicago, Enrico Fermi Institute, 5640 S. Ellis Ave., Chicago, IL 60637, United States*
ave@uchicago.edu

Abstract: In the fluorescence detection of ultra high energy ($\gtrsim 10^{18}$ eV) cosmic rays, the number of emitted fluorescence photons is assumed to be proportional to the energy deposited in air by shower particles. We have performed measurements of the fluorescence yield in atmospheric gases excited by electrons over energies ranging from keV to hundreds of MeV in several accelerators. We found that within the measured energy ranges the proportionality holds at the level of few %.



Latest Results from the Air Shower Simulation Programs CORSIKA and CONEX

T. PIEROG¹, R. ENGEL¹, D. HECK¹, S. OSTAPCHENKO^{1,2} AND K. WERNER³.

¹ *Forschungszentrum Karlsruhe, Institut für Kernphysik, Karlsruhe, Germany*

² *D.V. Skobeltsyn Institute of Nuclear Physics, Moscow State University, Moscow, Russia*

³ *SUBATECH, University of Nantes – IN2P3/CNRS– EMN, Nantes, France*

pierog@ik.fzk.de

Abstract: Interpretation of EAS measurements strongly depends on detailed air shower simulations. The uncertainty in the prediction of shower observables for different primary particles and energies is currently dominated by differences between hadronic interaction models. The new models QGSJET II-3 and EPOS 1.6, which reproduce all major results of existing accelerator data (including detailed data of RHIC experiments for EPOS), have been implemented in the air shower simulation programs CORSIKA and CONEX. We show predictions of these new models and compare them with those from older models such as QGSJET01 or SIBYLL. Results for important air shower observables are discussed in detail.

Introduction

The experimental method of studying ultra-high energy cosmic rays is an indirect one. Typically, one investigates various characteristics of extensive air showers (EAS), a huge nuclear-electromagnetic cascade induced by a primary particle in the atmosphere, and uses the obtained information to infer the properties of the original particle, its energy, type, direction etc. Hence, the reliability of ultra-high energy cosmic ray analyses depends on the use of proper theoretical and phenomenological descriptions of the cascade processes.

The most natural way to predict atmospheric particle cascading in detail seems to be a direct Monte Carlo (MC) simulation of EAS development, like it is done, for example, in the CORSIKA program [1]. As a very large computation time is required at high energy, an alternative procedure was developed to describe EAS development numerically, based on the solution of the corresponding cascade equations. Combining this with an explicit MC simulation of the most energetic part of an air shower allows us to obtain accurate results both for average EAS characteristics and for their fluctuations in CONEX program [2].

After briefly describing recent changes introduced in CORSIKA and CONEX, we will present the lat-

est results for important air shower observables obtained with these models.

Improvements of CORSIKA and CONEX

Last year QGSJET II-3 [3] and this year EPOS 1.6 [4] have been introduced in both CORSIKA and CONEX as new hadronic interaction models. These models have quite different philosophies. The first one is dedicated to cosmic ray physics and based on the re-summation of enhanced pomeron graphs to all orders [5]. The latter one is designed for high energy physics and partially relies on a more phenomenological approach, aiming at a nearly perfect description of accelerator data, in particular new RHIC measurements. Some results are presented in the following (see also [6]).

Concerning the particle tracking algorithms, the most important improvement in the last release of CORSIKA (6.611) is the possibility to combine the SLANT/UPWARD/CURVED options [7] in order to simulate air showers with any kind of zenith angle, including upward going showers (from 0° to 180°). The calculation of slant depth distances has been improved using the work of [8] as also employed in CONEX. In Fig. 1 the mean longitudinal

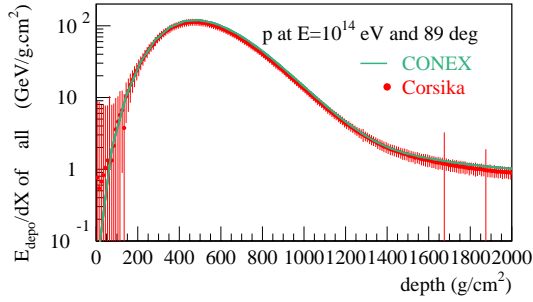


Figure 1: Mean longitudinal energy deposit profile in $\text{GeV g}^{-1} \text{cm}^2$ as a function of the slant depth in g cm^{-2} for proton induced 89° inclined showers at 10^{14} eV simulated with CORSIKA (red dots) and CONEX (green line) using QGSJET01.

energy deposit profile is shown as a function of the slant depth for proton induced showers of 89° at 10^{14} eV, simulated with CORSIKA and CONEX using QGSJET01 [9]. Even for this extreme zenith angle, very good agreement between the two programs is found.

Furthermore, in order to improve muon propagation, the Sternheimer density correction of the ionization energy loss has been extended to apply also to muons in both CORSIKA and CONEX, based on work by Kokoulin & Bogdanov [10]. The effect of the density correction can be seen in Fig. 2.

A major technical improvement was achieved in CORSIKA by replacing the old version manager CMZ by the combination of AUTOCONF/AUTOMAKE tools for the installation and selection of options in CORSIKA. Compilation has not to be done by the user anymore, rather Makefiles are generated by AUTOMAKE. Options are selected by a shell script using AUTOCONF and standard C preprocessor commands in the CORSIKA source code.

Finally, the interfaces to FLUKA 2006.3 [11] and HERWIG 6.51 [12] have been updated.

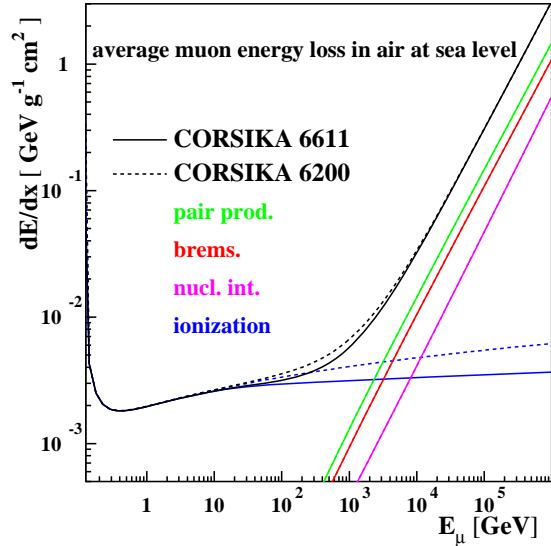


Figure 2: Muon energy loss in $\text{GeV g}^{-1} \text{cm}^2$ as a function of total muon energy in GeV for CORSIKA versions 6.200 (dashed) and 6.611 (full).

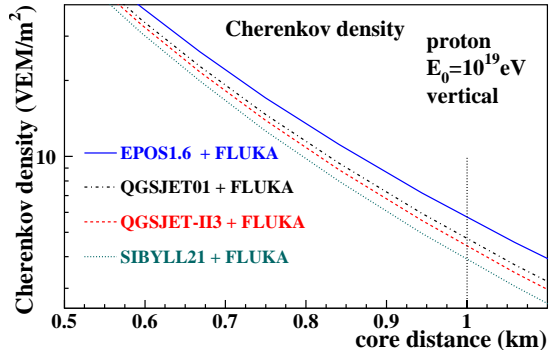


Figure 3: Mean lateral distribution function of Cherenkov density for 10^{19} eV vertical proton induced showers and different high-energy hadronic interaction models, EPOS 1.6 (full), QGSJET01 (dashed-dotted), QGSJET II-3 (dashed) and SIBYLL 2.1 (dotted).

Latest results

In the following air shower simulation results using EPOS 1.6 and QGSJET II-3 are presented and compared to former results using QGSJET01 [9] or SIBYLL 2.1 [13, 14].

In Fig. 3, CORSIKA-based estimates for the lateral distribution of the Cherenkov signal in Auger tanks [15] are shown. The tank signal has been simulated in a simplified way as only the relative differences between the model results are of importance here. Due to a much larger muon number at ground in EPOS [6, 16], the density at 1 km shows an excess of about 30 to 40% compared to QGSJET II-3 while the latter is well in between QGSJET01 and SIBYLL. Such an excess is of crucial importance for the reconstruction of the primary energy and composition with the Auger surface detector alone [17]. Compared to other models, using EPOS would decrease the energy reconstructed from lateral densities and could lead to a lighter primary cosmic ray composition.

The higher muon number from EPOS is mainly due to a larger baryon-antibaryon pair production rate in the individual hadronic interactions in showers. By predicting more baryons, more energy is kept in the hadronic shower component even at low energy. As a consequence, the calorimetric energy as measured by fluorescence light detectors is reduced since more energy is transferred to neutrinos and muons. In Fig. 4 the conversion factor from the visible calorimetric energy to the real energy is plotted as a function of the primary energy of the showers. QGSJET II-3 gives results very similar to SIBYLL. As expected, EPOS shows a conversion factor which is up to 3.5% higher than other models at low energy.

As shown in Fig. 5, the mean depth of shower maximum, X_{\max} , for proton and iron induced showers simulated with CONEX is nevertheless not very different for EPOS. Up to 10^{19} eV, all models agree within 20g cm^{-2} . EPOS proton induced showers show a slightly higher elongation rate in that range while QGSJET II-3 has a slightly lower one. Above this energy, both QGSJET01 and QGSJET II-3 elongation rates decrease due to the very large multiplicity of these models at ultra-high energy. Below 10^{18} eV, an analysis of X_{\max} data would lead to a composition of primary cosmic rays that is heav-

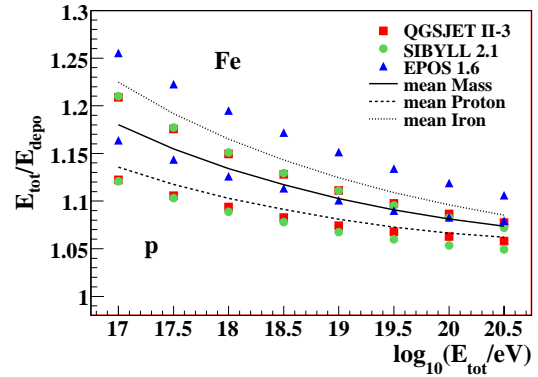


Figure 4: Mean factor for the conversion of observed (calorimetric) energy to total energy for iron (dotted) or proton (dashed) induced showers. The conversion factor is shown for QGSJET II-3 (circles), SIBYLL 2.1 (squares) and EPOS 1.6 (triangles). The mean conversion factor (full line) is calculated by averaging all proton and iron predictions.

ier using QGSJET II-3 compared to EPOS. Above 10^{18} eV the situation is reversed.

Conclusions

New versions of CORSIKA and CONEX have been released recently with two new hadronic interaction models. The models differ in several important aspects in the approach of reproducing data. In QGSJET II-3, high parton density effects are treated by re-summing enhanced pomeron graphs to all orders, but energy conservation at amplitude level is not implemented. On the other hand, in EPOS, energy conservation at amplitude level is fully implemented, but high-density effects are treated by a phenomenological parametrization. EPOS is particularly well-tuned to describe available accelerator data including heavy ion collisions measured at RHIC. The differences of the model predictions are large: At high energy, proton induced air showers simulated with EPOS have even more muons at ground than iron induced showers simulated with QGSJET II-3. Comparison to cosmic ray data, for example, from the KASCADE

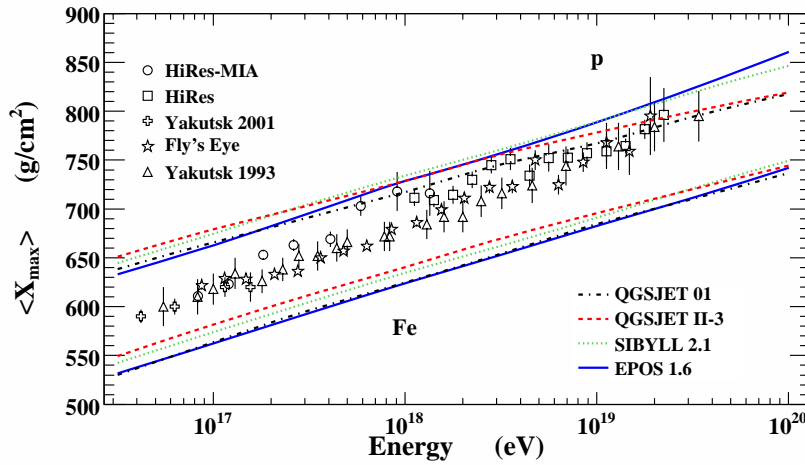


Figure 5: Mean X_{\max} for proton and iron induced showers as a function of the primary energy. Predictions of different high-energy hadronic interaction models, QGSJET01 (dashed-dotted), QGSJET II-3 (dashed), SIBYLL 2.1 (dotted) and EPOS 1.6 (full), are compared to data. Refs. to the data can be found in [18]

detector, are now needed to support or disfavour the EPOS predictions [19].

Acknowledgments: The CORSIKA and CONEX authors would like to thank all users who contributed to the development of the programs by helping to detect and solve problems. We are particularly grateful to R.P. Kokoulin and A.G. Bogdanov for their very useful work and comments on muon interactions and energy loss.

References

- [1] D. Heck *et al.*, Wissenschaftliche Berichte FZKA 6019, Forschungszentrum Karlsruhe, 1998.
- [2] T. Bergmann *et al.*, *Astropart. Phys.* 26 (2007) 420–432 and astro-ph/0606564.
- [3] S. Ostapchenko, *Phys. Rev. D* 74 (2006) 014026 and hep-ph/0505259.
- [4] K. Werner *et al.*, *Phys. Rev. C* 74 (2006) 044902 and hep-ph/0506232.
- [5] S. Ostapchenko, *Phys. Lett. B* 636 (2006) 40–45 and hep-ph/0602139.
- [6] T. Pierog and K. Werner, These proceedings #0905 (2007).
- [7] D. Heck, Wissenschaftliche Berichte FZKA 7254, Forschungszentrum Karlsruhe, 2006.
- [8] V. Chernatkin, *Simulation des gerbes dues aux rayons cosmiques a très hautes énergies* PhD thesis Université de Nantes 2005.
- [9] N. N. Kalmykov, S. S. Ostapchenko, and A. I. Pavlov, *Nucl. Phys. Proc. Suppl.* 52B (1997) 17–28.
- [10] R. P. Kokoulin and A. G. Bogdanov, 2007 private communication.
- [11] A. Ferrari *et al.*, CERN-2005-010.
- [12] G. Corcella *et al.*, hep-ph/0210213, 2002.
- [13] R. S. Fletcher, T. K. Gaisser, P. Lipari, and T. Stanev, *Phys. Rev. D* 50 (1994) 5710–5731.
- [14] R. Engel, T. K. Gaisser, P. Lipari, and T. Stanev, in Proceedings of 26th ICRC (Salt Lake City) vol. 1, p. 415, 1999.
- [15] J. Abraham *et al.* (Pierre Auger Collab.), *Nucl. Instrum. Meth.* A523 (2004) 50–95.
- [16] T. Pierog and K. Werner, astro-ph/0611311, 2006.
- [17] R. Engel *et al.* (Pierre Auger Collab.), These proceedings #0605 (2007).
- [18] R. Engel and H. Klages, *Comptes Rendus Physique* 5 (2004) 505–518.
- [19] H. Ulrich *et al.* (KASCADE-Grande Collab.), These proceedings #0178 (2007).



The Hadronic Interaction Model EPOS and Air Shower Simulations: New Results on Muon Production

T. PIEROG¹ AND K. WERNER².

¹ *Forschungszentrum Karlsruhe, Institut für Kernphysik, Karlsruhe, Germany*

² *SUBATECH, University of Nantes – IN2P3/CNRS– EMN, Nantes, France*

pierog@ik.fzk.de

Abstract: Since about one decade, air shower simulations based on the hadronic interaction models QGSJET and SIBYLL predict very similar results for the main observables. For instance, the mean depth of the shower maximum X_{\max} agrees within 5% between the different models and are in relative good agreement with the measurements. However the number of muons at ground differs substantially between these 2 models and the data. Recently a new hadronic interaction model EPOS has been introduced in air shower simulation programs. This model has originally been used to analyse hadron-hadron as well as heavy ion physics at RHIC and SPS energies, and it gives very interesting results in air shower simulations: we find for example a large increase in the number of muons at ground as compared to the former models. Results will be discussed in detail, in particular the role of the baryons and anti-baryons in the air shower development.

Introduction

Air shower simulations are a very powerful tool to interpret ground based cosmic ray experiments. However, most simulations are still based on hadronic interaction models being more than 10 years old. Much has been learned since, in particular due to new data available from the SPS and RHIC accelerators.

In this paper, we discuss air shower simulations based on EPOS, the latter one being a hadronic interaction model, which does very well compared to RHIC data [3, 1], and also all other available data from high energy particle physics experiments (ISR, CDF and especially SPS experiments at CERN).

EPOS is a consistent quantum mechanical multiple scattering approach based on partons and strings [6], where cross sections and the particle production are calculated consistently, taking into account energy conservation in both cases (unlike other models where energy conservation is not considered for cross section calculations [9]). A special feature is the explicit treatment of projectile and target remnants, leading to a very good description of baryon and antibaryon production as

measured in proton-proton collisions at 158 GeV at CERN [10]. Nuclear effects related to Cronin transverse momentum broadening, parton saturation, and screening have been introduced into EPOS [16]. Furthermore, high density effects leading to collective behavior in heavy ion collisions are also taken into account [15].

EPOS Basics

One may consider the simple parton model to be the basis of high energy hadron-hadron interaction models, which can be seen as an exchange of a “parton ladder” between the two hadrons. In EPOS, the term “parton ladder” is actually meant to contain two parts [6]: the hard one, as discussed above, and a soft one, which is a purely phenomenological object, parameterized in Regge pole fashion.

In additions to the parton ladder, there is another source of particle production: the two off-shell remnants, see fig. 1. We showed in ref. [10] that this “three object picture” can solve the “multi-strange baryon problem” of conventional high energy models, see ref. [5].

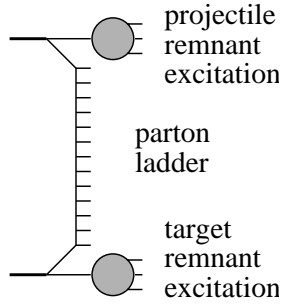


Figure 1: Elementary parton-parton scattering: the hard scattering in the middle is preceded by parton emissions attached to remnants. The remnants are an important source of particle production even at RHIC energies.

Multiple scattering is introduced based on Gribov's multiple scattering theory, as in other models, in order to ensure unitarity. In EPOS, however, we explicitly care about the fact that the total energy has to be shared among the individual elementary interactions. This is usually ignored, although it is required by theoretical consistency.

A consistent quantum mechanical formulation of the multiple scattering requires not only the consideration of the (open) parton ladders, discussed so far, but also of closed ladders, representing elastic scattering. The closed ladders do not contribute to particle production, but they are crucial since they affect substantially the calculations of partial cross sections. Actually, the closed ladders simply lead to large numbers of interfering contributions for the same final state, all of which have to be summed up to obtain the corresponding partial cross sections. It is a unique feature of our approach to consider explicitly energy-momentum sharing at this level (the "E" in the name EPOS).

Energy momentum sharing and remnant treatment are the key points of the model concerning air shower simulations because they directly influence the multiplicity and the inelasticity of the model. Some other new features – not discussed here but important for particle physics and accelerator data comparisons – are the treatment of high density effects, described in [16, 15].

Air Shower Simulations

In the following, we discuss air shower simulations, based on the shower programs CORSIKA[8] or CONEX[4], using EPOS or QGSJET II-3[11] (as a reference) as interaction model.

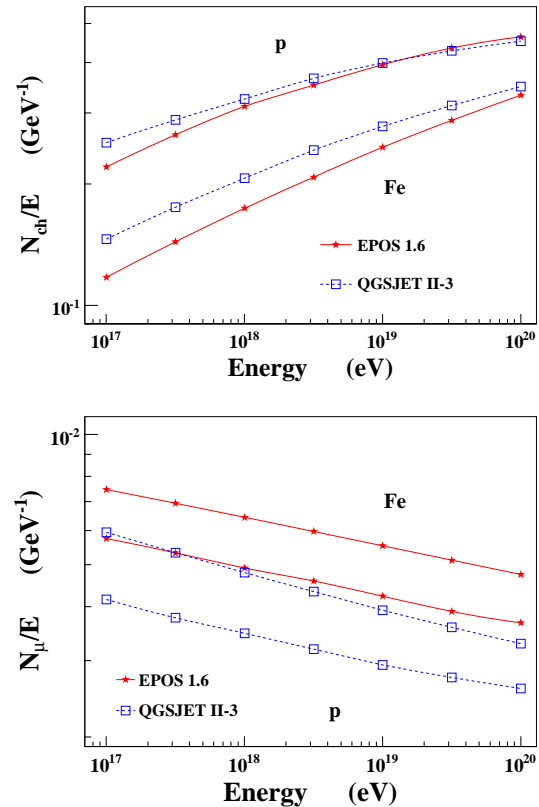


Figure 2: Total number of charged particles (upper plot) and muons (lower plot) at ground divided by the primary energy as a function of the primary energy for proton and iron induced shower using EPOS (full lines) and QGSJET II-3 (dotted lines) as high energy hadronic interaction model.

Air shower simulations are very important to analyze the two most common type of high energy cosmic ray experiments: fluorescence telescopes and surface detectors. In the first ones, one observes directly the longitudinal shower development, from which the energy and the depth of shower maximum X_{max} can be extracted. Comparing the latter with models allows us to have in-

formations on the mass of the primary. EPOS results concerning X_{\max} are in good agreement with former models and experimental data as shown in [13].

Concerning particles measured at ground by air shower experiment, the situation is quite different. Whereas the number of charged particles is very similar for EPOS and QGSJET II-3 (see fig. 2), EPOS produces a much higher muon flux, in particular at high energy. At 10^{20} eV EPOS is more than 40% higher and gives even more muons with a primary proton than QGSJET II-3 for iron induced showers.

The muon excess from EPOS compared to other models will affect all experimental observables depending on simulated muon results. In the case of the Pierre Auger observatory (PAO), this will affect mostly the results on inclined showers, for which the electromagnetic component is negligible at ground. It is interesting to notice that the PAO claims a possible lack of muons in air showers simulated with current hadronic interaction models [7].

The muon production process

During the hadronic air shower development, the energy is shared between neutral pions which convert their energy into the electromagnetic component of the shower, and charged hadrons which continue the hadronic cascade producing muons [12]. The ratio of the two (referred to as R) is a measure of the muon production.

Comparing EPOS to other models, this ratio R of neutral pions to charged hadrons produced in individual hadronic interactions is significantly lower, especially for pi-air reactions, as seen in fig. 3. This will increase the muon production, as discussed above.

Furthermore, the reduced ratio R is partly due to an enhanced baryon production, as shown in fig. 4. This will increase the number of baryon initiated sub-showers. Since the ratio R is much softer in case of proton-air interactions compared to pion-air interactions, as shown in fig. 5, this will even more reduce R , providing a significant additional source of muons. Indeed, simulations show that a pion induced shower produces about 30% less

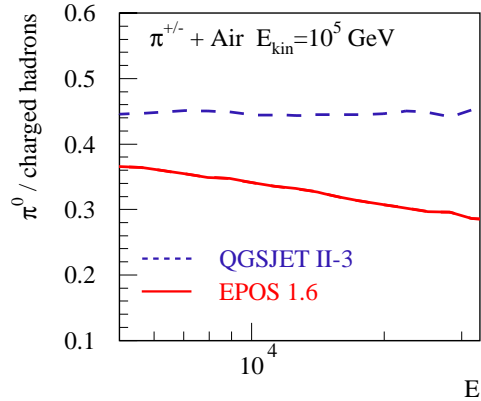


Figure 3: Ratio of the number of π^0 over the number of charged particles as a function of the energy of the secondary particles at 10^5 GeV kinetic energy with EPOS (full line) or QGSJET II-3 (dashed line) in pion-air.

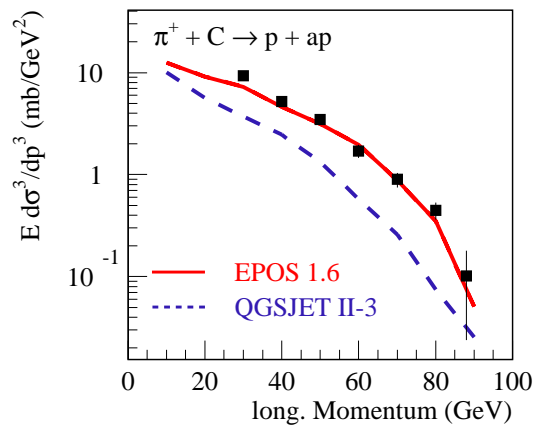


Figure 4: Model comparison: longitudinal momentum distributions of protons in pion carbon collisions at 100 GeV from EPOS (full) and QGSJET II-3 (dashed) compared to data[2].

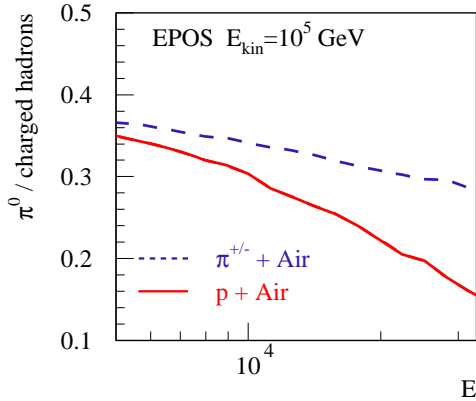


Figure 5: Ratio of the number of π^0 over the number of charged particles as a function of the energy of the secondary particles at 10^5 GeV kinetic energy in proton-air (full line) or pion-air (dashed line) for EPOS.

muons than a proton induced shower. This feature of the air shower development is in fact model independent and can easily be understood because of the leading particle effect [14].

Summary

EPOS is a new interaction model constructed on a solid theoretical basis. It has been tested very carefully against all existing hadron-hadron and hadron nucleus data, also those usually not considered important for cosmic rays. In air shower simulations, EPOS provides more muons than other models, which was found to be linked to an increased baryon production.

Acknowledgments

The authors would like to thank Ralph Engel, Dieter Heck and Sergej Ostapchenko for fruitful discussions.

References

- [1] B. I. Abelev et al. Strange particle production in p + p collisions at $s^{*(1/2)} = 200$ -gev. *nucl-ex/0607033*, 2006.
- [2] D. S. Barton et al. Experimental study of the a-dependence of inclusive hadron fragmentation. *Phys. Rev.*, D27:2580, 1983.
- [3] R. Bellwied. Strange particle production mechanisms in proton proton collisions at rhic. *Acta Phys. Hung.*, A27:201–204, 2006.
- [4] T. Bergmann et al. One-dimensional hybrid approach to extensive air shower simulation. *Astropart. Phys.*, 26:420–432, 2007.
- [5] M. Bleicher et al. Overpopulation of anti-omega in p p collisions: A way to distinguish statistical hadronization from string dynamics. *Phys. Rev. Lett.*, 88:202501, 2002.
- [6] H. J. Drescher et al. Parton-based gribov-regge theory. *Phys. Rept.*, 350:93–289, 2001.
- [7] R. Engel et al. Test of hadronic interaction models with data from the pierre auger observatory. *These proceedings*, #0605, 2007.
- [8] D. Heck et al. Corsika: A monte carlo code to simulate extensive air showers. FZKA-6019, 1998.
- [9] M. Hladik et al. Self-consistency requirement in high-energy nuclear scattering. *Phys. Rev. Lett.*, 86:3506–3509, 2001.
- [10] F. M. Liu et al. Constraints on models for proton-proton scattering from multistrange baryon data. *Phys. Rev.*, D67:034011, 2003.
- [11] S. Ostapchenko. Non-linear screening effects in high energy hadronic interactions. *Phys. Rev.*, D74:014026, 2006.
- [12] T. Pierog et al. Impact of uncertainties in hadron production on air-shower predictions. *Czech. J. Phys.*, 56:A161–A172, 2006.
- [13] T. Pierog et al. Latest results of air shower simulation programs corsika and conex. *These proceedings*, #0899, 2007.
- [14] T. Pierog and K. Werner. astro-ph/0611311.
- [15] K. Werner. Core-corona separation in ultra-relativistic heavy ion collisions. *Phys. Rev. Lett.*, 98:152301, 2007.
- [16] K. Werner et al. Parton ladder splitting and the rapidity dependence of transverse momentum spectra in deuteron gold collisions at rhic. *Phys. Rev.*, C74:044902, 2006.

Pion production in proton- and pion-carbon collisions at 12 GeV/c measured with HARP

C. MEURER¹, J. BLÜMER^{1,2}, R. ENGEL¹, A. HAUNGS¹, A. ROTH¹ AND THE HARP COLLABORATION

¹ *Forschungszentrum Karlsruhe, Institut für Kernphysik, 76021 Karlsruhe, Germany*

² *Universität Karlsruhe, Institut für Experimentelle Kernphysik, 76128 Karlsruhe, Germany*

Christine.Meurer@ik.fzk.de

Abstract: Motivated by the importance of the measurement of proton and pion interactions with light nuclei for tuning hadronic interaction models used in neutrino flux and extensive air shower simulations, we analyze pion production in p-C and pi-C reactions at 12 GeV/c measured in the fixed target experiment HARP at CERN-PS. We present momentum spectra of positive and negative pions and compare them with predictions of frequently used hadronic interaction models.

Introduction

The current generation of astroparticle physics detectors or experiments allows high precision and high statistics measurements. Part of the gain in precision of these experiments is related to the increase of available computing power and recent progress in developing detailed Monte Carlo simulations for calculating predictions for both detector signals and background effects. One central element of these complex calculations is often the simulation of particle interactions and particle production. Whereas it is known how electromagnetic or electroweak interactions can be simulated, hadronic interactions are still not sufficiently well understood. In fact, in several areas, our limited understanding of hadronic interactions has become the dominating source of systematic uncertainties (see, for example, [1, 2, 3, 4]).

Within the foreseeable future no breakthrough in the calculation of particle production processes within QCD is expected, underlining the importance of hadron production measurements. Data on the interactions of protons and pions with light nuclei of the Earth's atmosphere, as they are needed in particular in astrophysical applications, are very sparse [5, 6, 1].

In this work we present double-differential pion production spectra of proton and pion interactions

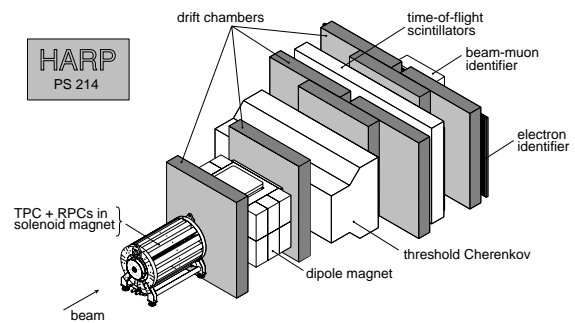


Figure 1: Setup of the HARP detector [7].

with carbon nuclei at 12 GeV/c beam momentum. The measurements were done with the fixed target HAdRon Production experiment PS214, HARP¹, at the CERN proton synchrotron (PS). Note that hadron production spectra on carbon are expected to be very similar in shape to those on nitrogen and oxygen [5].

Experimental setup and data analysis

The HARP setup [7] consists of a forward spectrometer (TOF, drift chambers, Cherenkov detector, electromagnetic calorimeter) and a large-angle

1. <http://harp.web.cern.ch/harp/>

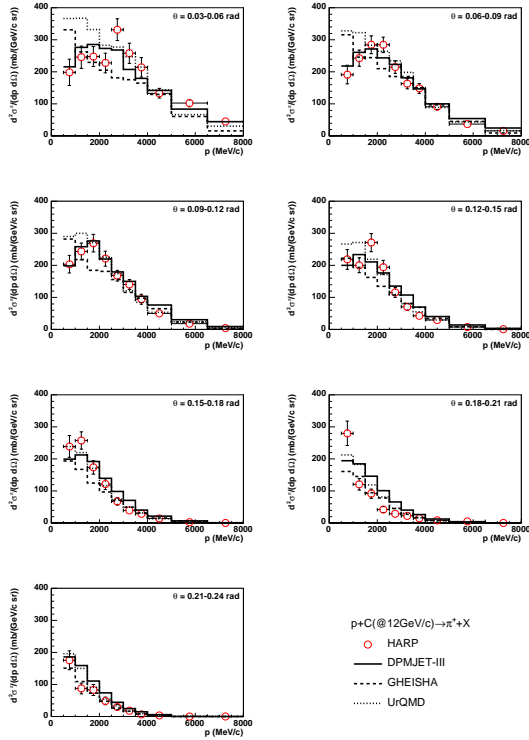


Figure 2: Inclusive production cross section of π^+ in p-C interactions at 12 GeV/c. The predictions of the models DPMJET III [10, 11], GHEISHA [12], and UrQMD [13] are also shown.

detection system (TPC), see Fig. 1. The forward spectrometer is built around a dipole magnet with an integral field of 0.66 Tm for momentum reconstruction. The forward detector system covers angles up to 250 mrad and is ideally suited for minimum bias particle production measurements. It is employed in the analysis presented here.

A detailed description of the event selection and track reconstruction of the carbon data set can be found in [8]. In the following only a brief overview is given. Particle identification is discussed in [9].

The pion and proton data sets were taken in two short runs in June and September 2002. More than one million triggers with positive beam and half a million triggers with negative beam were collected. In addition about 900k empty target events were recorded to correct for background interactions. A

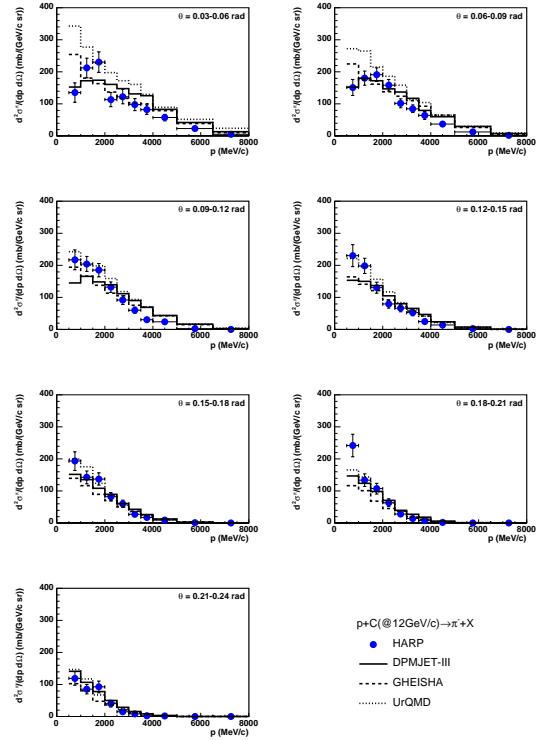


Figure 3: Inclusive production cross section of π^- in p-C interactions at 12 GeV/c. The predictions of the models DPMJET III [10, 11], GHEISHA [12], and UrQMD [13] are also shown.

thin carbon target of thickness of 5% of an interaction length was used. Events were selected according to the detected beam particle and beam position. After quality cuts about 460k p-C and 350k π^- -C events were left for analysis.

To ensure high quality track reconstruction, secondary particle tracks were selected only in the detector hemisphere in which the magnetic field of the dipole would bent the particle trajectory towards the beam axis. A matched hit in the TOF wall and several hits in the drift chamber system were required. About 100k secondary particle tracks in p-C and a similar number of tracks in π^- -C interactions passed the selection cuts.

The measured particle spectra were corrected for detector acceptance and reconstruction resolution effects using the Bayesian unfolding technique of

D'Agostini [14]. The detector acceptance and resolution is calculated by reconstructing a set of single track Monte Carlo simulations based on GEANT4 [15]. All relevant processes such as energy loss, absorption and re-interaction are considered. Empty target subtraction and a correction for kaons being misidentified as pions is applied.

Results

The double-differential pion production cross sections in proton-carbon interactions are shown in Figs. 2 and 3. The leading particle effect is clearly seen for positively charged pions.

The error bars indicate statistical and systematic errors added in quadrature. The size of both errors is of the same order and varies from 4% to 14% depending on the secondary particle momentum. Only for the highest momenta the statistical error clearly dominates and reaches more than 20%. The dominant sources of systematic uncertainty are the subtraction of tertiary interactions and the overall momentum scale.

The data are compared with predictions of the models DPMJET III [10, 11], GHEISHA [12], and UrQMD [13]. There is no obvious trend of one model giving a much better description of the data sets than the others. For example, the DPMJET predictions give a good description of the π^+ spectra but clear discrepancies are seen for π^- cross sections. The situation is similar for the other models.

In Fig. 4 we show the pion production cross sections for π^- -carbon interactions. These cross sections are particularly valuable for estimating tertiary interactions and give also a low-energy anchor point for tuning models used in air shower simulations. Again the error bars indicate both the systematic and statistical errors. A comparison of this data set with model predictions is in preparation.

Finally it should be mentioned that the analysis of pion production in proton-nitrogen and proton-oxygen interactions at 12 GeV/c is in progress. First results will be shown at the conference.

References

- [1] T. K. Gaisser and M. Honda, *Ann. Rev. Nucl. Part. Sci.* 52 (2002) 153–199 and *hep-ph/0203272*.
- [2] T. Antoni *et al.* (KASCADE Collab.), *Astropart. Phys.* 24 (2005) 1–25 and *astro-ph/0505413*.
- [3] T. Abu-Zayyad *et al.* (HiRes-MIA Collab.), *Phys. Rev. Lett.* 84 (2000) 4276 and *astro-ph/9911144*.
- [4] A. A. Watson, *Nucl. Phys. Proc. Suppl.* 151 (2006) 83–91 and *astro-ph/0410514*.
- [5] C. Meurer, J. Blümer, R. Engel, A. Haungs, and M. Roth, *Czech. J. Phys.* 56 (2006) A211 and *astro-ph/0512536*.
- [6] R. Engel, T. K. Gaisser, and T. Stanev, *Phys. Lett.* B472 (2000) 113–118 and *hep-ph/9911394*.
- [7] M. G. Catanesi *et al.* (HARP Collab.), *Nucl. Instrum. Meth.* A571 (2007) 527–561.
- [8] C. Meurer, PhD thesis, Universität Karlsruhe, 2007.
- [9] M. G. Catanesi *et al.*, *Nucl. Instrum. Meth.* A572 (2007) 899–921.
- [10] S. Roesler, R. Engel, and J. Ranft, in *Proc. of Int. Conf. on Advanced Monte Carlo for Radiation Physics, Particle Transport Simulation and Applications (MC 2000)*, Lisbon, Portugal, 23-26 Oct 2000, A. Kling, F. Barao, M. Nakagawa, L. Tavora, P. Vaz eds., Springer-Verlag Berlin, p. 1033-1038 (2001), 2000.
- [11] S. Roesler, R. Engel, and J. Ranft, Prepared for 27th International Cosmic Ray Conference (ICRC 2001), Hamburg, Germany, 7-15 Aug 2001, p. 439.
- [12] H. Fesefeldt, preprint PITHA-85/02, RWTH Aachen, 1985.
- [13] M. Bleicher *et al.*, *J. Phys. G: Nucl. Part. Phys.* 25 (1999) 1859.
- [14] G. D'Agostini, *Nucl. Instrum. Meth.* A362 (1995) 487–498.
- [15] S. Agostinelli *et al.* (GEANT4 Collab.), *Nucl. Instrum. Meth.* A506 (2003) 250–303.

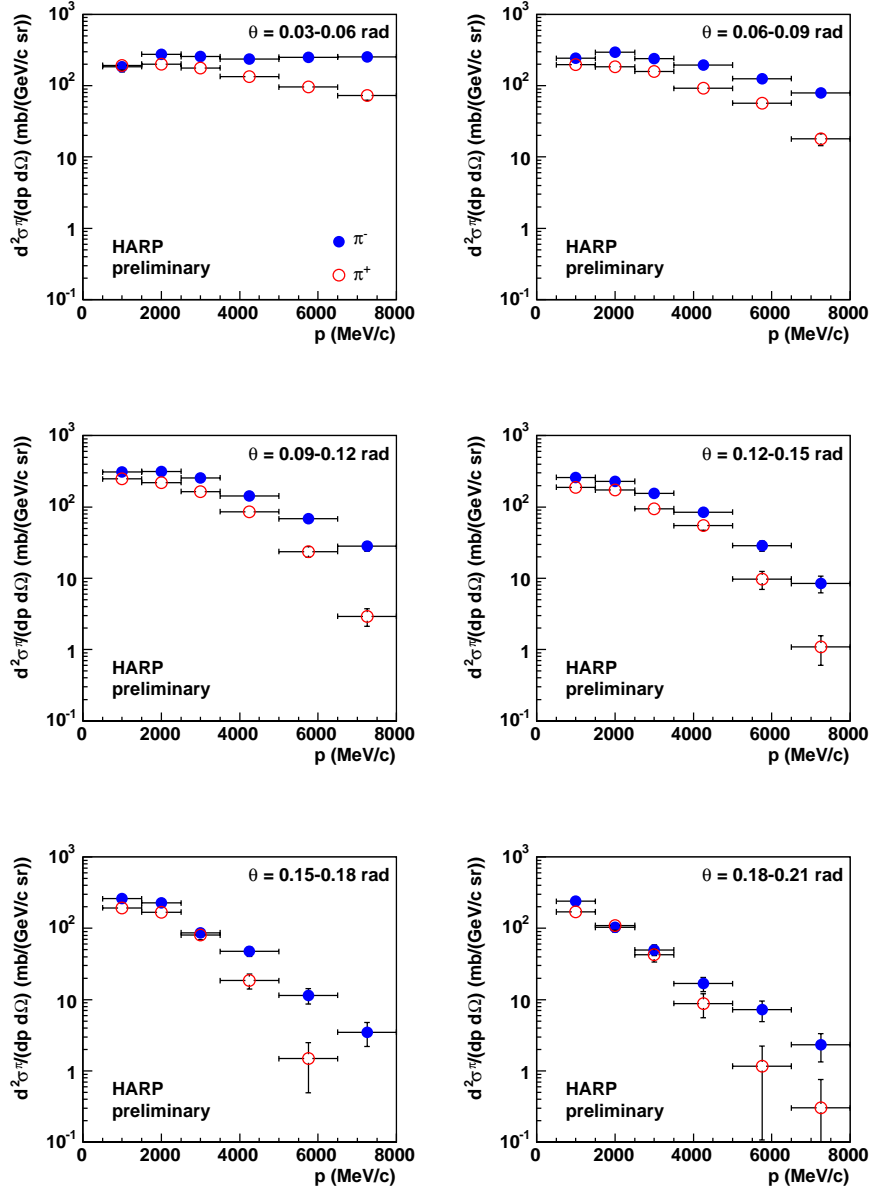


Figure 4: Inclusive charged pion production cross section in π^- -C interactions at 12 GeV/c.



On the relation between the proton-air cross section and fluctuations of the shower longitudinal profile

R. ULRICH, J. BLÜMER, R. ENGEL, F. SCHÜSSLER AND M. UNGER

¹*Institut für Kernphysik, Forschungszentrum Karlsruhe, Postfach 3640, 76021 Karlsruhe, Germany*
Ralf.Ulrich@ik.fzk.de

Abstract: The current status and prospects of deducing the proton-air cross section from fluorescence telescope measurements of extensive air showers are discussed. As it is not possible to observe the point of first interaction, X_1 , directly, other observables closely linked to X_1 must be inferred from the measured longitudinal profiles. This introduces a dependence on the models used to describe the shower development. Systematic uncertainties arising from this model dependence, from the reconstruction method itself and from a possible non-proton contamination of the selected shower sample are discussed.

Introduction

Indirect cosmic ray measurements by means of extensive air shower (EAS) observations are difficult to interpret. Models needed for a deeper understanding of the data have to be extrapolated over many decades in energy. This is the case for high energy (HE) interaction models, but also applies to the primary composition of cosmic rays. Unfortunately a changing primary composition and changes in the HE interaction characteristics can have similar effects on EAS development and are difficult to separate.

One of the key parameters for EAS development is the cross section σ_{p-air} of a primary proton in the atmosphere. Of course, only the part of the cross section leading to secondary particle production is relevant for EAS development, which we call for simplicity here σ_{p-air} . But also the production cross section contains contributions which cannot be observed in EAS. As diffractive interactions of primary particles with air nuclei do not (target dissociation) or weakly (projectile dissociation) influence the resulting EAS, any measurement based on EAS is insensitive to these interactions. Therefore, we define an effective cross section to require an inelasticity $k_{inel} = 1 - \frac{E_{max}}{E_{tot}}$ of at least 0.05

$$\sigma_{p-air}^* = \sigma_{p-air}(k_{inel} \geq 0.05). \quad (1)$$

In the following the amount of traversed matter before an interaction with $k_{inel} \geq 0.05$ is called X_1 . Taking this into account the reconstructed value of σ_{p-air}^* needs to be altered by a model dependent correction $\sigma_{p-air}^{model}(k_{inel} < 0.05)$. This correction amounts to 2.4 % for SIBYLL [1], 3.9 % for QGSJETII.3 [2] and 5.5 % for QGSJET01 [3], resulting in a model uncertainty of ~ 3 %.

All EAS simulations are performed in the CONEX [4] framework. To account for the limited reconstruction accuracy of a realistic EAS detector, X_{max} is folded with an Gaussian function having 20 gcm^{-2} width, which corresponds roughly to the resolution of the Pierre Auger Observatory [5].

X_{max} -distribution ansatz

The most prominent source of shower fluctuations is the interaction path length of the primary particle in the atmosphere. However the EAS development itself adds a comparable amount of fluctuations to observables like X_{max} . This is mainly due to the shower startup phase, where the EAS cascade is dominated by just a few particles. Our approach to fit the full distribution of X_{max} does therefore handle the primary interaction point explicitly and

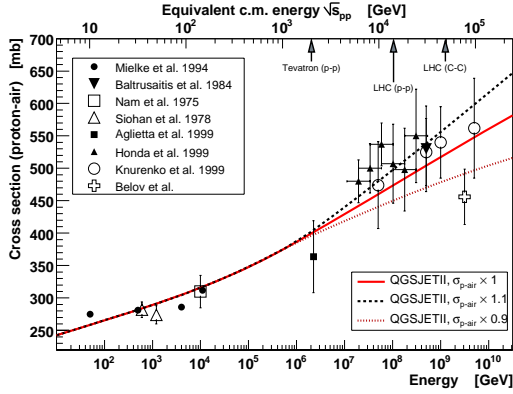


Figure 1: Impact of a 10 % change of $\sigma_{p\text{-air}}$ in QGSJETII at 10 EeV. Data from [6, 8, 9, 10, 11, 12, 13].

the EAS development in a parametric way

$$\begin{aligned} \frac{dP}{dX_{\max}^{\text{exp}}} &= \int dX_{\max} \int dX_1 \frac{e^{-X_1/\lambda_{p\text{-air}}^*}}{\lambda_{p\text{-air}}^*} \\ &\times P_{\Delta X}(\Delta X + X_{\text{shift}}, \lambda_{p\text{-air}}^*) \\ &\times P_{X_{\max}}(X_{\max}^{\text{exp}} - X_{\max}), \end{aligned} \quad (2)$$

where ΔX was introduced as $X_{\max} - X_1$. Thus the X_{\max} -distribution is written as a double convolution, with the first convolution taking care of the EAS development and the second convolution handling the detector resolution. In this model we have two free parameters $\lambda_{p\text{-air}}^*$, which is directly related to $\sigma_{p\text{-air}}$, and X_{shift} , needed to reduce the model dependence. Note that Eq. (2) differs from the HiRes approach [6] and that used in the simulation studies in [7] by explicitly including the cross section dependence in $P_{\Delta X}$.

The simulated $P_{\Delta X}$ -distributions can be parametrized efficiently with the Moyal function

$$P_{\Delta X}(\Delta X) = \frac{e^{-\frac{1}{2}(t+e^{-t})}}{\beta\sqrt{2\pi}} \quad \text{and} \quad t = \frac{\Delta X - \alpha}{\beta} \quad (3)$$

using the two free parameters α and β .

Impact of $\sigma_{p\text{-air}}$ on EAS development

To include the cross section dependence of $P_{\Delta X}$ in a cross section analysis at 10 EeV, we modified

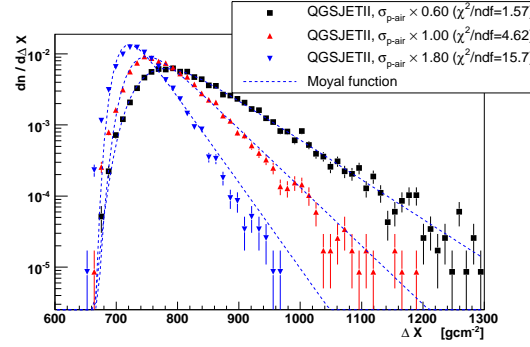


Figure 2: Example fits of Eq. (3) to simulated $P_{\Delta X}$ -distributions at 10 EeV.

CONEX for several HE models such that the cross section used in the simulation is replaced by

$$\sigma_{p\text{-air}}^{\text{modified}}(E) = \sigma_{p\text{-air}}(E) \cdot (1 + f(E)), \quad (4)$$

with the energy dependent factor $f(E)$, which is equal to 0 for $E \leq 1$ PeV and

$$f(E) = (f_{10\text{EeV}} - 1) \cdot \frac{\log_{10}(E/1 \text{ PeV})}{\log_{10}(1 \text{ EeV}/1 \text{ PeV})} \quad (5)$$

for $E > 1$ PeV, reaching $f_{10\text{EeV}}$ at $E = 10$ EeV. This modification accounts for the increasing uncertainty of $\sigma_{p\text{-air}}$ for large energies (see Fig. 1). Below 1 PeV (Tevatron energy), $\sigma_{p\text{-air}}$ is predicted within a given HE model by fits to the measured $p\bar{p}$ cross section.

The cross section dependence of $P_{\Delta X}$ and the corresponding parametrizations are shown in Fig. 2.

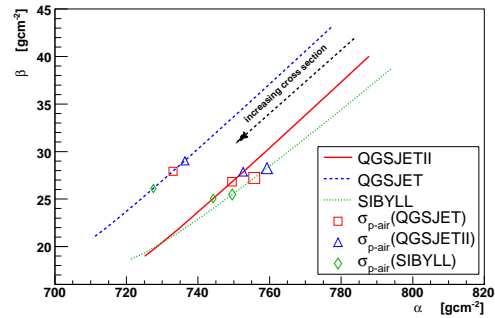


Figure 3: Resulting $\sigma_{p\text{-air}}$ -dependence of the parametrized $P_{\Delta X}$ -distribution. The markers denote the location of the original HE model cross sections.

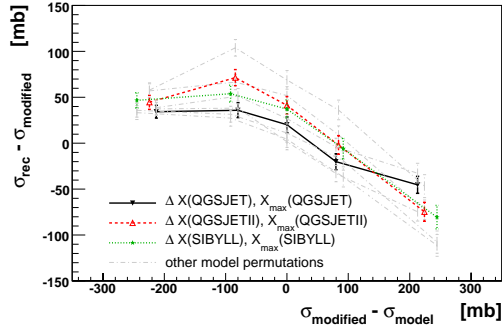


Figure 4: Sensitivity and HE model dependence of the $\sigma_{p\text{-air}}$ reconstruction for a pure proton composition at 10 EeV.

At large ΔX , the simulated distributions are not perfectly reproduced by the parametrizations. This effect worsens for large cross sections, as can be observed from the increasing χ^2/ndf (see Fig. 2). Also the deviation of the Moyal function from the $P_{\Delta X}$ -distribution depends on the HE model. It is biggest for QGSJETII and smallest for SIBYLL. Unfortunately this disagreement produces a systematic overestimation of ~ 30 mb for the reconstructed $\sigma_{p\text{-air}}$. This is visible in all the following results and will be addressed in future work by making the parametrization more flexible.

The dependence of α and β on $\sigma_{p\text{-air}}$ can be interpolated with a polynomial of 2nd degree. Fig. 3 gives an overview of this interpolation in the α - β plane. Obviously the $P_{\Delta X}$ predicted by different HE model are not only a consequence of the different model cross sections.

Results

Pure proton composition

In Fig. 4 we show the reconstructed $\sigma_{p\text{-air}}^{\text{rec}}$ for simulated showers with modified high energy model cross section, $\sigma_{p\text{-air}}^{\text{modified}}$. The original HE cross section $\sigma_{p\text{-air}}^{\text{modified}} - \sigma_{p\text{-air}}^{\text{model}} = 0$ can be reconstructed with a statistical uncertainty of ~ 10 mb, whereas the uncertainty caused by the HE models is about ± 50 mb. At smaller cross sections the reconstruction results in a slight overestimation (< 50 mb). But for larger cross sections there occurs a significant underestimation of the input cross section. This is mainly due to the worse de-

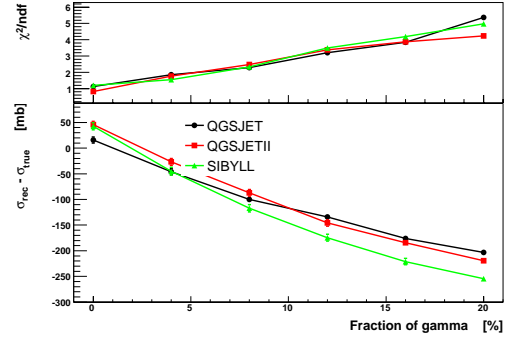


Figure 5: Systematic caused by photon primaries at 10 EeV.

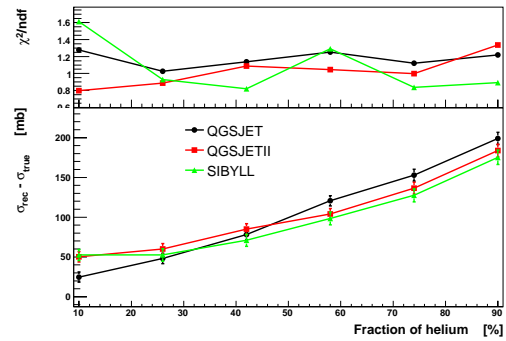


Figure 6: Systematic caused by helium primaries at 10 EeV.

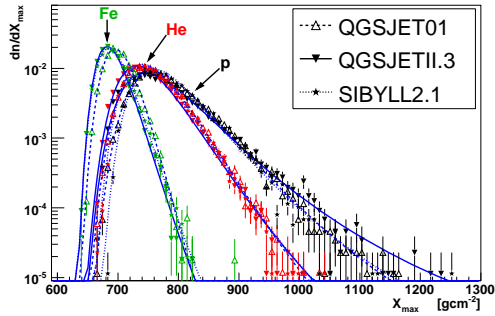
scription of $P_{\Delta X}$ by the used Moyal function for large values of $\sigma_{p\text{-air}}$ (see last section).

Photon primaries

Primary photons generate deeply penetrating showers. Even a small fraction of photon showers has a noticeable effect on the tail of the X_{max} -distribution [7]. Fig. 5 demonstrates how much a few percent of photons could influence the reconstructed $\sigma_{p\text{-air}}$. The current limit on the photon flux is 2 % at 10 EeV [14]. Note that there is a clear trend of an increasing χ^2/ndf with increasing photon fraction, meaning the photon signal is not compatible with the proton model.

Helium primaries

On the contrary, helium induced EAS are very similar to proton showers. Therefore their impact on $\sigma_{p\text{-air}}$ is significant and very difficult to suppress, see Fig. 6. Interestingly, even for large helium contributions there is no degradation of the quality of the pure proton model fit (χ^2/ndf is flat). Thus it


 Figure 7: Composition impact on X_{\max} at 10 EeV.

is not possible in a simple way to distinguish between a 25% proton / 75% helium mixture or just a pure proton composition with a cross section increased by about 150 mb.

Outlook: Mixed primary composition

Fluctuations and the mean value of the X_{\max} -distribution are frequently utilized to infer the composition of primary cosmic rays [15]. It is well understood how nuclei of different mass A produce shower maxima at different depth $X_{\max}(A)$ and how shower-to-shower fluctuations decrease with A (semi-superposition model).

The relative change of the X_{\max} -distribution from a pure proton to a pure mass A primary composition can be evaluated using CONEX. To fit X_{\max} -distributions we use the formula [16]

$$\frac{dP}{dX_{\max}}(A) = N \cdot e^{-\left(\frac{\sqrt{2}(X_{\max} - X_{\text{peak}})}{\gamma \cdot (X_{\max} - X_{\text{peak}} + 3 \cdot \delta)}\right)^2} \quad (6)$$

with four parameters N , X_{peak} , γ and δ . The normalization constant N was not fitted, but set to reproduce the known number of events. Fig. 7 shows how the X_{\max} -distributions for proton, helium and iron primaries are positioned relative to each other for several HE models. This relative alignment can be utilized during $\sigma_{\text{p-air}}$ -fits to reduce the composition dependence. The total mixed composition X_{\max} -distribution is then the weighted sum of the individual primaries

$$\frac{dP}{dX_{\max}^{\text{mix}}}(X_{\max}) = \sum_i \omega_i \frac{dP}{dX_{\max}}(A_i, X_{\max}) \quad (7)$$

where the weights ω_i are additional free parameters to be fitted together with X_{shift} and $\lambda_{\text{p-air}}^*$. The shape of $\frac{dP}{dX_{\max}}(A)$ for $A > 1$ is always assumed to change relative to the proton distribution.

First studies indicate that the correlation between the reconstructed composition and the corresponding $\sigma_{\text{p-air}}$ does not allow a measurement of the cross section. The situation is expected to be more promising if the parameter X_{shift} is fixed, however, the model dependence of the analysis will then be larger than shown here.

References

- [1] R. Engel et al., volume 1, page 415. 26th ICRC Utah, 1999.
- [2] S. Ostapchenko, *Nucl. Phys. (Proc. Suppl.)*, 151:143, 2006.
- [3] N.N. Kalmykov et al., *Nucl. Phys. B (Proc. Suppl.)*, 52B:17, 1997.
- [4] T. Bergman et al., *Astropart. Phys.* 26, 26:420, 2007.
- [5] B.R. Dawson [Pierre Auger Collaboration], 30th ICRC, these proceedings, #976, 2007.
- [6] K. Belov et al., *Nucl. Phys. (Proc. Suppl.)*, 151:197, 2006.
- [7] R. Ulrich et al., 14th ISVHECRI Weihai, astro-ph/0612205, 2006.
- [8] H.H. Mielke et al., *J. Phys. G*, 20:637, 1994.
- [9] M. Aglietta et al., *Nucl. Phys. A (Proc. Suppl.)*, 75A:222, 1999.
- [10] R.M. Baltrusaitis et al., *Phys. Rev. Lett.*, 15:1380, 1984.
- [11] S.P. Knurenko et al., volume 1, page 372. 26th ICRC Utah, 1999.
- [12] M. Honda et al., *Phys. Rev. Lett.*, 70:1993, 1993.
- [13] T.K. Gaisser et al., *Phys. Rev. D*, 36:1350, 1987.
- [14] M. Healy [Pierre Auger Collaboration], 30th ICRC, these proceedings, #602, 2007.
- [15] M. Unger [Pierre Auger Collaboration], 30th ICRC, these proceedings, #594, 2007.
- [16] J.A.J. Matthews, private communication, 2007.



Simulation studies of the charge ratio of the muon density distribution in EAS as measured by the WILLI detector triggered by a mini-array

B. MITRICA^a, O. SIMA^b, I.M. BRANCUS^a, H. REBEL^c, A. HAUNGS^c, A. SAFTOIU^a.

^a *National Institute of Physics and Nuclear Engineering, Bucharest, Romania*

^b *Department of Physics, University of Bucharest, Romania*

^c *Institut für Kernphysik, Forschungszentrum Karlsruhe, Germany*

bogdan.mitrica@nipne.ro

Abstract: The WILLI calorimeter, installed in NIPNE Bucharest, is operated since several years for measuring charge ratio of atmospheric muons at low energies ($E < 1$ GeV), particularly exploring its directional dependence. Recently it was proposed to combine WILLI detector with a mini-array of 12 scintillators in order to measure muon charge ratio of the muon density of EAS lateral distributions. Such experimental studies could provide detailed information on the shower development under the influence of the geomagnetic field and probably also on hadronic interaction. As part of the proposed approach the ratio of the averaged μ^+ to μ^- -densities of the radial and azimuthal lateral EAS distribution observed with folding with the finite WILLI angular acceptance, is investigated. The study is based on simulated showers generated for protons and various heavier primary nuclei by the Monte Carlo program CORSIKA in the energy range 10^{13} - 10^{15} eV. The μ^+ to μ^- ratio as registered in average by the WILLI device, thought to be triggered by a mini-array, is studied in dependence of the distance of the WILLI location from the shower core and of the azimuthal and zenithal directions of EAS incidence. The results exhibit the principal feasibility, but also some inherent problems of the WILLI device and of the considered experimental arrangement to explore the effects looked for.

Introduction

The ratio of the numbers of positive to negative muons in the atmospheric muon flux, which is dominated by the production of muons through low energy air showers (EAS) in the atmosphere, has been relatively often investigated. This muon charge ratio R_μ , whose value is governed by the proton excess in the flux of the primary cosmic rays, is dependent of the direction of observation, since the muon tracks are influenced by the geomagnetic field and differently bent in East and West direction. This influence leads to the well known East-West effect of the muon charge ratio of atmospheric muons (i.e with unspecified EAS origin) [1].

In contrast the charge ratio of the muon density of single EAS registered with well specified observation conditions (energy, direction of incidence, distance from the shower axis etc.) has been seldom considered and is experimentally unexplored. Re-

cently the features of the charge ratio of the density of the EAS muon component have been extensively studied on basis of Monte Carlo simulations [2] revealing that the radial and azimuthal muon density distributions of EAS observed by surface detector are strongly influenced by the magnetic field of the Earth. The features depend on the direction of EAS incidence (zenith θ and azimuth Φ angles) relative to the geomagnetic field, in addition to the energy of the registered muons.

In this paper some considerations are presented, how the WILLI detector [3], when being triggered by EAS observation of a small detector array, may be used to explore some experimental information about the predicted features. It should be explicitly noted that WILLI does not allow the determination of R_μ of the observed EAS individually, but only counting the numbers of μ^+ and of μ^- , forming after observation of many showers an averaged value of R_μ .

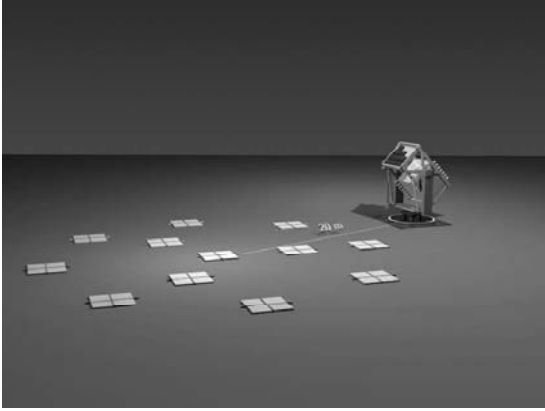


Figure 1: Sketch of the geometrical layout of a mini-array for triggering the nearby located WILLI device for muon detection by registering EAS [2].

Concept of an experimental arrangement

The WILLI detector [3, 4] installed for studying the muon charge ratio of atmospheric muons discriminates positive and negative muons by measuring the life time of muons stopped in the detector layers: Stopped positive muons decay with a lifetime of $2.2 \mu\text{s}$, while negative muons are captured in atomic orbits, thus leading to an effectively smaller lifetime depending on the stopping material. From the adjustment of the measured decay curve to the actual mean value of the life time the value of R_μ can be deduced. Details of the method are described elsewhere [3]. It largely avoids the uncertainties due to different detection efficiencies and geometrical acceptances of muons of different charges which affect the results of magnetic spectrometers. In the present configuration the WILLI setup is able to get directed to a pre-chosen direction of muon incidence (zenith and azimuth angle) [4] for studies of the East-West effect of atmospheric muons [5] e.g..

The application of the WILLI device for experimental studies of the features of the radial and azimuthal variation of the charge ratio of the muon density distribution in EAS needs a link to the EAS registration by a nearby located detector array, specifying the characteristics (core location, direction of incidence etc.) of the triggering EAS. Fig.1

displays a highly schematic sketch of an eventual geometrical layout of a mini-array of 12 detector units, whose spatial distribution defines also the window of primary energies of the observed EAS.

The necessary simulation studies of the performance of such a mini-array and of the expected trigger rate (roughly estimated to be in the order of 1 event/min) are in progress. In particular, the layout studies must also include an adequate electronic system for triggering and data acquisition since only one stopped muon per shower can be handled in the present system. In the present studies we study, how the finite angular acceptance of the WILLI spectrometer, positioned at a particular accurately defined distance from the shower core and observing muons from a particular direction will affect the pronounced predicted variation of the charge ratio of the observed muon density.

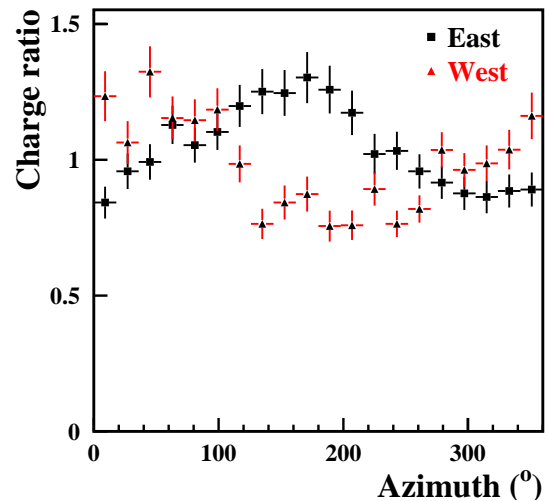


Figure 2: Dependence of the charge ratio on the azimuthal position of WILLI around shower core (radial distance: 150-200 m). Proton showers ($E=10^{15}$ eV, $\theta=45^\circ$) coming from East (squares) and from West (triangles). WILLI is oriented parallel to the shower axis.

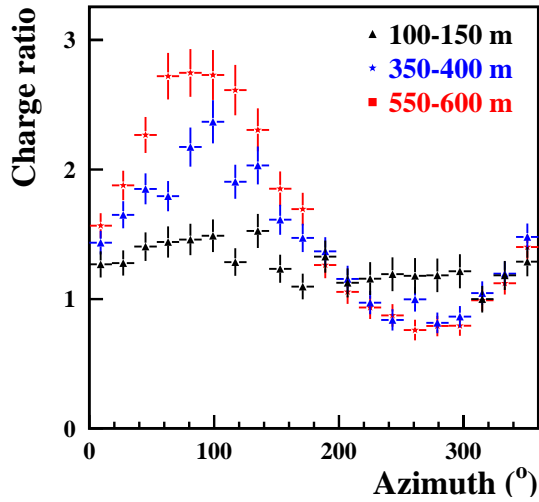


Figure 3: Dependence of the charge ratio on the azimuthal position of WILLI around shower core for various radial ranges. Proton showers ($E=10^{15}$ eV, $\theta=45^\circ$) coming from North. WILLI is oriented parallel to the shower axis.

Simulations of the charge ratio of the EAS muon density distribution as seen by WILLI

The following results, displayed in Figs. 2-6, are based on simulations by the EAS Monte Carlo simulation code CORSIKA (vers.6.0) [6] using finally the same set of simulations (about 60000 showers in total) as in [2], but including the criteria of muon registration by WILLI. For the present exploratory study the hardware triggering and vetoing conditions and the software cuts implemented in the WILLI data acquisition and analysis system were replaced by the condition that a single muon from a shower event hits WILLI. Furthermore this muon should have the energy $E < 1$ GeV (with the threshold slightly dependent on the angle of incidence) and the incidence angle filtered with a gaussian angular acceptance with a dispersion similar to that determined in [3].

As expected from the theoretical studies [2] the figures indicate that the azimuthal variation of the R_μ gets more pronounced with increasing core

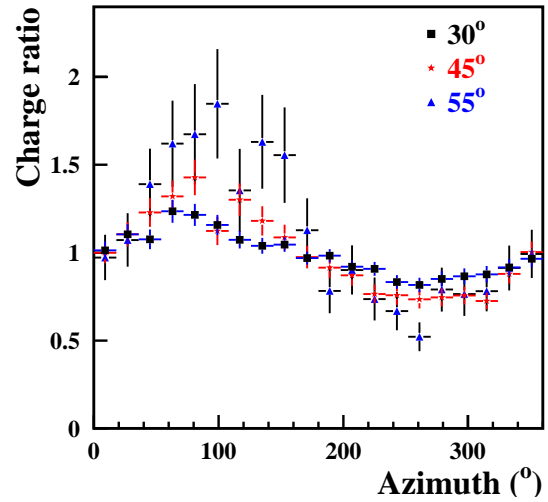


Figure 4: Dependence of the charge ratio on the azimuthal position of WILLI around shower core for proton showers ($E=10^{15}$ eV) with several zenith angles coming from North. Radial distance: 200-250 m. WILLI is oriented parallel to the shower axis in each case.

distance. Actually the salient features are shown for core distances ≥ 100 m. The features at smaller distances follow the general trend, but need for demonstration a larger statistical accuracy, i.e. within the present procedure a larger number of analysed EAS, actually approaching the experimental reality. Differences of R_μ between iron and proton induced showers are small, at least at the energies studied in this work.

Concluding remarks

The application of the WILLI calorimeter as device for measuring the charge ratio of the EAS muon density needs some modifications of the apparatus, especially for triggering by the mini-array and the acquisition of the low energy muons [3]. EAS muons have an energy spectrum which is harder than that of atmospheric muons and less rich of muons which are able to get stopped in the actual WILLI device. This feature implies a serious limitation of the statistical accuracy of results of

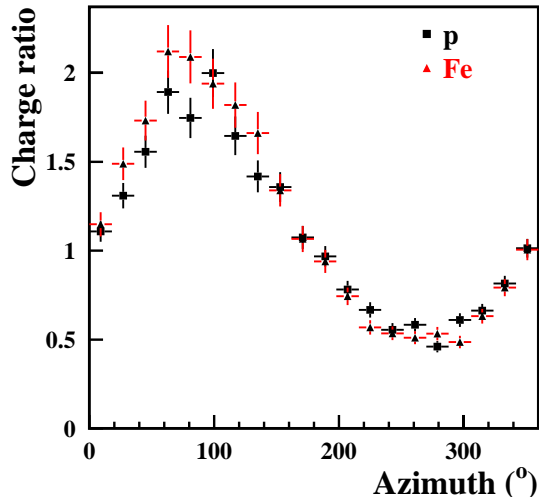


Figure 5: Dependence of the charge ratio on the azimuthal position of WILLI around shower core for proton (squares) and Fe (triangles) showers ($E=10^{15}$ eV, $\theta=45^\circ$) coming from North; radial distance: 450-500 m. WILLI is oriented parallel to the shower axis.

WILLI. Hence the WILLI should to be additionally equipped with some absorber material for degradation of the muon energy in the direction of observation. For devising the mini-array (intended to be set up with 12 scintillator units from the former Central Detector of KASCADE in Forschungszentrum Karlsruhe) special attention should be put to the accuracy of the core location since inaccuracies of the core location are propagated in the azimuthal (and radial) position of the WILLI device with respect to the incoming shower and may smear out variations of the R_μ (azimuth). Therefore careful performance studies, optimising the layout of the planned mini-array are requested.

Acknowledgements

This work is supported by the Romanian Ministry of Education and Research (grant CEEX 05-D11-79/2005).

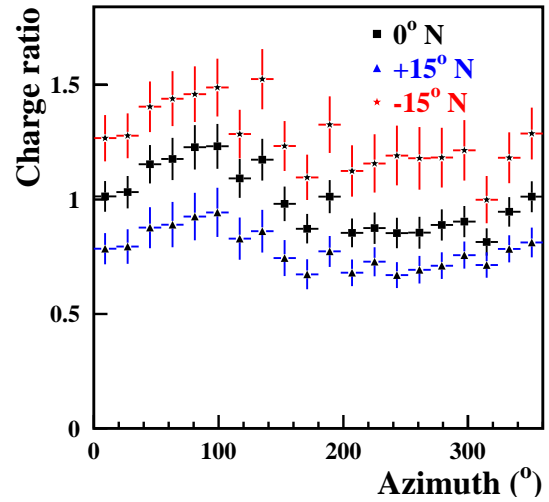


Figure 6: Dependence of the charge ratio on the azimuthal position of WILLI around shower core for proton showers ($E=10^{15}$ eV, $\theta=45^\circ$) coming from North. Radial distance: 200-250 m. WILLI is oriented parallel to the shower axis (squares), $+15^\circ$ N (towards East, triangles) and -15° N (towards West, stars).

References

- [1] O.C. Allkofer et al., Journ. Geophys. Research 90 (1985) 3537.
- [2] H. Rebel and O. Sima, Romanian Rep. Phys. 59 (2007) 427; H.Rebel et al., Report FZKA 7294, Forschungszentrum Karlsruhe 2007; H.Rebel et al., Proc. of 30th ICRC, Merida, Mexico 2007.
- [3] B. Vulpescu et al., Nucl. Instr. Methods A 414 (1998) 1699; B. Vulpescu et al., J. Phys. G: Nucl. Part. Phys. 27 (2001) 977.
- [4] I. M. Brancus et al., Nucl. Phys. A 271 (2003) 1044c.
- [5] I. M. Brancus et al., Proc. ISVHECRI, Weihen, China 2006, Nucl. Phys. B (in press).
- [6] D. Heck et al., Report FZKA 6019 Forschungszentrum Karlsruhe 1998.



The muon charge ratio in cosmic ray air showers

H. REBEL^a, O. SIMA^b, A. HAUNGS^a, J. OEHLISCHLÄGER^a.

^a *Institut für Kernphysik, Forschungszentrum Karlsruhe, Germany*

^b *Department of Physics, University of Bucharest, Romania*

Heinrich.Rebel@ik.fzk.de

Abstract: The muon charge ratio of the lateral muon density distributions in single Extended Air Showers (EAS) is studied on basis of Monte Carlo simulations, in view of proposals to measure this observable in coincidence with EAS observations. Differences of the azimuthal variation of the muon densities of opposite charges and the azimuthal variation of the muon charge ratio appear to be very much pronounced, dependent on the direction of the EAS incidence and the position of the observer in respect to the Earth's magnetic vector. The influence of the geomagnetic field, which induces comparable effects in radio emission from EAS, is obviously of great interest for understanding the shower development.

Introduction

The flux, the energy spectrum and the charge ratio of atmospheric muons, resulting from the decay of pions and kaons which are produced in collisions of primary cosmic rays with the air molecules, have been studied extensively over wide range of energies at sea level as well as on high mountain altitudes and during balloon ascents. The studies comprise several aspects, in particular they provide information on the composition of cosmic rays and on characteristic features of the hadronic interaction and of the influence of the geomagnetic field on the primary and secondary components of cosmic radiation. The investigations show that the ratio of the number of positive to negative atmospheric muons $R_{\mu}^{atm} = N_{\mu^+}/N_{\mu^-}$ is experimentally varying between the values of about 1.2 -1.3 [1]. As detailed analyses [2] show, the excess of the positive charge reflects mainly the excess of protons of primary cosmic rays and less eventual small differences of the production of positive and negative parent particles of the muons. The Earth's magnetic field influences the flux of primary cosmic rays entering the Earth atmosphere leading to the well-known East-West asymmetry and the latitude effect. In addition the geomagnetic field bends the trajectories of the charged particles of the secondary cosmic rays which get curved. The ef-

fect is particularly dominant for the muon component which is less affected by Coulomb scatterings processes. This leads to the East-West effect of the muon charge ratio: the observation that the ratio of positive and negative atmospheric muons proves to be different for muons arriving the spectroscopic device from West from those arriving from East direction (see [3]). The finding originates from the fact that in the East-West plane due to different bendings, muons of positive and negative charges have different path lengths from the locus of production to the observer. Hence the decay probability of low energy muons is differently modified.

The features are slightly different for the muon charge ratio in Extensive Air Showers (EAS) whose axes have well defined angles (θ, Φ) of incidence, not only relative to the zenith direction, but also relative to the vector of the magnetic field of the Earth. The total charge ratio integrated over all muons of the EAS is only determined by the hadronic interaction and the decay of the parent particles, and no more by the composition of cosmic rays. However, due to various effects the lateral distribution $\rho(r, \phi)$ of the density of positive and negative muons and its charge ratio $R_{\mu}(r, \phi)$ vary radially (with the distance r from the EAS centre) as well as azimuthally (with the EAS intrinsic azimuth ϕ , counted clockwise in the horizontal

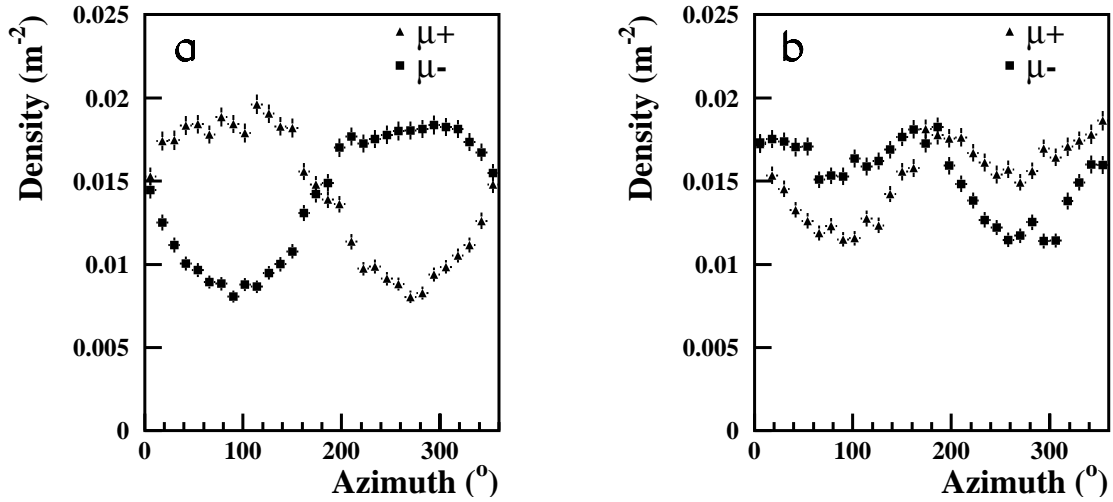


Figure 1: The mean azimuthal μ^+ and μ^- - distributions of proton induced inclined EAS ($\theta = 45^\circ$) incident from (a) North and (b) South with the primary energy of 10^{15} eV at a distance of 45-50 m from the shower axis.

plane from the axis defined by the direction from the shower center towards North).

In this paper we study in particular the azimuthal variation of the lateral density distribution of EAS muons of both opposite charges separately and the resulting variation of the muon charge ratio. The studies are based on EAS simulations using the Monte Carlo simulation code CORSIKA (vers. 6.0) [4] ($E_\mu^{thres}=100$ MeV). In order to be specific we demonstrate the main features by considering p and Fe induced EAS, with the primary energy of 10^{15} eV, incident with a zenith angle $\theta = 45^\circ$, but comparing different azimuthal directions of incidence, in particular from North and from South. The magnetic inclination of observation locus (Karlsruhe) is adopted to be about 65° with the magnetic field pointing downwards. The studies are in context of various actual [5] and future attempts [6] to measure the muon charge ratio with a spectroscopic device coupled to EAS observation by small detector arrays.

Azimuthal asymmetries in the lateral distribution of charged EAS particles

The origin of azimuthal asymmetries of the lateral distributions of charged EAS particles is mainly attributed to the attenuation and to geometrical effect of showers with inclined incidence. Assuming that the EAS starts from infinity and neglecting any influence of the geomagnetic field for the moment, we have cylindrical symmetry around the shower axis. For inclined showers incident to the observation plane, charged particles arriving first ("early" azimuthal region) experience less attenuation than particles arriving later ("late" azimuthal region) due to larger travel distances. Additionally there appear effects from the projection of the normal shower plane to the observational plane. It should be noted that the attenuation of the particle density is largely obscured and counter-balanced, when the measured particle densities are reconstructed from the measured energy deposits in scintillation detectors, since the dependence of the energy deposit per particle from the angle of particle incidence works in opposite direction.

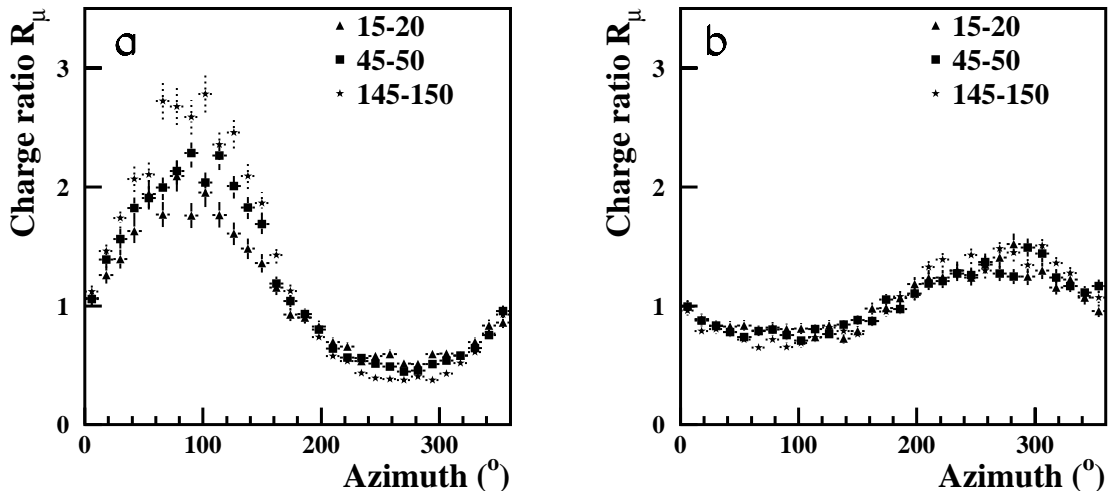


Figure 2: Azimuthal variation of the charge ratio $R_{\mu}(r, \phi)$ of the mean muon density distribution of proton induced inclined EAS ($\theta = 45^{\circ}$) incident from (a) North and (b) South with the primary energy of 10^{15} eV at various distances $r(m)$ from the shower axis.

Influence of the geomagnetic field on the azimuthal lateral μ^{+} and μ^{-} - distributions

Figures 1 and 2 display some selective examples of the results for proton induced EAS observed in the observational plane as function of the azimuth angle ϕ . Fe induced showers show similar features. The asymmetry for EAS incident from various directions can be explained by different relative angles to the Earth magnetic vector. When the geomagnetic field is switched off, the azimuthal μ^{+} and μ^{-} - distributions show practically only the variation due to geometric and attenuation effects, for μ^{+} and μ^{-} similar, so that the charge ratio value stays with $R_{\mu}(r, \phi) = 1$. Obviously differences in the π^{+} and π^{-} productions remain rather small at the considered energies (and within the invoked hadronic interaction model: QGSJET). This finding is underlined by the value of the muon charge ratio integrated over all distances and azimuth angles $R_{\mu} = 1.028 \pm 0.002$ for the cases shown in Figure 2.

The influence of the geomagnetic field and the separation of μ^{+} and μ^{-} increase with the path

length (slant depth) of the muon trajectories in the atmosphere. Hence the $R_{\mu}(r, \phi)$ variation gets more pronounced with increasing distances from the shower core, with the threshold (Fig.3) of observed muon energies (since muons of higher energies stem dominantly from earlier generations) and with the zenith angle EAS incidence (see Fig.4). Recently this feature has been regarded in view of a separation of positive and negative muons by the Earth's magnetic field [7], for the case of very inclined showers of primary energies high enough so that the muon component observed at ground remains sufficiently intensive for observation.

Concluding remarks

EAS simulations show that the lateral density distributions of the positive and negative muons are varying not only with the (radial) distance from the shower axis, but also with the azimuth relative to the plane of the incident shower. The reasons are different. In addition to the attenuation effects of charged particles of inclined showers in the atmosphere by the variation of the travelling distances, the geomagnetic field affects dominantly the travel

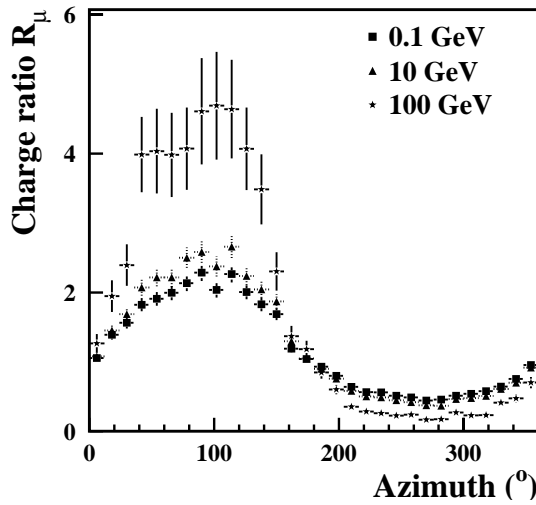


Figure 3: Azimuthal variation of the charge ratio R_μ of the muon density distribution of proton induced EAS of inclined incidence ($\theta = 45^\circ$), incident from North with the primary energy of 10^{15} eV, observed at a radial distance of 45-50m. Comparison of different detection thresholds.

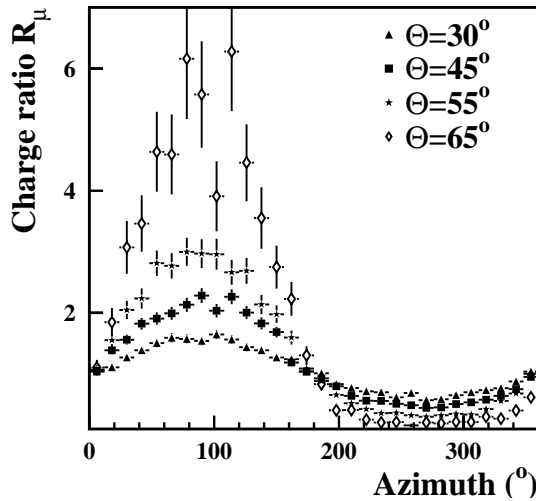


Figure 4: Azimuthal variation of the charge ratio R_μ of the muon density distribution of proton induced EAS with different zenith angles incident from North with the primary energy of 10^{15} eV, observed at a radial distance of 45-50m. Comparison of different zenith angles of incidence.

of positive and negative muons with deflections in opposite directions. The geomagnetic effects depend on the direction of the EAS axis relative to the Earth's magnetic vector. This leads to an azimuthal variation of the muon charge ratio of the muon density distribution. In the extreme case of very inclined showers (with long slant depths) the Earth field might be used as magnetic separator. Obviously these features which are not yet experimentally explored [5], [6], [8] in a systematic way, are of great interest for the understanding of the EAS development. It should be mentioned that some findings for the muon component induced by the geomagnetic field resemble features observed for the radio emission from EAS [3]. Furthermore the quantitative results would also provide some detailed information about the hadronic interaction, in particular when observing higher energy muons.

Acknowledgements

These studies have been triggered by the discussion of a concept to investigate experimentally the muon charge ratio in the lateral muon density distribution of EAS by extending the WILLI apparatus [6]. One of us (O.S) acknowledges travel support by the Romanian Ministry of Education and Research (grant CEEEX 05-D11-79/2005).

References

- [1] T. Hebbeker and C. Timmermans, *Astropart. Phys.* 18, 107 (2002).
- [2] J. Wentz et al. *J. Phys. G: Nucl. Part. Phys.* 27, 1699 (2001); *J. Phys. Rev. D* 67, 073020 (2003).
- [3] H. Rebel et al. Report FZKA 7294 Forschungszentrum Karlsruhe 2007.
- [4] D. Heck et al. Report FZKA 6019 Forschungszentrum Karlsruhe 1998.
- [5] S. Tsuji et al. *Proc. of 29th ICRC, Pune* (2005) 6, 213; *ibid* 8, 233.
- [6] I. M. Brancus et al. *Proc. ISVHECRI, Weihei* (2006), *Nucl. Phys. B* (in press).
- [7] B. K. Xue and Bo-Qiang Ma, *Astropart. Phys.* 27, 286 (2007); M. Ave, R. A. Vasquez and E. Zas, *Astropart. Phys.* 14, 91 (2000).
- [8] A. M. Ivanov et al. *JETP Lett.* 69, 288 (1999).



Measurement of the Air Fluorescence Yield with the AirLight Experiment

TILO WALDENMAIER¹, JOHANNES BLÜMER^{2,3}, DANAYS GONZALEZ², HANS KLAGES².

¹*Bartol Research Institute, DPA, University of Delaware, Newark, DE 19716, U.S.A.*

²*Forschungszentrum Karlsruhe, Institut für Kernphysik, P.O.Box 3640, 76021 Karlsruhe, Germany*

³*Universität Karlsruhe, Institut für Experimentelle Kernphysik, P.O.Box 6980, 76128 Karlsruhe, Germany*
tilo@bartol.udel.edu

Abstract: The present uncertainties of the air fluorescence yield are the limiting factor for the energy reconstruction of ultra-high energy cosmic rays measured by fluorescence telescopes. The AirLight experiment has measured the pressure and energy dependence of the air fluorescence yield for the eight strongest nitrogen transitions with a precision of about 15 % for low energy electrons between 250 keV and 2000 keV. Furthermore the influence of water vapor has been investigated. This paper introduces the experimental method and summarizes the results.

Introduction

The measurement of air fluorescence is used by many modern experiments (i.e. HiRes [9], Pierre Auger Observatory [1]) to detect extensive air showers (EAS), induced by ultra-high energy cosmic rays. The secondary EAS particles (mostly electrons and positrons) deposit their energy in the atmosphere by exciting or ionizing the air molecules which afterwards partially relax by emitting fluorescence photons. As pointed out by Bunner [3] most of these photons in the wavelength range between 300 nm and 400 nm originate from transitions of the second positive (2P) system of molecular nitrogen and the first negative (1N) system of molecular nitrogen ions. These faint emissions can be measured by fluorescence telescopes, allowing the observation of the longitudinal development of EAS through the atmosphere and a calorimetric determination of the primary cosmic-ray energy. The conversion factor between the deposited energy and the number of emitted fluorescence photons is the so-called fluorescence yield $Y_{\lambda}(p, T)$ which depends on the air pressure p and temperature T as well as on the wavelength λ of the emitted photons. This method is considered to provide the most direct measure of the primary cosmic-ray energy, it is however limited by the present uncertainties of the fluorescence yield of about 15 % to 30 % and the lack

of knowledge about its energy dependence. In recent years this gave rise to a number of new laboratory experiments (i.e. Kakimoto et al. [6], Nagano et al. [8], AIRFLY [2], FLASH [5] or **AirLight**) aiming a precise measurement of the fluorescence yield over a wide energy, pressure and temperature range. This paper reports about the results of the **AirLight** experiment at Forschungszentrum Karlsruhe in Germany and is extracted from the Ph.D. thesis [10] of the corresponding author.

The AirLight Experiment

The setup of the AirLight experiment is similar to the experiments done by Kakimoto and Nagano et al. [6, 8]. As is shown in Fig. 1 it consists of a cylindrical aluminum chamber in which electrons are injected along the chamber axis. The electrons are emitted from a ⁹⁰Sr-source situated at the top of the chamber and are collimated by several lead rings. The electron source has an activity of 37 MBq with an end point energy of 2.3 MeV. After having traversed 10 cm of gas (dry air, pure nitrogen, or a nitrogen-oxygen mixture) the electrons are stopped in a plastic scintillator to determine their energy with an energy resolution of about 10 % at 1 MeV. The electron rate at the scintillator alters between 10 kHz and 20 kHz, depending on the pressure in the chamber which can be

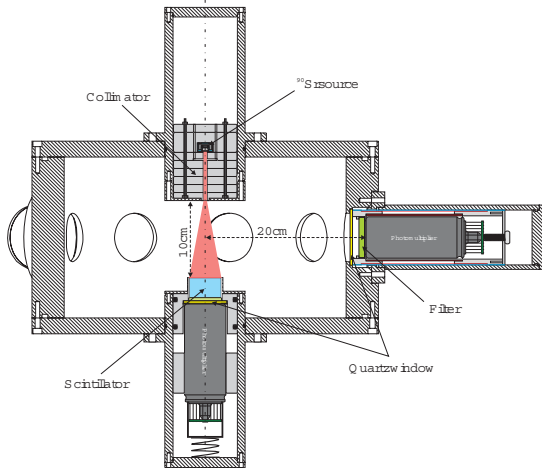
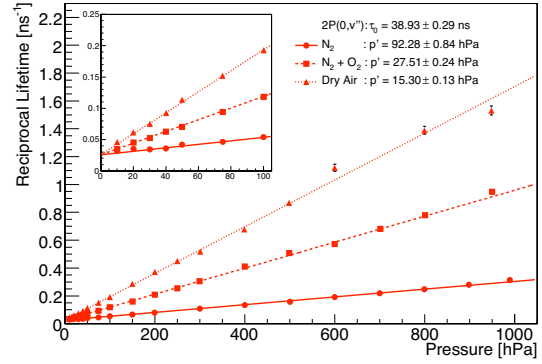


Figure 1: Sketch of the AirLight chamber.

varied between 2 hPa and 1000 hPa. Seven Photonis photomultipliers (PMTs) are mounted perpendicular around the electron beam. Six of them are equipped with narrow band interference filters matched to the most prominent nitrogen bands, whereas one PMT is measuring the integral fluorescence spectrum through a broad band M-UG6 filter as it is used in the telescopes of the Pierre Auger Observatory [1]. The experiment is measuring coincidences between the electron signal in the scintillator and photon signals in any of the PMTs within a coincidence window of 120 ns.

Fluorescence Process

The nitrogen fluorescence spectrum is a band spectrum caused by vibrational perturbations of the molecular energy states. All transitions of the 2P or the 1N system correspond to the same electronic transition respectively. The energy of the transitions is only modified by the different vibrational levels v' and v'' of the initial and final electronic states. Accordingly the label $2P(v',v'')$ denotes a vibrational transition $v' \rightarrow v''$ within the second positive (2P) electronic system. The de-excitation of an excited electronic-vibrational state v' is a competition between radiative and radiationless processes. Radiationless processes (quenching) occur via collisional energy transfer to other molecules and thus strongly depend on the pressure and the temperature of the air. Instead of this


 Figure 2: Pressure dependence of the reciprocal lifetimes for the $2P(0,v'')$ transitions.

the transition probabilities for radiative transitions $v' \rightarrow v''$ are constant. This causes the nitrogen fluorescence spectrum to be assembled of several sub-spectra for each vibrational level v' . The intensity ratios between transitions within a sub-spectrum are always constant but the absolute intensities of the individual sub-spectra vary differently with pressure and temperature according to the different strength of the quenching. The quenching strength is directly related to the lifetime $\tau_{v'}(p, T)$ of an excited state v' which decreases the faster with increasing p and T the stronger the quenching. In the absence of collisional quenching the lifetime $\tau_{v'}(p, T)$ is constant and equals to the intrinsic lifetime $\tau_{v'}^0$ of the electronic-vibrational state. The probability for radiative transition can be expressed as the fraction of the lifetime $\tau_{v'}(p, T)$ at given p and T to the intrinsic lifetime $\tau_{v'}^0$. All these general relations are taken into account by the following approach for the fluorescence yield $Y_{v',v''}(p, T)$ for a transition $v' \rightarrow v''$:

$$Y_{v',v''}(p, T) = Y_{v'}^0 \cdot R_{v',v''} \cdot \frac{\tau_{v'}(p, T)}{\tau_{v'}^0} \quad (1)$$

In this expression the intensity ratios $R_{v',v''}$ are defined with respect the most intensive transition, the so-called main transition, of the electronic-vibrational system. In this work the main transitions are $2P(0,0)$, $2P(1,0)$ and $1N(0,0)$. The intrinsic yield $Y_{v'}^0$ corresponds to the fluorescence yield of the main transition in the absence of collisional quenching where $\tau_{v'}(p, T) = \tau_{v'}^0$.

The pressure and temperature dependence of the lifetime $\tau_{v'}(p, T)$ can be derived using kinetic gas

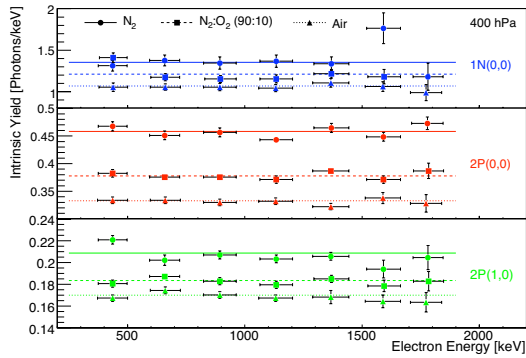


Figure 3: Energy dependence of the intrinsic fluorescence yield.

theory [10]. In first order the reciprocal lifetime behaves like

$$\frac{1}{\tau_{v'}(p, T)} = \frac{1}{\tau_{v'}^0} + \frac{p}{kT} \cdot \sum_i f_i \cdot Q_i^{v'}(T) \quad , \quad (2)$$

where the sum goes over all gas constituents i with fractions $f_i = p_i/p$. For air the fractions $f_{N_2} = 0.78$ and $f_{O_2} = 0.21$ have been used. The water vapor fraction f_{H_2O} has been individually derived from its partial pressure p_{H_2O} . The quenching of Argon and other trace gases turned out to be negligible. The quenching strength of each constituent is characterized by the quenching rate constants $Q_i^{v'}(T)$ which are proportional to \sqrt{T} if the collisional cross-sections are assumed to be constant.

Measurement & Data Analysis

The dataset used for this analysis consists of about 50 measurements in dry air, pure nitrogen and a nitrogen-oxygen mixture (90:10) performed between August and November 2005. The study of different nitrogen-mixtures is a useful cross-check for the quantitative understanding of the quenching process. In addition several runs with pure nitrogen plus a variable amount of water vapor have been carried out in order to study humidity effects. The measurements were done at room temperature at pressures ranging from 3 hPa to 990 hPa. One single run lasted between 12 and 30 hours, depending on type and pressure of the gas.

The data analysis is based on the investigation of the time difference spectra between the electron

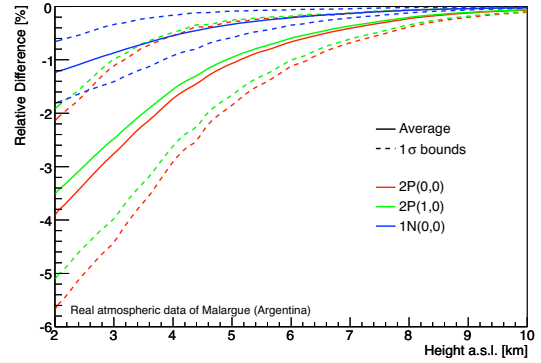


Figure 4: Relative differences between the fluorescence yield of the main transitions with and without taking into account the water vapor in the atmosphere. 1σ -bands correspond to daily humidity variations.

and photon signals in individual filter channels. The fluorescence signals can be statistically distinguished from uncorrelated background by their exponential time distribution. A gaussian-convoluted exponential fit to the time spectra results in the lifetime $\tau_{v'}$ and the number of fluorescence photons. In general there are additional contributions of other nitrogen bands in one filter channel, and the measured time spectra are a superposition of several nitrogen transitions. In order to break up the different contributions a global χ^2 -fit to the complete dataset (all channels and runs) has been applied. A good relative calibration of the individual filter channels is essential for this procedure [10]. The fit was constrained by the physical relations between the lifetimes and the intensities as explained in the previous section. An example for the pressure dependence of the reciprocal lifetimes in the three gas mixtures is given in Fig. 2 for the $2P(0, v'')$ -system. The single data points result from a global fit which was only constraint by equation (1) whereas the lines correspond to the results obtained by further constraining the fit by relation (2). Both fits agree with each other but only the latter one results in a minimal and consistent set of parameters which are summarized in Table 1. Since the quenching does not depend on the excitation process, the above fitting procedure was applied on the whole usable energy range from 250 keV to 2000 keV in order to maximize statistics. To study the energy dependence of the fluo-

| Band | λ [nm] | Y_0 [Ph./keV] | $R_{v',v''}$ | τ_0 [ns] | Q_{N_2} | Q_{O_2} | Q_{H_2O} |
|----------|----------------|-------------------|--------------|-----------------|-----------------|-----------------|------------------|
| 2P(0,0)* | 337.1 | 0.338 ± 0.001 | 1.00 | 38.9 ± 0.3 | 0.11 ± 0.00 | 2.76 ± 0.01 | 5.43 ± 0.12 |
| 2P(0,1) | 357.7 | | 0.69 | | | | |
| 2P(0,2) | 380.5 | | 0.29 | | | | |
| 2P(1,0)* | 315.9 | 0.172 ± 0.001 | 1.00 | 32.9 ± 0.5 | 0.29 ± 0.00 | 2.70 ± 0.03 | 5.78 ± 0.17 |
| 2P(1,2) | 353.7 | | 0.33 | | | | |
| 2P(1,3) | 375.5 | | 0.34 | | | | |
| 2P(1,4) | 399.8 | | 0.46 | | | | |
| 1N(0,0)* | 391.4 | 1.048 ± 0.007 | 1.00 | 65.2 ± 18.7 | 5.00 ± 0.17 | 5.24 ± 0.79 | 16.02 ± 1.09 |

Table 1: Parameters for the eight strongest nitrogen transitions. Transitions from the same vibrational state v' have the same values for $Y_{v'}^0$, $\tau_{v'}^0$ and $Q_i^{v'}$ as their main transitions marked with an *. The quenching rate constants $Q_i^{v'}$ are quoted for $T = 20^\circ\text{C}$ in [$10^{-10} \text{ cm}^3 \text{ s}^{-3}$]. The quoted errors are statistical only.

rescence yield the fit was repeated on seven sub-samples of 250 keV energy bins. It turned out that in the investigated energy range the intrinsic yield $Y_{v'}^0$ does not depend on the energy of the exciting electrons as is shown in Fig. 3. In order to derive these values the detection efficiencies for the individual bands as well as the energy deposit in the chamber have been carefully determined as described in [10].

The quenching of water vapor has been investigated by adding different concentrations of water vapor to 30 hPa of pure nitrogen. The quenching rate constants Q_{H_2O} have been determined by a linear fit of expression (2) to the reciprocal lifetimes versus the water vapor partial pressure as described in [10]. The water vapor quenching turned out to be rather strong especially for the 1N-system where it is 3 times stronger than for oxygen as can be seen in Table 1. However due to the relatively small amount of water vapor in the atmosphere the net effect on the fluorescence yield is in the order of a few per cent as is illustrated in Fig. 4 for real atmospheric profiles measured at the Auger site [7].

Results & Conclusions

The analysis procedure described above leads to a consistent description of the fluorescence process with a minimal set of parameters. These parameters have been determined for the 8 strongest nitrogen bands and are summarized in Table 1. It has been shown elsewhere [10] that the contribution of neglected nitrogen bands to the total fluorescence yield is less than 4 %. Using the values

of Table 1 the fluorescence yield in dry or humid air can be calculated for any atmospheric pressure and temperature by means of equation (1) and (2) with a systematic uncertainty of about 15 %. This error can be further reduced to less than 10 % by an end-to-end calibration of the whole setup using Rayleigh-scattering of a nitrogen laser beam [4]. Water vapor in the lower atmosphere further reduces the fluorescence yield by about 4 % at the Auger site. Currently this effect is still concealed by the systematic uncertainties of the fluorescence yield but might become an issue when these uncertainties are further reduced.

References

- [1] J. Abraham et al. *Nucl. Instrum. Meth.*, A523:50–95, 2004.
- [2] M. Ave et al. *astro-ph/0703132*.
- [3] A. N. Bunner. PhD thesis, Graduate School of Cornell University, February 1967.
- [4] D. M. Gonzalez et al. Laser Calibration of the Air Fluorescence Yield Experiment AirLight. *These proceedings: icrc0228*.
- [5] P. Huntmeyer et al. *AIP Conf. Proc.*, 698:341–344, 2004.
- [6] F. Kakimoto et al. *Nucl. Instrum. Meth.*, A372:527–533, 1996.
- [7] B. Keilhauer et al. *astro-ph/0507275*.
- [8] M. Nagano et al. *Astropart. Phys.*, 22:235–248, 2004.
- [9] R. W. Springer et al. *Nucl. Phys. Proc. Suppl.*, 138:307–309, 2005.
- [10] T. Waldenmaier. *Report FZKA, 7209*, 2006. <http://bibliothek.fzk.de/zb/berichte/FZKA7209.pdf>.



Laser Calibration of the Air Fluorescence Yield Experiment AirLight

D. M. GONZALEZ^{1,2}, J. BLUEMER^{1,2}, H. KLAGES², T. WALDENMAIER^{2,3}

¹ *Universität Karlsruhe, Institut fuer Experimentelle Kernphysik*

² *Forschungszentrum Karlsruhe, Institut fuer Kernphysik*

³ *University of Delaware, Department of Physics and Astronomy*
 danays.gonzalez@ik.fzk.de

Abstract: The relative fluorescence efficiency for MeV electrons in nitrogen and air has been measured with high precision by the AirLight experiment [1]. The range from 300 nm to 400 nm was spanned using a 300 nm to 400 nm broad-band (M-UG6) filter and 5 narrow-band filters. Fluorescence photons were detected by seven 2-inch PMTs in coincidence with the signals of a plastic scintillator, which stopped the collimated beam from a ⁹⁰Sr electron source. The main source of error for the absolute scale of the fluorescence yield is the uncertainty of the efficiency of the PMTs for single photon detection in the UV domain. Therefore, using the original AirLight setup, the ⁹⁰Sr electron beam was substituted by a pulsed N2 laser beam with a wavelength of 337 nm and similar geometry. The scintillator at the beam stop was replaced by a calibrated energy probe to measure the laser energy in each pulse. The beam intensity is reduced by a stepped density filter to achieve count rates from the Rayleigh scattering similar to the fluorescence measurements. A narrow-band filter (337 nm), a M-UG6 broad-band filter, and a quartz window will be applied to three original PMTs of the fluorescence measurements. The experimental procedures and first results are discussed.

Introduction

Ultra high energy cosmic rays (UHECR) are comprised of elementary particles, nuclei, and electromagnetic radiation of extraterrestrial origin, with energies of 10^{18} eV or higher. When UHECR enters the Earth's atmosphere, they generate a correlated cascade of secondary particles, also called extensive air showers (EAS). The passage of these charged particles through the atmosphere results in the ionization and excitation of air molecules, inducing fluorescence in nitrogen molecules. Important parameters of an EAS are: its longitudinal development, i.e., the number of particles in the shower depending on the amount of materials penetrated by the shower at a given point in its development (slant depth); and the amount of photons per deposited energy. Accordingly, there are several experimental setups (AIRFLY, AirLight, FLASH, MACFLY, among others), where the fluorescence yield is measured accurately for different electron beam energies.

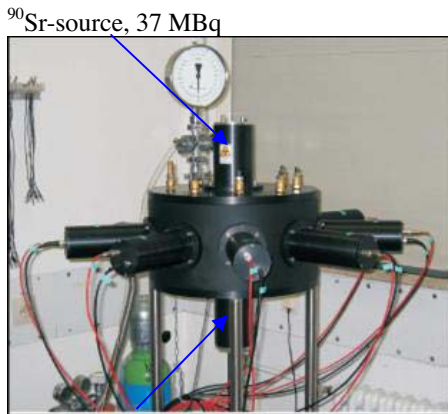
The AirLight Experiment at Forschungszentrum Karlsruhe was created to measure the fluorescence yield of electrons in nitrogen and air under atmospheric conditions as they appear in extensive air showers [1]. Electrons emitted from ⁹⁰Sr-source, with usable energies from 250 keV to 2000 keV, produce fluorescence light in nitrogen and air. This fluorescence is measured by photon detectors around the electron beam. Measurements of the absolute fluorescence yield between 300 nm and 400 nm for MeV electrons have been performed with high precision, the results are described in another paper presented at this conference [2].

The aim of the absolute calibration for the AirLight Experiment is to improve the absolute accuracies obtained for the single nitrogen bands from the current 15% to values in the order of 10% or below, by decreasing the uncertainty of the efficiency of the photomultiplier tubes (PMTs) for single photon detection in the UV domain. The PMT efficiencies will be measured by comparison to an energy meter with accuracy of $\pm 5\%$ (NIST calibrated UV LaserProbe RjP465

Silicon Energy Probe). The experimental setup and the method used for the absolute calibration will be described in the following sections.

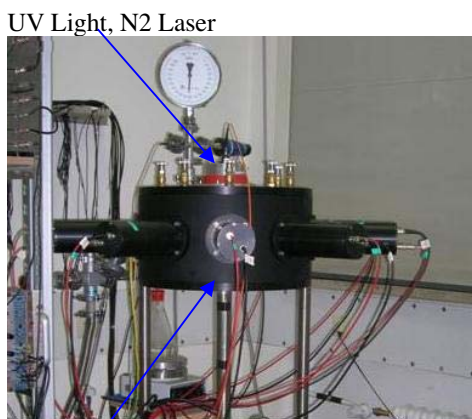
Experimental setup for the AirLight Absolute Calibration

As shown in Figure 1, using the original AirLight setup, the electron beam from the ⁹⁰Sr-source was substituted by a pulsed nitrogen laser beam with a wavelength of 337.1 nm and similar geometry. The scintillator at the beam’s end was replaced by a photodiode calibrated at NIST, to measure the laser energy in each pulse.



Electron detector-Plastic Scintillator

Figure 1a: AirLight



Laser probe-Silicon Energy Probe

Figure 1: The original AirLight setup (a) and the absolute calibration setup, showing the original

and the new beam sources as well as the original and the new detectors at the beam stop

The absolute calibration is done by using the Rayleigh scattering of a nitrogen laser beam. An optical fiber is used to guide the laser beam to the top of the chamber. A detailed schematic representation of the experiment is illustrated in Figure 2. The laser output energy of 120 μJ is reduced by a stepped density filter to achieve count rates around 1 p.e., then the laser beam is splitted into two beams. One of the beams is guided with an optical fiber to a Photonis XP 2262 PMT, which is used as the trigger PMT. The other beam is guided by an optical fiber to a box, in which the laser beam is collimated and then converted from an inherently depolarized light into a circularly polarized light. The purpose is to have the same amount of scattered light in the direction of all PMTs. The light then enters the chamber through a quartz window, passing another collimator (black tube), which ensures that there will be no Rayleigh scattered light before the desired distance from the center of the chamber. This collimator tube prevents the PMTs from ‘seeing’ the quartz window. There are seven PMTs, placed symmetrically, around the beam. The photodiode is located inside the chamber, with a small aperture of the same diameter as that one of the collimator tube. The distances, from the end of the collimator tube to the center and from the center to the photodiode, are equal.

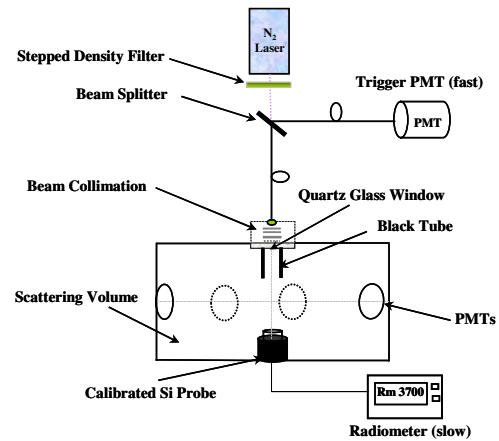


Figure 2: Schematic representation of the absolute calibration setup. In addition to the beam collima-

tor, there are 2 linear polarizers, one $\lambda/4$ plate and another linear polarizer used for crosschecking.

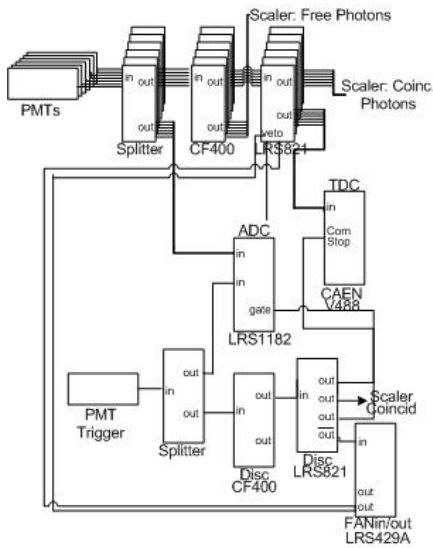


Figure 3: Simplified NIM-logic of the data acquisition system, including the trigger PMT

The photodiode is triggered externally with a frequency of about 10 Hz and 20 μ s later the laser is triggered. A simplified NIM-Logic of the data acquisition system, triggered by the PMT, is shown in Figure 3. The signal of the trigger PMT, as well as the signals of the other seven PMTs, are recorded with an ADC and readout by a computer. Simultaneously with the PMTs signals, the silicon probe, coupled to the radiometer, measures the energy of each laser pulse. The pressure and temperature inside the chamber are recorded as well. The data acquisition software is written in LabView 5.1.1, from National Instruments, following the data acquisition system of the AirLight experiment [1].

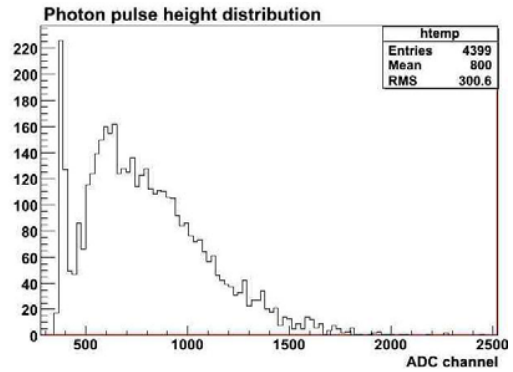


Figure 4a: ADC-histogram, showing the pedestal of the PMT and the p.e. distribution

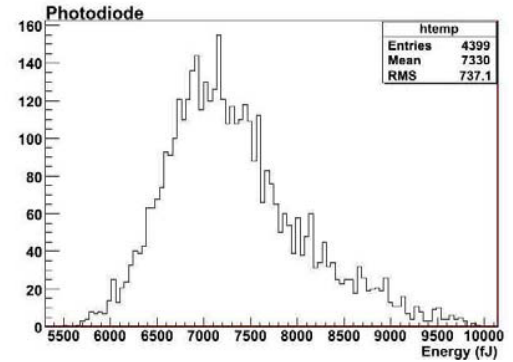


Figure 4b: Energy distribution per laser pulse

Figure 4 shows the pulse height distribution of one of the PMTs and the corresponding energy distribution per laser pulse, detected by a calibrated silicon probe. As can be seen in Figure 4, the pulse height distribution of the PMT obtained under the present laser setting does not correspond to that of a single photoelectron distribution. This is due to the fact that the second, and perhaps even the third, p.e-peak are still visible. This means that the intensity of the laser is still too high and must be reduced in future measurements.

Calculation of the number of photons reaching the iris of the PMT

Once the Rayleigh scattering is well understood [3,4,5], it can be used for the calculation of the precise number of Rayleigh scattering photons, and then for the absolute calibration of the PMTs

for the AirLight setup [6]. The number of scattered photons (N_{photon}) reaching the iris of the PMT is:

$$N_{\text{photon}} = N_L \sigma_{\text{tot}} N_{\text{mol}} A$$

where, N_L is the number of photons in each laser pulse and N_{mol} is the molecular number density. The total Rayleigh scattering cross section (σ_{tot}) was calculated from Bucholtz [4]:

$$\sigma(\lambda) = \frac{24\pi^3}{\lambda^4 N_s^2} \frac{(n_s^2 - 1)^2}{(n_s^2 + 2)^2} \left| \frac{6 + 3p_n}{6 - 7p_n} \right|$$

where, λ is the wavelength (in cm), N_s is the molecular number density for stp N_2 , n_s is the refractive index for stp N_2 and p_n is the depolarization factor.

For a preliminary estimate, an isotropic scattering was considered. This way, it is possible to take into consideration only the geometry of the experiment, and to use the value of the acceptance calculated in [1], $A = 0.25\%$. A precise calculation of the total hypothetical number of photons Rayleigh scattered from the beam axis will be performed by means of a Geant4 simulation. The estimated value for N_{photon} was 5.0115×10^6 . Using this value the energy needed for 1p.e is approximately 20 pJ/pulse.

Summary

Preliminary results obtained with the experimental setup for the absolute calibration of the AirLight Experiment, using Rayleigh scattered light are presented. The measurements that are ongoing (without filters) will be compared with results previously obtained by the AirLight experiment [1]. There will be additional measurements of the PMTs with a M-UG6 broad-band filter, with the narrow-band filter (337nm) and with the quartz window. The calibration measurements must be performed at various pressures, from near vacuum until ambient pressure. As mentioned before, the Geant4 simulation for the calculation of the total hypothetical number of photons Rayleigh scattered from the beam axis is still necessary.

Acknowledgements

The authors are grateful to Guenter Woerner, who constructed the mechanical structure for the laser calibration bench, and provided useful and helpful assistance.

References

- [1] T. Waldenmaier, Ph.D. thesis, University of Karlsruhe (TH), April, 2006. URL <http://bibliothek.fzk.de/zb/berichte/FZKA7209.pdf>
- [2] T. Waldenmaier, J. Bluemer, D. M. Gonzalez, H. Klages. Measurement of the Air Fluorescence Yield with the AirLight Experiment, these proceedings.
- [3] H. Naus and W. Ubachs, Opt. Lett, #25, 5, pages 347+, 2000.
- [4] A. Bucholtz, Appl. Optics, #34, 15, pages 2765+, 1995.
- [5] R. B. Miles *et. al.*, Review Article Laser Rayleigh scattering, Meas. Sci. Technol. #12, pages R33+, 2001.
- [6] J. N. Sakurai, M. Fukushima, L. Wiencke, PMT absolute calibration using the Rayleigh scattering in Nitrogen air. URL <http://www.auger.de/events/air-light-03/talks/Sakurai.pdf>
- [7] P. Huentemeyer for the FLASH collaboration, ICRC Proc. 00 pages 101+, 2005.



The TRACER Project: Instrument Concept, Balloon Flights, and Analysis Procedures

D. MÜLLER, M. AVE, P.J. BOYLE, F. GAHBAUER, C. HÖPPNER, J. HÖRANDEL^a, M. ICHIMURA^b, D. MÜLLER AND A. ROMERO-WOLF

The University of Chicago, 5640 South Ellis Avenue, Chicago, IL 60637, USA

(a) University of Karlsruhe, Germany (b) Hirosaki University, Japan

dmuller@uchicago.edu

Abstract: Accurate measurements of the composition and energy spectra of cosmic rays beyond the TeV energy region have been an experimental challenge for years. TRACER (“Transition Radiation Array for Cosmic Energetic Radiation”), is currently the largest cosmic-ray detector for direct measurements, and has been developed for long-duration balloon flights. The instrument is unconventional in that it uses only electromagnetic processes, such as measurements of ionization energy loss, Cherenkov light, and transition radiation, to make precision measurements that span more than four decades in energy, from 1 GeV/nucleon to energies beyond 10 TeV/nucleon. In its first long-duration balloon flight from Antarctica in December 2003, TRACER measured the energy spectra of the primary galactic cosmic-ray nuclei from oxygen ($Z = 8$) to iron ($Z = 26$). For a second LDB flight from Sweden in July 2006, the instrument was modified and upgraded in order to include the important light nuclei from boron ($Z = 5$) to nitrogen ($Z = 7$). We discuss the performance of TRACER in these two flights, review the response of the individual detector components, and the techniques employed in the data analysis.

Introduction

The TRACER instrument (“Transition Radiation Array for Cosmic Energetic Radiation”) has been developed to provide direct measurements of the elemental composition and energy spectra of cosmic-ray nuclei. The measurements should reach energies approaching the cosmic-ray “knee”, hence the instrument exhibits the largest geometric factor ($\sim 5\text{m}^2\text{ster}$) thus far realized in balloon-borne observations. TRACER has had three balloon flights: a test flight in New Mexico [1], and two long-duration balloon flights, in Antarctica [2] and in the Northern Hemisphere, respectively. In this paper, we shall summarize the overall program, including the key design and performance characteristics of the detector system.

Instrument Description

In order to minimize the mass-to-area ratio of the instrument, TRACER uses purely electromagnetic

techniques to determine charge Z and energy E (or the Lorentz-factor $\gamma = E/mc^2$) of cosmic-ray nuclei; a nuclear interaction in the detector is not needed, and in fact, not desired. Thus, TRACER employs a combination of Cherenkov counters, plastic scintillators, gaseous detectors for specific ionization, and transition radiation detectors. The particles encountered in high-latitude flights may have a wide range of energies, from sub-relativistic energies ($< 1\text{GeV/nucleon}$) up to the rare high-energy particles of interest here, with energies higher by four orders of magnitude.

The discrimination of the rare high-energy particles from the much more abundant (by about four orders of magnitude) low-energy flux represents a particular challenge for TRACER. This discrimination is achieved with an acrylic Cherenkov counter, combined with ionization measurements with plastic scintillators and gas proportional tubes (“ dE/dx counter”). For sub-relativistic particles above the Cherenkov threshold, the Cherenkov signal increases with energy and reaches saturation around $\gamma \sim 10$, while the ionization signal de-

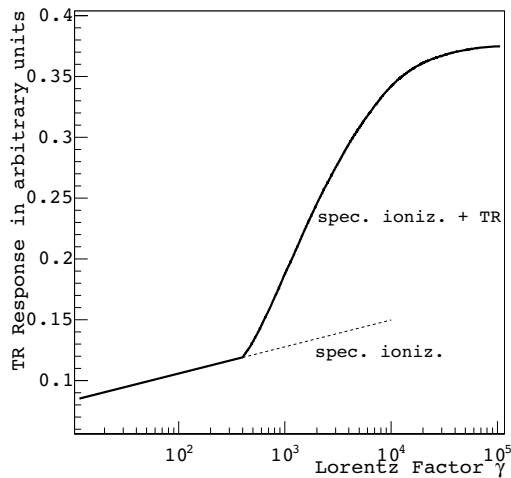


Figure 1: Energy response of the Transition Radiation Detector

creases according to the Bethe-Bloch formula and reaches minimum ionization around $\gamma = 3.9$. The signal remains at that level for the plastic scintillator, but increases again slowly with energy for the gaseous detectors (the “relativistic rise”). The signals of the Cherenkov counter do not only identify sub-relativistic particles, but also measure their energies.

The very highest particle energies ($\gamma > 500$) are identified with a transition radiation detector (TRD), which again, employs gas proportional tubes. The response of the TRD is shown in Figure 1. Up to the TR threshold ($\gamma \approx 400$), its response is identical to the that of the gaseous dE/dx counter, but at higher energies, the superimposed TR x-rays lead to a combined signal that rises steeply with energy. These detector elements are combined in TRACER as shown in figure 2. The instrument contains two plastic scintillators (2 m x 2 m, 0.5 cm thick) on the top and bottom and one acrylic Cherenkov counter (2 m x 2 m, 1.3 cm thick) at the bottom. For the 2006 balloon flight, a second, identical Cherenkov counter was added on top of the detector. Sandwiched between the top and bottom counters are 1584 single-wire proportional tubes (2 cm diameter, 2 m length) which are arranged in layers in two orthogonal directions as

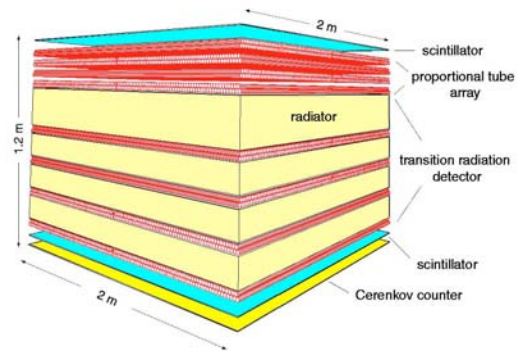


Figure 2: Schematic drawing of TRACER

shown: half of the tubes at the top measure the ionization energy loss, while the other half is interspersed below plastic-fiber radiators to form a TRD.

Balloon Flights

A one-day test flight of TRACER was performed from Fort Sumner, NM, in 1999, and the results have been published in Gahbauer et al. [1]. A long-duration flight from McMurdo, Antarctica, was launched in December 2003, and yielded data with zero dead time for ten days. The analysis of these data is now complete, and results will be presented here and in two related papers in these proceedings (Boyle et al. [3] and Ave et al. [4]). For these flights, the readout electronics was limited in dynamic range; hence, the elements covered ranged from oxygen ($Z = 8$) to iron ($Z = 26$). After the 2003 flight, the electronics were upgraded to permit inclusion of the important light secondary nuclei in the measurement. Hence, the elements from boron ($Z = 5$) to iron ($Z = 26$) are now covered. In order to improve the charge resolution, a second acrylic Cherenkov counter was installed. TRACER was then launched for a second long-duration flight from Kiruna, Sweden, in July 2006. Unfortunately, this flight had to be terminated after 4.5 days afloat, due to lack of an agreement which would have permitted continuation of the flight over northern Russia.

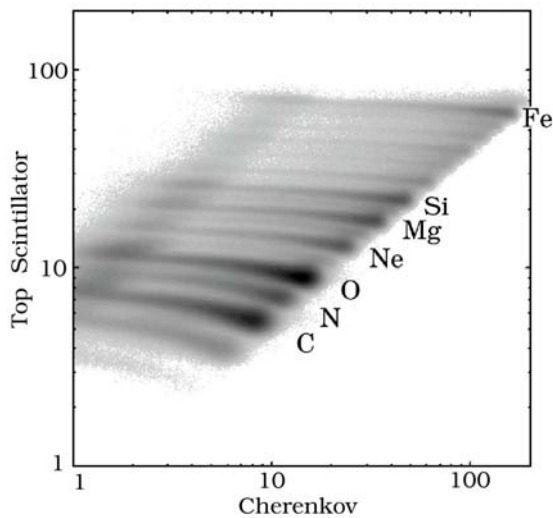


Figure 3: Scatter plot of top scintillator vs. Cherenkov signal in arbitrary units.

Data Analysis

We now shall briefly summarize the analysis procedures used for the 2003 flight. The analysis proceeds in the following steps: First the trajectory of each particle through the instrument is reconstructed, using the signals measured in the proportional and TRD tubes. Utilizing the fact that the signals are proportional to the pathlength through the tubes (within statistical fluctuations), one obtains a positional accuracy of 2-3 mm, which is much smaller than the tube radius. Subsequently, the signals of scintillators and Cherenkov counters are corrected for spatial non-uniformities in response according to response maps determined with muons before the flight, and verified by the flight data themselves.

Individual elements are cleanly identified from cross-correlations of scintillator and Cherenkov signals as shown in Figure 3. Cross-correlations between Cherenkov signals and ionization signals nuclei provide the means to separate low- and high-energy particles (i.e., below or above minimum ionization), see Höppner [5] and Romero-Wolf [2]. The magnitude of the Cherenkov signals determines the low-energy spectrum, from about 0.5 to 5 GeV/nucleon. The important and rare high-

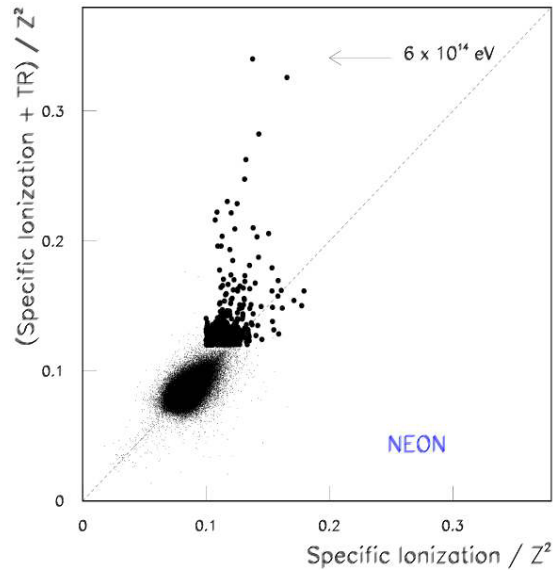


Figure 4: Scatter plot of TR vs. dE/dx signal for neon nuclei. The units are arbitrary.

energy particles are cleanly identified in a cross-correlation of the signals of the ionization tubes (“dE/dx counters”) with those measured with the TRD tubes. This is shown in Figure 4 for neon nuclei. Note that, for this figure, low energy particles (below minimum ionization) are removed. As expected, the majority of events lead to identical signals in dE/dx and TRD tubes; they have energies between a few GeV/nucleon and about 400 GeV/nucleon. At higher energies, the appearance of transition radiation enhances the TRD signals. This enhancement is the means to assign energies in the 500 GeV/nucleon to 10,000 GeV/nucleon region to these particles. Note how cleanly these rare high-energy particles can be identified: there are no background counts whatsoever in the “off-regions” of the scatter plot!

In order to determine the differential energy spectra on top of the atmosphere from these measurements, the selection efficiencies of the data analysis need to be known. As Table 1 shows, these are, in general, quite high. As an example for the results, Figure 5 shows the differential energy spectrum for neon nuclei. Note that the spectrum shown represents absolute intensities; there is no arbitrary normalization.

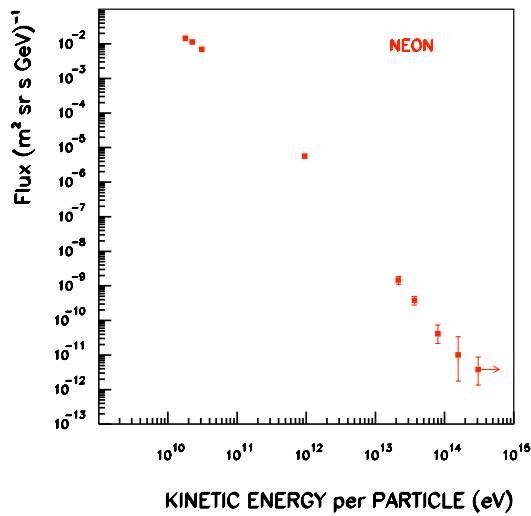


Figure 5: Differential energy spectrum for the single element neon from TRACER 2003.

Table 1: Efficiencies, i.e. fractions of surviving particles, for oxygen and iron.

| | Oxygen | Iron |
|--------------------------|--------|------|
| Interaction - Atmosphere | 82% | 72% |
| Interaction - Instrument | 65% | 48% |
| Tracking Efficiency | 95% | 95% |
| Top Charge Efficiency | 89% | 90% |
| Bot Charge Efficiency | 100% | 100% |

Conclusion

The 2003 flight of TRACER has determined the energy spectra of the major primary nuclei for oxygen ($Z = 8$) to iron ($Z = 26$). These results, and their interpretation, will be shown in the accompanying papers of Boyle [3] and Ave [4]. The analysis of the 2006 flight data, which also include measurements of the lighter cosmic-ray nuclei, down to boron ($Z = 5$), is currently in progress.

While the TRACER results extend our knowledge of the cosmic ray composition well into the 10^{14} eV per particle energy region, this upper limit is purely due to counting statistics; the detector response would permit measurements to consider-

ably higher energies if larger exposures become available.

Acknowledgments

This work has been supported by NASA grants NAG5-5305, NN04WC08G and NNG06WC05G. MI acknowledges the Grant-in-Aid for Scientific Research of the Japan Society for the Promotion of Science(JSPS), No. 17540226. Numerous students have participated in this research under support from the Illinois Space Grant Consortium. We gratefully acknowledge the services of the University of Chicago Engineering Center and the Columbia Scientific Balloon Facility.

References

- [1] F. Gahbauer et al. *ApJ*, 607:333, 2004.
- [2] A. Romero-Wolf et al. *Proc. 29th ICRC*, 3:97, 2005.
- [3] P. J. Boyle et al. *Proc. 30th ICRC*, 2007.
- [4] M. Ave et al. *Proc. 30th ICRC*, 2007.
- [5] C. Höppner et al. *Proc. 29th ICRC*, 3:73, 2005.



Cosmic Ray Energy Spectra of Primary Nuclei from Oxygen to Iron: Results from the TRACER 2003 LDB Flight

P.J. BOYLE, M. AVE, C. HÖPPNER, J. HÖRANDEL^a, M. ICHIMURA^b, D. MÜLLER AND A. ROMERO-WOLF

The University of Chicago, 5640 South Ellis Avenue, Chicago, IL 60637, USA

(a) University of Karlsruhe, Germany (b) Hirosaki University, Japan

jojo@donegal.uchicago.edu

Abstract: The first long-duration balloon flight of TRACER in 2003 provided high-quality measurements of the primary cosmic-ray nuclei over the range oxygen ($Z = 8$) to iron ($Z = 26$). The analysis of these measurements is now complete, and we will present the individual energy spectra and absolute intensities of the nuclei O, Ne, Mg, Si, S, Ca, Ar, and Fe. The spectra cover the energy range from 1 GeV/nucleon to more than 10 TeV/nucleon, or in terms of total energy, to several 10^{14} eV per particle. We compare our results with those of other recent observations in space and on balloons and notice, in general, good agreement with these data for those regions where overlap exists. We also compare our data with information that has recently been inferred from air shower observations.

Introduction

TRACER (Transition Radiation Array for Cosmic Energetic Radiation) is a very large instrument designed to study cosmic ray nuclei above a TeV/nucleon. In 2003 TRACER had a 10 day balloon flight in Antarctica yielding an exposure of 50 m^2 steradian days at a residual atmosphere of 3.9 g/cm^2 . During the flight TRACER collected 50 million cosmic ray nuclei with charge $Z \geq 8$. The analysis of this data-set is now complete and we present here the energy spectra for eight elements O, Ne, Mg, Si, S, Ar, Ca and Fe. The results cover over four decades in energy and are given as absolute intensities, without arbitrary normalizations.

Absolute Intensities

Depending on the method of energy assignment, each event that passes the data analysis cuts is classified either as a *Cerenkov Event*, *dE/dx Event* or *Transition Radiation Event*. These events are sorted into energy bins, using the response curves described by Müller (these proceedings [1]). The width of each energy bin is commensurate with the energy resolution and varies with energy E and

charge Z. As the relative intrinsic signal fluctuations decrease proportional to $1/Z$, the energy resolution improves with increasing charge. To convert from the number of events N_i in a particular energy bin ΔE to an absolute differential flux dN_i/dE at the top of the atmosphere one must compute the exposure factor, effective aperture, efficiency of the cuts and unfold the instrument response :

$$\frac{dN_i}{dE} = \frac{N_i}{\Delta E} \cdot \frac{1}{T_l} \cdot \frac{1}{\varepsilon_i} \cdot \frac{1}{A_i} \cdot C_i \quad (1)$$

with T_l the live-time, ε_i the efficiency of analysis cuts, A_i the effective aperture and C_i the “overlap correction” due to misidentified events from neighbouring bins. The effective aperture is :

$$A_i = A \cdot 2\pi \int_{\theta=0}^{\pi/2} P_I(\theta) P_D(\theta) \cos\theta \, d(\cos\theta) \quad (2)$$

with A the area of the detector ($2.06 \text{ m} \times 2.06 \text{ m}$), $P_I(\theta)$ the probability of survival in the atmosphere and the instrument as a function of zenith angle θ , $P_D(\theta)$ the probability that a particle passing through the instrument will be detected. The Overlap corrections are determined with Monte Carlo simulations and are typically $\leq 20\%$ (i.e. $0.8 \leq$

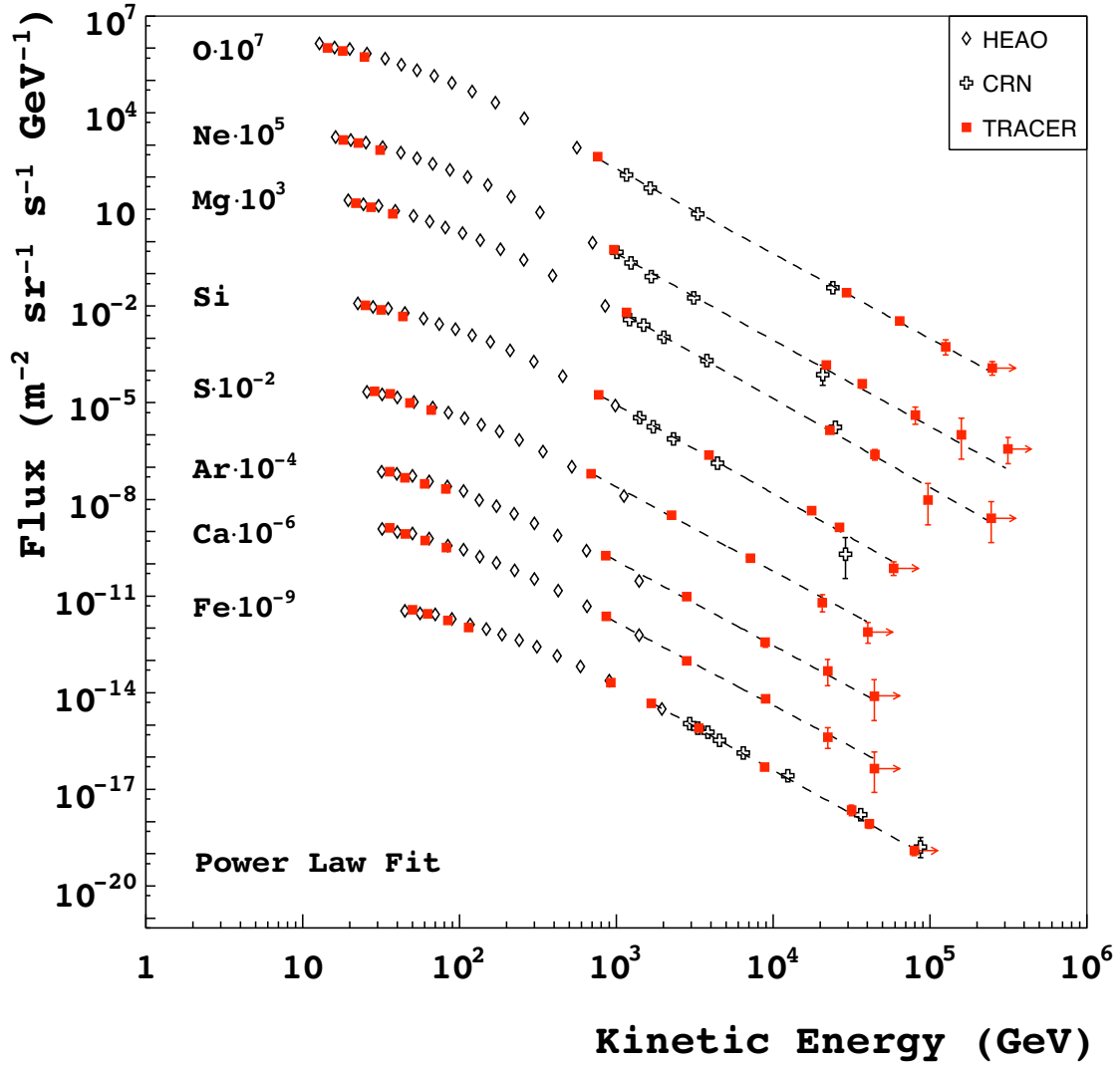


Figure 1: Differential energy spectra for the cosmic ray nuclei : O, Ne, Mg, Si, S, Ar, Ca and Fe. Results from the TRACER 2003 Antarctica flight are indicated by the red squares. Existing data from the HEAO-3 experiment (open diamonds) [2] and the CRN experiment (open crosses) [3] are shown for comparison. The dashed line represents an independent power-law fit to each spectrum above 20 GeV/nucleon.

$C_i \leq 1.2$). An example of efficiencies etc is given for oxygen and iron in Table 1 of Müller [1]. The energy assigned for each bin is defined as :

$$E = \frac{1}{E_2 - E_1} \cdot \frac{1}{1 - \alpha} \cdot (E_2^{1-\alpha} - E_1^{1-\alpha})^{-1/\alpha} \quad (3)$$

where α is the power-law exponent of the differential energy spectrum. The method is discussed in detail by Lafferty and Wyatt [4].

Resulting Energy Spectrum

The energy spectra, in terms of absolute intensities, for the elements O, Ne, Mg, Si, S, Ar, Ca and Fe are presented in Figure 1. We note the large range in intensity (ten decades) and particle energy (four decades) covered by TRACER. This has been achieved by three complementary measurements in one detector : the Cerenkov counter ($\sim 10^{11}$ eV), the relativistic rise of the ionization signal in gas ($\sim 10^{11} - 10^{13}$ eV) and the Transition Radiation Detector ($> 10^{13}$ eV) [1]. Data from the TRACER 2003 flight are indicated by the red squares. For clarity the intensity of each element is multiplied by a factor shown on the left. Existing data from measurements in space with HEAO-3 (open diamonds) and CRN (open crosses) are shown for comparison. As can be seen, the energy spectra for O, Ne, Mg and Fe extend up to and beyond 10^{14} eV. No evidence for any significant change in spectral slope is evident at the highest energies. The energy spectrum of each element (from TRACER and CRN) is fit to a power law above 20 GeV/nucleon. The resulting spectral indices (Figure 2) are remarkably similar, with an average of 2.65.

Figure 3 compares the TRACER results for iron with results from a number of other investigations. Below 10^{12} eV we show results from HEAO-3 [2] and at higher energies from CRN [3] on the space shuttle and from the ATIC-2 [5] and RUNJOB balloon experiments [6]. The dashed line represents a power-law fit with an exponent of -2.7 and describes the data well above 10^{12} eV. Figure 3 also illustrates the variety of detection techniques used in measuring the energy of heavy nuclei. Within the statistical uncertainties (which in some measurements are quite large), the data indicate fairly

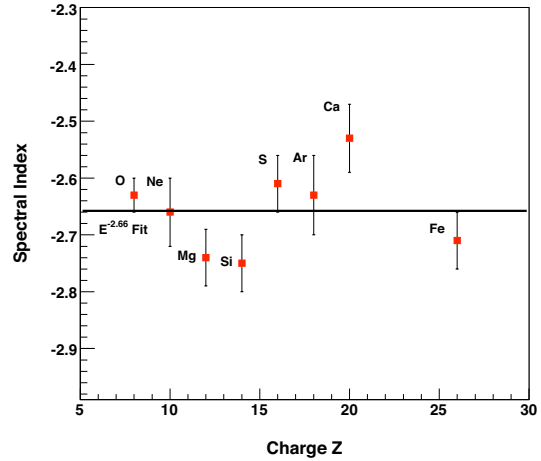


Figure 2: Spectral indices of a best power-law fit to the combined TRACER and CRN data above 20 GeV/nucleon. The line indicates the an average spectral fit of $E^{-2.65}$.

consistent results. The Transition Radiation technique of TRACER can, in principle, provide measurements with energies up to around 10^{15} eV. The range of the current results is limited by the exposure available. Also presented in Figure 3 are recent results from the ground based HESS Imaging Air Cerenkov Telescope using the Direct Cerenkov Technique (green triangles). These results are the first examples of a new technique for measurements from the ground [7]. Two flux values are presented for each energy indicating ambiguities from different interaction models [8]. Again, these data are consistent with TRACER.

Comparison with Air-shower Data

Data for oxygen and iron for TRACER are compared in Figure 4 with spectra derived from indirect observations of the EAS-TOP collaboration [9], and of the KASCADE group for two different nucleus-nucleus interaction models [10]. However, these groups do not report results for individual elements: the fluxes for the ‘‘CNO group’’ probably have about twice the intensity than oxygen alone, while the ‘‘iron group’’ probably is dominated by iron. Our results do not yet overlap with the en-

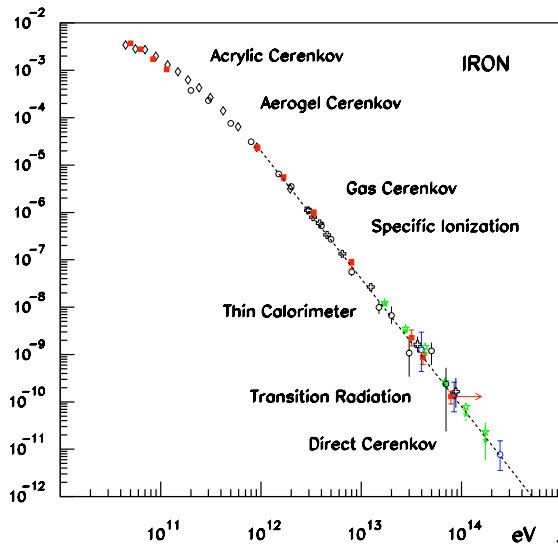


Figure 3: Iron energy spectrum above 10^{10} eV per particle in units of $\text{m}^2 \text{ster}^{-1} \text{s}^{-1}$, highlighting the complementarity between detection techniques. TRACER (red squares), HEAO-3 [2] (black diamonds), CRN [3] (black crosses), ATIC-2 [5] (black open circles), RUNJOB [6] (blue open circles) and HESS [8] (green stars).

ergy region of the air shower data, but the gap is becoming smaller, in particular for oxygen. Additional measurements will indeed lead to significant constraints on the air shower interpretations.

Conclusion

The TRACER 2003 data represent the most detailed measurements to date for heavy nuclei above a TeV/nucleon with single charge resolution. While the results do not reveal any surprising features in the cosmic ray energy spectra at high energies, they begin to provide stringent constraints on the conventional models on galactic propagation. The analysis of the TRACER results in the context of these models is discussed in these proceedings (Ave et al. [11]).

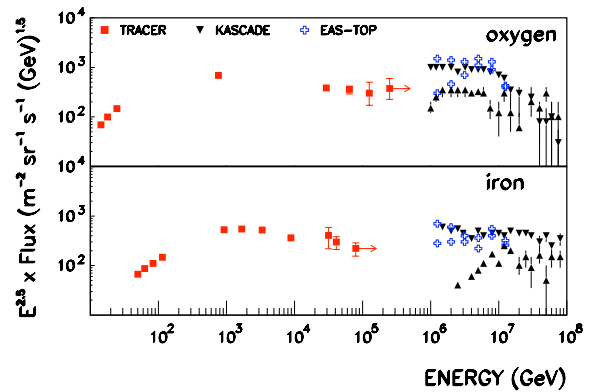


Figure 4: Energy Spectra from TRACER and from the interpretation of air shower data of KASCADE (for two different interaction models) and of EAS-TOP (two data points for each energy are given, representing upper and lower limits). The spectra are for oxygen and for iron for TRACER, but for the “CNO-group” and the “Fe-group” for the other observations.

We acknowledge support as summarized in Müller et al [1].

References

- [1] D. Müller et al. *Proc. 30th ICRC*, 2007.
- [2] J. J. Engelmann et al. *A&A*, 233:96, 1990.
- [3] D. Müller et al. *ApJ*, 374:356–365, 1991.
- [4] J. D. Lafferty and T. R. Wyatt. *NIM A*, 355:541, 1995.
- [5] A. D. Panov et al. *ArXiv e-print*, 2006.
- [6] V. A. Derbina et al. *ApJ, L*, 628:L41, 2005.
- [7] D. B. Kieda et al. *Proc. 27th ICRC*, 4:1533, 2001.
- [8] F. Aharonian et al. *Phys. Rev. D*, 75(4):042004–, 2007.
- [9] G. Navarra et al. *Proc. 28th ICRC*, 1:147, 2003.
- [10] T. Antoni et al. *Aph*, 24:1–2, 2005.
- [11] M. Ave et al. *Proc. 30th ICRC*, 2007.



Propagation of High-Energy Cosmic Rays through the Galaxy: Discussion and Interpretation of TRACER Results

M. AVE, P.J. BOYLE, C. HÖPPNER, J. HÖRANDEL^a, M. ICHIMURA^b AND D. MÜLLER

The University of Chicago, 5640 South Ellis Avenue, Chicago, IL 60637, USA

(a) University of Karlsruhe, Germany (b) Hirosaki University, Japan

jojo@donegal.uchicago.edu

Abstract: The long-duration balloon flights of TRACER provide new measurements of the intensities and energy spectra of the arriving cosmic-ray nuclei with $5 \leq Z \leq 26$ at high energies. In order to determine the particle composition and energy spectra at the cosmic-ray sources, changes occurring during the interstellar propagation of cosmic rays must be known. We use a simple propagation model with energy-dependent pathlength and derive constraints on the propagation parameters from a self-consistent fit to the measured energy spectra. We use the model to obtain the relative abundances of the cosmic ray nuclei at the acceleration site.

Introduction

The TRACER long-duration balloon flight in 2003 has provided a rather comprehensive data set on the energy spectra of primary cosmic ray nuclei from oxygen to iron ($Z = 8$ to 26) up to energies around, and for some species above, 10^{14} eV. Where comparisons with previous measurements can be made, satisfying agreement between different data sets exists [1]. The energy spectra reach similar, if not identical, power-law slope towards high energy, and spectral breaks of any kind are not noticeable. This strongly indicates a common origin of these elements. However, in order to determine the spectra and relative abundances at the sources, the mode of galactic propagation must be understood.

Propagation Model

At relativistic energies, the fate of a cosmic-ray nucleus propagating from the acceleration site to the observer is determined by the competing actions of escape from the galaxy by diffusion and by loss due to nuclear interaction in the interstellar medium (ISM). For simplicity, one may characterize these processes by two parameters, the escape pathlength Λ_{esc} , and the interaction path-

length Λ_{int} . In general, Λ_{esc} depends on energy, while Λ_{int} scales with $A^{-2/3}$ (where A = atomic number), i.e., Λ_{int} decreases with increasing nuclear charge Z . The energy dependence of Λ_{esc} is usually derived from the intensity ratio of secondary to primary cosmic rays; here we use the parameterization given by Yanasak et al. [2], where R = particle rigidity, and $\beta = v/c$.

$$\Lambda_{esc} = \frac{26.7\beta}{(\beta R)^{0.58} + \left(\frac{\beta R}{1.4}\right)^{-1.4}} + \Lambda_0 \quad (1)$$

This is illustrated in Figure 1. We note that the escape pathlength approaches the commonly accepted form $\Lambda(E) \propto E^{-0.6}$ at high energy, but we also notice that at energies around and above 100 GeV/nucleon the observational data provide little constraint on $\Lambda_{esc}(E)$. It is quite possible that Λ_{esc} approaches a non-zero residual value Λ_0 at high energy.

In the simplest form, the relation between the observed energy spectrum $N_i(E)$ of a cosmic ray nucleus and the spectrum at the source $Q_i(E)$ is :

$$N_i(E) \propto \Lambda \cdot (Q_i(E) + \text{spallation term}) \quad (2)$$

with

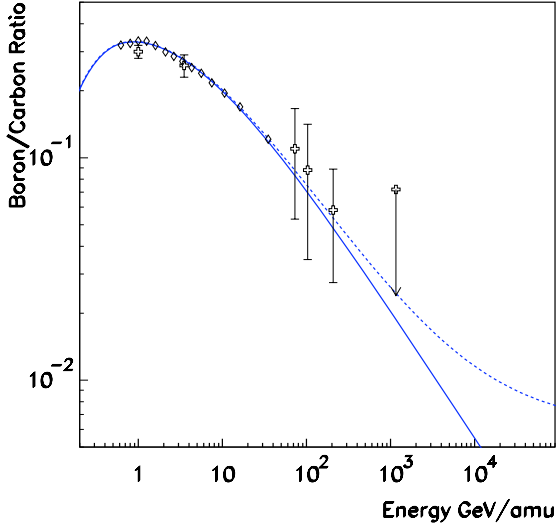


Figure 1: Boron to carbon ratio with data from HEAO-3 and CRN. The solid line represents a parameterization given by Yanasak [2]. The addition of a residual pathlength of $\Lambda_0 = 0.1 \text{ g/cm}^2$ to the Yanasak parametrization is presented by the dashed line.

$$\frac{1}{\Lambda} = \frac{1}{\Lambda_{esc}(E)} + \frac{1}{\Lambda_{int}(Z)}, \quad (3)$$

and “spallation term” refers to the production of this species by nuclear spallation in the ISM.

Over certain energy regions, Λ_{esc} and Λ_{int} are commensurate, as shown in Figure 2, and in general, the smaller of the two parameters is the one which dominates in equation 3. We assume that the source energy spectrum is a power law with exponent α , i.e. $Q_i(E) \propto E^{-\alpha}$. A power law exponent not much in excess of $\alpha = 2.0$ would be expected for strong shocks in supernova shock acceleration models. We now compare the observed cosmic-ray spectra (see Figure 1 in Boyle [1]) with the predictions of this simple propagation model. We assume that all species have the same source index α , but we use the value of α and that of the residual pathlength Λ_0 as fit parameters. Figure 3 shows the energy spectra (multiplied with $E^{2.5}$), together with fitted curves corresponding to $\alpha = 2.3$ and $\Lambda_0 = 0 \text{ g/cm}^2$ (dashdot line) and 0.1 g/cm^2 (solid line). Clearly, the fits shown are quite good, but may not be unique. A χ^2 -test of the spectra of all elements

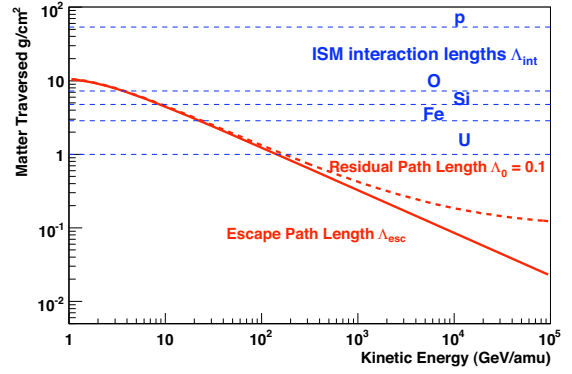


Figure 2: Escape path length (red curve) and interaction path length (dashed lines) versus energy. The interaction pathlengths are given for several elements including, for illustration, protons and uranium.

(from oxygen to iron) leads to the contour lines shown in Figure 4. A slight increase in the power-law index from $\alpha = 2.2$ to 2.4 could be compensated with values of Λ_0 from 0 to 0.5 g/cm^2 . However, the larger the value of α , the more difficult it is to accommodate in shock-acceleration scenarios. It is clear that a direct measurement of Λ_{esc} at higher energies and high precision is essential to resolve this issue.

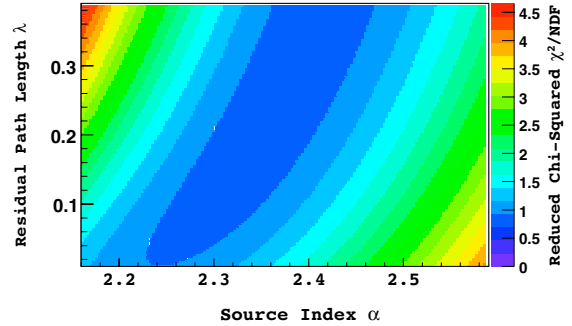


Figure 4: Composite χ^2 for Λ_0 and α for the eight TRACER elements.

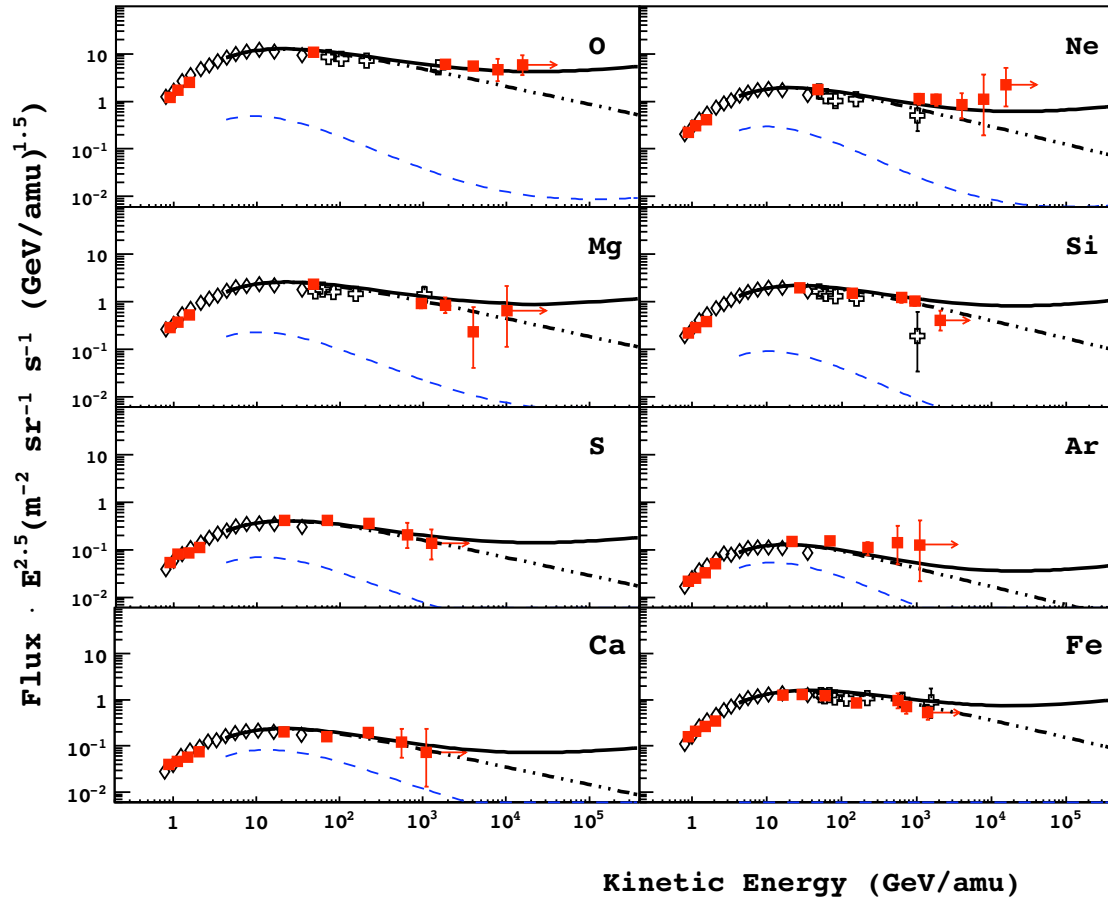


Figure 3: Differential energy spectra, multiplied with $E^{2.5}$, from TRACER (solid squares), HEAO-3 [3] (open diamonds), and CRN [4] (open crosses). The black curves refer to predictions from a simple propagation model (dash-dot line $\alpha = 2.3$ and $\Lambda_0 = 0 \text{ g}/\text{cm}^2$; solid line $\alpha = 2.3$ and $\Lambda_0 = 0.1 \text{ g}/\text{cm}^2$) and the blue dashed line is the contribution of secondary particles. Note the energy scale is in GeV/amu .

Simple Consequences of the Model

We may construct “expected” energy spectra for all nuclei, taking $\alpha = 2.3$ and $\Lambda_0 = 0.1 \text{ g/cm}^2$, and then generate single power-law fits to these spectra over 20 to 1000 GeV/nucleon. This index would slowly change with energy, as shown in Figure 5. However, the change is not as significant as to be observable in the experimental data. We also may use the propagation model to determine the fraction of secondary, spallation-produced nuclei in each observed spectrum. This is shown in Figure 3 (blue dashed lines), indicating a secondary contribution just in the 1-percent region in most cases.

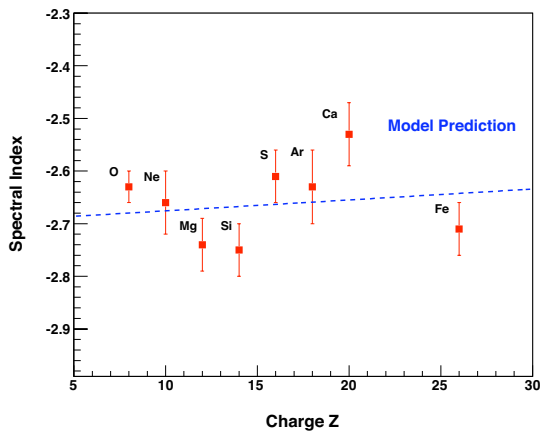


Figure 5: The best fit power law indices from TRACER 2003 as a function of charge Z . The dashed line represents a theoretical evolution of the spectral index using the propagation model detailed in the text.

Finally, we determine the relative abundances of the elements at the cosmic-ray source (Figure 6), and again verify the well-known anti-correlation with the first ionization potential or with volatility.

Conclusion

The TRACER results on the elemental composition of cosmic ray nuclei lead to a number of details that characterize the source of high-energy cosmic rays. In general, they provide support for a shock acceleration mechanism in supernova remnants, and for a common origin of all species. As the measurements extend into the $10^{14} - 10^{15} \text{ eV}$

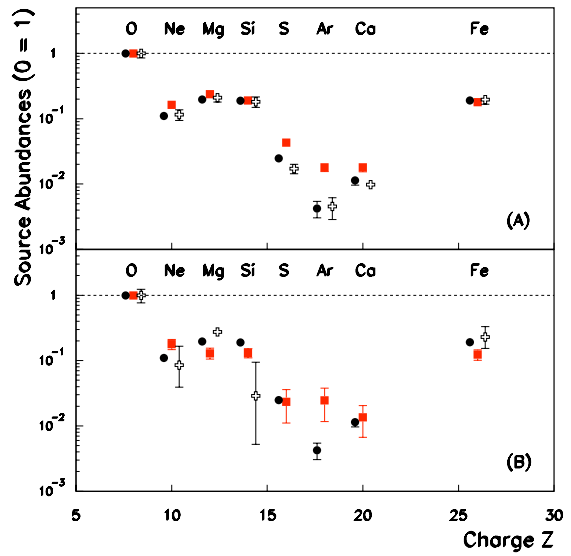


Figure 6: Galactic cosmic ray source abundances from TRACER (red squares) and CRN (crosses) normalized to oxygen and compared to the HEAO-3 results at 1-30 GeV/n (circles). (A) CRN at 100 GeV/n and TRACER at 10-250 GeV/n (B) CRN at 1000 GeV/n and TRACER $> 250 \text{ GeV/n}$. Note that the charge Z is offset for each element for clarity.

region, it is noteworthy that there does not seem to be an indication for any irregular behavior of any of the spectra. The most important task for new measurements appears to be an extension of the secondary-primary intensity ratio to higher energies. We expect that the TRACER results from its 2006 flight, which are currently being analyzed, will lead to new results in this area.

We acknowledge support as summarized in Müller et al. [5] and we are grateful to significant contributions by college student J. Marshall.

References

- [1] P. J. Boyle et al. *Proc. 30th ICRC*, 2007.
- [2] N. E. Yanasak et al. *ApJ*, 563:768–792, 2001.
- [3] J. J. Engelmann et al. *A&A*, 233:96, 1990.
- [4] D. Müller et al. *ApJ*, 374:356–365, 1991.
- [5] D. Müller et al. *Proc. 30th ICRC*, 2007.



On the origin of the knees in the cosmic-ray energy spectrum

J.R. HÖRANDEL^a, N.N. KALMYKOV^b, A.A. SILAEV^c, AND A.V. TIMOKHIN^c.

^a *Institute for Experimental Nuclear Physics, University of Karlsruhe, Germany, now at Department of Astrophysics, Radboud University Nijmegen, The Netherlands*

^b *Skobeltsyn Institute of Nuclear Physics, Lomonosov Moscow State University, Moscow, Russia*

^c *Faculty of Physics, Lomonosov Moscow State University, Moscow, Russia*

hoerandel@ik.fzk.de

Abstract: Combining diffusion equation solutions with direct Monte-Carlo simulations of charged particle trajectories, the propagation of cosmic rays in the Galaxy is investigated. Different assumptions on the shape of the regular Galactic magnetic fields and source distributions are considered and their influence on cosmic-ray life times and the energy spectrum obtained at Earth is examined. The origin of the knee in the energy spectrum at $4 \cdot 10^{15}$ eV and the second knee at $4 \cdot 10^{17}$ eV is discussed. It is investigated whether the knee can be explained by propagation effects only and if the second knee is due to the end of the galactic component with a strong contribution of elements heavier than iron.

Introduction

The knee in the energy spectrum of cosmic rays (CRs) at $\sim (4 - 5) \cdot 10^{15}$ eV was first observed almost 50 years ago [9], but its origin is still under discussion and it is generally believed to be a corner stone in understanding the origin of CRs.

The verification of various hypotheses of the CR origin and the nature of the knee in their energy spectrum is complicated by the fact that the CR spectra at the sources and at the Earth are different. The change of the energy spectrum during propagation is related to the energy dependence of the CR life time in the Galaxy.

Using a combined approach, which includes the solution of a diffusion equation for the CR density in the Galaxy and a method of numerical calculations of trajectories, we have performed a calculation of the energy spectrum at Earth in the energy range $10^{12} - 10^{20}$ eV.

The method of numerical integration of trajectories is traditionally used for the calculation of the spectrum at high energies [14, 6, 5] but it is not too efficient at low energies as the calculation time needed is inversely proportional to particle energy.

The diffusion model is more suitable at lower energies and the CR energy spectrum may be obtained by the solution of the diffusion equation for the CR density in the Galaxy [5, 11]. There are no computing difficulties inherent to the numerical simulation of trajectories, but the diffusion approach is limited by a certain energy boundary — the energy of a proton should not exceed 10^{17} eV [5].

In our calculations we tested different assumptions about the structure of the regular magnetic fields of the Galaxy, and also different spatial distributions of CR galactic sources, to determine to what degree this uncertainty will influence results of the calculations.

The results obtained were used to verify the hypotheses of the origin of the knee in the energy spectrum using experimental data as obtained at Earth.

Assumptions about magnetic fields

The magnetic field used in the calculations included a regular and a chaotic component

$$\vec{B} = \vec{B}_{reg} + \vec{B}_{chaot}. \quad (1)$$

For the regular magnetic field component a model from Ptuskin et al. [11] was used

$$B_z = 0, B_r = 0, B_\phi \propto \exp\left(-\frac{z^2}{z_0^2} - \frac{r^2}{r_0^2}\right), \quad (2)$$

where $z_0 = 5$ kpc, $R_0 = 10$ kpc, and

$$B_\phi(z = 0) = 2.15\mu\text{G} \cdot \sin\left(2\pi \frac{r - 9.35 \text{ kpc}}{6.2 \text{ kpc}}\right) \quad (3)$$

according to the Rand-Kulkarni model [13].

The poloidal component of the regular magnetic field [10] was also taken into account. The chaotic magnetic field in the simulation of the particle trajectories was defined according to the algorithm used in [15], generating irregularities on the scale $L = 100$ pc. In addition, we simulated interactions of charged particles with magnetic irregularities of smaller scales. For the spatial distribution of CR sources, a uniform distribution in the galactic disk and a radial distribution of supernovae remnants in the galactic disk [8] were used. Different models of the regular magnetic field and also different assumptions on the CR source distributions did not influence the main results of our calculations.

The knee in the energy spectrum

In the framework of the diffusion model, the knee in the CR energy spectrum at Earth can be explained by a change of the character of the dependence of the diffusion coefficient on energy. This dependence changes from

$$D_\perp \sim E^m, \quad (4)$$

where $m = 0.2 - 0.6$ is a parameter of the model, to

$$D_A \sim E, \quad (5)$$

since the Hall diffusion coefficient D_A is proportional to the Larmor radius of a particle (for more details, see [11]).

In order to get a sharp steepening $\Delta\gamma \approx 0.8$ in the elemental spectra of CRs at energies around $4 \cdot 10^{15}$ eV, we assumed $m \approx 0.2$, as suggested in [11]. Furthermore, the intense rise of the diffusion coefficient with energy (if we assume $m = 0.4 - 0.8$) leads to excessive anisotropy — it is more than 10% at an energy of 10^{16} eV for $m = 0.6$ [2].

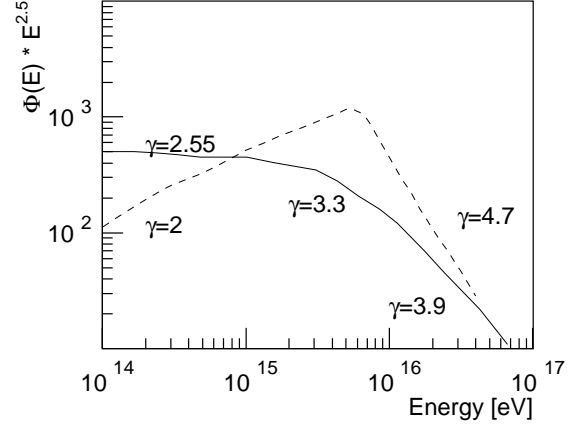


Figure 1: The energy spectra of protons in sources. The curves are normalized at 10^{15} eV. The solid line represents the spectrum obtained from the KASCADE spectrum, the dashed line is the source spectrum according to the standard picture of CR acceleration [12].

If one takes into account the complex CR mass composition, the value of $\Delta\gamma$ decreases to $\approx 0.4 - 0.5$ in the all-particle spectrum [11], which is consistent with experimental data [7]. Thus, the knee in the all-particle spectrum at an energy of about $4 \cdot 10^{15}$ eV can be explained as the result of the changes in conditions of the propagation in the Galaxy (from the diffusion to the drift in the large scale magnetic field of the Galaxy). But the situation with elemental spectra of CR is more problematic.

The energy spectra for various nuclear groups obtained by KASCADE and other air shower experiments can be approximated by the ansatz (the polygono model) [3, 4]

$$I_z(E) = I_0(Z)E^{-\gamma_z} \cdot \left(1 + \left(\frac{E}{E_k(Z)}\right)^\zeta\right)^{-\frac{\Delta\gamma}{\zeta}}, \quad (6)$$

where Z is the charge of the particle, γ_z the exponent before the knee which is obtained from direct measurements, $E_k(Z) = Z \cdot E_k(Z = 1)$ the energy corresponding to the knee; as well as $\zeta \approx 2$ and $\Delta\gamma = 2$ characterizing the shape of the knee structure in the spectra. The observed change of the exponent of the spectrum should be compared to the value $1 - m \approx 0.8$. This value follows from a dif-

fusion model to explain the origin of the knee [11]. It is obvious that the experimental value of $\Delta\gamma$ is essentially greater; hence, at least a part of the observed $\Delta\gamma$ should stem from the peculiarities of the energy spectrum at the sources. It is instructive to point out that at higher energies (above 10^{17} eV) the diffusion coefficient becomes proportional to E^2 and, formally, one could get a sharp knee. But the diffusion approach produces wrong results at such energies and an essentially more complicated transport equation is needed.

Taking the spectra measured at Earth as parameterized with equation 6 and taking into account the dependence of the CR life time on energy, obtained by numerical calculation of trajectories the spectra at the sources can be estimated. The result is presented in Fig. 1 as solid line. It represents the proton spectrum at the sources. The result indicates that the relatively sharp knee in the elemental spectra at the Earth (see e.g. [4]) can not be explained in the context of the diffusion model only, and it is necessary to assume a change of spectra in sources at corresponding energies.

For a final conclusion it is necessary to ultimately establish the exact shape of the spectra for elemental groups.

The second knee in the spectrum

Using spectra at the sources similar to the one shown in Fig. 1 the spectra at Earth have been estimated [5]. As source composition, the abundances of elements from hydrogen to uranium as measured in the solar system [1] have been weighted with $Z^{3.2}$. This choice is arbitrary to a certain extent, but may be motivated by a higher efficiency in the injection or acceleration processes for nuclei with high charge numbers. The abundances are scaled with a factor which is identical for all elements to obtain approximately the absolute values as expected at the Earth according to the poly gonato model. At the source, a power law $\propto E^{-2.5}$ has been assumed for all elements with a knee, caused e.g. by the maximum energy attained during the acceleration, at $Z \cdot 4.5$ PeV, with a power law index -3.5 above the respective knee. Using the derived propagation path length and interaction length, the amount of interacting particles has been

determined. Secondary products generated in spallation processes are taken into account, assuming that the energy per nucleon is conserved in these reactions. They are added to the corresponding spectra with smaller Z . The spectra thus obtained are compared to spectra according to the poly gonato model in Fig. 2.

Two features should be noted: The absolute fluxes at Earth are predicted quite well, especially when considering that only a simple scaling law has been introduced for the abundances at the sources, starting with the composition in the solar system. More important for the present discussion is the shape of the spectra. As expected, the shape of the proton spectrum is not influenced by the (few) interactions during propagation and the difference of the spectral index at the source and at Earth $\gamma = -2.71$ [3] can be explained by the energy dependence of the escape path length $\propto E^{-0.2}$. On the other hand, it can be recognized that due to nuclear interactions the spectra for heavier elements are flatter. The slopes obtained with the simple approach for the CNO, silicon, and iron groups agree well with the steepness as expected from the poly gonato model. For heavy elements at low energies secondary products generated in spallation processes play an important role for the shape of the spectrum. At low energies many nuclei interact due to the large escape path length and the small interaction length, thus, the spectra of nuclei without any interaction deviate from power laws. However, the spallation products of heavier elements at higher energies compensate the effect and the resulting spectra are again approximately power laws, as can be seen in Fig. 2.

Summary and Conclusion

The propagation pathlength and escape time of cosmic rays in the galaxy has been calculated in a combined approach solving a diffusion equation and numerically calculate the trajectories of particles in the Galaxy. To explain the relatively steep fall-off of the observed energy spectra for elemental groups at their respective knees, the modulation of the spectrum due to propagation solely is not sufficient. An additional steepening of the spectra at the source is necessary, e.g. caused by the max-

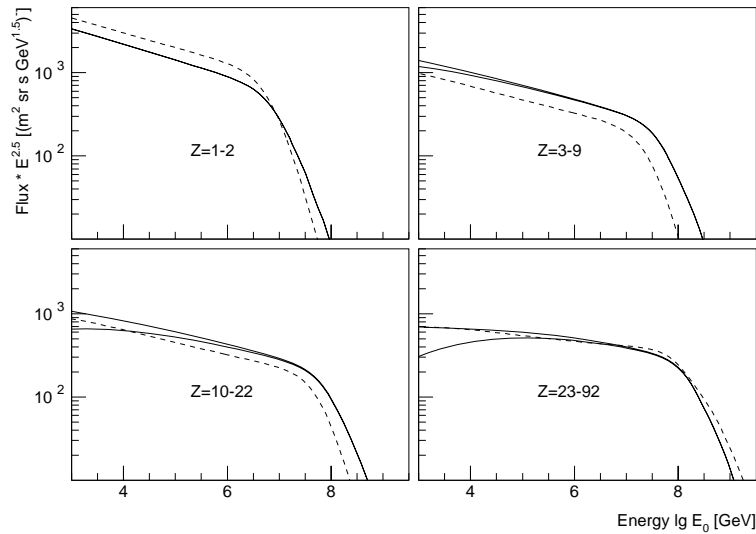


Figure 2: Energy spectra at Earth for elements with nuclear charge Z as indicated. The dashed lines represent spectra according to the poly gonato model, the solid lines are expected from the diffusion model discussed, see text. Two solid lines are shown in each panel, representing an estimate for the uncertainties [5].

imum energy attained during acceleration. It can be concluded that the knee in the energy spectrum of cosmic rays has its origin most likely in both, acceleration and propagation processes.

It seems to be reasonable that the second knee around 400 PeV $\approx 92 \cdot E_k(p)$ is due to the cut-off of the heaviest elements in galactic cosmic rays. Considering the calculated escape path length and nuclear interaction length within the diffusion model, it seems to be reasonable that the spectra for heavy elements are flatter as compared to light elements. The calculations show also that even for the heaviest elements at the respective knee energies more than about 50% of the nuclei survive the propagation process without interactions. This may explain why ultra-heavy elements could contribute significantly ($\sim 40\%$) to the all-particle flux at energies around 400 PeV and thus explain the second knee in the energy spectrum.

References

- [1] A.G.W. Cameron. *Space Sci. Rev.*, 15:121, 1973.
- [2] M. Hillas. *Proc. 26th Int. Cosmic Ray Conf., Salt Lake City*, 4:225, 1999.
- [3] J.R. Hörandel. *Astropart. Phys.*, 19:193, 2003.
- [4] J.R. Hörandel. *astro-ph/0702370*, 2007.
- [5] J.R. Hörandel et al. *Astropart. Phys.*, 27:119, 2007.
- [6] S. Karakula et al. *Proc. Phys. Soc. A.*, 5:904, 1972.
- [7] G.B. Khristiansen. *Proc. 24th Int. Cosmic Ray Conf., Rome*, 2:772, 1995.
- [8] K. Kodaira. *Publ. Astron. Soc. Japan*, 26:255, 1974.
- [9] G.V. Kulikov and G.B. Khristiansen. *JETP*, 35:635, 1958.
- [10] M. Prouza and R. Šmida. *Astron. & Astroph.*, 410:1, 2003.
- [11] V.S. Ptuskin et al. *Astron. & Astroph.*, 268:726, 1993.
- [12] V.S. Ptuskin and V.N. Zirakashvili. *Astron. & Astroph.*, 429:755, 2005.
- [13] R.J. Rand and S.R. Kulkarni. *Astrophys. J.*, 343:760, 1989.
- [14] K.O. Thielheim and W. Langhoff. *Proc. Phys. Soc. A.*, 1:694, 1968.
- [15] V.N. Zirakashvili et al. *Izv. RAN ser. phys.*, 59:153, 1995.



Confinement of Cosmic Rays in Dark Matter clumps

W. DE BOER¹, V.ZHUKOV^{1,2}

¹ *Institut für Experimentelle Kernphysik, Universität Karlsruhe (TH), 76128 Karlsruhe, Germany*

² *Skobeltsyn Institute of Nuclear Physics, Moscow State University, 119992 Moscow, Russia*

zhukov@physik.uni-karlsruhe.de

Abstract: Some part of the relic Dark Matter is distributed in small-scale clumps which survived structure formation in inflation cosmological scenario. The annihilation of DM inside these clumps is a strong source of stable charged particles which can have a substantial density near the clump core. The streaming of the annihilation products from the clump can enhance irregularities in the galactic magnetic field. This can produce small scale variations in diffusion coefficient affecting propagation of Cosmic Rays.

Introduction

The Cosmic Ray (CR) propagation in the Galactic disk is described as a resonant scattering on the magneto hydrodynamic turbulences (MHD) with the scale equal to the particle Larmor radius $k_r^{-1} \sim r_g = pc/ZeB$ in the galactic magnetic field B . The MHD turbulences can propagate in space as Alfvén waves with the velocity $v_a \sim B/\sqrt{4\pi\rho_H}$, which depends on the interstellar gas density ρ_H and is in the order of 10-100 km/s. The spectral density of the waves is usually associated with fluctuations in interstellar medium (ISM) and follows a power law $W(k) \propto k^{\alpha-2}$, where $\alpha = 1/3$ for the Kolmogorov spectrum. The MHD waves interact with the CR and ISM and can be enhanced or damped, depending on the energy flow. The kinetic equation for the spectral density $W(r, k)$ in spherical coordinates can be written as [11]:

$$\frac{\partial W}{\partial t} + \frac{1}{r^2} \frac{\partial}{\partial r} v_a r^2 W - \frac{\partial v_a}{\partial r} \frac{\partial}{\partial k} k W = (G - S)W \quad (1)$$

The G term describes the enhancement of turbulences due to streaming of CR particles and S represents the damping. The growth of turbulences occurs when the CR streaming velocity v_s is larger than the Alfvén speed v_a [17]. The streaming velocity depends on the gradient of the CR density f which satisfies the diffusion equation:

$$\frac{1}{r^2} \frac{\partial}{\partial r} D \frac{\partial}{\partial r} r^2 f - V_c \frac{\partial f}{\partial r} - \frac{1}{r^2} \frac{\partial}{\partial r} r^2 V_c \frac{p}{3} \frac{\partial f}{\partial p} = -q(p, r), \quad (2)$$

where $q(r, p)$ is the source function, V_c is the convection velocity and energy losses are neglected.

The diffusion coefficient D at resonance is related to $W(k, r)$ as [1]: $D(r) \approx v r_g^2 B^2 / 12\pi W(k_r, r)$ and a high level of turbulences corresponds to a local confinement of particles. Since the enhancement and damping strongly depend on the local environment, this opens a possibility for large and small scale variations in propagation parameters and therefore CR density. On the large scale the MHD waves can be damped in the galactic disk of $z \sim 100$ pc, leading to a large diffusion coefficient. Outside the disk the $W(k, r)$ can be larger and propagation is dominated by convection if $V_c > D/r$ [15]. On small scales the diffusive propagation can be affected near the CR sources or in the dense gas clouds [13, 18]. In the model with isotropic propagation the locally observed CR fluxes are used to evaluate the CR distribution in the whole Galaxy and then to calculate the diffusive gamma rays [12]. The obtained size of diffusion zone of 1-4 kpc is compatible with observations of secondary CR (B, Be, subFe) but contradicts smaller angular gradients observed in diffusive gamma rays which requires larger halo [4]. The isotropic model also does not explain the excess of gamma rays in GeV range [10, 12]. The galactic rotation curve points to a large mass in the galactic halo which can be associated with the Dark Matter (DM). The DM can self annihilate and produce stable particles which will contribute to the gamma rays and CR fluxes. Here we consider how the DM can affect the galactic model.

Dark Matter annihilation in clumps

The N-body cosmological simulations and analytical calculations show that in the inflation scenario the smallest DM structures originate from initial primordial fluctuations. These primordial DM clumps are partially destroyed during evolution contributing to the bulk DM but 0.001-0.1 of relic DM can still reside in the clumps, depending on initial conditions [9, 8]. The density profile inside the clumps is cuspy $\rho_{cl} \propto 1/r^{1.5-2.0}$ but is probably saturated at some critical density ρ_0 forming a dense core. The clump mass distribution follows $n(M)dM \sim M^{-2}$ with the minimum mass defined by free streaming of DM particles just after kinetic decoupling $M_{cl}^{min} \sim 10^{-8} - 10^{-6}M_{\odot}$ [2]. The local number density distribution n_{cl} of such clumps can vary in the range of $\sim 0.1 - 100 \text{ pc}^{-3}$ depending on density profile and tidal destruction [2, 8]. Inside the clump, the DM of mass m_{χ} will annihilate producing stable particles: protons, antiprotons, positrons, electrons and gamma rays, which can be observed on top of the ordinary CR fluxes. The luminosity of the clump for a i -component is: $q_i(r, p) = \frac{\langle \sigma v \rangle Y_i(p)}{m_{\chi}^2} \int \rho(x)_{cl}^2 dx$, where Y_i is the yield per annihilation. For most of DM candidates the annihilation goes into fermions, predominantly quark-antiquarks, which after fragmentation will produce for $m_{\chi} = 100 \text{ GeV}$: ~ 3 positrons or electrons, 0.3 protons or antiprotons and 8 gamma at 1 GeV. The precise energy spectrum is well measured in accelerator experiments, for protons and antiprotons below 1 GeV the $q(p) \sim \text{const}$ and for electrons and positrons $q(p) \sim p^{-1}$. The $\langle \sigma v \rangle$ is the thermally averaged annihilation cross section which can be estimated from the observed relic DM density in time of decoupling ($T_{dec} \sim \frac{m_{\chi}}{20}$) $\langle \sigma v \rangle \approx \frac{(2 \cdot 10^{-27} \text{ cm}^3 \text{ s}^{-1})}{\Omega_{\chi} h^2}$, where $\Omega_{\chi} h^2 = 0.113 \pm 0.009$ [16]. Nowadays ($T \sim 1.8K < T_{dec}$) the cross section can be the same or only smaller [6]. However the total annihilation signal can be boosted by clumpiness of DM, so called boost factor. The clumps are much denser than the bulk profile and most of the signal will come from the core of most abundant smallest clumps. The DM annihilation (DMA) signal is decreasing fast with the DM mass, at least as m_{χ}^2 , and the boost factor is limited by $< 10^3$ [2] thus limiting the observabil-

ity of heavy DM $m_{\chi} > 100 \text{ GeV}$. Taking a clump with $M_{cl} = 2 \cdot 10^{-8} M_{\odot}$ and 100 AU size with the average density of 100 GeV/cm^3 , the total yield for GeV charged particles will be $\sim 10^{23} \text{ s}^{-1}$ for $m_{\chi} = 100 \text{ GeV}$. Assuming the isothermal distribution of clumps in the galactic halo of 20 kpc diameter and normalizing at $n_{cl}(8.5 \text{ kpc}) = 10 \text{ pc}^{-3}$, the total luminosity from the DM annihilation in GeV range in 100 years will be $\sim 10^{45}$ particles, to be compared with the SNR explosion delivering $\sim 10^{51}$ particles per explosion in the galactic disk. Despite small luminosity the DM clump is a compact and constant source and the local density of produced particles can significantly exceed the galactic average $\langle \rho_{cr} \rangle \sim 10^{-10} \text{ cm}^{-3}$ producing a gradient in CR density distribution.

MHD turbulences initiated by DM annihilation

The streaming of charged DMA products from the cuspy clump will increase the level of local MHD turbulences. The amplification of MHD waves parallel to magnetic field lines can be presented as [17, 1]: $G(r, k) \approx \frac{\pi^2 e^2 v_a}{k c^2} \int \int dp d\mu v p^2 (1 - \mu^2) \delta(p|\mu| - \frac{eB}{kc}) \times (\frac{\partial f}{\partial \mu} + \frac{v_a p}{v} \frac{\partial f}{\partial p})$, where μ is the cosine of scattering angle and $\frac{\partial f}{\partial \mu} \sim \frac{p^2 c^2}{4\pi^2 e^2 W} \frac{\partial f}{\partial r}$ is the anisotropic term of the CR density distribution which can be obtained from integration of diffusion equation (2). The transverse waves are averaged out along propagation path and scattering is not efficient, that is, only turbulences along local field lines will be amplified by streaming, this asymmetry is neglected in this study. The growth is reduced by different damping mechanisms. Different possibilities can be considered: a dense molecular cloud with $\rho_H \sim 10 - 10^5 \text{ cm}^{-3}$, a hot plasma region and the galactic halo. The strongest damping takes place in the dense neutral gas n_H due to ions-neutral friction which dissipates energy as $S_H \sim \frac{1}{2} \langle \sigma_{col} v_a \rangle n_H$, where $\langle \sigma_{col} v \rangle \sim 10^{-9} \text{ cm}^3 \text{ s}^{-1}$ is the collisional cross section [?]. In the hot underdense gas the growth is suppressed by larger v_a and ionized gas density n_{HII} [17]. The collision of opposite waves leads to a nonlinear damping proportional to the level of magnetic turbulences $S_{nl} \approx \frac{4\pi v_t W}{B^2 r_g^2} = S_{nl}^0 W$, v_t is the gas thermal velocity $\sim v_a$ [1]. The fast magne-

tosonic waves with the Kraichnan spectrum can be also dumped at small scales by the CR themselves [14], this is not considered here. The simplified solution of the kinetic equation for $W(r, k = k_r)$ (1), neglecting momentum dependency for GeV particles, convection term in (2) and assuming point like source function $q(r) = q_0\delta(r)$, has a form:

$$W(r) \sim \frac{\exp(-g/r - s_H r)}{r^2(C_0 + s_{nl}\exp(-g/r - s_H r)/g)}$$

where $g \sim \langle\sigma v\rangle Y_{tot} \frac{\rho_a^2}{cm_\chi^2}$ is related to the total clump liminosity, $s_H = S_H/v_a$, $s_{nl} = S_{nl}^0/v_a \ll s_H$ are the dampings, and C_0 is a normalization factor. In the steady state it will result in an exponential increase of $W(r)$ near the clump core followed by a decrease $\propto r^{-2}$, see Figure 1. Since the spectrum of annihilated particles is limited by m_χ , the $W(k)$ distribution will be cutoff at $k \sim \frac{eE}{m_\chi}$. Thus the anisotropic streaming will create a region around a clump with small diffusion D_{in} , aligned with the local B field and with the size defined by the clump DM density, annihilation and dumping rates. The velocity of the clump proper motion and the convection speed should be below the local v_a in order to have stable environments for the growth. The turbulences will be strongly suppressed in the dense gas region although the DMA particles produced in the cusp of the clump still can be confined. In the underdense area in the galactic disk, like the Local Bubble, or in the galactic halo, the DM clump can be a substantial source of small scale MHD waves. The effect on CR propagation will be especially large if the diffusion coefficient inside clumps is much smaller than outside $D_{in} \ll D_{ext}$. The confinement zones with the size of r_{cl} can trap the annihilation products and CR for a time $\sim r_{cl}^2/D_{in}$ thus increasing local CR density. In a self-consistent model the zone with a large diffusion is limited by the thin galactic disk and the convection is dominant in the halo[15]. If the convection and distance between clumps are large enough, the back scattering of DMA produced particles into galactic disk can be small and will contribute a little to the observed CR fluxes, but the gamma rays and radio waves from these areas can be observed. First, the gamma rays produced directly from annihilation will produce a bump in the spectrum at $E \sim 0.1m_\chi$ [7]. This can reproduce the gamma

rays energy spectrum and angular gradients observed by EGRET [10, 7]. Second, the electrons and positrons trapped near the clump will contribute to the lower energy gamma rays via Inverse Compton and to radio waves by the synchrotron radiation. The DMA contributions to the charged CR will depend on the location of nearest clumps and the local environment. The local confinement combined with a large external convection and anisotropic diffusion will reduce the fluxes of antiprotons and positrons from DMA in comparison with the DMA gamma flux [3]. The secondary CR from nuclear interactions will be reduced too but can be recovered if CR are trapped in local molecular cloud structure [5].

Conclusion

The annihilation of DM in clumps can be a source of MHD waves which affect the propagation of CR with $E < m_\chi$. The growth of the MHD waves can be large for the light DM candidate, like the SUSY neutralino with $m_\chi \sim 100$ GeV which has largest annihilation cross section, and cuspy DM clump profile. The created turbulences are damped by ion-neutral interactions in the dense gas regions but in the galactic halo or underdense areas the DM clumps can produce trapping zones with increased particle density. The gamma rays from the DM annihilation in clumps can be related to the observed by EGRET excess in GeV range. The DMA gamma rays angular profiles depend upon clumps distribution in the galaxy. The abundantly produced in DM annihilation electrons and positrons will lose energy via inverse Compton and synchrotron radiation contributing to the low energy gamma rays and radio waves. The contribution of charged DMA products to the observed CR fluxes will strongly depend on the local propagation parameters and can be reduced in case of anisotropic propagation and small scale confinement.

Acknowledgments

The authors thanks H.J. Völk, V.S. Ptuskin, V. I. Dokuchaev and B. Moore for useful discussions.

References

- [1] V. S. Berezinskii, S. V. Bulanov, V. A. Dogiel, and V. S. Ptuskin. *Astrophysics of cosmic rays*. Amsterdam: North-Holland, 1990., 1990.
- [2] V. Berezinsky, V. Dokuchaev, and Y. Eroshenko. *Phys. Rev. D*, 68(10):103003, November 2003.
- [3] L. Bergström, J. Edsjö, M. Gustafsson, and P. Salati. *JCAP*, 5:6, 2006.
- [4] D. Breitschwerdt, V. A. Dogiel, and H. J. Völk. *Astron. Astrophys.*, 385:216, 2002.
- [5] B. D. G. Chandran. *Astroph. J.*, 529:513, 2000.
- [6] W. de Boer, C. Sander, V. Zhukov, A. V. Gladyshev, and D. I. Kazakov. *Phys. Rev. Lett.*, 95(20):209001, 2005.
- [7] W. de Boer, C. Sander, V. Zhukov, A. V. Gladyshev, and D. I. Kazakov. *Astron. Astrophys.*, 444:51, 2005.
- [8] T. Goerdt, O. Y. Gnedin, B. Moore, J. Diekmann, and J. Stadel. *MNRAS*, 375:191, 2007.
- [9] A. V. Gurevich, K. P. Zybin, and V. A. Sirota. *Sov. Phys. Usp.*, 167:913, 1997.
- [10] S. D. Hunter and et al. *Astroph. J.*, 481:205, 1997.
- [11] R. Kulsrud and W. P. Pearce. *Astroph. J.*, 156:445, 1969.
- [12] Igor V. Moskalenko, A. W. Strong, J. F. Ormes, and S. G. Mashnik. *Adv. Space Res.*, 35:156, 2005.
- [13] P. Padoan and J. Scalzo. *Astroph. J. Lett.*, 624:L97, 2005.
- [14] V. S. Ptuskin and et al. *Astroph. J.*, 642:902, 2006.
- [15] V. S. Ptuskin, H. J. Voelk, V. N. Zirakashvili, and D. Breitschwerdt. *Astron. Astrophys.*, 321:434, 1997.
- [16] D. N. Spergel and et al. *Astroph. J. Supp.*, 148:175, 2003.
- [17] D. G. Wentzel. *ARA&A*, 12:71, 1974.
- [18] E. G. Zweibel and J. M. Shull. *Astroph. J.*, 259:859, 1982.

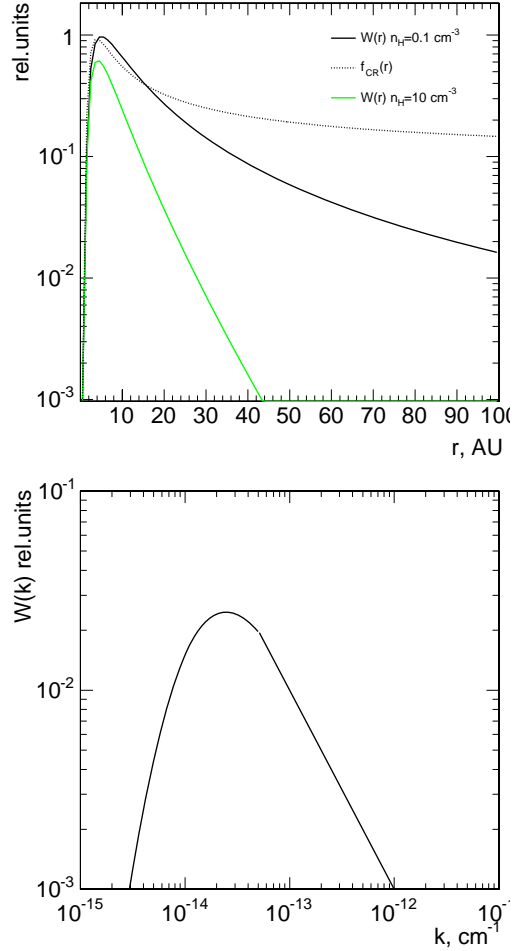


Figure 1: The $W(r)$ spatial distribution and particles distributions f_{CR} in the DM clump for GeV particles, $v_a \sim 10^6 \text{ cm/s}$ and $B \sim 1 \mu\text{G}$. The energy spectrum of $W(k)$ for $m_\chi = 100 \text{ GeV}$.

KASCADE-Grande Collaboration

(as of July 2007)

W.D. Apel^a, J.C. Arteaga^{a,1}, F. Badea^{a,2}, K. Bekk^a, M. Bertaina^b, J. Blümer^{a,c}, H. Bozdog^a, I.M. Brancus^d, M. Brüggemann^e, P. Buchholz^e, A. Chiavassa^b, F. Cossavella^c, K. Daumiller^a, V. de Souza^c, F. Di Pierro^b, P. Doll^a, R. Engel^a, J. Engler^a, M. Finger^c, D. Fuhrmann^f, P.L. Ghia^g, H.J. Gils^a, R. Glasstetter^f, C. Grupen^e, A. Haungs^a, D. Heck^a, J.R. Hörandel^{c,3}, T. Huege^a, P.G. Isar^a, K.-H. Kampert^f, D. Kickelbick^e, H.O. Klages^a, Y. Kolotaev^e, P. Luczak^h, H.J. Mathes^a, H.J. Mayer^a, C. Meurer^a, J. Milke^a, B. Mitrica^d, A. Morales^a, C. Morello^g, G. Navarra^b, S. Nehls^a, J. Oehlschläger^a, S. Ostapchenko^{a,4}, S. Over^e, M. Petcu^d, T. Pierog^a, S. Plewnia^a, H. Rebel^a, M. Roth^a, H. Schieler^a, O. Simaⁱ, M. Stümpert^c, G. Toma^d, G.C. Trinchero^g, H. Ulrich^a, J. van Buren^a, W. Walkowiak^e, A. Weindl^a, J. Wochele^a, J. Zabierowski^h

^a *Institut für Kernphysik, Forschungszentrum Karlsruhe, 76021 Karlsruhe, Germany*

^b *Dipartimento di Fisica Generale dell'Università, 10125 Torino, Italy*

^c *Institut für Experimentelle Kernphysik, Universität Karlsruhe, 76021 Karlsruhe, Germany,*

^d *National Institute of Physics and Nuclear Engineering, 7690 Bucharest, Romania*

^e *Fachbereich Physik, Universität Siegen, 57068 Siegen, Germany*

^f *Fachbereich Physik, Universität Wuppertal, 42097 Wuppertal, Germany*

^g *Istituto di Fisica dello Spazio Interplanetario, INAF, 10133 Torino, Italy*

^h *Soltan Institute for Nuclear Studies, 90950 Lodz, Poland*

ⁱ *Department of Physics, University of Bucharest, 76900 Bucharest, Romania*

¹ *permanent address: CINVESTAV, Mexico D.F., Mexico*

² *on leave of absence from Nat. Inst. of Phys. and Nucl. Engineering, Bucharest, Romania*

³ *now at: Dept. of Astrophysics, Radboud University Nijmegen, The Netherlands*

⁴ *on leave of absence from Moscow State University, 119899 Moscow, Russia*

LOPES Collaboration

(as of May 2007)

W.D. Apel^a, J.C. Arteaga^{a,1}, T. Asch^b, J. Auffenberg^c, F. Badea^{a,2}, L. Bähren^d, K. Bekk^a, M. Bertaina^e, P.L. Biermann^f, J. Blümer^{a,9}, H. Bozdog^a, I.M. Brancus^h, M. Brüggemannⁱ, P. Buchholzⁱ, S. Buitink^j, H. Butcher^d, A. Chiavassa^e, F. Cossavella^g, K. Daumiller^a, V. de Souza^g, F. Di Pierro^e, P. Doll^a, R. Engel^a, H. Falcke^{d,j}, H. Gemmeke^b, P.L. Ghia^k, R. Glasstetter^c, C. Grupenⁱ, A. Haungs^a, D. Heck^a, J.R. Hörandel^j, A. Horneffer^j, T. Huege^a, P.G. Isar^{a,3}, K.-H. Kampert^c, D. Kickelbickⁱ, Y. Kolotaevⁱ, O. Krömer^b, J. Kuijpers^j, S. Lafebre^j, P. Luczak^l, H.J. Mathes^a, H.J. Mayer^a, C. Meurer^a, J. Milke^a, B. Mitrica^h, C. Morello^k, G. Navarra^e, S. Nehls^a, A. Nigl^j, J. Oehlschläger^a, S. Ostapchenko^{a,4}, S. Overⁱ, M. Petcu^h, J. Petrovic^{j,5}, T. Pierog^a, S. Plewnia^a, J. Rautenberg^c, H. Rebel^a, M. Roth^a, H. Schieler^a, O. Sima^m, K. Singh^j, M. Stümpert^g, G. Toma^h, G.C. Trinchero^k, H. Ulrich^a, J. van Buren^a, W. Walkowiakⁱ, A. Weindl^a, J. Wochele^a, J. Zabierowski^l, J.A. Zensus^f

^a Institut für Kernphysik, Forschungszentrum Karlsruhe, 76021 Karlsruhe, Germany

^b Inst. Prozessdatenverarbeitung und Elektronik, Forschungszentrum Karlsruhe, Germany

^c Fachbereich Physik, Universität Wuppertal, 42097 Wuppertal, Germany

^d ASTRON, 7990 AA Dwingeloo, The Netherlands

^e Dipartimento di Fisica Generale dell'Università, 10125 Torino, Italy

^f Max-Planck-Institut für Radioastronomie, 53010 Bonn, Germany

^g Institut für Experimentelle Kernphysik, Universität Karlsruhe, 76021 Karlsruhe, Germany

^h National Institute of Physics and Nuclear Engineering, 7690 Bucharest, Romania

ⁱ Fachbereich Physik, Universität Siegen, 57068 Siegen, Germany

^j Dept. of Astrophysics, Radboud University Nijmegen, 6525 ED Nijmegen, The Netherlands

^k Istituto di Fisica dello Spazio Interplanetario, INAF, 10133 Torino, Italy

^l Soltan Institute for Nuclear Studies, 90950 Lodz, Poland

^m Department of Physics, University of Bucharest, 76900 Bucharest, Romania

¹ permanent address: CINVESTAV, Mexico D.F., Mexico

² on leave of absence from Nat. Inst. of Phys. and Nucl. Engineering, Bucharest, Romania

³ on leave of absence from Inst. for Space Science, Bucharest, Romania

⁴ on leave of absence from Moscow State University, 119899 Moscow, Russia

⁵ now at: NIKHEF, Amsterdam, The Netherlands



The Pierre Auger Collaboration

J. ABRAHAM⁶, P. ABREU⁵⁷, M. AGLIETTA⁴³, C. AGUIRRE⁸, D. ALLARD²², I. ALLEKOTTE¹, J. ALLEN⁷⁶, P. ALLISON⁷⁸, C. ALVAREZ⁴⁷, J. ALVAREZ-MUÑIZ⁶³, M. AMBROSIO⁴⁶, L. ANCHORDOQUI^{77, 89}, S. ANDRINGA⁵⁷, J.C. ANJOS¹⁰, A. ANZALONE⁴², C. ARAMO⁴⁶, S. ARGIRÒ⁴⁰, K. ARISAKA⁸¹, E. ARMENGAUD²², F. ARNEODO⁴⁴, F. ARQUEROS⁶⁰, T. ASCH²⁸, H. ASOREY¹, P. ASSIS⁵⁷, B.S. ATULUGAMA⁷⁹, J. AUBLIN²¹, M. AVE⁸², G. AVILA⁴, T. BÄCKER³², D. BADAGNANI⁵, A.F. BARBOSA¹⁰, H.M.J. BARBOSA¹³, D. BARNHILL⁸¹, S.L.C. BARROSO¹⁰, P. BAULEO⁷⁰, J. BEATTY⁷⁸, T. BEAU²², B.R. BECKER⁸⁷, K.H. BECKER²⁶, J.A. BELLIDO^{88, 79}, S. BENZVI⁷², C. BERAT²⁵, T. BERGMANN³¹, P. BERNARDINI⁴¹, X. BERTOU¹, P.L. BIERMANN²⁹, P. BILLOIR²⁴, O. BLANCH-BIGAS²⁴, F. BLANCO⁶⁰, P. BLASI^{35, 45}, C. BLEVE⁶⁶, H. BLÜMER^{31, 27}, M. BOHÁČOVÁ²⁰, C. BONIFAZI¹⁰, R. BONINO⁴³, M. BORATAV²⁴, J. BRACK⁸³, P. BROGUEIRA⁵⁷, W.C. BROWN⁷¹, J.M. BRUNET²², P. BUCHHOLZ³², N.G. BUSCA⁸², K.S. CABALLERO-MORA³¹, B. CAI⁸⁵, D.V. CAMIN³⁶, J.N. CAPDEVIELLE²², R. CARUSO³⁹, A. CASTELLINA⁴³, O. CATALANO⁴², G. CATALDI⁴¹, L. CAZÓN-BOADO⁸², R. CESTER⁴⁰, J. CHAUVIN²⁵, A. CHIAVASSA⁴³, J.A. CHINELLATO¹³, A. CHOU⁷³, J. CHYE⁷⁵, P.D.J. CLARK⁶⁵, R.W. CLAY⁷, S.B. CLAY⁷, E. COLOMBO³, R. CONCEIÇÃO⁵⁷, B. CONNOLLY⁷², F. CONTRERAS⁴, J. COPPENS^{51, 53}, A. CORDIER²³, U. COTTI⁴⁹, S. COUTU⁷⁹, C.E. COVAULT⁶⁸, A. CREUSOT⁵⁸, J. CRONIN⁸², S. DAGORET-CAMPAGNE²³, K. DAUMILLER²⁷, B.R. DAWSON⁷, R.M. DE ALMEIDA¹³, L.A. DE CARVALHO¹³, C. DE DONATO³⁶, S.J. DE JONG⁵¹, G. DE LA VEGA⁶, W.J.M. DE MELLO JUNIOR¹³, J.R.T. DE MELLO NETO¹⁷, I. DE MITRI⁴¹, V. DE SOUZA³¹, L. DEL PERAL⁶¹, O. DELIGNY²¹, A. DELLA SELVA³⁷, C. DELLE FRATTE³⁸, H. DEMBINSKI³⁰, C. DI GIULIO³⁸, J.C. DIAZ⁷⁵, C. DOBRIGKEIT¹³, J.C. D'OLIVO⁵⁰, D. DORNIC²¹, A. DOROFEEV⁷⁴, M.T. DOVA⁵, D. D'URSO³⁷, M.A. DUVERNOIS^{84, 85}, R. ENGEL²⁷, L. EPELE⁵, M. ERDMANN³⁰, C.O. ESCOBAR¹³, A. ETCHEGOYEN³, P. FACAL SAN LUIS⁶³, H. FALCKE^{54, 51}, G. FARRAR⁷⁶, A.C. FAUTH¹³, D. FAZIO³⁹, N. FAZZINI⁷³, A. FERNÁNDEZ⁴⁷, F. FERRER⁶⁸, S. FERRY⁵⁸, B. FICK⁷⁵, A. FILEVICH³, A. FILIPČIČ⁵⁸, I. FLECK³², R. FONTE³⁹, D. FUHRMANN²⁶, W. FULGIONE⁴³, B. GARCÍA⁶, D. GARCIA-PINTO⁶⁰, X. GARRIDO²³, H. GEENEN²⁶, G. GELMINI⁸¹, H. GEMMEKE²⁸, P.L. GHIA⁴³, M. GILLER⁵⁶, H. GLASS⁷³, M.S. GOLD⁸⁷, G. GOLUP¹, F. GOMEZ ALBARRACIN⁵, M. GÓMEZ BERISSO¹, R. GÓMEZ HERRERO⁶¹, P. GONÇALVES⁵⁷, M. GONÇALVES DO AMARAL¹⁸, D. GONZALEZ³¹, J.G. GONZALEZ⁷⁴, M. GONZÁLEZ⁴⁸, D. GÓRA^{31, 55}, A. GORGI⁴³, P. GOUFFON¹¹, V. GRASSI³⁶, A. GRILLO⁴⁴, C. GRUNFELD⁵, C. GRUPEN³², Y. GUARDINCERRI⁵, F. GUARINO³⁷, G.P. GUEDES¹⁴, J. GUTIÉRREZ⁶¹, J.D. HAGUE⁸⁷, J.C. HAMILTON²⁴, D. HARARI¹, S. HARMSMA⁵², J.L. HARTON⁷⁰, A. HAUNGS²⁷, M.D. HEALY⁸¹, T. HEBBEKER³⁰, D. HECK²⁷, C. HOJVAT⁷³, P. HOMOLA⁵⁵, J. HRANDEL⁵¹, A. HORNEFFER⁵¹, M. HORVAT⁵⁸, M. HRABOVSKÝ²⁰, T. HUEGE²⁷, M. IARLORI³⁵, A. INSOLIA³⁹, F. IONITA⁸², A. ITALIANO³⁹, M. KADUCAK⁷³, K.H. KAMPERT²⁶, B. KEILHAUER³¹, E. KEMP¹³, R.M. KIECKHAFER⁷⁵, H.O. KLAGES²⁷, M. KLEIFGES²⁸, J. KLEINFELLER²⁷, R. KNAPIK⁷⁰, J. KNAPP⁶⁶, D.-H. KOANG²⁵, Y. KOLOTAEV³², A. KOPMANN²⁸, O. KRMER²⁸, D. KÜMPFEL²⁶, N. KUNKA²⁸, A. KUSENKO⁸¹, G. LA ROSA⁴², C. LACHAUD²², B.L. LAGO¹⁷, D. LEBRUN²⁵, P. LEBRUN⁷³, J. LEE⁸¹, M.A. LEIGUI DE OLIVEIRA¹⁶, A. LETESSIER-SELVON²⁴, M. LEUTHOLD³⁰, I. LHENRY-YVON²¹, R. LÓPEZ⁴⁷, A. LOPEZ AGÜERA⁶³, M.C. MACCARONE⁴², C. MACOLINO³⁵, S. MALDERA⁴³, M. MALEK⁷³, G. MANCARELLA⁴¹, M.E. MANCEÑIDO⁵, D. MANDAT²⁰, P. MANTSCH⁷³, A.G. MARIAZZI⁵, I.C. MARIS³¹, D. MARTELLO⁴¹, J. MARTÍNEZ⁴⁸, O. MARTÍNEZ⁴⁷, H.J. MATHES²⁷, J. MATTHEWS^{74, 80}, J.A.J. MATTHEWS⁸⁷, G. MATTHIAE³⁸, G. MAURIN²², D. MAURIZIO⁴⁰, P.O. MAZUR⁷³, T. MCCAULEY⁷⁷, M. MCEWEN⁷⁴, R.R. MCNEIL⁷⁴, M.C. MEDINA³, G. MEDINA-TANCO⁵⁰, A. MELI²⁹, D. MELO³, E. MENICETTI⁴⁰

A. MENSHIKOV²⁸, CHR. MEURER²⁷, R. MEYHANDAN^{52, 74}, M.I. MICHELETTI³, G. MIELE³⁷, W. MILLER⁸⁷, S. MOLLERACH¹, M. MONASOR^{60, 61}, D. MONNIER RAGAIGNE²³, F. MONTANET²⁵, B. MORALES⁵⁰, C. MORELLO⁴³, E. MORENO⁴⁷, J.C. MORENO⁵, C. MORRIS⁷⁸, M. MOSTAFÁ⁸⁸, M.A. MULLER¹³, R. MUSSA⁴⁰, G. NAVARRA⁴³, L. NELLE⁵⁰, C. NEWMAN-HOLMES⁷³, D. NEWTON⁶³, T. NGUYEN THI⁹⁰, N. NIERSTENHFER²⁶, D. NITZ⁷⁵, H. NOGIMA¹³, D. NOSEK¹⁹, L. NOŽKA²⁰, J. OEHLISCHLÄGER²⁷, T. OHNUKI⁸¹, A. OLINTO⁸², L.F.A. OLIVEIRA¹⁷, V.M. OLMOS-GILBAJA⁶³, M. ORTIZ⁶⁰, S. OSTAPCHENKO³¹, L. OTERO⁶, M. PALATKA²⁰, J. PALLOTTA⁶, G. PARENTE⁶³, E. PARIZOT²², S. PARLATI⁴⁴, M. PATEL⁶⁶, T. PAUL⁷⁷, V. PAVLIDOU⁸², M. PECH²⁰, J. PEKALA⁵⁵, R. PELAYO⁴⁸, I.M. PEPE¹⁵, L. PERRONE⁴¹, S. PETRERA³⁵, P. PETRINCA³⁸, Y. PETROV⁷⁰, DIEP PHAM NGOC⁹⁰, DONG PHAM NGOC⁹⁰, T.N. PHAM THI⁹⁰, A. PICHEL², R. PIEGAIA⁵, T. PIEROG²⁷, M. PIMENTA⁵⁷, V. PIRRONELLO³⁹, O. PISANTI³⁷, M. PLATINO³, J. POCHON¹, T.A. PORTER⁷⁴, L. PRADO JUNIOR¹³, P. PRIVITERA³⁸, M. PROUZA⁷², E.J. QUEL⁶, J. RAUTENBERG²⁶, H.C. REIS¹², S. REUCROFT⁷⁷, B. REVENU²², J. ŘÍDKÝ²⁰, S. RIGGI³⁹, M. RISSE²⁶, V. RIZI³⁵, S. ROBBINS²⁶, M. ROBERTS⁷⁹, C. ROBLEDÓ⁴⁷, G. RODRIGUEZ⁶³, D. RODRÍGUEZ FRÍAS⁶¹, J. RODRIGUEZ MARTINO³⁸, J. RODRIGUEZ ROJO³⁸, G. ROS^{60, 61}, J. ROSADO⁶⁰, M. ROTH²⁷, C. ROUCELLE²⁴, B. ROUILLÉ-D'ORFEUIL²⁴, E. ROULET¹, A.C. ROVERO², F. SALAMIDA³⁵, H. SALAZAR⁴⁷, G. SALINA³⁸, F. SÁNCHEZ²⁶, M. SANTANDER⁴, C.E. SANTO⁵⁷, E.M. SANTOS¹⁰, F. SARAZIN⁶⁹, S. SARKAR⁶⁴, R. SATO⁴, V. SCHERINI²⁶, H. SCHIELER²⁷, F. SCHMIDT⁸², T. SCHMIDT³¹, O. SCHOLTEN⁵², P. SCHOVÁNEK²⁰, F. SCHÜSSLER²⁷, S.J. SCIUTTO⁵, M. SCUDERI³⁹, A. SEGRETO⁴², D. SEMIKOZ²², M. SETTIMO⁴¹, R.C. SHELLARD¹⁰, I. SIDELNIK³, B.B. SIFFERT¹⁷, G. SIGL²², N. SMETNIANSKY DE GRANDE³, A. SMIAŁKOWSKI⁵⁶, R. ŠMÍDA²⁰, B.E. SMITH⁶⁶, G.R. SNOW⁸⁶, P. SOKOLSKY⁸⁸, P. SOMMERS⁷⁹, J. SOROKIN⁷, H. SPINKA^{67, 73}, R. SQUARTINI⁴, E. STRAZZERI³⁸, A. STUTZ²⁵, F. SUAREZ⁴³, T. SUOMIJÄRVI²¹, A.D. SUPANITSKY⁵⁰, M. SUTHERLAND⁷⁸, J. SWAIN⁷⁷, Z. SZADKOWSKI⁵⁶, J. TAKAHASHI¹³, A. TAMASHIRO², A. TAMBURRO³¹, O. TAŞÇAU²⁶, R. TICONA⁹, J. TIPPENBERG⁵, C. TIMMERMANS^{53, 51}, W. TKACZYK⁵⁶, C.J. TODERO PEIXOTO¹³, B. TOMÉ⁵⁷, A. TONACHINI⁴⁰, D. TORRESI⁴², P. TRAVNICEK²⁰, A. TRIPATHI⁸¹, G. TRISTRAM²², D. TSCHERNIAKHOVSKI²⁸, M. TUEROS⁵, V. TUNNICLIFFE⁶⁵, R. ULRICH²⁷, M. UNGER²⁷, M. URBAN²³, J.F. VALDÉS GALICIA⁵⁰, I. VALIÑO⁶³, L. VALORE³⁷, A.M. VAN DEN BERG⁵², V. VAN ELEWYCK²¹, R.A. VÁZQUEZ⁶³, D. VEBERIČ⁵⁸, A. VEIGA⁵, A. VELARDE⁹, T. VENTERS⁸², V. VERZI³⁸, M. VIDELA⁶, L. VILLASEÑOR⁴⁹, S. VOROBIOV⁵⁸, L. VOJVODIC⁷³, H. WAHLBERG⁵, O. WAINBERG³, T. WALDENMAIER³¹, P. WALKER⁶⁵, D. WARNER⁷⁰, A.A. WATSON⁶⁶, S. WESTERHOFF⁷², C. WIEBUSCH³⁰, G. WIECZOREK⁵⁶, L. WIENCKE⁸⁸, B. WILCZYŃSKA⁵⁵, H. WILCZYŃSKI⁵⁵, C. WILEMAN⁶⁶, M.G. WINNICK⁷, J. XU²⁸, T. YAMAMOTO⁸², P. YOUNK⁷⁵, E. ZAS⁶³, D. ZAVRTANIK⁵⁸, M. ZAVRTANIK⁵⁸, A. ZECH²⁴, A. ZEPEDA⁴⁸, M. ZIOLKOWSKI³²

¹ Centro Atómico Bariloche (CNEA); Instituto Balseiro (CNEA and UNCuyo); CONICET, 8400 San Carlos de Bariloche, Río Negro, Argentina

² Instituto de Astronomía y Física del Espacio (CONICET), CC 67, Suc. 28 (1428) Buenos Aires, Argentina

³ Departamento de Física, Centro Atómico Constituyentes, CNEA, Av. Gral. Paz 1499, (1650) San Martín, Buenos Aires, Argentina

⁴ Pierre Auger Southern Observatory, Av. San Martín Norte 304, (5613) Malargüe, Prov. De Mendoza, Argentina

⁵ Universidad Nacional de la Plata, Facultad de Ciencias Exactas, Departamento de Física and IFLP/CONICET; Univ. Nac. de Buenos Aires, FCEyN, Departamento de Física, C.C. 67, (1900) La Plata, Argentina

⁶ Universidad Tecnológica Nacional, Regionales Mendoza y San Rafael; CONICET; CEILAP-CITEFA, Observatorio Meteorológico de Mendoza, Av. Arq. Carlos Thays s/n, 5500 Mendoza, Argentina

⁷ University of Adelaide, Dept. of Physics, Adelaide, S.A. 5005, Australia

⁸ Universidad Católica de Bolivia, Av. 16 Julio 1732, POB 5829, La Paz, Bolivia

⁹ Universidad Mayor de San Andrés, Av. Villazón N 1995, Monoblock Central, Bolivia

¹⁰ Centro Brasileiro de Pesquisas Físicas, Rua Dr. Xavier Sigaud, 150, CEP 22290-180 Rio de Janeiro, RJ, Brazil

¹¹ Universidade de São Paulo, Inst. de Física, Cidade Universitária Caixa Postal 66318, Caixa Postal 66318, 05315-970 São Paulo, SP, Brazil

¹² Universidade de São Paulo, Instituto Astronômico e Geofísico, Cidade Universitária, Rua do Matao 1226, 05508-900 São Paulo, SP, Brazil

- ¹³ *Universidade Estadual de Campinas, Gleb Wataghin Physics Institute (IFGW), Departamento de Raios Cosmicos e Cronologia, CP 6165, 13083-970, Campinas, SP, Brazil*
- ¹⁴ *Univ. Estadual de Feira de Santana, Departamento de Fisica, Campus Universitario, BR 116, KM 03, 44031-460 Feira de Santana, Brazil*
- ¹⁵ *Universidade Federal da Bahia, Campus da Ondina, 40210- 340 Salvador, BA, Brazil*
- ¹⁶ *Universidade Federal do ABC, Centro de Ciências Naturais e Humanas, Rua Santa Adélia, 166, Bairro Bangu, 09.210-170 Santo André, SP, Brazil*
- ¹⁷ *Univ. Federal do Rio de Janeiro (UFRJ), Instituto de Física, Cidade Universitaria, Caixa Postal 68528, 21945-970 Rio de Janeiro, RJ, Brazil*
- ¹⁸ *Univ. Federal Fluminense, Inst. de Fisica, Campus da Praia Vermelha, 24210-340 Niterói, RJ, Brazil*
- ¹⁹ *Charles University, Institute of Particle & Nuclear Physics, Faculty of Mathematics and Physics, V Holesovickach 2, CZ-18000 Prague 8, Czech Republic*
- ²⁰ *Institute of Physics of the Academy of Sciences of the Czech Republic, Na Slovance 2, CZ-182 21 Praha 8, Czech Republic*
- ²¹ *Institut de Physique Nucléaire, Université Paris-Sud 11 and IN2P3/CNRS, 15, rue Georges Clemenceau, 91400 Orsay, France*
- ²² *Laboratoire AstroParticule et Cosmologie, Université Paris VII, 11, Place Marcelin Berthelot, F-75231 Paris CEDEX 05, France*
- ²³ *Laboratoire de l'Accélérateur Linéaire, Université Paris-Sud 11 and IN2P3/CNRS, BP 34, Batiment 200, F-91898 Orsay cedex, France*
- ²⁴ *Laboratoire de Physique Nucléaire et de Hautes Energies, Université Paris 6 & 7 and IN2P3/CNRS, 4 place Jussieu, 75252 Paris Cedex 05, France*
- ²⁵ *Laboratoire de Physique Subatomique et de Cosmologie (LPSC), IN2P3/CNRS, Université Joseph-Fourier (Grenoble 1), 53, ave. des Martyrs, F-38026 Grenoble CEDEX, France*
- ²⁶ *Bergische Universität Wuppertal, Fachbereich C - Physik, GaußStr. 20, D - 42097 Wuppertal, Germany*
- ²⁷ *Forschungszentrum Karlsruhe, Institut für Kernphysik, Postfach 3640, D - 76021 Karlsruhe, Germany*
- ²⁸ *Forschungszentrum Karlsruhe, Institut für Prozessdatenverarbeitung und Elektronik, Postfach 3640, D - 76021 Karlsruhe, Germany*
- ²⁹ *Max-Planck-Institut für Radioastronomie, Auf dem Hügel 69, D - 53121 Bonn, Germany*
- ³⁰ *RWTH Aachen, III. Physikalisches Institut A, Physikzentrum, Huyskensweg, D - 52056 Aachen, Germany*
- ³¹ *Universität Karlsruhe (TH), Institut für Experimentelle Kernphysik (IEKP), Postfach 6980, D - 76128 Karlsruhe, Germany*
- ³² *Universität Siegen, Fachbereich 7 Physik - Experimentelle Teilchenphysik, Emmy Noether-Campus, Walter- Flex-Str. 3, D - 57068 Siegen, Germany*
- ³⁵ *Dipartimento di Fisica dell'Università de l'Aquila and INFN, Via Vetoio, I-67010 Coppito, Aquila, Italy*
- ³⁶ *Dipartimento di Fisica dell'Università di Milano and Sezione INFN, via Celoria 16, I-20133 Milan, Italy*
- ³⁷ *Dipartimento di Fisica dell'Università di Napoli "Federico II" and Sezione INFN, Via Cintia 2, 80123 Napoli, Italy*
- ³⁸ *Dipartimento di Fisica dell'Università di Roma II "Tor Vergata" and Sezione INFN, Via della Ricerca Scientifica, I- 00133 Roma, Italy*
- ³⁹ *Dipartimento di Fisica dell'Università di Catania and Sezione INFN, Corso Italia, 57, I-95129 Catania, Italy*
- ⁴⁰ *Dipartimento di Fisica Sperimentale dell'Università di Torino and Sezione INFN, Via Pietro Giuria, 1, I-10125 Torino, Italy*
- ⁴¹ *Dipartimento di Fisica, Università del Salento and Sezione INFN, via Arnesano, I-73100 Lecce, Italy*
- ⁴² *Istituto di Astrofisica Spaziale e Fisica Cosmica di Palermo (INAF), Via Ugo La Malfa 153, I-90146 Palermo, Italy*
- ⁴³ *Istituto di Fisica dello Spazio Interplanetario (INAF), sezione di Torino and Dipartimento di Fisica Generale dell'Università and INFN Torino, Via P. Giuria 1, 10125 Torino, Italy*
- ⁴⁴ *INFN, Laboratori Nazionali del Gran Sasso, Strada Statale 17/bis Km 18+910, I-67010 Assergi (L'Aquila), Italy*
- ⁴⁵ *Osservatorio Astrofisico di Arcetri, Largo E. Fermi 5, I-50125 Florence, Italy*
- ⁴⁶ *Sezione INFN di Napoli, Complesso Universitario di Monte Sant' Angelo, Via Cinthia, I-80126 Napoli, Italy*

- ⁴⁷ *Benemérita Universidad Autónoma de Puebla (BUAP), Ap. Postal J – 48, 72500 Puebla, Puebla, Mexico*
- ⁴⁸ *Centro de Investigación y de Estudios Avanzados del IPN (CINVESTAV), Apartado Postal 14-740, 07000 México, D.F., Mexico*
- ⁴⁹ *Universidad Michoacana de San Nicolas de Hidalgo (UMSNH), Edificio C-3 Cd Universitaria, C.P. 58040 Morelia, Michoacan, Mexico*
- ⁵⁰ *Universidad Nacional Autonoma de Mexico (UNAM), Apdo. Postal 20-364, 01000 Mexico, D.F., Mexico*
- ⁵¹ *Institute of Mathematics, Astrophysics and Particle Physics (IMAPP), Radboud University, 6500 GL Nijmegen, Netherlands*
- ⁵² *Kernfysisch Versneller Instituut (KVI), University of Groningen, Zernikelaan 25, NL-9747 AA Groningen, Netherlands*
- ⁵³ *NIKHEF, POB 41882, NL-1009 DB Amsterdam, Netherlands*
- ⁵⁴ *ASTRON, PO Box 2, 7990 AA Dwingeloo, Netherlands*
- ⁵⁵ *Institute of Nuclear Physics PAN, Radzikowskiego 52, 31-342 Cracow, Poland*
- ⁵⁶ *University of Łódź, Pomorska 149/153, 90 236 Łódź, Poland*
- ⁵⁷ *Laboratório de Instrumentação e Física Experimental de Partículas, Avenida Elias Garcia, 14-1, P-1000-149 Lisboa, Portugal*
- ⁵⁸ *University of Nova Gorica, Laboratory for Astroparticle Physics, Vipavska 13, POB 301, SI-5000 Nova Gorica, Slovenia*
- ⁶⁰ *Departamento de Física Atomica, Molecular y Nuclear, Facultad de Ciencias Fisicas, Universidad Complutense de Madrid, E-28040 Madrid, Spain*
- ⁶¹ *Space Plasmas and Astroparticle Group, Universidad de Alcalá, Pza. San Diego, s/n, 28801 Alcalá de Henares (Madrid), Spain*
- ⁶³ *Departamento de Física de Partículas, Campus Sur, Universidad, E-15782 Santiago de Compostela, Spain*
- ⁶⁴ *Rudolf Peierls Centre for Theoretical Physics, University of Oxford, Oxford OX1 3NP, United Kingdom*
- ⁶⁵ *Institute of Integrated Information Systems, School of Electronic Engineering, University of Leeds, Leeds LS2 9JT, United Kingdom*
- ⁶⁶ *University of Leeds, School of Physics and Astronomy, Leeds, LS2 9JT, United Kingdom*
- ⁶⁷ *Argonne National Laboratory, HEP Division, Argonne, IL 60439, United States*
- ⁶⁸ *Case Western Reserve University, Dept. of Physics, Cleveland, OH 44106, United States*
- ⁶⁹ *Department of Physics, Colorado School of Mines, Golden, CO 80401, United States*
- ⁷⁰ *Colorado State University, Department of Physics, Fort Collins, CO 80523, United States*
- ⁷¹ *Department of Physics, Colorado State University, Pueblo, CO 81001, United States*
- ⁷² *Columbia University, Dept. of Physics, New York, NY 10027, United States*
- ⁷³ *Fermilab, MS367, POB 500, Batavia, IL 60510-0500, United States*
- ⁷⁴ *Louisiana State University, Dept. of Physics and Astronomy, Baton Rouge, LA 70803-4001, United States*
- ⁷⁵ *Michigan Technological University, Physics Dept., 1400 Townsend Drive, Houghton, MI 49931-1295, United States*
- ⁷⁶ *New York University, Physics Department, 4 Washington Place, New York, NY 10003, United States*
- ⁷⁷ *Northeastern University, Department of Physics, 110 Forsyth Street, Boston, MA 02115-5096, United States*
- ⁷⁸ *Ohio State University, 2400 Olentangy River Road, Columbus, OH 43210-1061, United States*
- ⁷⁹ *Pennsylvania State University, Department of Physics, 104 Davey Lab, University Park, PA 16802-6300, United States*
- ⁸⁰ *Southern University, Dept. of Physics, Baton Rouge, LA 70813-0400, United States*
- ⁸¹ *University of California, Los Angeles (UCLA), Department of Physics and Astronomy, Los Angeles, CA 90095, United States*
- ⁸² *University of Chicago, Enrico Fermi Institute, 5640 S. Ellis Ave., Chicago, IL 60637, United States*
- ⁸³ *University of Colorado, Physics Department, Boulder, CO 80309-0446, United States*
- ⁸⁴ *High Energy Physics Group, University of Hawaii, 2505 Correa Rd., Honolulu, HI 96822, United States*
- ⁸⁵ *University of Minnesota, School of Physics and Astronomy, 116 Church St. SE, Minneapolis, MN 55455, United States*

⁸⁶ *University of Nebraska, Dept. of Physics and Astronomy, 116 Brace Lab, Lincoln, NE 68588-0111, United States*

⁸⁷ *University of New Mexico, Dept. of Physics and Astronomy, 800 Yale, Albuquerque, NM 87131, United States*

⁸⁸ *University of Utah, 115 S. 1400 East # 201, Salt Lake City, UT 84112-0830, United States*

⁸⁹ *University of Wisconsin-Milwaukee, Dept. of Physics, Milwaukee, WI 53201, United States*

⁹⁰ *Institute for Nuclear Science and Technology (INST), 5T-160 Hoang Quoc Viet Street, Nghia Do, Cau Giay, Hanoi, Vietnam*